

<https://doi.org/10.15388/vu.thesis.490>

<https://orcid.org/0000-0001-7169-5717>

VILNIUS UNIVERSITY

CENTER FOR PHYSICAL SCIENCES AND TECHNOLOGY

Rimantė Bandzevičiūtė

# Fiber Based ATR IR Spectroscopy for Cancerous Tissue Diagnostics

**DOCTORAL DISSERTATION**

Natural Sciences,  
Physics (N 002)

VILNIUS 2023

The dissertation was prepared between 2018 and 2022 at the Institute of Chemical Physics, Vilnius University.

**Academic supervisor** – prof. dr. Justinas Čeponkus (Vilnius University, Natural Sciences, Physics, N 002).

**Academic consultant** – Prof. Habil. Dr. Gerald Steiner (Dresden University of Technology, Natural Sciences, Physics, N 002).

This doctoral dissertation will be defended in a public meeting of the Dissertation Defence Panel:

**Chairman** – Prof. Dr. Eglė Lastauskienė (Vilnius University, Natural Sciences, Biology, N 010).

**Members:**

Prof. Dr. Saulius Bagdonas (Vilnius University, Natural Sciences, Physics, N 002),

Dr. Iryna Doroshenko (Taras Shevchenko National University of Kyiv, Natural Sciences, Physics, N 002),

Dr. Renata Karpič (Center for Physical Sciences and Technology, Natural Sciences, Physics, N 002),

Dr. Lina Mikoliūnaitė (Center for Physical Sciences and Technology, Natural Sciences, Chemistry, N 003).

The dissertation shall be defended at a public meeting of the Dissertation Defence Panel at 11:00 on 3<sup>rd</sup> of July 2023 in Room A101 of the National Center for Physical Sciences and Technology.

Address: Saulėtekio av. 3, NFTMC, Room A101, Vilnius, Lithuania

Tel. +37052648884 ; el. paštas office@ftmc.lt

The text of this dissertation can be accessed at the libraries of Vilnius University, as well as on the website of Vilnius University:

[www.vu.lt/lt/naujienos/ivykiu-kalendorius](http://www.vu.lt/lt/naujienos/ivykiu-kalendorius)

<https://doi.org/10.15388/vu.thesis.490>

<https://orcid.org/0000-0001-7169-5717>

VILNIAUS UNIVERSITETAS  
FIZINIŲ IR TECHNOLOGIJOS MOKSLŲ CENTRAS

Rimantė Bandzevičiūtė

# Šviesolaidinė ATR IR spektroskopija vėžinių audinių diagnostikoje

**DAKTARO DISERTACIJA**

Gamtos mokslai,  
Fizika (N 002)

VILNIUS 2023

Disertacija rengta 2018 – 2022 metais Vilniaus universiteto Cheminės fizikos institute.

**Mokslinis vadovas** – prof. dr. Justinas Čeponkus (Vilniaus universitetas, gamtos mokslai, fizika, N 002).

**Mokslinis konsultantas** – prof. habil. dr. Gerald Steiner (Drezdeno technikos universitetas, gamtos mokslai, fizika, N 002).

Gynimo taryba:

**Pirmininkė** – prof. dr. Eglė Lastauskienė (Vilniaus universitetas, gamtos mokslai, biologija, N 010).

**Nariai:**

prof. dr. Saulius Bagdonas (Vilniaus universitetas, gamtos mokslai, fizika, N 002),

dr. Iryna Doroshenko (Kijevo Taraso Ševčenkos nacionalinis universitetas, gamtos mokslai, fizika, N 002),

dr. Renata Karpič (Fizinių ir technologijos mokslų centras, gamtos mokslai, fizika, N 002),

doc. dr. Lina Mikoliūnaitė (Fizinių ir technologijos mokslų centras, gamtos mokslai, Chemija, N 003).

Disertacija ginama viešame Gynimo tarybos posėdyje 2023 m. liepos mėn. 3 d. 11 val. Nacionalinio fizinių ir technologijos mokslų centro A101 konferencijų salėje.

Adresas: Saulėtekio al. 3, NFTMC, A101, Vilnius, Lietuva.

Tel. +37052648884 ; el. paštas office@ftmc.lt

Disertaciją galima peržiūrėti Vilniaus universiteto, Fizinių ir technologijos mokslų centro bibliotekose ir VU interneto svetainėje adresu:

<https://www.vu.lt/naujienos/ivykiu-kalendorius>

## TABLE OF CONTENTS

LIST OF ABBREVIATIONS .....	8
INTRODUCTION.....	10
GOAL AND TASKS OF THE THESIS .....	13
STATEMENTS OF THE THESIS.....	13
PUBLICATIONS INCLUDED IN THE THESIS .....	14
PUBLICATIONS NOT INCLUDED IN THE THESIS .....	14
CONFERENCE PROCEEDINGS .....	15
CONFERENCE ABSTRACTS.....	15
SCIENTIFIC NOVELTY.....	17
AUTHOR'S CONTRIBUTION.....	18
1. CHAPTER 1. APPLICATION OF IR SPECTROSCOPY FOR BIOMEDICAL DIAGNOSTICS .....	20
1.1. IR spectroscopy of cancerous tissues.....	20
1.2. IR fiber probes .....	23
1.3. IR spectra interpretation and analysis .....	26
1.4. The reliability of diagnostic methods.....	27
2. CHAPTER 2. DESIGN OF FIBER-BASED ATR IR SPECTROSCOPIC SYSTEM .....	30
2.1. Modification of commercial FT-IR spectrometer Alpha (Bruker Optik GmbH, Ettlingen, Germany) for fiber-based measurements .....	30
2.2. Design of the ATR probe .....	36
2.2.1.OCT imaging of the ATR probe tip.....	36
2.2.2.Geometry of the ATR crystal and penetration depth of the IR radiation into the sample.....	36
2.3. Determination of the sample composition .....	39
3. CHAPTER 3. APPLICATION FOR KIDNEY CANCER .....	43
3.1. Kidney cancer .....	43
3.2. Experimental details.....	45
3.2.1. Tissue sample collection.....	45

3.2.3. Statistical analysis.....	47
3.3. Spectroscopic analysis: results and discussion .....	50
3.3.1. Tissue smears measured by using conventional ATR spectrometer.....	50
3.3.2. Tissue smears and tissues measured by using fiber-based spectroscopy system .....	59
4. CHAPTER 4. APPLICATION FOR URINARY BLADDER CANCER.....	69
4.1. Urinary bladder cancer.....	69
4.2. Experimental details.....	70
4.2.1. Tissue sample collection.....	70
4.2.2. FT-IR spectroscopy measurements of tissue samples.....	70
4.2.3. Statistical analysis.....	71
4.3. Spectroscopic analysis: results and discussion .....	71
5. CHAPTER 5. APPLICATION FOR PANCREAS CANCER.....	90
5.1. Pancreatic disorders .....	90
5.2. Experimental details.....	91
5.2.1. Tissue sample preparation.....	91
5.2.2. FT-IR spectroscopy measurements of tissue samples.....	92
5.2.3. Statistical analysis.....	92
5.3. Results and discussion .....	92
5.3.1. Intraoperative case analysis.....	101
6. CHAPTER 6. APPLICATION FOR LIVER CANCER.....	105
6.1. Liver tumors.....	105
6.2. Experimental details.....	106
6.2.1. Tissue sample preparation.....	106
6.2.2. FT-IR spectroscopy measurements of tissue samples.....	106
6.2.3. Statistical analysis.....	107
6.3. Results and discussion .....	107
OVERVIEW AND FUTURE PROSPECTS.....	117

CONCLUSIONS .....	119
BIBLIOGRAPHY .....	121
APPENDIX .....	140
SANTRAUKA LIETUVIŲ KALBA.....	171
ACKNOWLEDGEMENTS .....	190
CURRICULUM VITAE .....	191
NOTES .....	193

## LIST OF ABBREVIATIONS

- 5-ALA – 5-aminolaevulinic acid
- ATP - Adenosine triphosphate
- ATR – Attenuated total reflection
- CCC – Cholangiocellular carcinoma
- ccRCC – Clear cell renal cell carcinoma
- DAPI – 4',6-diamidino-2-phenylindole
- DNA - Deoxyribonucleic acid
- DTGS – Deuterated triglycine sulphate
- ECM – Extracellular matrix
- FIR – Far-Infrared
- FT-IR – Fourier transform infrared
- Ge – Germanium
- H&E - Hematoxylin and eosin
- HAL - Hexaminolevulinate
- HCA – Hierarchical cluster analysis
- HCC – Hepatocellular carcinoma
- ICG - Indocyanine green
- IPMN – Intraductal papillary mucinous neoplasm
- IR - Infrared
- IRE – Internal reflectance element
- MCT – Mercury cadmium telluride
- MIBC – Muscle-invasive bladder cancer
- MIR – Middle infrared
- MIR – Mid-Infrared



NIR – Near-Infrared

NMIBC – Non-muscle-invasive bladder cancer

NPV – Negative prognostic value

OCT - Optical coherence tomography

PC – Principle component

PCA – Principal component analysis

PDAC – Pancreatic ductal adenocarcinoma

PDD – Photodynamic diagnosis

PPV – Positive prognostic value

RCC – Renal cell carcinoma

RNA - Ribonucleic acid

S/N – Signal to noise ratio

SDHB - Succinate dehydrogenase-deficient

SMA - SubMiniature version A

TURB – Transurethral resection of urinary bladder

VIS - Visible

WHO – World Health Organization

WLC – White light cystoscopy

## INTRODUCTION

Cancer is a leading cause of death with estimated 19.3 million new cases and 10 million cancer related deaths worldwide in 2020 [1]. Treatment of cancer covers various methods of which surgery, chemotherapy and radiation therapy are the most widely applied approaches. The most frequent and in certain cases the only curative treatment for various types of solid tumors is surgical operation. The final outcome of the patient, quality of life after the surgery and overall survival highly depends on the resection margin status of the malignant tumor.

In order to prevent recurrence of the tumor, it has to be entirely excised, while as much functional healthy tissue as possible should be preserved to minimise the risk of complications and save vital functions of the organ. Microscopic infiltrations of tumorous cells can be invisible by macroscopic evaluation of the tissue in resection area. Thus, intraoperative histopathologic consultation is performed to aid the surgeon to evaluate surgical resection margins and ensure the clearance of microscopic tumor infiltrations in marginal area. Histological frozen section examination is often applied to aid the surgical decision making, however, it has some limitations. The assessment of the resected tissue specimen takes additional time that results in prolongation of the surgical operation and anaesthesia time. The tissue sample that is being analysed has to be frozen by using liquid nitrogen, and then sliced. In addition, hematoxylin and eosin (H&E) staining should be applied prior the microscopic evaluation. The examination is performed in a specified pathology laboratory; thus the resected sample has to be transferred from the operating room. The transportation, tissue preparation and evaluation can last around 40 minutes [2], and if the tissue sample is of inappropriate quality, the examination has to be repeated. Although frozen section examination is considered a reliable method and is routinely used as a standard of practice for tissue evaluation [3]–[6], some studies describe discrepancy between frozen section examination and final pathology diagnosis [7], with discrepancy rates of 5 – 15 % [8]. The accuracy and discrepancy rates vary depending on tissue type and institution where analysis was performed [4], [7]. Discrepancy is mostly caused by interpretation and sampling issues [4]. The accuracy of diagnosis is affected by quality of the sample, limited time for interpretation and experience of the pathologist. Also, some sampling errors due to technical reasons can arise here. Tissue structure, sectioning and staining can be affected by freezing, which can lead to difficulties of interpretation. Moreover, only few areas of the suspicious tissue can be

examined due to limited time [9]. Regarding the issues highlighted above, new rapid and reliable methods for intraoperative tissue evaluation are required.

Methods of optical spectroscopy including fluorescence, Raman scattering, and infrared (IR) spectroscopy become more and more widely applied for the investigation of biological tissues in the field of surgical oncology. Fluorescence guided surgery is already being used for several types of oncological surgery [8], [10]. During the surgery, this method allows to visualize different tissue types such as normal tissue and malignant lesions that would not be visible under the naked eye inspection. However, there are some limitations. In order to visualize different tissue types, fluorescence contrast agent has to be inserted into the body before the investigation to be accumulated in the targeted tumorous tissue area. Suitable contrast agents should be chosen for specific tissues since different tumors have different biomarkers. Currently, the most frequently employed fluorophores are indocyanine green (ICG), methylene blue, 5-aminolevulinic acid (5-ALA) and fluorescein sodium, however, valid contrast agents have not yet been established for several types of tumors [8]. While establishing a suitable contrast agent, attention should be paid to its pharmacokinetic profile and features of biomarkers of the specific tissue [11], [12].

In this regard, vibrational spectroscopy methods (Raman scattering and Infrared absorption) have advantage since they are label-free methods without requirement of tissue staining or chemical processing prior to the examination.

Methods of spontaneous and coherent Raman scattering spectroscopy were applied for the tumorous tissue identification in human and animal models and showed promising results [13]. In particular, applied fiber-based technique for examination of various tissue types showed the ability to perform the investigation under *in vivo* conditions [14]–[17]. However, Raman spectroscopy has some limitations. Raman scattering is a relatively weak process therefore particularly sensitive detectors should be used so that signals of low intensity could still be observed. Also, depending on the wavelength and power of the laser that is used for the excitation of the Raman scattering, undesirable effects of fluorescence background in the Raman spectra can be observed. Attention should be paid to the surrounding light sources as well: radiation from the other light sources used in the operating room could interfere with the operating mode of the detector and have influence on the obtained spectra. Additionally, the usage of laser radiation in Raman spectroscopy can be problematic: the power of the laser and the integration time of the measurement should be carefully selected in order to avoid the damage of the tissue. At the same time, laser power and integration time should be sufficient to ensure detectable Raman signal intensity and

reasonable duration of the experiment so the surgery and anaesthesia time is not prolonged.

Meanwhile, power of IR radiation used in spectral analysis is low, thus, it is non-destructive for biological tissues and a spectrum can be obtained quite fast. IR spectroscopy is already used for cancer investigation by applying the method for a wide range of samples including tissues [18]–[20], cells [21]–[23], blood [24]–[28], sputum [29], urine [30], bladder wash [31], bile [32] or even extracellular vesicles [33]–[36]. Applied methods cover conventional techniques such as infrared transmission, microspectroscopy and attenuated total reflection (ATR). In most cases, conventional methods require a special sample preparation as well as placement of the samples to the special compartment inside the spectrometer. Also, standard spectrometers usually are bulky and non-manoeuvrable which is an obstacle for the implementation of the method into the operating room. Application of fiber optics for the IR spectroscopy brings the method one step closer to clinical diagnostics. This provides the capability of performing the spectral measurements under *in situ* conditions without the requirement for tissue transfer. Moreover, mobile devices of small dimensions could be coupled with fiber optics thus allowing the transfer of the equipment almost anywhere in the operating room without disturbing the flow of the surgery.

## GOAL AND TASKS OF THE THESIS

Taking into account all the challenges of tumorous tissue diagnostics mentioned above, there is an obvious need for portable, real time and reliable spectroscopic system capable of tissue assessment performed under *in situ* and even under *in vivo* conditions. The main goal of the thesis is to adapt the fiber based ATR IR spectroscopy system for the application for biological tissue investigation suitable to perform under intraoperative conditions. To achieve this goal, following tasks were formulated:

1. To investigate the suitable configuration and parameters of the fiber based ATR IR spectroscopy set-up for biological tissue examination.
2. To implement the fiber based ATR IR spectroscopy system for spectra collection of freshly resected human tissues of various types of cancer: kidney, urinary bladder, pancreas and liver.
3. To characterize spectral markers suitable for kidney, urinary bladder, pancreas and liver tumorous tissue identification.
4. To apply statistical data analysis techniques for the classification of spectra of different tissue groups.
5. To determine the possibilities and limits of an intraoperative application of fiber based ATR IR spectroscopy for cancerous tissue diagnostics.

## STATEMENTS OF THE THESIS

1. Spectroscopic system based on fiber ATR IR probe coupled with conventional portable spectrometer and external MCT detector, is sensitive enough for collecting informative spectra of freshly resected tissues.
2. Spectra, collected using fiber-based set-up, provides characteristic properties of different tissue types. Spectral markers such as glycogen, collagen and fructose 1,6-bisphosphatase can be used as spectral markers for differentiation of normal and tumorous tissues.
3. There is no universal spectral tumor marker suitable for cancer detection in all human organs. The specific set of spectral markers for tumorous tissue identification should be established for each organ.
4. Fiber-based ATR IR spectroscopy combined with appropriate statistical analysis methods applied for various human organ (kidney, bladder, pancreas and liver) tissues allows successful differentiation of normal and tumorous tissue up to 100 %.

## PUBLICATIONS INCLUDED IN THE THESIS

1. M. Pučetaitė, M. Velička, V. Urbonienė, J. Čeponkus, R. Bandzevičiūtė, F. Jankevičius, A. Želvys, V. Šablinskas, G. Steiner, Rapid intra-operative diagnosis of kidney cancer by ATR-IR spectroscopy of tissue smears, *Journal of biophotonics*, 2018, **11**, 1. DOI: 10.1002/jbio.201700260.
2. V. Šablinskas, R. Bandzevičiūtė, M. Velička, J. Čeponkus, V. Urbonienė, F. Jankevičius, A. Laurinavičius, D. Dasevičius, G. Steiner, Fiber attenuated total reflection infrared spectroscopy of kidney tissue during live surgery, *Journal of biophotonics*, 2020, **13**, 1. DOI: 10.1002/jbio.202000018.
3. R. Bandzevičiūtė, J. Čeponkus, M. Velička, V. Urbonienė, F. Jankevičius, A. Želvys, G. Steiner, V. Šablinskas, Fiber based infrared spectroscopy of cancer tissues, *Journal of molecular structure*, 2020, **1220**, 1. DOI: 10.1016/j.molstruc.2020.128724.
4. R. Bandzevičiūtė, G. Platkevičius, J. Čeponkus, A. Želvys, A. Čekauskas, V. Šablinskas, Differentiation of Urothelial Carcinoma and Normal Bladder Tissues by Means of Fiber-based ATR IR Spectroscopy, *Cancers*, 2023, **15**, 499. DOI: 10.3390/cancers15020499
5. R. Bandzeviciute, G. Steiner, K. Liedel, J. Golde, E. Koch, T. Welsch, C. Kahlert, D. Stange, M. Distler, J. Weitz, J. Ceponkus, V. Sablinskas, and C. Teske, Fast and label-free intraoperative discrimination of malignant pancreatic tissue by attenuated total reflection infrared spectroscopy, *Journal of Biomedical Optics*, 2023, **28**, 045004. DOI: 10.1117/1.JBO.28.4.045004

## PUBLICATIONS NOT INCLUDED IN THE THESIS

1. V. Vicka, A. Vickienė, J. Tutkus, J. Stanaitis, R. Bandzevičiūtė, D. Ringaitienė, S. Vosylius, J. Šipylaitė, Immediate aspiration of the drug infused via central venous catheter through the distally positioned central venous dialysis catheter: An experimental study, *JVA: The journal of vascular access*, 2021, **22**, 94. DOI: 10.1177/1129729820924555.
2. R. Bikmurzin, R. Bandzevičiūtė, A. Maršalka, A. Maneikis, L. Kalėdienė, FT-IR Method Limitations for  $\beta$ -Glucan Analysis, *Molecules*, 2022, **27**, 4616. DOI: 10.3390/molecules27144616.
3. M. Snicorius, M. Drevinskaite, M. Miglinas, A. Cekauskas, M. Stadulyte, R. Bandzeviciute, J. Ceponkus, V. Sablinskas, A. Zelvyys, A

Novel Infrared Spectroscopy Method for Analysis of Stone Dust for Establishing Final Composition of Urolithiasis, 2023, **47**, 36-42. DOI: 10.1016/j.euros.2022.11.007.

## CONFERENCE PROCEEDINGS

1. V. Šablinskas, M. Velička, M. Pučetaitė, V. Urbonienė, J. Čeponkus, R. Bandzevičiūtė, F. Jankevičius, T. Sakharova, O. Bibikova, G. Steiner, Proc. SPIE 10497, Imaging, Manipulation, and Analysis of Biomolecules, Cells, and Tissues XVI, 1049713. 2018 DOI: 10.1117/12.2289393
2. R. Bandzeviciute, G. Steiner, K. Liedel, J. Golde, E. Koch, T. Welsch, C. Kahlert, D. Stange, M. Distler, J. Weitz, J. Ceponkus, V. Sablinskas, and C. Teske, Fiber-based ATR-IR spectroscopy for an intraoperative diagnosis of normal pancreatic tissue, pancreatitis, and malignant pancreatic lesions, Proc. SPIE 12368, Advanced Biomedical and Clinical Diagnostic and Surgical Guidance Systems XXI, 123680H. 2023 DOI: 10.1117/12.2647405.

## CONFERENCE ABSTRACTS

1. R. Bandzevičiūtė, V. Urbonienė, F. Jankevičius, V. Šablinskas, Computer Assisted Identification of Cancerous Kidney Tissue by Means of FTIR Spectroscopy, Open Readings 61, Vilnius, Lithuania, 2018.
2. V. Sablinskas, M. Velicka, M. Pucetaite, V. Urboniene, J. Ceponkus, R. Bandzeviciute, F. Jankevicius, G. Steiner, In situ detection of cancerous kidney tissue by means of fiber ATR-FTIR spectroscopy, SPIE Photonics West, San Francisco, USA, 2018.
3. M. Velicka, M. Pucetaite, V. Urboniene, R. Bandzeviciute, J. Ceponkus, F. Jankevicius, V. Sablinskas, G. Steiner, ATR-FTIR spectroscopy: towards in vivo detection of cancerous tissue areas, 34th European Congress on Molecular Spectroscopy, Coimbra, Portugal, 2018.
4. R. Bandzevičiūtė, R. Platakytė, S. Adomavičiūtė, M. Velička, J. Čeponkus, V. Urbonienė, F. Jankevičius, V. Šablinskas, Optical fiber based spectroscopic device for in vivo detection of pathological tissue areas, Life Science Baltics, Vilnius, Lithuania, 2018.
5. G. Mickūnaitė, R. Bandzevičiūtė, Vibrational Spectroscopy of Human Gallstones, Open Readings 62, Vilnius, Lithuania, 2019.

6. R. Bandzeviciute, M. Velicka, J. Ceponkus, V. Urboniene, F. Jankevicius, V. Sablinskas, G. Steiner, Fiber Based Infrared Spectroscopy of Various Cancer Tissues, 15th International Conference on Molecular Spectroscopy, Wroclaw-Wojanow, Poland, 2019.
7. G. Mickūnaitė, R. Bandzevičiūtė, J. Čeponkus, G. J. Rudzikaitė, E. Olekaitė, A. Kirkliauskienė, V. Hendrixson, V. Šablinskas, Tulžies pūslės akmenų susiformavimo tyrimas Ramano sklaidos spektroskopiniu metodu, 43-ioji Lietuvos Nacionalinė fizikos konferencija, Kaunas, Lithuania, 2019.
8. R. Bandzevičiūtė, J. Čeponkus, M. Velička, V. Urbonienė, G. Mickūnaitė, F. Jankevicius, V. Šablinskas, G. Steiner, Šviesolaidinė ATR infraraudonoji spektroskopija vėžinių audinių diagnostikai, 43-ioji Lietuvos Nacionalinė fizikos konferencija, Kaunas, Lithuania, 2019.
9. G. Mickūnaitė, A. Kamarauskienė, J. Čeponkus, E. Lastauskienė, R. Bandzevičiūtė, Study of Pathogenic Bacteria and Fungi by Means of FT-IR ATR Spectroscopy, Open Readings 64, Vilnius, Lithuania, 2021.
10. R. Bandzevičiūtė, G. Platkevičius, J. Čeponkus, G. Mickūnaitė, A. Čekauskas, A. Želvys, V. Šablinskas, Detection of Malignant Human Bladder Tissue by Means of Fiber Based ATR IR Spectroscopy, Open Readings 64, Vilnius, Lithuania, 2021.
11. G. Anužienė, R. Bandzevičiūtė, E. Lastauskienė, J. Čeponkus, Patogeninių mikroorganizmų identifikavimas ATR IR spektriniu metodu, 44-oji Lietuvos Nacionalinė fizikos konferencija, Vilnius, Lithuania, 2021.
12. R. Bandzevičiūtė, J. Čeponkus, V. Šablinskas, C. Teske, G. Steiner, Šviesolaidinės ATR IR spektroskopijos taikymas kasos vėžinių audinių tyrimui, 44-oji Lietuvos Nacionalinė fizikos konferencija, Vilnius, Lithuania, 2021.
13. M. Stadulytė, R. Bandzevičiūtė, J. Čeponkus, M. Snicorius, A. Želvys, V. Šablinskas, Infrared Spectroscopy of Urinary Deposits. Open Readings 65, Vilnius, Lithuania, 2022.
14. G. Anužienė, R. Bandzevičiūtė, E. Lastauskienė, J. Čeponkus, ATR IR Spectroscopy Application for the Identification of Pathogenic Bacteria and Fungi, Open Readings 65, Vilnius, Lithuania, 2022.
15. R. Bandzevičiūtė, K. Liedel, C. Teske, C. Riediger-Schweipert, J. Čeponkus, V. Šablinskas, G. Steiner, Application of Fiber ATR IR



- Spectroscopy for Tumorous Liver Tissue Identification, Open Readings 65, Vilnius, Lithuania, 2022.
16. M. Snicorius, A. Želvys, M. Miglinas, M. Stadulytė, R. Bandzevičiūtė, J. Čeponkus, V. Šablinskas, FTIR ATR spectroscopy of urinary sediments and computed tomography as prediction tools for final stone composition, 7th Baltic Meeting in conjunction with the EAU (Baltic22), Vilnius, Lithuania, 2022.
  17. G. Platkevičius, R. Bandzevičiūtė, J. Čeponkus, A. Čekauskas, A. Želvys, V. Šablinskas, Ex vivo analysis of bladder urothelium and bladder cancer tissues by means of fiber based attenuated total reflection infrared spectroscopy, 7th Baltic Meeting in conjunction with the EAU (Baltic22), Vilnius, Lithuania, 2022.
  18. R. Bandzevičiūtė, J. Čeponkus, C. Teske, K. Liedel, G. Platkevičius, A. Želvys, V. Šablinskas, G. Steiner, Application of Fiber-based FT-IR ATR Spectroscopy for Tissue Diagnostics During Oncological Surgery, 3rd Baltic Biophysics Conference, Vilnius, Lithuania, 2022.
  19. G. Anužienė, A. Čiužas, R. Bandzevičiūtė, E. Lastauskienė, J. Čeponkus, Identification of Pathogenic Bacteria and Fungi by Means of ATR-IR Spectroscopy, 3rd Baltic Biophysics Conference, Vilnius, Lithuania, 2022.
  20. R. Bandzevičiūtė, G. Steiner, K. Liedel, J. Golde, E. Koch, T. Welsch, C. Kahlert, D. Stange, M. Distler, J. Weitz, J. Čeponkus, V. Šablinskas, C. Teske, Fiber-based ATR-IR spectroscopy for an intraoperative diagnosis of normal pancreatic tissue, pancreatitis, and malignant pancreatic lesions, SPIE Photonics West, San Francisco, USA, 2023.

## SCIENTIFIC NOVELTY

The study presented in this work describe an application of IR spectroscopy for human normal and tumorous tissue investigation suitable to exploit under intraoperative conditions. Methods of vibrational spectroscopy have been applied for the tissue characterization and tissue type identification for decades. However, translation of IR spectroscopy for clinical applications is still not implemented due to several reasons. Equipment used for the IR spectra collection by applying conventional methods is bulky and not suitable for the use in the operating room while the measurements have to be performed by transferring the tissue specimen from the patient into a special sample compartment inside the spectrometer. Moreover, samples need to be especially prepared before the tissue evaluation. Regarding mentioned

reasons, IR spectroscopy have been seen as more suitable for laboratory applications for tissue characterisation than as a clinical diagnostic method.

In this work, fiber-based spectroscopy system was applied for the measurements of IR spectra. Used ATR fiber probe allows to perform measurements under *in situ* or even *in vivo* conditions what is important for the intraoperative applications. Several studies showed a potential of fiber-based IR spectroscopy applications for tumorous tissue investigation. However, due to the lack of studies the method is still not implemented in clinical applications. In this work, fiber-based ATR IR spectroscopy was applied for the delineation between normal and tumorous tissues of various human organs. Results presented in the thesis are promising and show the potential of aiding the surgeons to evaluate surgical resection margins intraoperatively.

## AUTHOR'S CONTRIBUTION

*Establishment of parameters of the fiber-based spectroscopy system.* Experimental work was performed by group of researchers led by prof. V. Šablinskas. The author of the thesis contributed to the preparation of the corresponding publication by performing a part of the experimental work, writing, data analysis. OCT imaging of the ATR element presented in the thesis was performed in collaboration with Jonas Golde. DAPI staining of a tissue smear presented in this thesis was performed with a collaboration with Christian Teske.

*Kidney tissue smear analysis by applying conventional FT-IR spectrometer Alpha.* Experimental work was performed by group of researchers led by prof. V. Šablinskas. The author of the thesis contributed to the preparation of the corresponding publication by performing a part of the experimental work. Data analysis presented in the thesis was performed by author of the thesis.

*Kidney unprocessed tissue and tissue smear analysis by applying fiber-based spectroscopy system.* Experimental work was performed by author of the thesis. The author of the thesis contributed to the preparation of the corresponding publication by performing the experimental work, a part of writing, data analysis. Statistical data analysis presented in the thesis was performed by author of the thesis.

*Urinary bladder unprocessed tissue and tissue smear analysis by applying fiber-based spectroscopy system.* The author of the thesis contributed to the preparation of the corresponding publication by performing experimental work, writing a substantial part of the publication, data analysis. Data analysis presented in the thesis was performed by author of the thesis.

*Pancreas tissue analysis by applying fiber-based spectroscopy system.* The author of the thesis contributed to the preparation of the corresponding publication by performing the major part of the experimental work, a part of writing, data analysis. Statistical analysis presented in the thesis was performed by author of the thesis. Image of pancreas resection *in vivo* as well as resected tissue complex provided by Christian Teske. H&E staining and imaging of resected pancreas tissue sample presented in the thesis was performed by Katja Liedel.

*Liver tissue analysis by applying fiber-based spectroscopy system.* Experimental work and analysis presented in this work performed by the author of the thesis.

# 1. CHAPTER 1. APPLICATION OF IR SPECTROSCOPY FOR BIOMEDICAL DIAGNOSTICS

## 1.1. IR spectroscopy of cancerous tissues

IR spectroscopy is sensitive and selective method for material analysis – each molecule has its own set of vibration frequencies corresponding to characteristic spectral bands from which components of the sample can be determined. Therefore, various molecules and molecular groups can be identified by applying IR spectroscopy. Moreover, by applying appropriate measuring set-up, almost any sample in different states (solid, liquid and gas) can be examined.

Cells of all the living organisms are constituted of four main molecular groups: nucleic acids, proteins, lipids and carbohydrates. Biological tissue is a complex structure in which molecular substances are distributed in certain proportions characteristic to a particular type of tissue. Cancer arises due to uncontrollable cell proliferation rates. Tumor growth starts due to genetic mutations in normal cells leading to an increase of cell proliferation rates, a low cell differentiation, an invasiveness and a development of a new vascular network [37]. However, a tumor itself consists not only of tumorous cells – it is a set of tumorous and host cells, immune cells, blood vessels and ECM (extracellular matrix) [38]. Without blood vessels a tumor can grow only small in size (few millimeters in diameter) as supply of oxygen and nutrients is crucial for growth of a tumor [37], [39]. For this reason, vascular endothelial growth factors and cytokines inducing growth of a tumor vascular network occur in an interstitial fluid. Moreover, cancerous cells have higher glucose consumption rates [40], that is related to changed metabolic pathways. Usually, demand of energy (in a form of adenosine triphosphate (ATP)) in mammalian cells is satisfied by converting glucose into pyruvate and, in presence of oxygen, oxidizing it to carbon dioxide and water. Under hypoxic conditions, pyruvate is converted into lactic acid (anaerobic glycolysis). However, in some types of tumors glucose is converted to lactic acid even under aerobic conditions, this process is referred as Warburg effect [41]. Some types of tumors due to increased demand of energy store glycogen in their cells as a source of energy; such behavior is observed in breast, kidney, uterus, bladder, ovary, skin and brain cancers [42]. Another important factor in cancer development – ECM. It regulates major part cellular behavior and developmental processes [43]. ECM works as physical scaffold for tumorous cells as well as takes a part in promoting the dissemination of tumorous cells [38]. Some types of tumors tend to deposit large amounts of ECM

components, such as collagen, fibronectin, elastin and laminin secreted by fibroblasts. This process of growth of ECM matrix in tumor stroma is referred as desmoplastic reaction which is a common feature of tumors such as pancreatic adenocarcinoma (PDAC) and cholangiocellular carcinoma (CCC). While invading into surrounding host tissues, tumorous cells have tendency to destroy structures of normal host tissues by secreting enzymes. For example, in case of urothelial carcinoma, decrease of collagen in normal urinary bladder tissue can be related to secretion of collagenase by tumorous cells [44]. In general, a variety of changes are being observed in the microenvironment, metabolic pathways of cells during tumor formation. There is a variety of cancers which can arise in different organs, every tumor type has its own features: genetic alterations, metabolic and signalling pathways, specific microenvironment. Due to these factors, diverse biochemical changes occur in the tissue. The changed biochemical composition could be observed in the IR spectra; thus cancerous tissues can be identified based on spectral differences.

Attempts to apply IR spectroscopy for normal and neoplastic tissue characterization were already made in the middle of the last century [45]. From that time IR spectrometers were drastically improved: working principles of very first IR spectrometers were based on light dispersion by using prisms; later diffraction gratings were employed to obtain spectra. Lastly, Fourier-Transform IR (FT-IR) spectrometers were developed which predominantly are being used nowadays. FT-IR spectrometer works by obtaining an interferogram and subsequently converting it to an IR spectrum by applying Fourier transformation. This type of spectrometers has some advantages, such as an improved signal-to-noise (S/N) ratio of spectra and higher operating speed since the signal can be recorded for all wavelengths at the same time. Moreover, a variety of measuring set-ups can be used to obtain IR spectra. The principle of measurement of IR spectra is based on passing a beam of IR radiation through a thin sample and determining the fraction of the radiation which is being absorbed by the sample. Very first experiments relied on this principle – conventional transmission spectra were being recorded. Nowadays, technologies have improved, thus a variety of measuring set-ups, including conventional transmission, reflectance and microscopy methods are used for recording of IR spectra hereby leading to an easier investigation even of complex samples. During recent decades, as a result of improvements of methods of IR spectroscopy, IR spectroscopy is being more and more widely used for the investigation of pathological tissues. IR spectroscopy is being applied for the investigation of a variety of cancers arising in different organs such as brain [20], [46]–[61], breast [19], [62]–[78], colon-rectum [79]–[93],

kidney [94]–[100], liver [22], [27], [28], [101], lungs [102]–[104], ovaries [23], [105]–[108], cervix [109]–[113], pancreas [26], [114]–[118], prostate [35], [119]–[124], skin [125]–[143], urinary bladder [21], [144] and others.

Historically, as a conventional technique, IR microspectroscopic imaging was applied for tissue cryo-sections for cancerous tissue investigation at first. By applying microspectroscopic imaging, small areas of tissues with high spatial resolution can be analysed. However, this methodology has some limitations. Tissue samples have to be pre-processed: if the measurements are performed in transmission mode, thin slices of tissue sample have to be prepared. In order to cut thin slices of the tissue by using microtome, tissues usually have to be hardened by replacing water of the tissue with reagents such as paraffin, or tissues have to be frozen. Before the tissue infiltration with paraffin, tissue sample usually is formalin-fixed and dehydrated by ethanol subsequently cleared by using xylene or other less toxic reagents such as isopropanol. However, tissue chemical pre-processing is disadvantageous for investigation by IR spectroscopy since chemical reagents have strong IR spectra. M. Stefanakis et al showed that spectral bands of paraffin overlap with tissue spectral bands while absorbance values of spectral band corresponding to lipids are reduced in human salivary gland tissue after tissue dewaxing [145]. Although M. Stefanakis et al reported that formalin fixation does not have an impact for human salivary gland tissue chemical composition [145], V. Zohdi et al demonstrated that biochemical composition is significantly changed after formalin fixation of rat heart and liver tissues [146]. Generally, tissue chemical pre-processing results in a more complicated tissue spectra interpretation. Several studies showed successful discrimination of paraffin-embedded tumorous tissue [147]–[149]; however, analysis of such samples is not suitable for intraoperative tissue assessment due to long duration of sample preparation and more difficult spectral analysis. IR spectroscopy of frozen tissue sections (cryo-sections) has some limitations as well. After freezing-thawing cycle of thin tissue sections, chemical composition of the tissue can be changed; therefore, possible spectral tumor markers can be lost. For example, group of researchers led by V. Šablinskas, showed that glycogen is not observable by applying IR microspectroscopy for tissue cryo-sections [95]. Later, the group performed studies by applying IR microspectroscopy for tissue smears which showed that glycogen is an important spectral marker for kidney tumorous tissue identification [96]. Even though successful classification of IR spectra of tissue cryo-sections was performed, in this case, more complicated statistical analysis and classification models have to be applied for spectra of tissue cryo-sections compared to analysis of spectra of tissue smears in order to delineate normal and tumorous tissues. Albeit the

method is accurate, the results are highly dependent on the qualification of the researcher. In order to obtain reliable spectra, the sampling area should be carefully chosen as well as good focus of the radiation into the sample has to be achieved. Moreover, the instrumentation is complex and the method is more expensive compared to other measuring set-ups. Due to mentioned reasons, integration of IR microscopic imaging into intraoperative applications is complicated. In this regard, ATR technique is a good choice for tissue examination as tissue samples do not require any complex preparation. By applying ATR technique, spectra collection relies on internal reflection phenomenon. A beam of IR radiation is being passed through an internal reflectance element (IRE) towards a sample placed directly on the IRE. The refractive index of the IRE is higher than the refractive index of the sample, thus internal reflection occurs at the IRE-sample surface. A fraction of IR radiation penetrates into the sample and is being absorbed. By determining the fraction of light which is being absorbed, IR spectrum is obtained. Since the radiation should not be passed through the whole sample, thickness of the sample is not restricted. Therefore, tissue specimens can be examined immediately after excision.

In order to translate the method to clinical diagnostics, measurements have to be performed in real time and as close as possible to the patient. This is implemented by applying fiber optics. By applying fiber optics, tissue samples can be investigated under *in situ* or even *in vivo* conditions. Some attempts to apply fiber-based IR spectroscopy for tumorous tissue examination were already made and showed promising results [84], [85]. However, the method still is not being applied in clinical routine. Translation into clinical use is not that straightforward – compared to conventional techniques, obtained signal to noise ratio is significantly lower by applying fiber-probes as well as tips of the probes have to be biocompatible and easily sterilisable.

## 1.2. IR fiber probes

Optical fibers are widely used for signal transmission. For the transmission of optical signals in visible (VIS) and near-IR (NIR) radiation range, usually conventional silica glass fibers are used. However, silica fibers are not suitable for transmission of mid-IR (MIR) and far-IR (FIR) radiation due to the radiation absorption.

First attempts to fabricate IR fibers were made in the mid-1960s by using chalcogenide glasses for the fiber production [150]. Such fibers made of arsenic trisulfide were reported in 1965 by N. S. Kapany et al [151]; however, optical losses in fibers were high and fibers were brittle. Nowadays, IR fibers

can be made of several materials and can be grouped into three classes such as glass (including materials such as fluoride, chalcogenide), crystalline (sapphire, halide) and hollow waveguides [152]. Selection of the material from which fibers are produced have to satisfy several criteria: fibers have to be transparent for the radiation of wavelengths between 2 and 25  $\mu\text{m}$ ; materials of the fiber core and cladding should be chosen that the refractive indices would satisfy internal reflection condition; the fiber should have suitable mechanical properties (have to be mechanically robust).

Despite the technical progress in production of IR fibers, signal losses of IR fibers are quite high compared to conventional silica fibers used for radiation transmission in VIS region. Signal losses generally arise due to impurities of the fiber (this results in radiation absorption and scattering effects), absorption of IR radiation by the material, mechanical damage (for example micro-bendings of the fiber), surface irregularities at the fiber ends, coupling of fibers with other components (air gaps between the fiber and other element result in losses associated with Fresnel reflection) [153]. Moreover, it was reported that polycrystalline silver halide fibers tend to absorb water from the atmosphere that leads to the loss of the signal to noise ratio in the spectral region associated with water absorption [154]. Mentioned factors restrict achievable signal to noise ratio, thus due to high signal losses, the length of IR fibers is limited as well as sensitive detectors should be used. Besides signal losses, IR fibers are more fragile than conventional silica glass fibers.

Another important component of the fiber probe is a probe tip. Inside of a probe tip, a sensor element is integrated. Sensors can be built for several different types of measurement techniques, such as attenuated total reflection, specular reflection or transmission [154]. Most frequently, ATR crystal is integrated in the probe tip. Proper selection of the material of which an ATR crystal is produced as well as optimal geometry of the crystal determine the suitability of the probe for the sample investigation. While using a fiber probe for biological tissue investigation, the material of the ATR crystal should be non-toxic for biological tissues since it has a contact with the tissue which is being analysed. Moreover, it has to be transparent in the spectral region in which spectrum is being obtained as well as refractive index has to be high enough to satisfy the internal reflection condition. Refractive indices of the sample and the ATR crystal determines the depth of penetration. Penetration depth determines the thickness of the sample from which spectral information is being obtained. In this regard, values of both refractive indices should be taken into account while selecting a proper material for the ATR crystal production.



Besides the material, geometry of the ATR crystal is also an important aspect. Depending on the geometry, specifically, the angle of incidence of IR radiation, different values of penetration depth into the sample are obtained. Moreover, different ATR tip configurations can be employed for probe production. Based on crystal geometry and number of reflections at the surface between an ATR crystal and a sample, ATR tip configurations can be divided into two large groups: ATR tips of two reflections (e.g. prisms and cones can employ two reflections) and ATR tips of multiple reflections (e.g. ATR elements of a loop shape, so-called ‘U-shaped’ ATR elements employ more than two reflections). Schematic illustration of these two types of ATR crystals is presented in Figure 1.1.

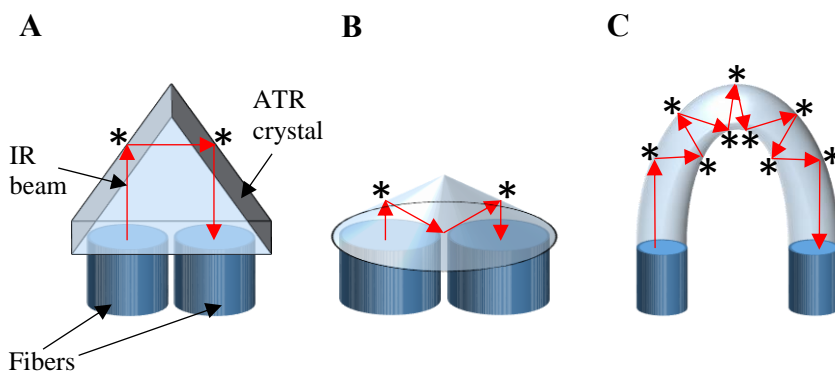


**Figure 1.1.** Configurations of ATR tips. ATR crystals of two (prism shaped (A) and cone shaped (B) crystals) and multiple (‘U-shaped’ crystal (C)) reflections. \* symbol indicates areas where evanescent field of IR radiation penetrates into a sample.

In general, ‘U-shaped’ ATR elements have larger contact area with a sample, thus, better sensitivity can be achieved by using this configuration. However, while applying the method for biological tissue investigation, the usage of ‘U-shaped’ ATR elements has some limitations. In order to obtain a sufficient signal, as large as possible surface area of the sensor should be covered with a sample. Regarding this aspect, for the sample investigation by using ‘U-shaped’ ATR elements, larger samples should be used. While analysing biological tissues, samples usually are of small dimensions, thus, regarding small contact area ‘U-shaped’ ATR elements are less effective for biological tissue investigation. Moreover, in some cases, for example while investigating firm materials, it could be difficult to ensure that the whole surface inside the loop would have a good contact with a sample. Additionally, cleaning and disinfection effectiveness of the ATR element which is an

important factor for human tissue analysis, also depends on a shape of the sensor. Thus selecting the geometry of the ATR elements for the probe production suitable for biological tissue investigation, attention should be paid to all mentioned issues.

### 1.3. IR spectra interpretation and analysis

While IR spectroscopy is a powerful and accurate method for chemical compound identification, determination of biochemical composition of biological tissues by applying IR spectroscopy is not that simple and straightforward. Biological samples are complex materials – they are constituted of a variety of chemical components. Large groups of compounds (such as proteins, lipids, carbohydrates and nucleic acids) are being found in most biological samples; however, proportions of various chemical components vary within the group of samples of the same nature. Moreover, spectral bands are relatively wide and are overlapping with each other. In this regard, IR spectra vary as well. Variations of spectra are observable even for the tissues of the same organ in different individuals. Such intra-class and inter-class variability burdens the interpretation of changes in biochemical composition of biological tissues due to pathology. In some cases, chemical alterations caused by pathological processes in tissues are rather small, thus statistical methods which could take into account the differences between the tissues of the same origin in different individuals and allowing to detect changes due to pathological processes at the same time are required.

Statistical methods applied for the analysis of spectra can be divided into two large groups such as supervised and unsupervised methods. Supervised methods are based on the labelled data set creation (the training set), and, according to defined characteristic properties of the training set spectra, spectra that are being analysed (the test set) are classified into the desired number of classes. Unsupervised methods of statistical analysis do not use a training set and are used for data clustering and visualization. These methods are useful for determination of presence of similar properties between the spectra and finding the outlier spectra. Application of unsupervised methods is a better choice for the analysis of smaller data sets due to the risk of overtraining. In case of smaller datasets, the choice of data used for the training set is more limited, thus as a result the training set possibly could not fully represent the whole scope of data.

Hierarchical cluster analysis (HCA) is one of the most frequently used unsupervised classification models. Two types of hierarchical clustering can be used: agglomerative and divisive clustering. The principle of the

agglomerative HCA is based on the merging of two similar clusters. Firstly, individual objects (e.g. spectra) are considered as single clusters. Subsequently, the most similar cluster (spectrum) is found and these two clusters are merged together. Further, the operation is repeated by merging another two clusters while all the clusters are merged into a one structure, named dendrogram – a tree-like branched graph. Divisive HCA is visualised as a dendrogram as well, however, the principle is reverse as for the agglomerative clustering – at first one cluster is being divided into two smaller clusters until all the clusters are divided into individual objects. Similarity between the clusters is described by distance (e.g. Euclidean distance) - the smaller the distance between two clusters is, the more similar data is.

Another frequently used unsupervised classification model is principal component analysis (PCA). The principle of the method is based on the reduction of dimensions of the dataset. Considering that the object contains characteristic properties (structure element) and less informative data (noise element), the principle of PCA is to separate these two parts and leave the noise part behind by transforming the coordinate system of variable space (e.g. wavenumbers of IR spectra and number of spectra) into a principle component (PC) coordinate space [155]. PCs are independent of each other; the number of PCs is lower compared to number of variables. The first PC represents the major part of variations while the second one represents the second largest part of variations, the third one represents the third largest part of variations, et cetera. PCA graph consists of two PC planes which usually are two highest PCs.

There is no universal data analysis method for IR spectra of all types of biological samples, thus methods of statistical data analysis have to be selected individually for each type of specimens. Further in this work it will be shown that there are no universal spectral tumor markers which would be suitable for all cancers or even for several types of cancer of the same organ - every tumor type is specific, arises from different cell types. In this regard, unique spectral tumor markers has to be investigated for each tumor type and discrimination method should be developed for each organ.

#### 1.4. The reliability of diagnostic methods

Various diagnostic methods are used for identification of presence or absence of diseases. An ideal diagnostic test should give a positive result when a patient has a disease and a negative result when a patient does not have it. However, not all diagnostic tests are ideal, thus false positive and false negative results of a test are obtained. Whereas the application of fiber-based

infrared spectroscopy was used for identification of various pathological tissues in this work, reliability of this diagnostic method was evaluated.

The evaluation of reliability of a new diagnostic test is based on comparison of results of the test to the results of a so called gold standard method. The gold standard is a routinely applied diagnostic method for a disease that provides the most reliable result. It is considered that the result of a gold standard method is not questionable and provides the evidence that disease is present or absent in the patient.

For the evaluation of reliability of a diagnostic test, values of sensitivity, specificity, positive (PPV) and negative prognostic values (NPV) are calculated. A table (Table 1.1) can be drawn up for establishment of mentioned parameters.

**Table 1.1.** Evaluation of a diagnostic test. Table for establishment of values of sensitivity, specificity, positive and negative prognostic values. Table based on data provided in [156].

		<b>Disease</b>	
		<b>Present</b>	<b>Absent</b>
<b>Test result</b>	<b>Positive</b>	True positive	False positive
	<b>Negative</b>	False negative	True negative

Sensitivity is a measure describing the ability of the test to identify the disease when a patient is diseased. Sensitivity is expressed as follows [157]:

$$Sensitivity = \frac{True\ positives}{True\ positives + False\ negatives}$$

Specificity is a measure describing the ability of the test to identify that the patient is disease free then the patient is not diseased. Specificity is expressed as follows [157]:

$$Specificity = \frac{True\ negatives}{True\ negatives + False\ positives}$$

Positive prognostic value describes the probability of being diseased when a result of a test is positive. Positive prognostic value is expressed as follows [157]:

$$PPV = \frac{True\ positives}{True\ positives + False\ positives}$$

Negative prognostic value describes the probability of not having a disease when a result of the test is negative. Negative prognostic value is expressed as follows [157]:

$$NPV = \frac{\textit{True negatives}}{\textit{True negatives} + \textit{False negatives}}.$$

While sensitivity and specificity of a test do not depend on the population and describes the test itself, PPV and NPV depend on the population and disease prevalence [157].

Although it is considered that results provided by the gold standard diagnostic method are correct, however, no method is 100 % accurate. For this reason, in some cases when the results of tissue type identification based on spectral analysis does not coincide with the tissue type set by surgeon or pathologist, it does not necessarily means that spectral analysis described in this work gives false results.

## 2. CHAPTER 2. DESIGN OF FIBER-BASED ATR IR SPECTROSCOPIC SYSTEM

### 2.1. Modification of commercial FT-IR spectrometer Alpha (Bruker Optik GmbH, Ettlingen, Germany) for fiber-based measurements

Measurements presented in the thesis were performed by using the fiber-based optical system for IR spectra collection. The system was created in the Institute of Chemical Physics of Faculty of Physics (Vilnius University, Lithuania) in cooperation with company ‘Art photonics’ (Art Photonics GmbH, Berlin, Germany). The system consists of the ATR silver halide fiber probe (Art Photonics GmbH, Berlin, Germany) attached to the commercial portable FT-IR spectrometer Alpha (Bruker Optik GmbH, Ettlingen, Germany) (referred as spectrometer Alpha in the following text) equipped with the external liquid nitrogen cooled MCT detector (Infrared Associates, Inc. Model IRA-20-00131). The block scheme of the system (referred as fiber-based spectroscopy system in the following text) is presented in Figure 2.1.

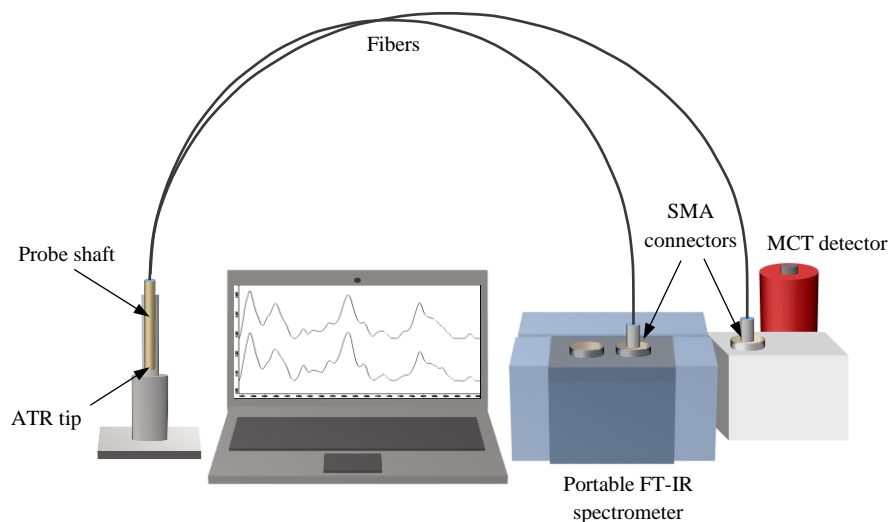


**Figure 2.1.** The block scheme of the fiber-based spectroscopy system

Portable spectrometer Alpha can be coupled with several modules, including ATR module (‘Platinum ATR’) and transmission module (‘Universal sampling module’). The latter module was modified for the adaptation for the use of optical fibers. In the modified system, the light propagating from the source to the detector is directed by two flat and two

parabolic mirrors. The SMA (SubMiniature version A) connectors were used for the connection of fibers to the spectrometer. The scheme of the set-up is presented in Figure 2.2.

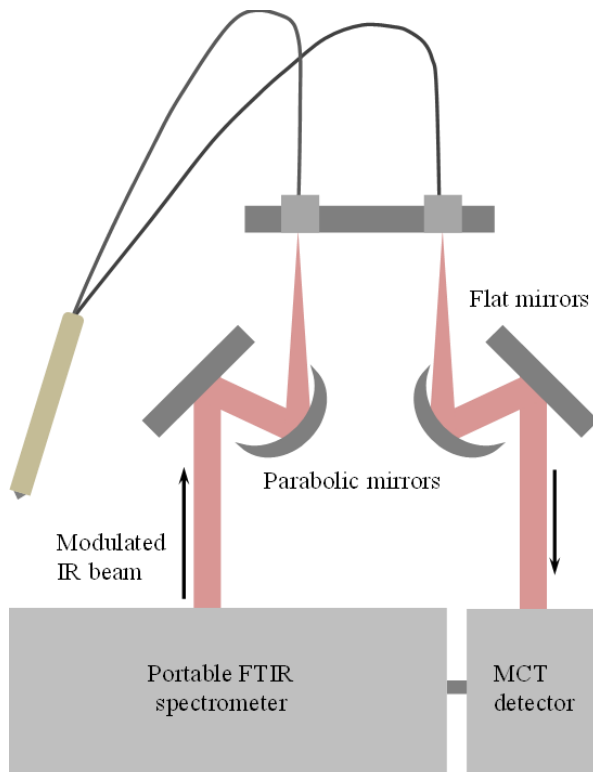


**Figure 2.2.** The scheme of the fiber-based spectroscopic system

As a standard, DTGS detectors usually are integrated inside the portable FT-IR spectrometers as well as in the latter spectrometer Alpha. DTGS detectors are quite compact and easy to exploit – they do not require cooling. The S/N (signal to noise) ratio of obtained spectra is high enough for the conventional samples thus DTGS detectors are the optimal choice for the measurements under usual conditions in the laboratory. However, when it comes to the use of optical fibers, the loss of the optical signal occurs due to absorption and scattering of the light. Therefore, more sensitive liquid nitrogen cooled MCT detectors should be used. In the described fiber-based set-up, the external MCT detector is attached. The detector is rather compact; therefore, such coupling enables to maintain the manoeuvrability of the whole spectroscopic system. Thus, the system remains portable that is important for the use in the operating room during the surgery.

In order to elucidate the potential of the fiber-based system to be used for spectral measurements, spectra of low concentration ethanol water solution (1:100) were measured by using both experimental setups: fiber-based spectroscopy system (coupled with either internal DTGS or external MCT detectors) and spectrometer Alpha (coupled with 'Platinum ATR' module with single reflection diamond ATR element and internal DTGS detector integrated). On the purpose to eliminate water absorption bands that overlaps with ethanol absorption bands in the IR absorption spectra, water spectrum was measured as a background. Both background and sample spectra were measured in  $400 - 4000 \text{ cm}^{-1}$  spectral region with  $4 \text{ cm}^{-1}$  resolution. 128 scans were performed for the acquisition of spectra. 3 term Blackmann-Harris apodization function and zero filling factor of 2 were applied.

Spectra, measured using fiber-based system and spectrometer Alpha coupled with DTGS detectors, are presented in Figure 2.3.

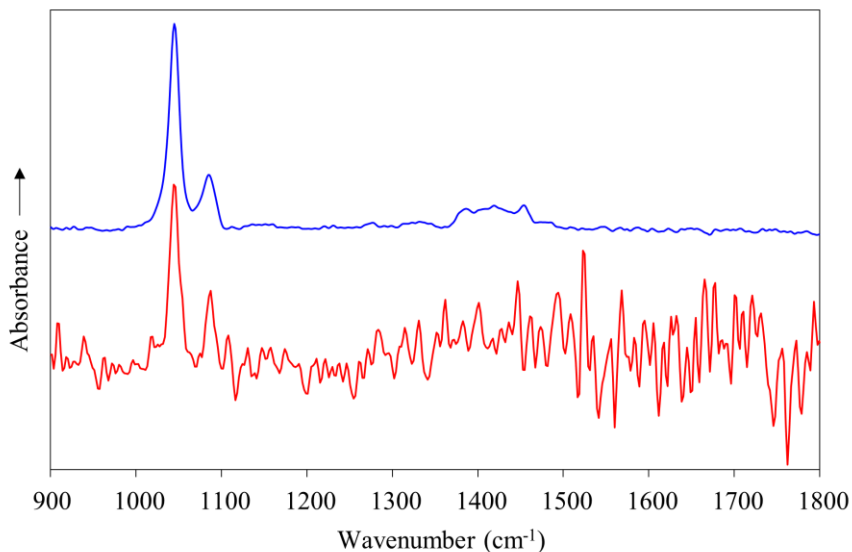


**Figure 2.3.** IR absorption spectra of 1:100 ethanol solution in water measured by using spectrometer Alpha (top) and fiber-based system (bottom). Both experimental setups coupled with DTGS detector.

The loss of up to 90% of optical signal in the fiber is expected, this results in elevated levels of the noise in the spectra measured by using fiber-based system. The S/N for the ethanol spectral band at  $1045 \text{ cm}^{-1}$  calculated in  $1300 - 1120 \text{ cm}^{-1}$  spectral range for “peak to peak” intensity is 28 for the spectrometer Alpha and 3 for the fiber-based system. Such huge drop of S/N in case of fiber-ATR probe attached to spectrometer Alpha is not appropriate



for the biological tissue analysis. The situation can be improved by coupling the system with a more sensitive MCT detector. IR absorption spectra of ethanol solution in water measured by using spectrometer Alpha coupled with internal DTGS detector, and the fiber-based system coupled with external MCT detector are presented in Figure 2.4.

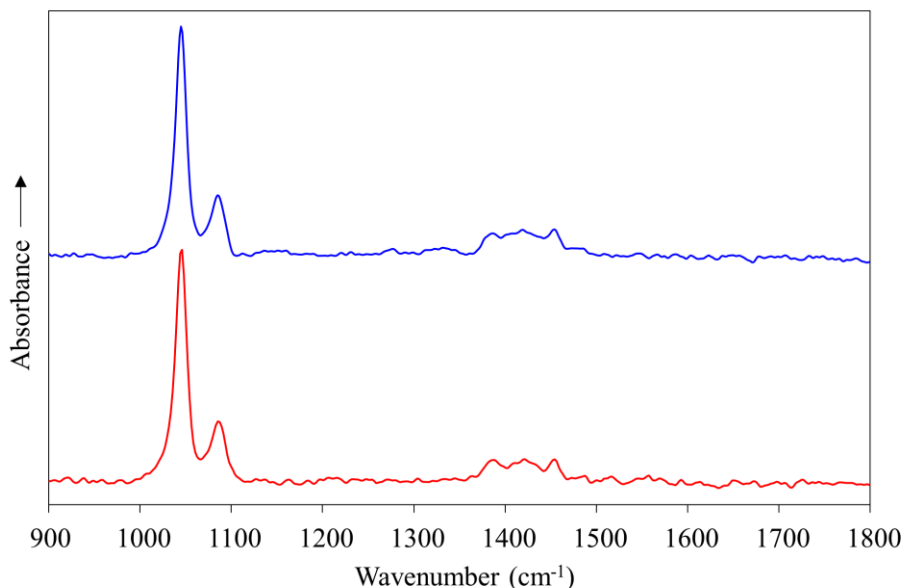


**Figure 2.4.** Infrared absorption spectrum of 1:100 ethanol solution in water measured by using spectrometer Alpha coupled with internal DTGS detector (top) and fiber-based system coupled with external liquid nitrogen cooled MCT detector.

The S/N ratio of the spectrum measured by using fiber-based system coupled with MCT detector is similar to the S/N ratio of the spectrum measured by using spectrometer Alpha coupled with internal DTGS detector. The S/N ratio values for the ethanol spectral band at  $1045\text{ cm}^{-1}$  calculated in  $1300 - 1120\text{ cm}^{-1}$  spectral range for the ‘peak to peak’ intensity are similar: 28 and 30 for spectrometer Alpha and fiber-based system, respectively. This result allows to state that quality of the spectra measured by using both set-ups are similar in the fingerprint region ( $950 - 1800\text{ cm}^{-1}$ ), thus, the fiber-based system is suitable for the measurements of biological samples.

The spectra measured by using fiber-based system coupled with MCT detector in high wavenumber ( $2700\text{-}3800\text{ cm}^{-1}$ ) spectral region are presented in Figure 2.5. In this case improvement by replacing DTGS detector with MCT detector is not so obvious. Indeed, S/N for the band at  $2982\text{ cm}^{-1}$  is 10

for spectrometer Alpha coupled with internal DTGS detector, while it is only 2 for fiber-based system coupled with external MCT detector. This can be explained due to the light scattering and absorption in the silver halide fibers. In case of application of fiber-based FT-IR spectroscopy for the cancerous tissue detection, inability to obtain high quality spectrum in high frequency region is not critical since the main spectral marker bands are located in the fingerprint spectral region between  $950$  and  $1800\text{ cm}^{-1}$ .

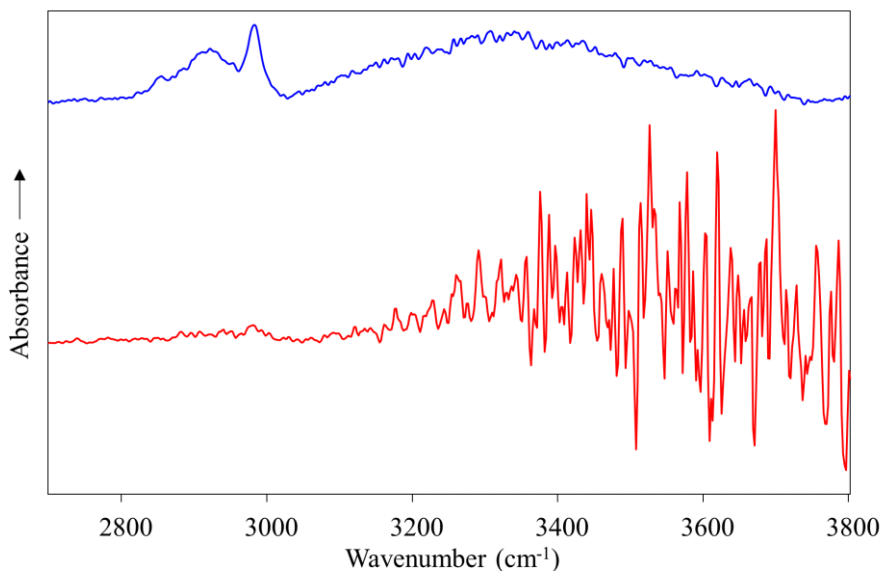


**Figure 2.5.** Infrared absorption spectra of 1:100 ethanol solution in water measured by using spectrometer Alpha coupled with internal DTGS detector (top) and fiber-based system coupled with external MCT detector (bottom).

The results of measured noise level in different spectral regions compared to the intensity of the strongest ethanol absorption band at  $1045\text{ cm}^{-1}$  are summarized in Table 2.1.

**Table 2.1.** Numerical values of S/N in different spectral regions obtained using spectrometer Alpha coupled with internal DTGS detector and fiber-based system coupled with external MCT detector. S/N calculated by taking S as the intensity of the band at 1045  $\text{cm}^{-1}$  and N - peak to peak amplitude of the noise in the selected spectral region.

Spectral range for peak to peak intensity, $\text{cm}^{-1}$	S/N			
	1200 - 1220	1700 - 1720	3000 - 3020	3400 - 3420
Conventional spectrometer with DTGS	76	61	51	40
Fiber based system with MCT	89	43	8	1

According to the calculated S/N values, fiber-based system coupled with external MCT detector could be used up to 3100  $\text{cm}^{-1}$ . Thus the main vibrations of organic molecules including some CH stretch vibration modes can be measured by means of this technique and only OH stretch spectral bands are not accessible.

The spectra of kidney tissue smears in spectral region of 900-1200  $\text{cm}^{-1}$  are presented in Fig. 2.6. Spectral markers of cancerous tissue are mainly related to glycogen vibrational modes and were obtained by both techniques.

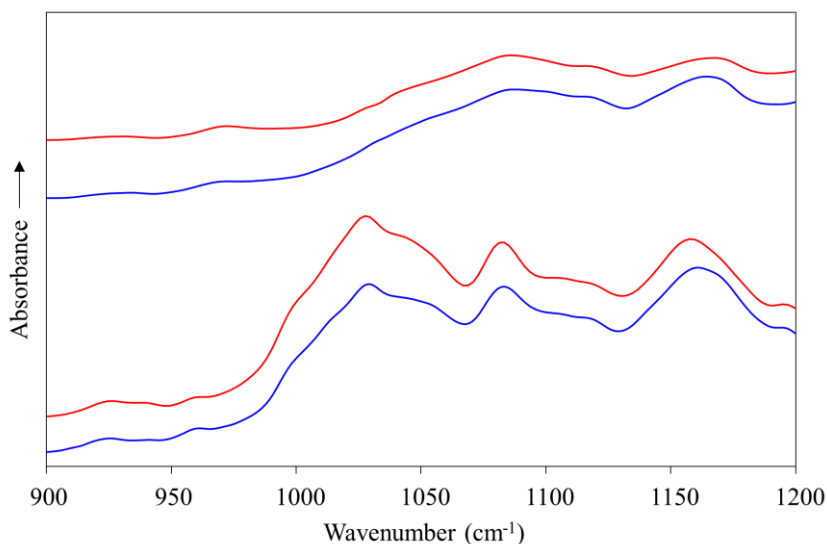


**Figure 2.6.** ATR IR spectra of normal (top) and cancerous (bottom) kidney tissue smears measured by using spectrometer Alpha coupled with DTGS detector (red) and fiber-based system coupled with MCT detector (blue).

The quality of spectra is similar and spectral markers of cancerous tissue smears at  $950 - 1180 \text{ cm}^{-1}$  are clearly visible thus the described system can be used for detection of cancerous tissue areas.

## 2.2. Design of the ATR probe

### 2.2.1. OCT imaging of the ATR probe tip

Optical coherence tomography (OCT) imaging of the ATR crystal was performed by using a commercial spectrometer-based polarization-sensitive OCT system (TEL220PSC2, Thorlabs GmbH, Germany) with a broad spectral range of approximately 1300 nm and a telecentric scanning lens (LSM03, Thorlabs GmbH, Germany) was used. After 3D imaging with a lateral step size of  $3 \mu\text{m}$ , the intensity, i.e., the amplitude sums of both Fourier transformed camera signals, was processed with custom MATLAB (MathWorks Inc., Natick, USA) software and down sampled to an isotropic voxel size of  $5 \mu\text{m}$  in each spatial direction. Assuming a flat image plane in the 3 mm diameter center of the objective's 10 mm field of view, this volume was used for determining the shape of the ATR crystal.

### 2.2.2. Geometry of the ATR crystal and penetration depth of the IR radiation into the sample

The changeable tip is attached to the probe at the end of the probe shaft. The tip is composed of an ATR crystal surrounded by protective tube material (polyetheretherketone). While performing measurements, the probe is pressed to the surface of the sample. The beam of IR radiation penetrates into the sample and a spectrum of the sample layer covered by the penetration depth is measured. In order to understand the origin of biochemical composition of the sample, it is important to determine the penetration depth of IR beam.

To investigate the precise geometry of the ATR crystal of the probe tip, OCT imaging was applied, and dimensions of the crystal as well as the beam path of IR radiation were determined (Figure 2.7.). The ATR crystal is cone-shaped with the height ( $h$ ) of  $610 \mu\text{m}$  and width ( $w$ ) of the base of  $2400 \mu\text{m}$ . Half of the top angle of the cone ( $\alpha$ ) can be calculated:

$$\text{tg}\alpha = \frac{w/2}{h} = 2, \alpha = 63^\circ \quad (2.1)$$

The resulting angle at the top of the cone is  $2\alpha = 126^\circ$ .

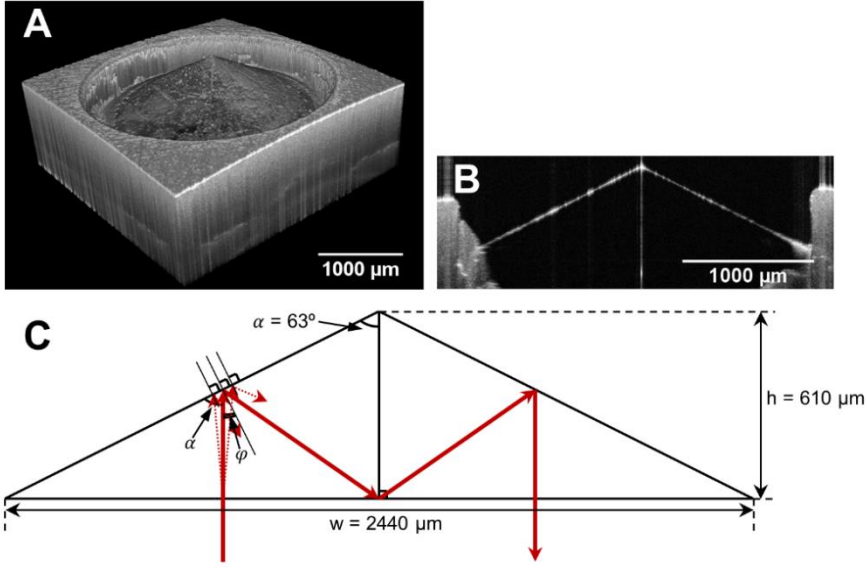


**Figure 2.7.** Geometry of the Ge ATR tip of the fiber probe: A – a 3D OCT image of the ATR tip, B – a cross-section image of the ATR tip, C – the beampath of IR radiation inside the ATR crystal.

Assuming that the beam of IR radiation traveling from the fiber is perpendicular to the ATR crystal surface, the angle of incidence to the surface between the crystal and the sample ( $\varphi$ ) can be expressed:

$$\varphi = 90^\circ - \alpha = 27^\circ. \quad (2.2)$$

Assuming that the refractive indexes for germanium and blood (the common example of biological samples) are  $n_1 \approx 4$  and  $n_2 \approx 1.3$  respectively, the critical angle  $\theta_c$  can be calculated:

$$\sin\theta_c = \frac{n_2}{n_1} = 0.325, \theta_c = 19^\circ \quad (2.3)$$

The depth of penetration ( $d_p$ ) is expressed by the Harrick equation:

$$d_p = \frac{\lambda}{2\pi n_1 \sqrt{\sin^2\varphi - \left(\frac{n_2}{n_1}\right)^2}}, \quad (2.4)$$

where  $\lambda$  is the wavelength of the radiation.

The most important spectral bands of the tissue spectra are located in the so-called fingerprint region ( $950 - 1800 \text{ cm}^{-1}$ ). For the wavenumber  $1800 \text{ cm}^{-1}$  ( $\lambda = 5.56 \mu\text{m}$ ), the depth of penetration is:

$$d_p(\lambda = 5.56 \mu\text{m}) = 0.7 \mu\text{m}. \quad (2.5)$$

For the wavenumber  $950 \text{ cm}^{-1}$  ( $\lambda = 10.53 \mu\text{m}$ ) the depth of penetration is:

$$d_p(\lambda = 10.53 \mu\text{m}) = 1.3 \mu\text{m}. \quad (2.6)$$

While the beam of radiation travels from the fiber to other optical medium, the direction of the beam is supposed to be perpendicular but due to the numerical aperture of the fiber, part of the radiation bends. The beam consists of a bundle of rays that are diverging; thus, outer rays are not perpendicular to the surface between two optical mediums (between fiber and air gap as well as between air gap and ATR crystal). Taking into account the numerical aperture (the effective numerical aperture is 0.3) of the fiber, the angle of acceptance ( $\beta$ ) is  $17^\circ$  for the air gap between the fiber and the ATR crystal. While the beam of the IR radiation travels from one optical medium (air; refractive index  $n_3 \approx 1$ ) to another (Ge ATR crystal;  $n_1 \approx 4$ ), it refracts (Figure 2.8).

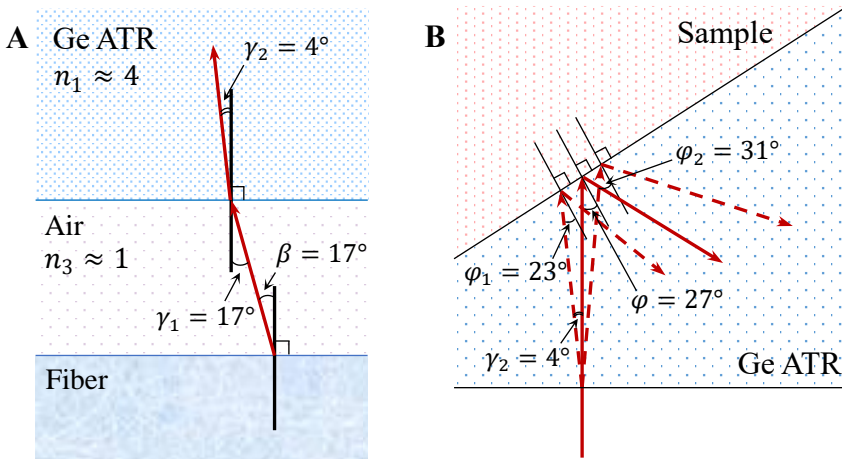


**Figure 2.8.** A - Schematic illustration of beampath of IR radiation through different optical mediums, B – angle of incidence to the surface between the crystal and the sample.

The refraction angle  $\gamma_2$  is expressed by the Snell's law:

$$\sin\gamma_2 = \frac{n_3 \sin\gamma_1}{n_1}, \text{ then } \gamma_2 = 4^\circ, \quad (2.7)$$

where  $\gamma_1$  is the angle of incidence for the beam traveling from the fiber to the air gap that is equal to the angle of acceptance ( $17^\circ$ ). The refraction angle  $\gamma_2$  defines the bending of the beam from the direction when the beam traveling from the fiber is perpendicular to the surface of the ATR crystal. The angle of incidence for the beam traveling in the ATR crystal towards the surface between the crystal and the sample varies from  $23^\circ$  ( $\varphi_1$ ) to  $31^\circ$  ( $\varphi_2$ ).

The maximum depth of penetration is observed when the angle of incidence has the nearest value to the critical angle ( $23^\circ$ ). In this case, for the wavenumber  $1800 \text{ cm}^{-1}$  ( $\lambda = 5.56 \text{ }\mu\text{m}$ ), the depth of penetration is:

$$d_p(\lambda = 5.56 \mu\text{m}) = 1.0 \mu\text{m}. \quad (2.8)$$

For the wavenumber  $950 \text{ cm}^{-1}$  ( $\lambda = 10.53 \mu\text{m}$ ) the depth of penetration is:

$$d_p(\lambda = 10.53 \mu\text{m}) = 1.9 \mu\text{m}. \quad (2.9)$$

The minimum depth of penetration is observed when the angle of incidence has the largest value ( $31^\circ$ ). In this case, for the wavenumber  $1800 \text{ cm}^{-1}$  ( $\lambda = 5.56 \mu\text{m}$ ), the depth of penetration is:

$$d_p(\lambda = 5.56 \mu\text{m}) = 0.5 \mu\text{m}. \quad (2.10)$$

For the wavenumber  $950 \text{ cm}^{-1}$  ( $\lambda = 10.53 \mu\text{m}$ ) the depth of penetration is:

$$d_p(\lambda = 10.53 \mu\text{m}) = 1.0 \mu\text{m}. \quad (2.11)$$

According to the calculations, two reflections occur at the ATR crystal-sample surface, one reflection occurs at the base of the crystal. While IR beam interacts with the sample, the depth of penetration varies from 0.5 to 1.0  $\mu\text{m}$  for the wavenumber  $950 \text{ cm}^{-1}$  and from 1.0 to 1.9  $\mu\text{m}$  for the wavenumber  $1800 \text{ cm}^{-1}$ . Later in this chapter it is shown that this is sufficient for obtaining biochemical information of both tissue components (ECM and cells).

Whereas the desired application of the fiber probe is the investigation of tissues in the operating room, thus the sterility of the equipment is crucial. The use of changeable probe tips assures the sterility of the probe surface which is in contact with the tissue since probe tips can be easily detached and sterilized.

### 2.3. Determination of the sample composition

In this work, two types of samples (native not pre-processed tissues and tissue smears) were investigated. Biological tissue samples consist of multiple components (e.g., ECM, cells). As it shown in previous section, penetration depth of IR radiation into the sample reaches 0.5 – 1.9  $\mu\text{m}$ , thus it is important to determine the components of the sample which are covered by the penetration depth. While placing the tissue onto the ATR crystal during the measurements, the ECM fills the space between tissue cells and the ATR crystal (Figure 2.9).

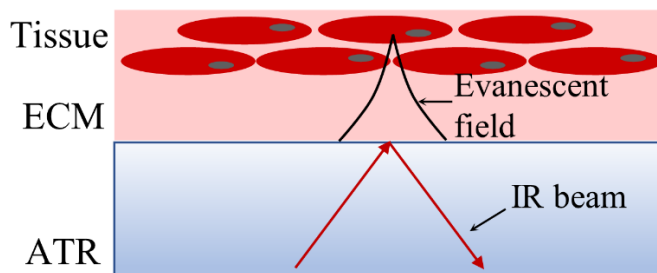


**Figure 2.9.** The schematic illustration of the ATR IR spectra measurements of a tissue sample

In this context, the term of ECM covers a network of proteins and fluid (mainly water and other dissolved molecules). In order to understand the origin of components which are observed in ATR IR spectra of freshly resected tissue, spectra of tissue and tissue smears (material which is left on the ATR crystal after placing and removing the tissue) were measured. ATR IR spectra of tissue and tissue smears of various tissue types (tumorous pancreatic, tumorous liver, normal bladder and normal kidney tissue) are presented in Figure 2.10.



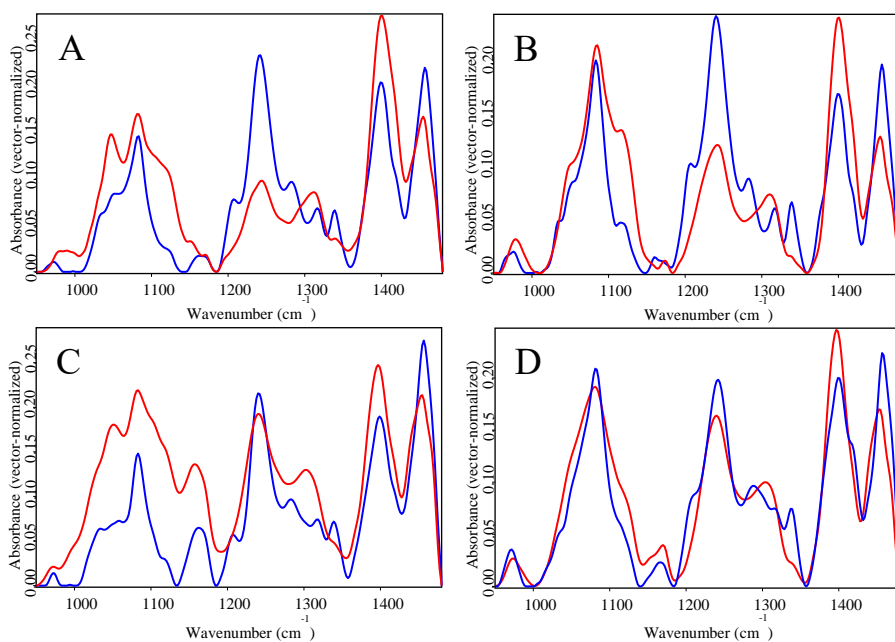


**Figure 2.10.** ATR IR spectra of fresh tissue (blue line) and tissue smears (red line) of: A – tumorous pancreas, B – tumorous liver, C – normal bladder and D – normal kidney tissue samples.

Profiles of spectra of various tissue types are different, however, some similarities between them can be observed. In the spectra of tissue, spectral bands located approximately at 1241, 1282, 1316 and 1339  $\text{cm}^{-1}$  which can be assigned to collagen [158] are observed. It is known that ECM consists mostly of protein fibers, such as collagen and fibronectin, also of glycosaminoglycans and proteoglycans. The presence of collagen bands in the tissue spectra indicates that the ECM of the tissue is represented. In comparison, not all of the mentioned spectral bands corresponding to collagen are observable in the spectra of tissue smears at the first glance. In contrast to spectra of tissues, two wide spectral bands located at 1240  $\text{cm}^{-1}$  (could be related to  $\nu(\text{PO}_2^-)$  vibrations of nucleic acids and Amide III groups of proteins) and 1304  $\text{cm}^{-1}$  (can be assigned to  $\delta(\text{C-H})$   $\delta(\text{C-O-H})$  vibrations, Amide III groups of proteins) and one less prominent band located at 1341  $\text{cm}^{-1}$  ( $\text{CH}_2$  wagging vibrations, possibly related to phospholipids, fatty acids, triglycerides, amino acid side chain) are observed in spectral region 1185 - 1357  $\text{cm}^{-1}$  in tissue smear spectra [158]. Despite these differences, the same spectral bands located at 1047  $\text{cm}^{-1}$  assigned to  $\nu(\text{C-O})$  vibrational modes of carbohydrates, 1082  $\text{cm}^{-1}$  assigned to  $\nu(\text{PO}_2^-)$  vibrational modes of nucleic acids, 1339  $\text{cm}^{-1}$  assigned to vibrational modes of  $\nu(\text{C-O})$  and  $\delta(\text{CH}_2)$  and 1456  $\text{cm}^{-1}$  assigned to  $\delta(\text{CH}_3)$

vibrations being related to proteins are observed in spectra of both types of samples (native tissue and tissue smears) [158]. In order to determine the origin of the components being observed in tissue smear spectra and understand if current penetration depth of IR radiation is sufficient enough for cell content observation, fluorescent DAPI (4',6-diamidino-2-phenylindole) staining of tissue smear was performed. Freshly cut surface of a tumorous pancreas tissue sample was gently pressed against a glass slide and after several seconds removed. The remaining material on the glass slide was fixed with paraformaldehyde for 2 minutes, rinsed twice with DPBS (Dulbecco's Phosphate Buffered Saline) solution and incubated with DAPI-DPBS solution (1:10000) for 15 minutes. The prepared slide was washed with DPBS and the imaging of the tissue smear was performed. EVOS® FL Auto Imaging System (Thermofisher scientific) with 405 nm laser excitation was used for the collection of microscopy images. Microscopic image of DAPI staining of tissue smear of tumorous pancreatic tissue is presented in Figure. 2.11. DAPI intercalates into DNA resulting in a blue color fluorescent radiation. Blue colored nuclei are visible on the slide indicating the remaining cells. These findings indicate that the spectra of tissue obtained by using the current fiber-based ATR IR spectroscopic system contains the biochemical information of both components of the tissue, the ECM and cells.

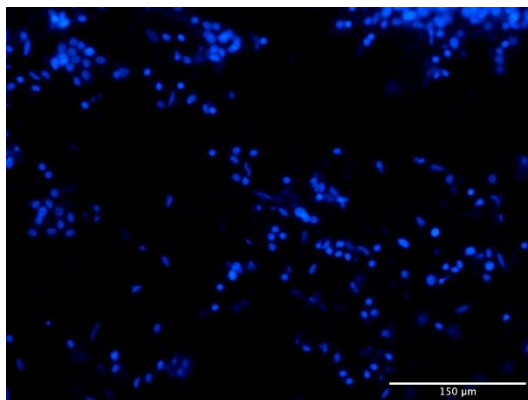


**Figure 2.11.** Microscopic image of DAPI-stained tissue smear of tumorous pancreatic tissue (PDAC) on the slide

### 3. CHAPTER 3. APPLICATION FOR KIDNEY CANCER

#### 3.1. Kidney cancer

The kidney is a paired organ in human body removing metabolic waste products by filtrating blood and secreting urine [159]. The kidney consists of functional units nephrons with average 1 million of them in a one kidney [159], [160]. Kidneys also participate in arterial blood pressure regulation by secretion of hormones renin and angiotensin; the latter can promote the production of aldosterone in adrenal glands [159], [161]. These secreted hormones have an impact on retention rates of salts and secreted urine.

Kidney cancer is among 20 most frequently diagnosed cancer types worldwide and is more common in men than in women with higher mortality rates in men [1], [162]. The highest incidence rate of kidney cancer in 2020 was in Lithuania [162]. According to the World Health Organization (WHO), kidney tumors can be classified to several tumor groups such as renal cell, metanephric, nephroblastic, cystic, mesenchymal, mixed epithelial and stromal, neuroendocrine, miscellaneous, and metastatic tumors [163]. The most common group of kidney tumors is renal cell tumors, including malignant (clear cell renal cell carcinoma, multilocular cystic renal neoplasm of low malignant potential, papillary renal cell carcinoma, hereditary leiomyomatosis and renal cell carcinoma – associated renal cell carcinoma, chromophobe renal cell carcinoma, collecting duct carcinoma, renal medullary carcinoma, MiT family translocation renal cell carcinomas, succinate dehydrogenase-deficient renal cell carcinoma, mucinous tubular and spindle cell carcinoma, tubulocystic renal cell carcinoma, acquired cystic disease-associated renal cell carcinoma, clear cell papillary renal cell carcinoma, unclassified renal cell carcinoma) and benign (papillary adenoma, oncocytoma) neoplasms [163]. Renal cell carcinoma (RCC) accounts more than 90 % diagnosed kidney cancer cases of which the most frequently diagnosed type is clear cell renal cell carcinoma (ccRCC) [164] arising from the proximal convoluted tubules epithelium [165] and accounting about 70 % of RCC cases [166]. Cell cytoplasm of ccRCC tumors is filled with glycogen and lipids including cholesterol, neutral lipids and phospholipids; these compounds prevents cytoplasm from staining by eosin and results in a clear appearance of cytoplasm of tumorous cells during routine histological tissue examination [166].

Surgery remains the most frequently applied approach for treatment of localized kidney cancer [164]. Depending on a tumor status, surgery can be performed as a partial or radical nephrectomy. In case of radical nephrectomy,

the whole kidney in some cases including other surrounding structures such as ureter, adrenal gland, lymph nodes and other structures is removed. During partial nephrectomy, nephron-sparing is performed by removing cancer lesion with a narrow surrounding area of normal tissue. The success of tumor resection highly depends on the ability to determine tumorous area not leaving islands of malignant cells infiltrated to the surrounding normal tissue. This is crucial to prevent local recurrence of the tumor. By macroscopic evaluation, infiltrations of malignant cells are not always observable. This can be illustrated by Figure 3.1.

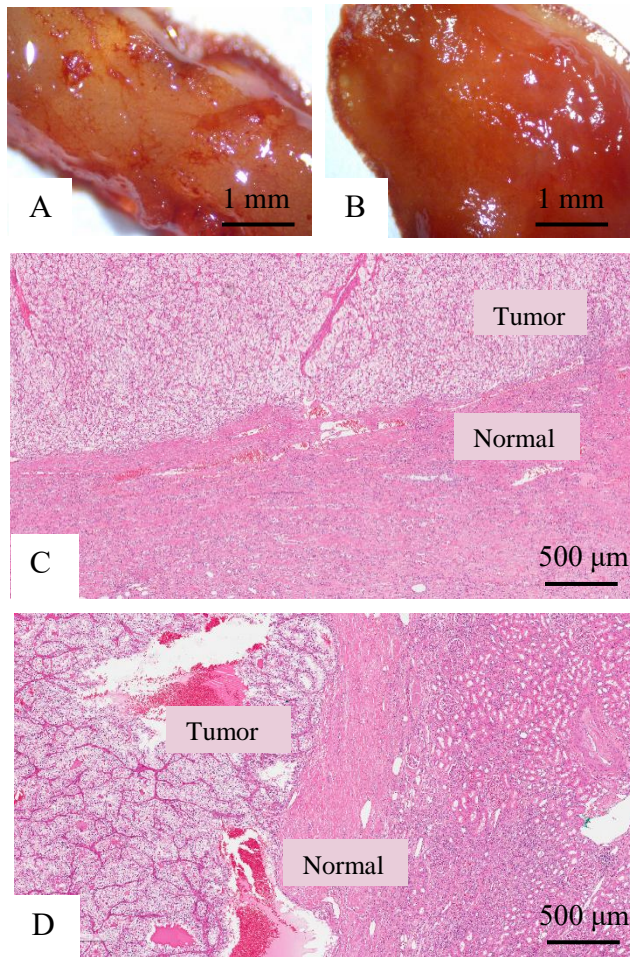


**Figure 3.1.** Photographs of normal (A) and tumorous (B) tissue samples, microscopy image of H&E stained tissue (C, D). After microscopic histopathological examination, the borderline between normal and tumorous kidney tissues is clearly visible.

While general differences between normal (Figure 3.1. A) and tumorous (Figure 3.1. B) tissues are in most cases visible, a sharp borderline between normal and malignant areas becomes clearly observable only after microscopic histopathological examination of fixed and stained tissue (Figure 3.1. C, D).

As a standard method used frozen section examination is a time consuming procedure which leads to prolonged surgery and anaesthesia time. Moreover, occlusion of the renal artery during partial nephrectomy has to be performed [167]. Prolonged duration of warm ischemia could lead to acute kidney injury and have negative consequences in kidney functioning [167], [168]. Thus the duration of the surgery should be kept as short as possible.

Fluorescence guided surgery for kidney tumor identification is being investigated by applying several contrast agents, however, most studies stay only in the research stage. While applying targeted molecular contrast agent EC17 for identification of RCC tumors during a surgery, study showed that application of this agent could improve visualization of a tumor [169]. However, study was performed only as a pilot study of 4 patients. Other study used ICG (indocyanine green) for visualization of renal cortical tumors during an open partial nephrectomy and showed hypofluorescence of malignant tumors, thus allowing delineation of malignant areas and normal renal parenchyma [170]. Method was applied for the comparison of outcomes of patients who underwent robotic partial nephrectomy combined with ICG induced fluorescence imaging with patients whom ICG induced fluorescence imaging was not applied, however authors came to a conclusion that ICG fluorescence improved warm ischemia time but positive margin rates were not improved [171]. Other studies suggest that more research with larger cohorts are required for the evaluation of advantages of the ICG induced fluorescence in robot-assisted partial nephrectomy [172].

## 3.2. Experimental details

### 3.2.1. Tissue sample collection

Human kidney tissue samples were obtained at the Urology Center of the Vilnius University Hospital Santaros Klinikos (Lithuania). The study was approved by the Regional Biomedical Research Ethics Committee (Document No 158200-15-803-312). Samples were collected during partial or radical nephrectomy performed as an open or a laparoscopic surgery due to kidney tumors. Freshly resected tissue samples were macroscopically examined by a

surgeon and assigned as ‘normal’ or ‘tumorous’. In all cases two tissue samples (normal and pathological) for each patient were received. In two cases, patients were diagnosed with pyelonephritis, non-specific fibrotic alterations; and fibrosis respectively after routine histological examination of the whole resected specimen. Resected tissue samples were evaluated either inside the operation theater next to the operation room immediately after surgery, either were placed on ice and transported to the spectroscopic laboratory for the measurements.

### 3.2.2. FT-IR spectroscopy measurements of tissue samples

Measurements were performed by using two measuring set-ups described in the Chapter 2. Portable FT-IR spectrometer Alpha (Bruker Optik GmbH, Ettlingen, Germany) equipped with single reflection diamond ATR module was used for the measurements of tissue smear spectra. In the first step, tissue sample was sliced and freshly cut surface of the sample was pressed against the ATR crystal. Then, the sample was removed from the crystal. The material which is remaining on the ATR crystal was air dried and resulting spectrum of the tissue smear was measured. In this manner, the impact of water absorption is eliminated.

Fiber-based spectroscopy system was used for the measurements of two sample types: spectra of native not pre-processed tissues and tissue smears were measured. In the first step, received tissue samples were sliced into several pieces and measurements were performed from freshly cut surface. The fiber probe was pressed against the freshly cut surface area and spectrum was measured afterwards, hereby obtaining a spectrum of native tissue. Secondly, after removing the probe from the tissue sample, the material which is remaining on the ATR crystal was air dried and resulting spectrum of tissue smear was measured.

Number of slices and measured spectra depended on the size of the sample, it usually varied between 1 and 3 cuts per sample. Spectra were collected in  $400 - 4000 \text{ cm}^{-1}$  spectral region with a  $4 \text{ cm}^{-1}$  resolution. 64 interferograms were recorded, averaged and Fourier transformed into IR absorption spectrum. Blackmann-Harris 3-Term apodization function, zero filling factor of 2 and phase correction (Power Spectrum phase correction method) were used while applying the Fourier transformation. Software build in ATR correction was performed using spectral software OPUS (Bruker Optik GmbH, Ettlingen, Germany). Described parameters were applied for both measuring set-ups. Before each measurement, tip cleaning was performed by wiping the tip surface by a soft cotton swab dampened with distilled water followed by

ethanol. Cleanliness of the tip was verified by measuring the spectrum of the ATR crystal without any sample on it and comparing the measured spectrum to the background spectrum measured before the experiment.

### 3.2.3. Statistical analysis

**Tissue smear spectra.** Statistical analysis (HCA and PCA) of tissue smear spectra was performed by using data analysis software OriginPro (OriginLab corporation). Prior statistical analysis, spectra were pre-processed: atmospheric compensation, baseline correction, vector normalization and offset correction were applied by using spectroscopy software OPUS. Statistical analysis was performed by applying standard procedures (Hierarchical Cluster Analysis and Principal Component Analysis) of the OriginPro software package. Analysis was performed in 950 – 1200  $\text{cm}^{-1}$  spectral range. While performing HCA, Ward clustering algorithm, Euclidean distance type were chosen. PCA analysis was performed by applying the method for the first derivative of spectra.

Different spectral regions were chosen for statistical analysis and different pre-processing of spectra (either first or second derivative of spectra was calculated by using spectroscopy software OPUS or not) was applied prior the analysis; however, the best results were obtained by using parameters and spectra pre-processing as mentioned above.

The algorithm for the automated tissue type identification was developed by using spectroscopy software OPUS. In the first step, library of normal and tumorous tissue smear spectra was created. In this regard, 30 spectra of normal kidney tissue smears and 30 spectra of tumorous kidney tissue smears were selected. Before adding spectra to the library, spectra were pre-processed by performing atmospheric compensation and baseline correction in spectral range between 950 – 1800  $\text{cm}^{-1}$ .

The code of the program was written by using 'Macro' function of spectroscopy software OPUS. The block diagram of the automated tissue assessment is presented in Figure 3.2.

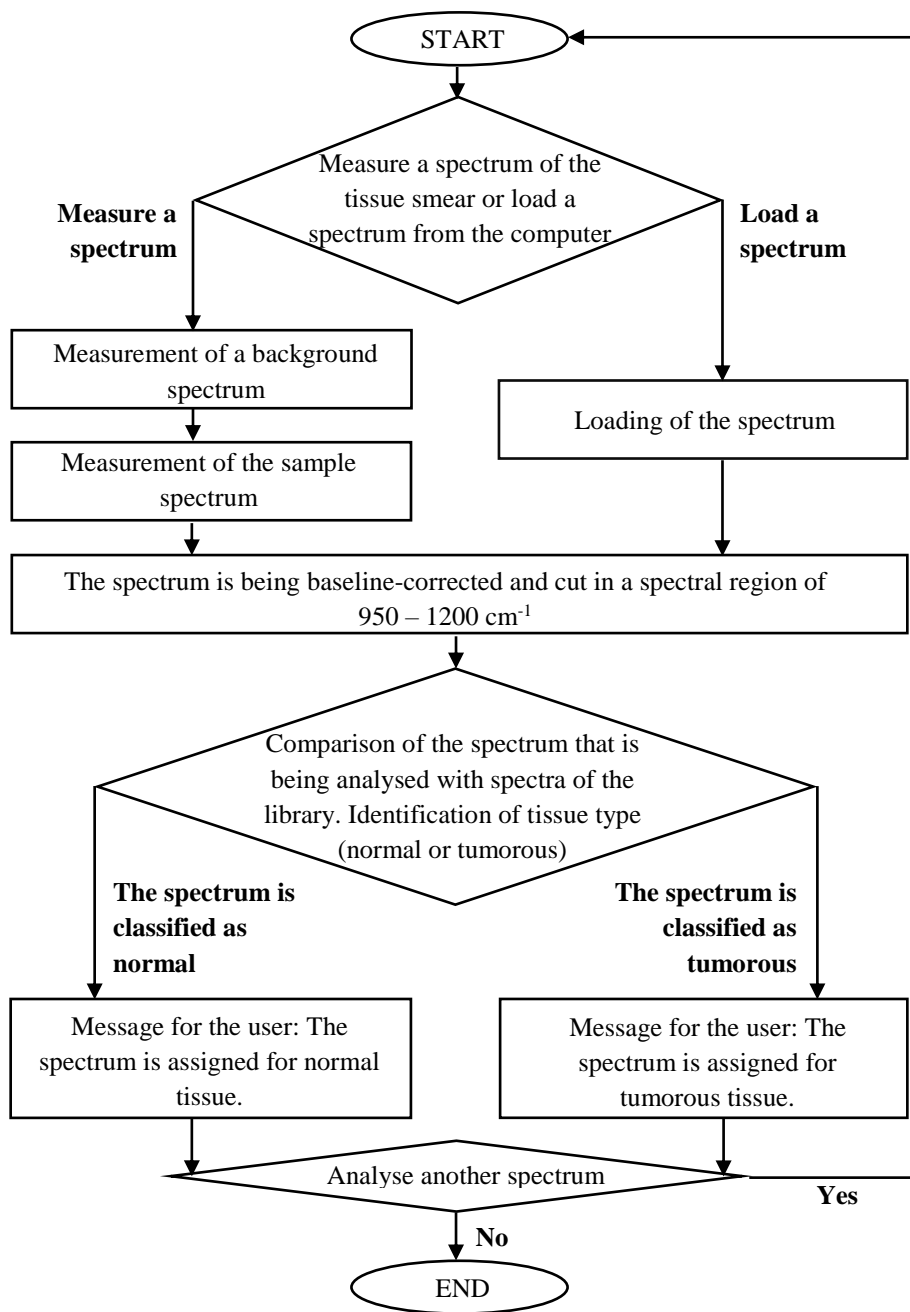


**Figure 3.2.** A block diagram of the program for the automated tissue analysis.



Program for the automated tissue analysis can be used for the evaluation of the previously measured spectra and for the spectra that are being measured during the analysis. The automated analysis starts by showing a message for the user to choose whether the algorithm will be applied for the previously measured spectrum or the spectrum will be measured during the analysis. Depending on the choice of the user, spectrum is loaded from the computer or is being measured in a real time. After loading or measuring the spectrum, the program pre-processes the spectrum, compares it with the spectra of the library and shows evaluation results (whether tissue sample is classified as normal or tumorous tissue) of the spectrum that is being analysed. After evaluation of the sample, program shows a message by asking the user to choose if the evaluation of spectra is complete or if another spectrum there will be evaluated. Depending on the choice of the user, program window closes or the program comes back to the start.

Pre-processing of spectra, library creation and library search (comparison of spectra) is performed by the spectroscopy software OPUS. 'Spectrum search' function is used for the comparison of spectra by applying 'Spectrum correlation' algorithm. Vector normalization, first derivative of spectra are set as 'Spectrum search' parameters. Different spectral regions and different spectrum search parameters ('Standard' and 'Spectrum correlation' (applying vector normalization, not calculating derivatives of spectra or calculating first and second derivatives of spectra) were chosen for the comparison of spectra; however, the best results were obtained by using parameters as mentioned above.

**Native unprocessed tissues.** Statistical analysis (HCA and PCA) of tissue smear spectra was performed by using data analysis software OriginPro. Prior statistical analysis, spectra were pre-processed: atmospheric compensation, baseline correction, vector normalization and offset correction were applied by using spectroscopy software OPUS. Statistical analysis was performed by applying standard procedures (Hierarchical Cluster Analysis and Principal Component Analysis) of the OriginPro software package. While performing HCA, Ward cluster algorithm, Euclidean distance type were chosen. Analysis performed in 950-1350  $\text{cm}^{-1}$  spectral region. PCA analysis performed for the first derivative of spectra in spectral region between 950 and 1081  $\text{cm}^{-1}$ .

Different spectral regions were chosen for statistical analysis and different pre-processing of spectra (either first or second derivative of spectra was calculated by using spectroscopy software OPUS or not) was applied prior the analysis; however, the best results were obtained by using parameters and spectra pre-processing as mentioned above.

### 3.3. Spectroscopic analysis: results and discussion

#### 3.3.1. Tissue smears measured by using conventional ATR spectrometer

In this section, analysis of spectra of dried tissue smears measured by using spectrometer Alpha is described. In total, cases of 127 patients were analysed. Summarised data is presented in Table 3.1. Final diagnosis is based on standard histology reports of the whole resected tissue specimen.

**Table 3.1.** Kidney tissue types collected during the study of tissue smear spectra measured by using conventional ATR spectrometer.

Tissue type	Number of tissue samples
Normal	127
Tumor	
ccRCC	104
Papillary RCC	8
Chromophobe RCC	3
Tubulocystic RCC	1
Multilocular RCC	2
Oncocytoma <sup>B</sup>	6
Angiomyolipoma <sup>B</sup>	1
Other	
Pyelonephritis, non-specific fibrotic alterations	1
Fibrosis	1
Total number of patients	127

B indicates benign tumors.

Spectra of each specimen were collected at several different areas of the sample: tissue sample was sliced, pressed against the ATR element and removed, thus tissue smear spectra were collected from each freshly cut surface. In case of every sample, obtained spectra were averaged and resulting spectrum was used for further analysis.

Mean spectra of kidney normal and tumorous tissue smears are presented in Figure 3.3. Main spectral band positions and their assignments are shown in Table 3.2.

Differences between normal and tumorous tissue smears are well defined. The most significant differences between normal and tumorous kidney tissue smears are observable in spectral region between 950 and 1200  $\text{cm}^{-1}$  where spectral bands mainly due to carbohydrates, glycoproteins and phosphate groups are located. Higher values of absorbance for the band positions at 1027  $\text{cm}^{-1}$  assigned to  $\nu(\text{C-O})$ ,  $\nu(\text{C-C})$ ,  $\delta(\text{C-O-H})$  vibrations and at 1155  $\text{cm}^{-1}$  assigned to  $\nu(\text{C-O})$  vibrations of glycogen are observed in tumorous kidney tissue. Spectral band located at 1081  $\text{cm}^{-1}$  is assigned to glycogen (experimental spectra of glycogen are presented in the Appendix, Figure A-01.). Increased glycogen levels in tumorous tissue indicated by higher absorbance values of mentioned spectral bands are observed in some types of tumors and used as the resource of energy for cell proliferation [42], [173]. It is known that accumulation of glycogen in cell cytosol is a common feature of ccRCC tumors [166], [174], [175]. The most frequently diagnosed tumor type among analysed tissue samples is ccRCC, thus glycogen spectral bands of high absorbance values are observable.

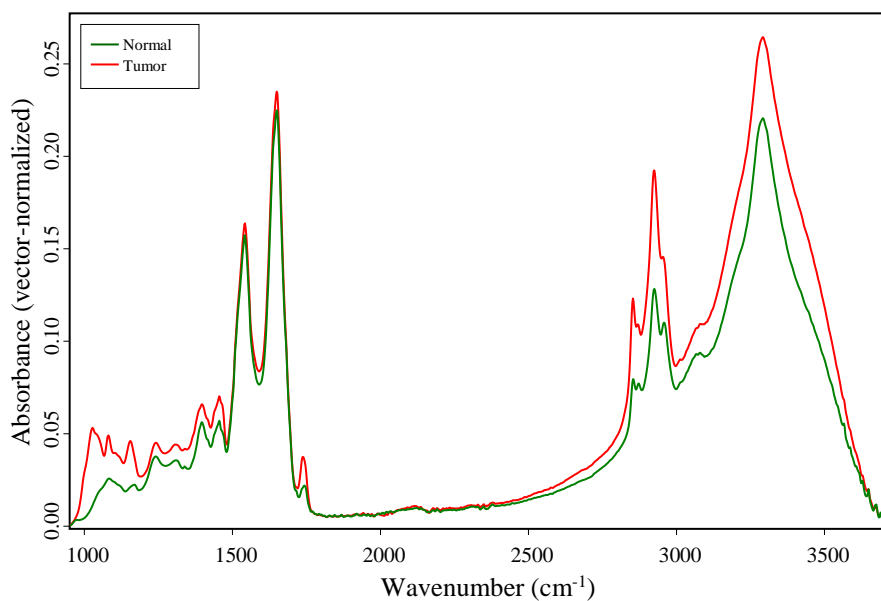


**Figure 3.3.** Mean ATR IR spectra of normal and tumorous kidney tissue smears. Spectra are baseline corrected and vector-normalized.

**Table 3.2.** Spectral bands of tissue smear spectra and their assignments. Assignments set according to [158].

Spectral band position, $\text{cm}^{-1}$		Assignment
Normal tissue	Tumorous tissue	
972	Not present	$\nu(\text{PO}_4)$ of nucleic acids and proteins $\text{OCH}_3$ of polysaccharides
Not present	997	$\nu(\text{CO})$ , $\nu(\text{CC})$
Not present	1027	$\nu(\text{C-O})$ , $\nu(\text{C-C})$ , $\delta(\text{C-O-H})$ of glycogen $\nu(\text{CO-O-C})$
1047 (sh)	1047	$\nu(\text{C-O})$ , $\delta(\text{C-O})$ of the C-OH of carbohydrates
1082	1081	$\nu(\text{PO}_2^-)$ ; glycogen*
1155 (sh)	1155	$\nu(\text{C-O})$
1170	Not present	$\nu(\text{C-O})$
1239	1242	$\nu(\text{PO}_2^-)$ , Amide III
1310	1310	Amide III
1339	1339	$\text{CH}_2$ wagging
1397	1397	$\delta(\text{CH}_3)$
1417 (sh)	1417 (sh)	$\nu(\text{C-N})$ , $\delta(\text{N-H})$ , $\delta(\text{C-H})$
1439 (sh)	1439 (sh)	$\delta(\text{CH}_2)$
1456	1456	$\delta(\text{CH}_3)$
1541	1541	Amide II
1650	1650	Amide I
1738	1738	$\nu(\text{C=O})$
2852	2852	$\nu(\text{CH}_2)$ of lipids
2924	2924	$\nu(\text{CH}_2)$ , $\nu(\text{CH}_3)$ of lipids
2958	2958	$\nu(\text{CH}_3)$
3074	3074	Amide B ( $\nu(\text{N-H})$ )
3289	3289	Amide A ( $\nu(\text{N-H})$ ), $\nu(\text{O-H})$

(sh) indicates a shoulder band

\*assignment of glycogen spectral band is based on the experimental data (see Appendix, Figure A-01)

Although differences between the mean spectra of normal and tumorous kidney tissues are clearly visible, variations of spectra inside these two tissue classes are quite high (Figure 3.4)

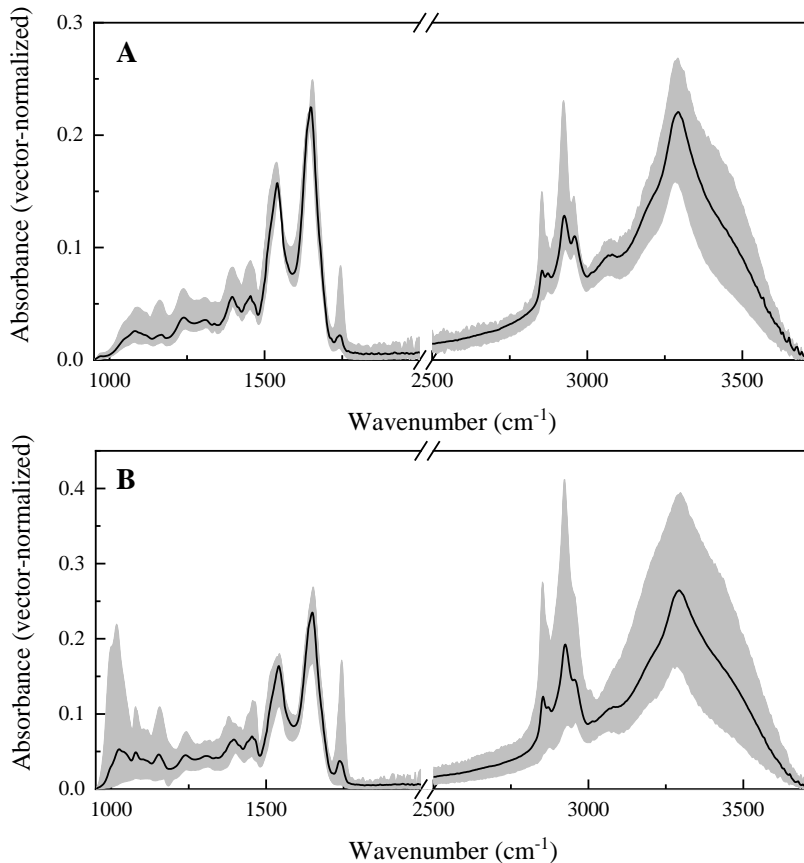


**Figure 3.4.** Mean spectra (black solid line) and variations of spectra of tissue smears taken from different patients (grey area) of kidney normal (A) and tumorous (B) tissue. Spectra are baseline corrected and vector-normalized.

Black lines correspond to the mean spectra of all the samples taken from different patients, while grey areas indicate the variations of spectra in different tissue classes. Variations of spectra in the tumorous tissue class are higher (Figure 3.4 B), especially for the spectral bands corresponding to glycogen (located at 1027, 1081 and 1155  $\text{cm}^{-1}$ ) which could be considered as a spectral tumor marker of kidney cancer. Higher variations in tumorous tissue spectra class could be linked to the diverse differentiation of tumorous cells and different grade of malignancy. Mean spectra of different malignancy grade (G1, G2 and G3) ccRCC tumorous tissue smears are presented in Figure 3.5. G1 malignancy grade tumors show lower levels of glycogen compared to higher malignancy grade tumors, while glycogen levels in G2 and G3 malignancy grade tumors are similar.

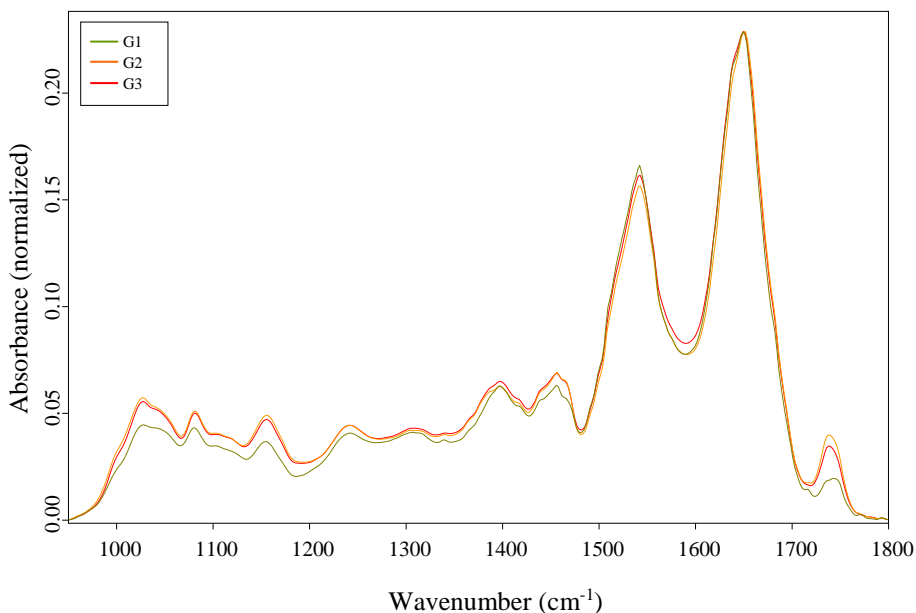


**Figure 3.5.** Mean spectra of G1, G2 and G3 grade tumorous tissue smears. Spectra are baseline corrected and normalized according to Amide I band.

Variations in normal tissue class are smaller and could be possibly linked to specific tissue functions: while the tissue is alteration free, it performs specific functions of an organ thus composition of tissue remains similar between different individuals. Present variations in spectra could be caused by individual differences in tissue constitution related to the environment, diet, lifestyle, habits, and characteristics of organism of the patient as well as the area from which tissue specimen was resected.

Methods of multivariate statistical analysis were applied for the evaluation of the IR spectroscopy to delineate normal and pathological kidney tissues. Dendrogram representing results of HCA analysis for classification of tumorous and non-tumorous tissue smears is shown in Figure 3.6 (enlarged clusters are presented in the Appendix, Figures A-02 – A-03).

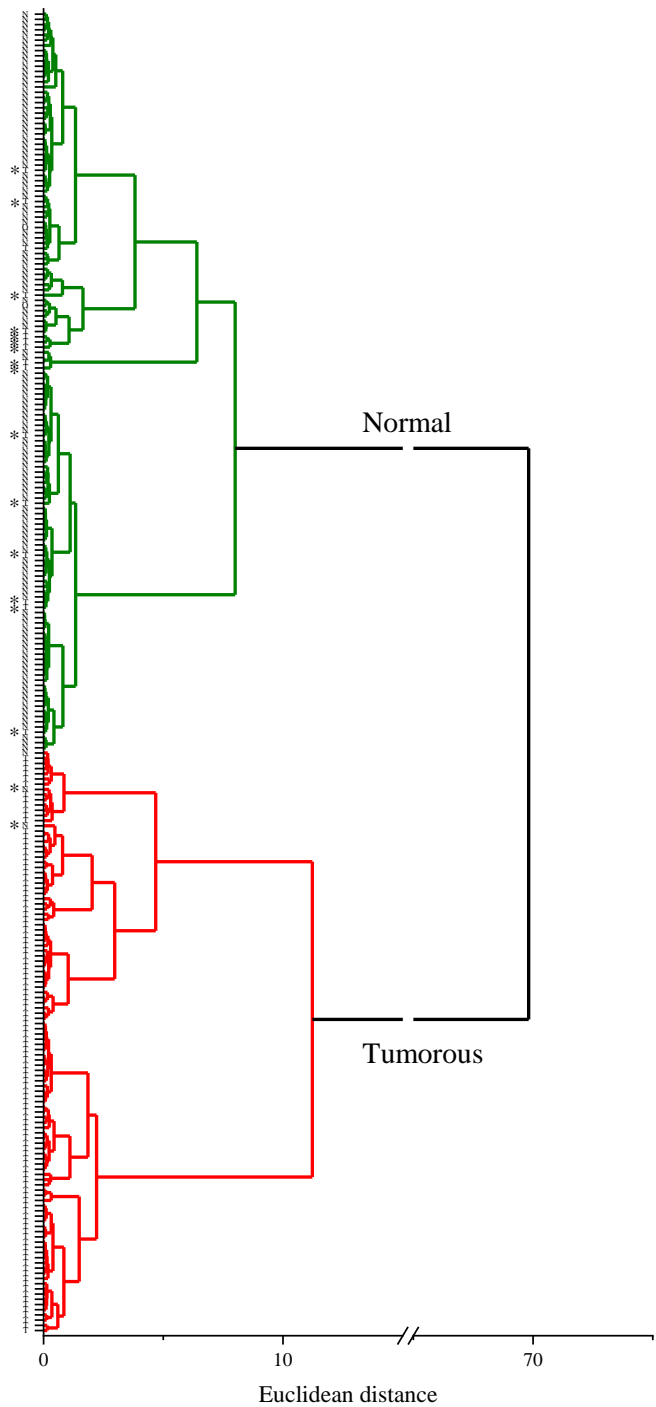


**Figure 3.6.** HCA dendrogram of non-tumorous and tumorous kidney tissue smears. Green cluster corresponds to the non-tumorous tissue class, red cluster corresponds to tumorous tissue class. Letters N, T and O represent spectra of each non-tumorous, tumorous and other tissues respectively. \* symbol indicates spectra which were assigned to the wrong tissue class.

Spectra of non-tumorous (normal, pyelonephritis with non-specific fibrotic alterations and fibrosis) and tumorous tissue smears are classified into two well separated clusters; large distance between clusters reveals a good separation between both tissue classes. Spectra of normal, pyelonephritis with non-specific fibrotic alterations as well as fibrosis tissue smear samples are grouped into one cluster labelled as non-tumorous tissue class. Only 3 normal tissue smear spectra (these spectra are indicated by \* symbol) out of 129 non-tumorous tissue smear spectra are classified as tumorous tissue that corresponds to 98 % accuracy for non-tumorous tissue smear sample classification. While analysing only normal tissue smear samples, the same 3 spectra out of 127 normal tissue smear spectra are classified as tumorous tissues that corresponds to 98 % accuracy for normal tissue smear classification as well. The possible reason of misclassification could be insufficient signal to noise ratio of spectra (these spectra are presented in the Appendix, Figure A-04). 16 spectra out of 125 spectra of tumorous tissue smears were classified as non-tumorous tissues that corresponds to 87 % accuracy for tumorous tissue smear classification. Spectra which were assigned to wrong tissue class are presented in the Appendix, Figure A-05. All tumorous tissue smear spectra which were assigned to normal tissue class show absence of glycogen spectral bands while presence of glycogen is a characteristic feature of kidney cancer (especially for ccRCC tumors). 6 spectra out of all 6 oncocytoma tissue smear spectra show absence of glycogen spectral bands and are assigned to normal tissue class. This finding suggests that presence of glycogen is an important and suitable criterion for identification of kidney tumors in most cases, however, it is inappropriate for identification of oncocytoma. Moreover, some spectra (spectrum 3) are of unsuitable quality or show higher levels of fats (representative spectrum of fatty tissue and assignment of spectral bands corresponding to fatty tissue spectrum are presented in the Appendix, Figure A-06).

PCA analysis was applied for non-tumorous and tumorous tissue smear spectra. Results of PCA analysis are presented in Figure 3.7. Data is classified into two clusters, corresponding to non-tumorous (left side of the diagram; green and blue dots correspond to normal and other non-tumorous tissue spectra) and tumorous (right side of the diagram; red, violet, orange, grey, cyan, pink and yellow dots correspond to ccRCC, papillary RCC, chromophobe RCC, tubulocystic RCC, multilocular RCC, angiomyolipoma and oncocytoma tumors, respectively) tissue smears. 3 spectra out 127 normal tissue smear spectra and 19 spectra out of 125 tumorous tissue smear spectra were assigned to tumorous and normal tissue classes, respectively; that corresponds to 98 % accuracy for normal and 85 % accuracy for tumorous



tissue smear classification. Both spectra of other non-tumorous tissue smears (pyelonephritis with non-specific fibrotic alterations and fibrosis) are assigned to the same cluster as normal tissue smears.

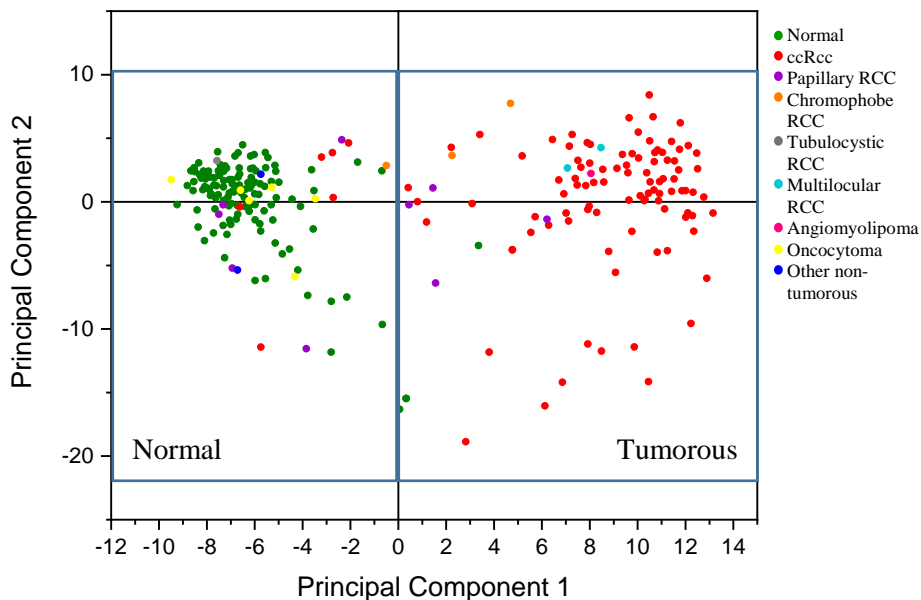


**Figure 3.7.** PCA diagram of kidney tissue smear spectra.

Spectra of normal tissue smears which were assigned to tumorous tissue class as well as spectra of tumorous tissue which were assigned to normal tissue class are presented in the Appendix (Figures A-07 – A-08). 1 spectrum out of 3 spectra of normal tissue smears classified as tumorous tissue by applying PCA analysis, coincides with spectrum of normal tissue smear which was assigned as tumorous tissue by applying HCA analysis. This spectrum (Appendix, Figure A-07, spectrum 3) shows insufficient signal to noise ratio and slightly increased levels of fats compared to mean spectrum of normal tissue smears while other two spectra (Appendix, Figure A-07, spectra 1-2) shows high levels of fats. Most tumorous tissue smear spectra classified as normal tissue smears by applying PCA analysis (12 out of 19 cases) were also classified as normal tissue smears by applying HCA analysis. All of the tumorous tissue smear spectra assigned as normal tissues by applying PCA analysis show absence of glycogen spectral bands as in case of HCA analysis.

Method of automated tissue analysis based on comparison of the spectrum that is being analysed with the spectra of the library was developed. The method was applied for the evaluation of 97 spectra of normal and 95 spectra

of tumorous kidney tissue smears. Only 5 spectra out of 97 normal kidney tissue smear spectra were assigned as tumorous tissue that corresponds to 95 % accuracy for normal tissue classification while 18 spectra out of 95 tumorous tissue smear spectra were classified as normal tissues corresponding to 81 % accuracy of tumorous tissue classification. 3 spectra out of 5 normal tissue smear spectra which were assigned to tumorous tissue class by applying automated tissue analysis coincide with normal tissue smear spectra classified as tumorous tissue by applying HCA analysis. Meanwhile 3 spectra out of these 5 spectra coincide with normal tissue smear spectra classified as tumorous tissue by applying PCA analysis. All 5 spectra of normal tissue identified as tumorous tissue are presented in the Appendix, Figure A-08; these spectra show either high levels of fats or are of insufficient signal to noise ratio as it was mentioned above. 12 spectra out of 18 tumorous tissue smear spectra which were identified as normal tissues by applying developed model of automated tissue type identification coincide with spectra of normal tissue smears classified as tumorous tissues by applying HCA analysis. All 18 spectra out of 18 tumorous tissue spectra classified as normal tissues by applying the developed model coincide with tumorous tissue smear spectra assigned as normal tissues by applying PCA analysis. These spectra are presented in the Appendix, Figure A-10; possible reasons for such classifications are absence of glycogen spectral bands, higher levels of fats in the tissue as it was discussed above.

Values of sensitivity, specificity, PPV and NPV were calculated and are presented in Table 3.3.

**Table 3.3.** Summarized values of sensitivity, specificity, positive and negative prognostic values for application of HCA, PCA analysis and developed automated tissue identification model for kidney tumorous tissue identification.

	<b>Method</b>		
	<b>HCA</b>	<b>PCA</b>	<b>Developed automated tissue identification model</b>
Sensitivity	87 %	85 %	81 %
Specificity	98 %	98 %	95 %
PPV	97 %	97 %	94 %
NPV	89 %	87 %	84 %

Despite lower value of sensitivity for application of developed model for automated tissue identification compared to HCA and PCA analysis, this

result does not generally mean that the developed model provides worse results. For example, automated analysis provides even better results of sensitivity compared with PCA analysis. This can be illustrated by lower number of tumorous tissue spectra which were assigned to normal tissue class by applying the developed model compared with PCA analysis. This can be explained by the fact that for the developed model for automated tissue identification spectra library (training set) is required. This results in lower number of spectra which are being classified – the larger scope of data is analysed, the better accuracy is achieved. Another important aspect for current classification results of tumorous tissues by applying all described methods is that the most frequently diagnosed tumor type is ccRCC (it was diagnosed for 83 % analysed patient cases) and only several cases of each other tumor type were analysed. It is known that increased levels of glycogen is a characteristic feature of ccRCC tumors. Larger data set of other tumor types for the establishment of spectral tumor markers and more precise analysis is required.

### 3.3.2. Tissue smears and tissues measured by using fiber-based spectroscopy system

In this section, analysis of spectra of tissue smears and unprocessed tissues measured by using fiber-based spectroscopy system is described. In total, cases of 34 patients were analysed. Summarised data is presented in table 3.4. Final diagnosis is based on standard histology reports of the whole resected tissue specimen.

**Table 3.4.** Kidney tissue types collected during the study of tissue smears and unprocessed tissues by using fiber-based spectroscopy system for the measurements.

Tissue type	Number of tissue samples
Normal	34
Tumor	
ccRCC	22
ccRCC, retention cysts	4
Papillary RCC	1
Papillary urothelial carcinoma of renal pelvis	1
Chromophobe RCC	2
Chromophobe RCC, retention cysts	1

Chromophobe RCC, papillary RCC	1
Oncocytoma, retention cysts <sup>B</sup>	1
SDHB RCC	1
Total number of patients	34

B indicates benign tumors.

Spectra of each specimen were collected at several different areas of the sample: tissue sample was sliced, pressed against the ATR element and removed, thus tissue smear spectra were collected from each freshly cut surface. In case of every sample, obtained spectra were averaged and resulting spectrum was used for further analysis.

**Tissue smears.** It was shown in Chapter 2 that spectra of kidney tissue smears measured by using spectrometer Alpha and by using fiber-based spectroscopy system are equivalent, thus, spectral tumor markers remain the same as it was described in previous section.

Methods of multivariate statistical analysis (HCA and PCA) and developed model for automated tissue analysis were applied for the delineation of normal and tumorous kidney tissue smears. Dendrogram representing results of HCA analysis for classification of normal and tumorous tissues is shown in Figure 3.8. Spectra of normal and tumorous kidney tissue smears are classified into two well separated clusters; large distance between clusters shows a good separation between both tissue classes. All spectra of normal tissue smears are grouped into one cluster that corresponds to 100 % accuracy for normal tissue classification. Only 4 out of 34 tumorous tissue smear spectra are classified as normal tissue smears (these spectra are indicated by \* symbol) that corresponds to 88 % accuracy for tumorous tissue smear classification. Spectra of tumorous tissue smears which were classified as normal tissues are presented in the Appendix, Figure A-10. All of these spectra show absence of glycogen while glycogen is an important marker for kidney tumors. Among these cases, patients were diagnosed with ccRCC tumor with retention cysts (1 patient), papillary RCC (1 patient), SDHB RCC tumor with retention cysts (1 patient) and chromophobe RCC with retention cysts (1 patient). As it was mentioned in previous section, larger database of spectra of other tumor types than ccRCC is required for the establishment of spectral tumor markers.

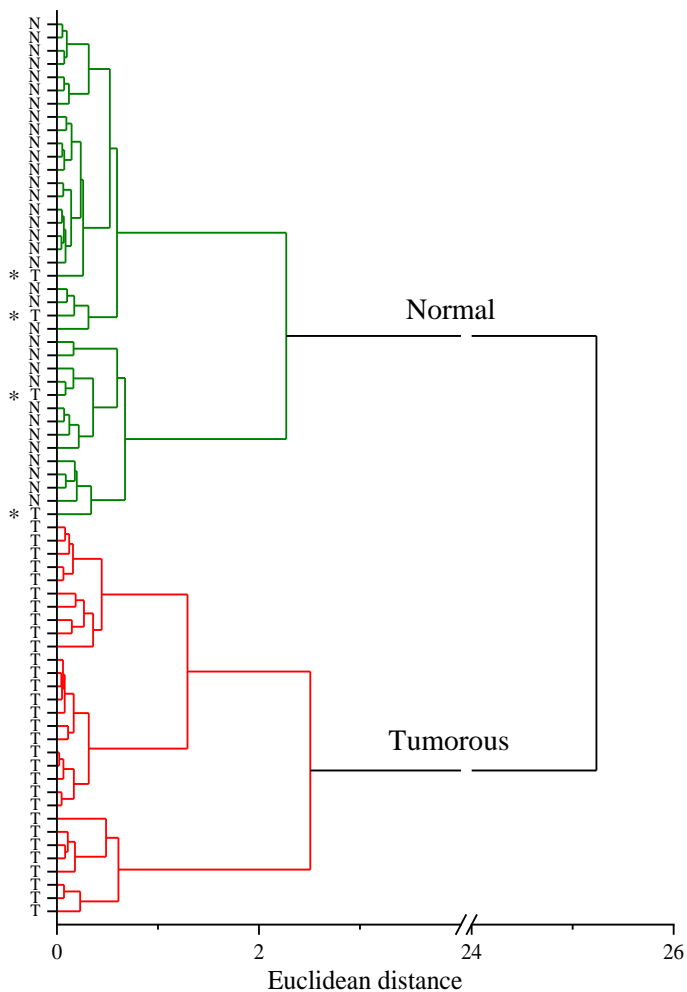


**Figure 3.8.** HCA dendrogram of normal and tumorous kidney tissue smears. Green cluster corresponds to the normal tissue class, red cluster corresponds to the tumorous tissue class. Letters N and T spectra of each normal and tumorous tissues respectively. \* symbol indicates spectra which were assigned to the wrong tissue class.

Results of PCA analysis are presented in Figure 3.9. data is classified into two clusters corresponding to normal (left side of the diagram; green dots) and tumorous (right side of the diagram; red dots) tissue smears.

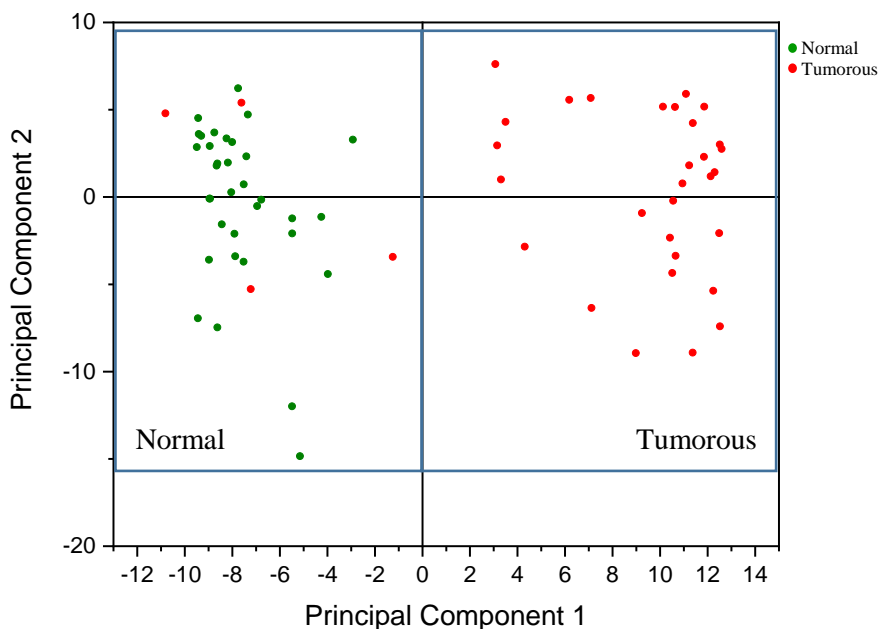


**Figure 3.9.** PCA diagram of kidney tissue smear spectra.

Application of PCA analysis gives the same results as the application of HCA analysis: all normal tissue smear samples were assigned to normal tissue cluster while the same 4 spectra out of 34 tumorous tissue smear spectra were assigned to normal tissue cluster.

After application of the developed model for automated tissue analysis, all normal tissue smears were classified as normal tissues while 4 spectra out of 34 tumorous tissue smear spectra were classified as normal tissues. These spectra coincide with spectra assigned as normal tissues by applying HCA and PCA analysis, suggesting that developed model for automated tissue identification gives similar results as multivariate statistical analysis. Summarized values of sensitivity, specificity, PPV and NPV are shown in the Table 3.5. It is important to mention that the spectra library remained the same as it was used for analysis of tissue smear spectra measured by using spectrometer Alpha.

**Table 3.5.** Summarized values of sensitivity, specificity, positive and negative prognostic values for application of HCA, PCA analysis and developed automated tissue identification model for kidney tumorous tissue identification.

	Method		
	HCA	PCA	Developed automated tissue identification model
Sensitivity	88 %	88 %	88 %
Specificity	100 %	100 %	100 %
PPV	100 %	100 %	100 %
NPV	89 %	89 %	89 %

**Native unprocessed tissues.** Mean spectra of kidney normal and tumorous tissue smears are presented in Figure 3.10. Strong and wide water absorption band located at  $1640\text{ cm}^{-1}$  and assigned to  $\delta(\text{O-H})$  vibrations is observed in tissue spectra. This spectral band overlaps with Amide I and Amide II spectral bands of the tissue. In this regard, analysis of the tissue spectra in this and following chapters of this work is performed in spectral range between  $950\text{-}1480\text{ cm}^{-1}$ . Main spectral band positions and their assignments are shown in Table 3.6.

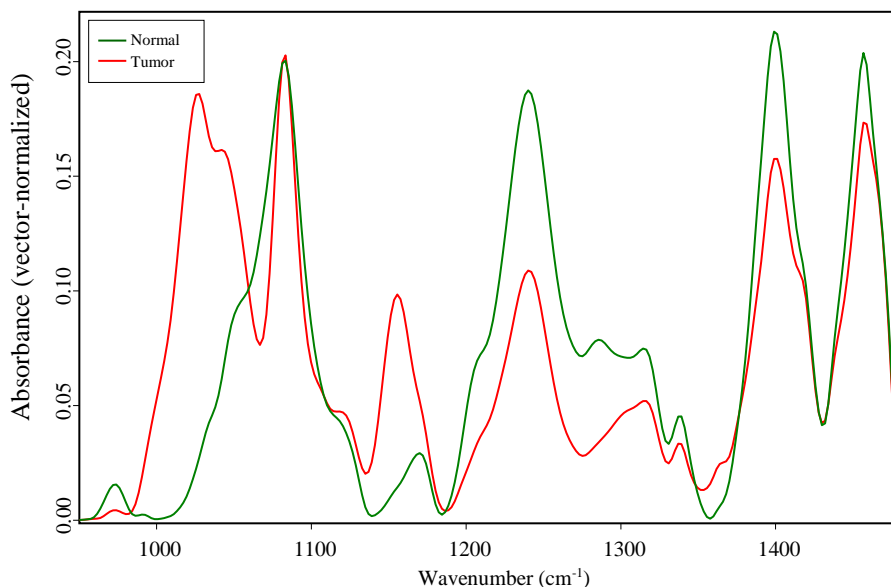


**Figure 3.10.** Mean ATR IR spectra of normal and tumorous kidney tissues. Spectra are baseline corrected and vector-normalized.

**Table 3.6.** Spectral bands of the unprocessed tissue spectra and their assignments. Assignments set according to [158].

Spectral band position, cm <sup>-1</sup>		Assignment
Normal tissue	Tumorous tissue	
972	972	v(PO <sub>4</sub> ) of nucleic acids and proteins OCH <sub>3</sub> of polysaccharides
Not present	1025	v(C-O), v(C-C), δ(C-O-H) of glycogen
Not present	1045	v(CO-O-C)
1048	Not present	v(C-O), δ(C-O) of the C-OH of carbohydrates
1082	1082	v(CO-O-C)
1121	1121	v(C-O), δ(C-O) of the C-OH of carbohydrates
Not present	1155	v(PO <sub>2</sub> ); glycogen*
1169	1169(sh)	v(C-O), δ(C-O), δ(C-O-H), δ(C-O-C) phosphodiester stretching
1207	1207	v(C-O)
1240	1240	v(C-O)
1285	Not present	Amide III
Not present	1302	v(PO <sub>2</sub> ), Amide III
1315	1315	Amide III
1337	1337	Amide III
Not present	1364	CH <sub>2</sub> wagging
1400	1400	v(C-O), δ(C-H), δ(N-H)
1457	1457	δ(CH <sub>3</sub> )
		δ(CH <sub>3</sub> )

(sh) indicates a shoulder band

\*assignment of glycogen spectral band is based on the experimental data (see Appendix, Figure A-01)

Spectra of normal and tumorous kidney tissues demonstrate obviously different spectral profiles. As well as for the tissue smear spectra, the most significant differences between normal and tumorous kidney tissue spectra are



observable in spectral region between 950 and 1200  $\text{cm}^{-1}$  where spectral bands mainly due to carbohydrates, glycoproteins and phosphate groups are located. Higher values of absorbance for the band positions at 1027  $\text{cm}^{-1}$  assigned to  $\nu(\text{C-O})$ ,  $\nu(\text{C-C})$ ,  $\delta(\text{C-O-H})$  vibrations and at 1155  $\text{cm}^{-1}$  assigned to  $\nu(\text{C-O})$  vibrations of glycogen are observed in tumorous kidney tissue. Although spectral band located at 1081  $\text{cm}^{-1}$  can be assigned to  $\nu(\text{PO}_2)$  vibrations of nucleic acids, together with increased absorbance values of spectral bands located at 1027 and 1155  $\text{cm}^{-1}$ , this spectral band is assigned to glycogen. Another important difference is for the spectral band located at 972  $\text{cm}^{-1}$  which could be assigned to  $\nu(\text{PO}_4)$  vibrations of nucleic acids or proteins and for the spectral band located at 1240  $\text{cm}^{-1}$  which could be assigned to  $\nu(\text{PO}_2)$  vibrations and Amide III groups of proteins. Higher absorbance values of these spectral bands are for the spectra of normal tissue. This finding could be related to decreased levels of fructose 1,6-bisphosphatase in tumorous kidney tissue. It is known that in case of ccRCC tumors, the amount of fructose 1,6-bisphosphatase is decreased [166], [175], [176]. Tumor cells express less of fructose 1,6-bisphosphatase thus reinforces Warburg-like metabolic shift. Decreased amount of this enzyme is associated with changed cellular metabolic processes and increased amount of glycolytic flux in tumorous cells as fructose 1,6-bisphosphatase antagonizes the glycolytic flux and inhibits the nuclear function of HIF- $\alpha$  metabolic regulator [166], [176].

As for the tissue smear spectra, variations of spectra in normal and tumorous tissue classes are quite high (Figure 3.11).

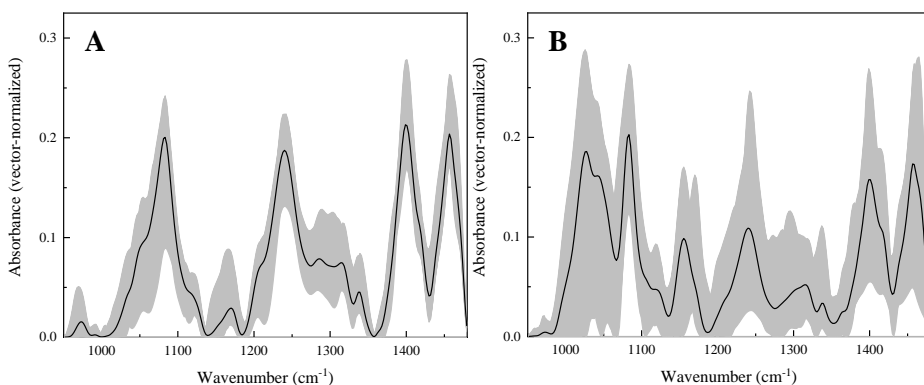


**Figure 3.11.** Mean spectra (black solid line) and variations of spectra of tissue taken from different patients (grey area) of kidney normal (A) and tumorous (B) tissue. Spectra are baseline corrected and vector-normalized.

Black lines correspond to the mean spectra of all the samples taken from different patients, while grey areas indicate the variations of spectra in

different tissue classes. Variations of spectra in the tumorous tissue class is higher compared to normal tissue class; variations are especially high for the spectral bands located at 1025, 1155 and 1240  $\text{cm}^{-1}$  considered as spectral markers of kidney cancer. As mentioned before, higher variations in tumorous tissue spectra class could be linked to the diverse differentiation of tumorous cells.

Methods of multivariate statistical analysis were applied for the evaluation of the IR spectroscopy to delineate normal and tumorous kidney tissues. Dendrogram representing results of HCA analysis for classification normal and tumorous tissues is shown in Figure 3.12.

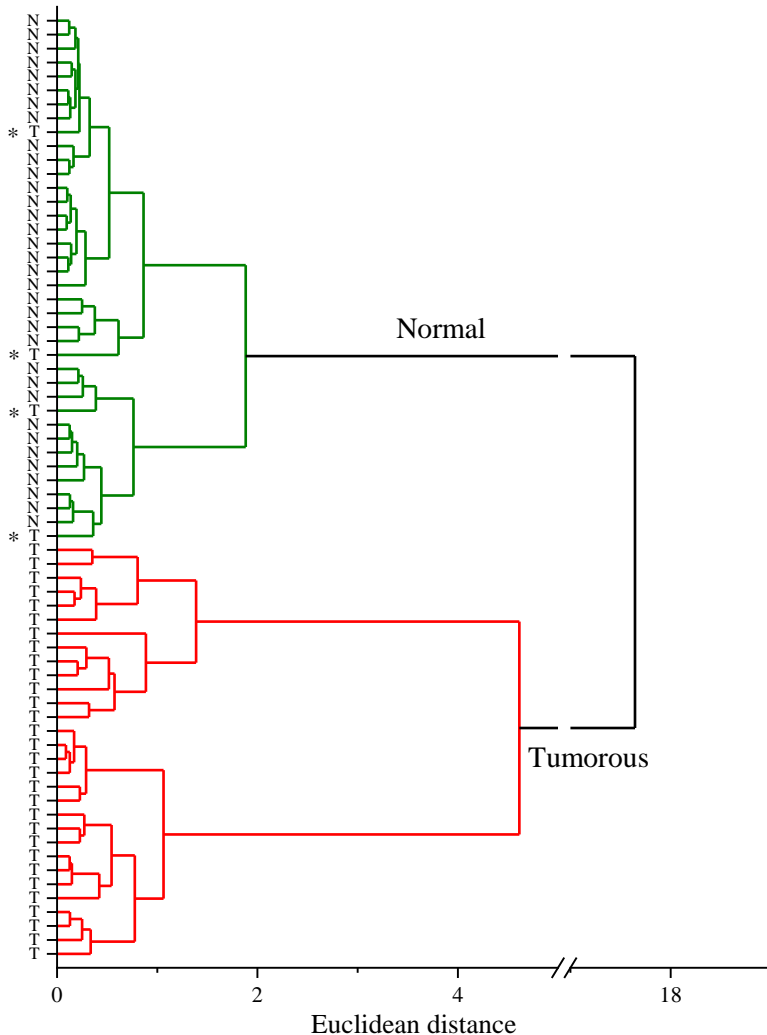


**Figure 3.12.** HCA dendrogram of normal and tumorous kidney tissues. Green cluster corresponds to the normal tissue class, red cluster corresponds to the tumorous tissue class. Letters N and T spectra of each normal and tumorous tissues respectively. \* symbol indicates spectra which were assigned to the wrong tissue class.

Spectra of normal and tumorous kidney tissues are classified into two well separated clusters; large distance between clusters shows a good separation between both tissue classes. All spectra of normal tissues are grouped into one cluster that corresponds to 100 % accuracy for normal tissue classification. Only 4 out of 34 tumorous tissue spectra are classified as normal tissue smears (these spectra are indicated by \* symbol) that corresponds to 88 % accuracy for tumorous tissue classification. Spectra of these tissue samples originate from the same patients as it was for the HCA analysis of tissue smears. Spectra of tumorous tissue smears which were classified as normal tissues are presented in the Appendix, Figure A-11. All of these spectra show absence of glycogen while glycogen spectral bands is an important marker for kidney tumor spectra.

Results of PCA analysis are presented in Figure 3.13. Data is classified into two clusters, corresponding to tumorous (left side of the diagram; red dots) and normal (right side of the diagram, green dots) tissues.

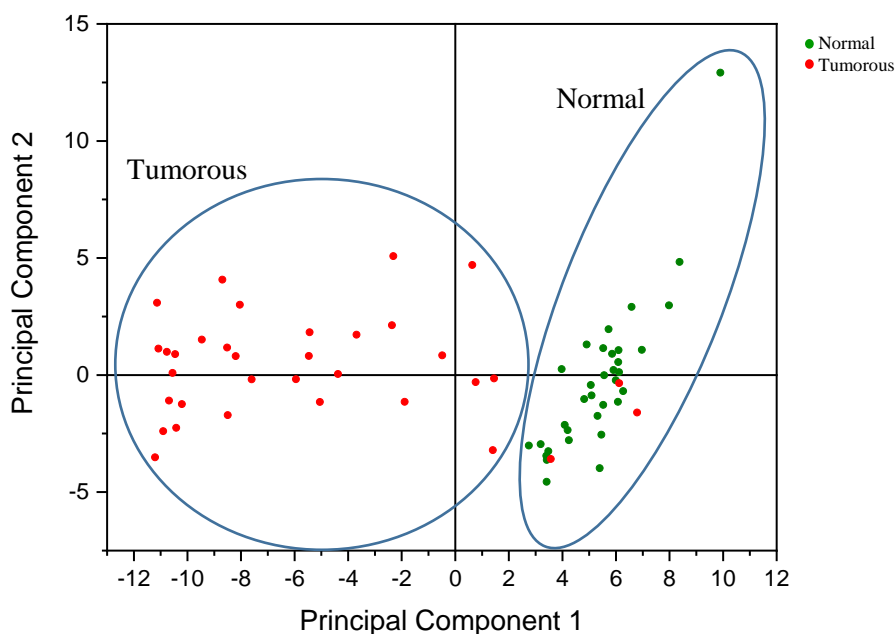


**Figure 3.13.** PCA diagram of kidney tissue spectra.

All spectra of normal tissues were assigned to normal tissue class while 3 spectra out of 34 spectra of tumorous tissues were classified as normal tissues, that corresponds to 100 % accuracy for normal and 91 % accuracy for tumorous tissue classification. Tumorous tissue spectra classified as normal

tissues by applying HCA analysis coincide with tumorous tissue spectra classified as normal tissue by applying PCA analysis. Summarized values of sensitivity, specificity, PPV and NPV are shown in the Table 3.7.

**Table 3.7.** Summarized values of sensitivity, specificity, positive and negative prognostic values for application of HCA and PCA analysis for kidney tumorous tissue identification.

	<b>Method</b>	
	<b>HCA</b>	<b>PCA</b>
Sensitivity	88 %	91 %
Specificity	100 %	100 %
PPV	100 %	100 %
NPV	89 %	92 %

Both methods (HCA and PCA) give similar results; meanwhile classification accuracy for kidney tissues and tissue smears are similar. This suggests that both tissue sample types (unprocessed tissues and tissue smears) are suitable for the tissue type evaluation; however, tissues are better applicable for intraoperative applications due to shorter duration of spectra collection.

## 4. CHAPTER 4. APPLICATION FOR URINARY BLADDER CANCER

### 4.1. Urinary bladder cancer

Urinary bladder is a hollow organ of urinary system responsible for storing and excreting urine originated from kidneys. Strong elastic walls of the bladder assure expansion of the bladder while collecting urine and a contraction during micturition.

Bladder cancer is among 10 most frequently diagnosed malignancies worldwide and is more common in men than in women with higher mortality rates in men [1], [177]. Epithelial neoplasms account around 99 % of urinary bladder cancer cases of which most prevalent type is urothelial (transitional cell) carcinoma with incidence rate of 90 %. Non-urothelial neoplasms account around 9 % of neoplasm cases including adenocarcinoma, small cell carcinoma, squamous cell carcinoma and rare neoplasms. Non-epithelial (mesenchymal) neoplasms account around 1 % of bladder tumors covering benign (such as hemangioma, leiomyoma, lipoma, neurofibroma, paraganglioma) and malignant (angiosarcoma, leiomyosarcoma, malignant fibrous histiocytoma, osteosarcoma, rhabdomyosarcoma) neoplasms [178]. Bladder cancer can be also classified as muscle-invasive bladder cancer (MIBC) and non-muscle-invasive (NMIBC) cancer. The latter type tumors involve only the urothelium or lamina propria without invasion to the detrusor muscle and accounts around 80 % of bladder cancer cases [179]. This type of tumors is locally treated and highly recurrent disease with 5-year recurrence rates varying from 31 % to 78 % [180]. Thus, the complete removal of malignant lesions is crucial for recurrence prevention. Management strategy of the disease depends on the status of neoplasm. In case of smaller localised tumors, procedure of transurethral resection of the bladder (TURB) is applied. The mainstay procedure of tissue diagnostics is white light cystoscopy (WLC) applied during the endoscopy of the urinary bladder via urethra followed by histopathological examination of resected tissue specimen. However, the false-negative rate of WLC method reaches 10-20 % [181]. Other method may be applied for diagnostics is photodynamic diagnosis (PDD), also called blue light cystoscopy. During the examination, photo-sensing agent 5-aminolaevulinic acid (5-ALA) or hexaminolevulinate (HAL) is instilled into the bladder causing porphyrins being accumulated in neoplastic cells. Subsequently, after illumination with blue light (380–450 nm), malignant areas result in fluorescent red light [181]. While PDD is characterised by better sensitivity rates, it shows lower specificity compared to WLC [182].

Due to limited accuracy of mentioned conventional diagnostic methods, new additional minimally invasive methods being able to improve diagnostic accuracy, are under development.

## 4.2. Experimental details

### 4.2.1. Tissue sample collection

Human urinary bladder tissue samples were obtained at the Urology Center of the Vilnius University Hospital Santaros Klinikos (Lithuania). The study was approved by the Regional Biomedical Research Ethics Committee (Document No. 2019/12-1178-665). Samples were collected from transurethral resections of urinary bladder (TURB) performed due to urothelial carcinoma. Freshly resected tissue samples were macroscopically examined by a surgeon and assigned as ‘tumor’, ‘normal’ or ‘cystitis’. In most cases two tissue samples (normal and pathological tissue) for each patient were received. In some cases, only one type of tissue (normal or pathological) sample per patient was received due to status of the surgery. Resected tissue samples placed on ice were transported to the spectroscopic laboratory for the measurements.

### 4.2.2. FT-IR spectroscopy measurements of tissue samples

Measurements were performed by using fiber-based spectroscopy system described in the Chapter 2. Two types of samples were analysed: spectra of native not pre-processed tissues and tissue smears were measured. In the first step, received tissue samples were sliced into several pieces and measurements were performed from freshly cut surface. The fiber probe was pressed against the freshly cut surface area and spectrum was measured afterwards, hereby obtaining a spectrum of native tissue. Secondly, after removing the probe from the tissue sample, the material which is remaining on the ATR crystal was air dried and resulting spectrum of tissue smear was measured. Number of slices and measured spectra depended on the size of the sample, it usually varied between 1 and 4 cuts per sample. Furthermore, in some cases, collected spectra of tissue smears were of insufficient quality and due to low signal to noise ratio were inappropriate for further analysis. Examples of low quality tissue smear spectra are shown in the Appendix, Figure A-13.

Spectra were collected in 400 – 4000  $\text{cm}^{-1}$  spectral region with a 4  $\text{cm}^{-1}$  resolution. 64 interferograms were recorded, averaged and Fourier transformed into IR absorption spectrum. Blackmann-Haris 3-Term apodization function, zero filling factor of 2 and phase correction (Power Spectrum phase correction method) were used while applying the Fourier transformation. Software build in ATR correction was performed using spectral software OPUS.

#### 4.2.3. Statistical analysis

Statistical analysis (HCA and PCA) was performed by using data analysis software OriginPro. Prior statistical analysis, spectra were pre-processed: atmospheric compensation, baseline correction, vector normalization and offset correction were applied by using spectroscopy software OPUS. Statistical analysis was performed by applying standard procedures (Hierarchical Cluster Analysis and Principal Component Analysis) of the OriginPro software package. While performing HCA, Ward cluster algorithm, Euclidean distance type were chosen. Different spectral regions were chosen for statistical analysis and different pre-processing of spectra (either first derivative of spectra was calculated by using spectroscopy software OPUS or not) was applied prior the analysis; however, only the best achieved results are presented in the following section.

#### 4.3. Spectroscopic analysis: results and discussion

In total, cases of 54 patients were analysed. Samples of native unprocessed tissue and tissue smears were investigated. Summarised data is presented in Table 4.1. Final diagnosis is based on standard histology reports of the whole resected tissue specimen.

**Table 4.1.** Tissue types collected during the study.

Tissue type	Number of native tissue samples	Number of tissue smear samples
Normal tissue	49	46
Urothelial carcinoma tissue		
High grade tumor	34	33
Low grade tumor	13	13
Non-specific cystitis	6	6

Both types (normal and pathological) of tissue were obtained not from every patient. In one case, it was not possible to obtain tumorous tissue. In 5 cases, patients were diagnosed with completely altered bladder thus the normal tissue was inappropriate for analysis. Number of tissue smear samples is smaller compared to tissue samples due to insufficient quality for analysis of spectra.

Spectra of each tissue specimen were collected at several different areas of the sample: tissue sample was sliced, and spectra were collected from each freshly cut surface. This was performed having in mind that biological tissues tend to be inhomogeneous. Hereby, as much as possible information about the sample constitution is collected. In case of every sample, obtained spectra were averaged and resulting mean spectrum was used for further analysis.

Mean spectra of normal, tumorous (low- and high-grade urothelial carcinoma) and cystitis bladder tissues are presented in Figure 4.1. Spectra of different tissue types demonstrate obviously different spectral profiles. While cystitis and normal bladder tissue spectra share similar properties, differences between normal and tumorous as well as cystitis and tumorous tissue spectra are well defined. Main spectral band positions and their assignments are shown in Table 4.2.

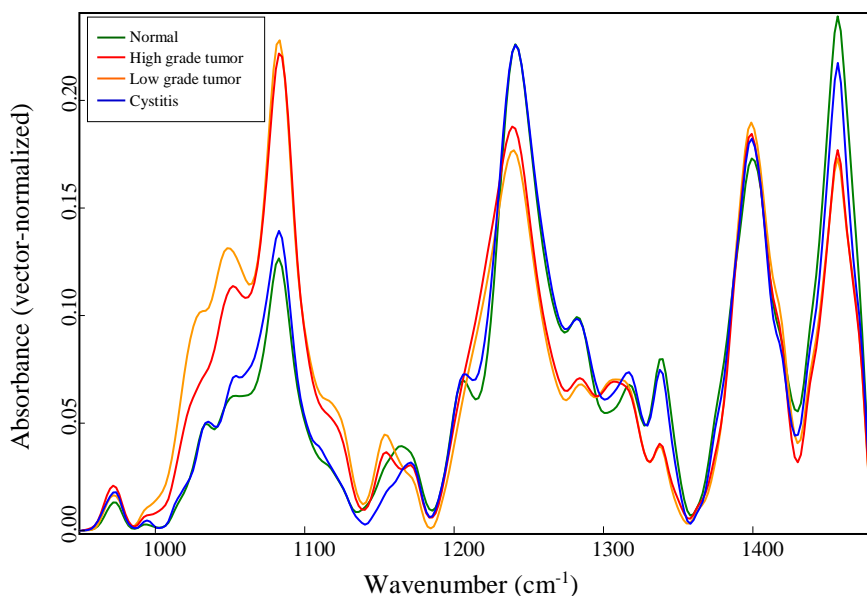


**Figure 4.1.** Mean ATR IR absorption spectra of normal, urothelial carcinoma (high-grade tumor and low-grade tumor) and cystitis tissue. Spectra are baseline corrected and vector-normalized.



Mean spectra of normal and cystitis bladder tissues compared to tumorous tissue spectra, represent more prominent spectral bands located at 1033, 1206, 1240, 1282, 1317 and 1339  $\text{cm}^{-1}$  which can be assigned to collagen [158] and are related to higher collagen levels in normal and cystitis bladder tissues. Collagen is one of the components of the lamina propria of urinary bladder and assures the tensile strength by transferring the tension from the bladder smooth muscle cells, during the expansion of the organ while storing urine [183]. Reduced collagen levels in tumorous bladder tissue can be related to increased enzymes secretion of collagenase into the tissue matrix and destruction of host tissue [44]. Spectra of tumorous bladder tissue demonstrate higher absorbance values of the spectral band located at 972  $\text{cm}^{-1}$  which could be assigned to  $\nu(\text{PO}_4)$  vibrations of nucleic acids. Also, spectral bands located at similar positions can be assigned to  $\nu(\text{PO}_4)$  vibrations of proteins and vibrational modes of  $\text{OCH}_3$  groups of polysaccharides. However, herewith the increased absorbance values of this spectral band, the stronger absorption is for the spectral band located at 1082  $\text{cm}^{-1}$  in tumorous tissue spectra and assigned to  $\nu(\text{PO}_2)$  vibrations of nucleic acids. These findings can be related to increased levels of nucleic acids in urothelial carcinoma tissue and higher rates of cell proliferation due to growth of the tumor.

Higher values of absorbance for the band positions at 1028  $\text{cm}^{-1}$  assigned to  $\nu(\text{C-O})$ ,  $\nu(\text{C-C})$ ,  $\delta(\text{C-O-H})$  vibrations and at 1154  $\text{cm}^{-1}$  assigned to  $\nu(\text{C-O})$  vibrations of glycogen are observed in urothelial carcinoma tissue spectra. Increased absorbance values of spectral bands assigned to glycogen are related to increased amount of glycogen in tumorous bladder tissues. Higher amount of glycogen is observed in some types of tumors and used as the resource of energy for cell proliferation [42], [173]. According to spectra, glycogen levels are higher in low grade urothelial carcinoma tissue compared to high-grade urothelial carcinoma tissue. This can be explained by increased energy demand and consumption of glycogen in higher grade tumors due to increased tumorous cell proliferation. The inverse relation of glycogen levels and cell proliferation rates is observed in some types of tumors [42]. A little bit higher amount of carbohydrates is observed in cystitis tissue compared to normal tissue but significantly lower compared to tumorous tissue spectra. This is indicated by spectral band located at 1052  $\text{cm}^{-1}$  and assigned to  $\nu(\text{CO-O-C})$ ,  $\nu(\text{C-O})$ ,  $\delta(\text{C-O})$  vibrations of the C-OH of carbohydrates and by spectral band located at 1110  $\text{cm}^{-1}$  which can be assigned to  $\nu(\text{C-O})$ ,  $\nu(\text{C-C})$  ring vibrations of polysaccharides and also to phosphate groups of RNA. In general, spectra of normal and cystitis tissues share similar features.

**Table 4.2.** Spectral bands and their assignments. Assignments set according to [158].

Spectral band position, cm <sup>-1</sup>			
Normal tissue	Urothelial Carcinoma tissue	Non-specific cystitis	Assignment
972	972	972	v(PO <sub>4</sub> ) of nucleic acids and proteins OCH <sub>3</sub> of polysaccharides
Not present	1028	Not present	v(C-O), v(C-C), δ(C-O-H) of glycogen
1033	Not present	1034	Collagen
1050	1048 (low-grade) 1052 (high-grade)	1052	v(CO-O-C) v(C-O), δ(C-O) of the C-OH of carbohydrates
1082	1082	1082	v(PO <sub>2</sub> );
Not present	Not present	1110 (sh)	v(C-O), v(C-C)
1121 (sh)	1121 (sh)	1121 (sh)	v(C-O), δ(C-O), δ(C-O-H), δ(C-O-C) phosphodiester stretching
1154 (sh)	1154	1154 (sh)	v(C-O)
1163	Not present	Not present	v(C-O)
1172 (sh)	1172	1171	v(C-O)
1206	Not present	1206	Amide III
1241	1239	1241	v(PO <sub>2</sub> ), Amide III
1282	1284	1282	Amide III
Not present	1307	Not present	v(CH <sub>2</sub> )
1317	1317 (sh)	1317	Amide III
1339	1339	1339	CH <sub>2</sub> wagging
1399	1399	1399	δ(CH <sub>3</sub> )
1457	1457	1457	δ(CH <sub>3</sub> )

(sh) indicates a shoulder band

Although differences between the mean spectra of normal, tumorous and cystitis tissues are clearly visible, variations of spectra inside these three tissue classes (normal, tumorous and cystitis tissues) are quite high (Figure 4.2)

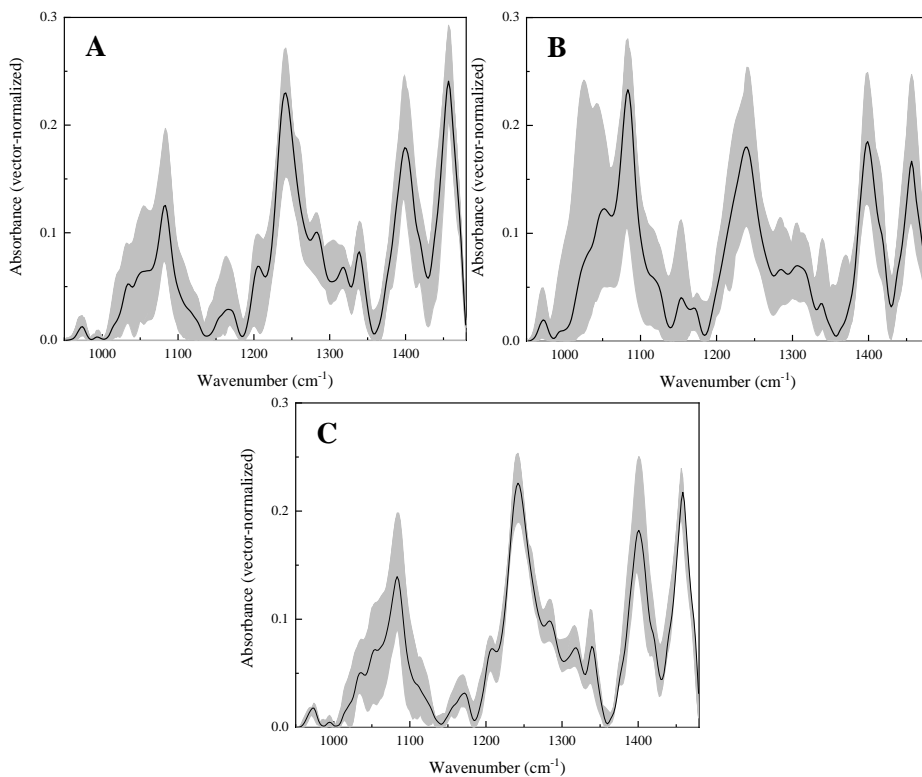


**Figure 4.2.** Mean spectra (black solid line) and variations of spectra of tissue taken from different patients (grey area) of normal (A), tumorous urothelial carcinoma (B) and cystitis (C) tissue. Spectra are baseline corrected and vector-normalized.

Black lines correspond to the mean spectra of all the samples taken from different patients, while grey areas indicate the variations of spectra in different tissue classes. Variations of spectra in the tumorous tissue class are higher (Figure 4.2 B), especially for the spectral bands corresponding to glycogen (located at 1028 and 1154  $\text{cm}^{-1}$ ) and collagen (1240, 1284, 1317, 1339 and 1457  $\text{cm}^{-1}$ ) and could be considered as spectral tumor markers of urothelial carcinoma. Higher variations in tumorous tissue spectra class could be linked to the diverse differentiation of tumorous cells. During development of a tumor, cells lose their functions and change their morphological features. Thus, depending on the tumor features and development, variations of amounts of specific components can vary in individual cases. Meanwhile, variations in normal and cystitis tissue spectra classes are smaller (Figure 2 A

and C) compared to the tumorous tissue class. Smaller variations in normal tissue class could be linked to specific tissue functions: while the tissue is alteration free, it performs specific functions of an organ thus composition of tissue remains similar between different individuals. Present variations in spectra could be caused by individual differences in tissue constitution related to the environment, diet, lifestyle, habits, and characteristics of organism of the patient as well as the area from which tissue specimen was resected. Small variations in spectra of cystitis tissue class can be determined by a small scope of cystitis tissue samples (only 6 cases were included in the study).

Methods of multivariate statistical analysis were applied for the evaluation of the IR spectroscopy to delineate normal and pathological bladder tissues. Dendrogram representing results of HCA analysis for classification of benign and malignant tissues is shown in Figure 4.3. Analysis performed for the first derivative of spectra in spectral region from 950 to 1480  $\text{cm}^{-1}$ .

Spectra of all normal and cystitis tissue samples are grouped into one cluster labelled as benign tissue class, meanwhile 8 spectra of urothelial carcinoma tissue are also classified as benign tissue. Thus, allowing to discriminate benign and malignant tissues with 100 % and 83 % accuracy respectively. In order to delineate normal and cystitis tissue samples, HCA analysis in spectral region between 950 and 1480  $\text{cm}^{-1}$  of first derivative of spectra was applied for these two tissue groups. The dendrogram representing results of HCA analysis is presented in the Appendix, Figure A-14. Two clusters are observed in the dendrogram; however, classification of normal and cystitis tissues is impossible. Half of cystitis tissue spectra (3 spectra out of 6) is assigned to one cluster while another half of cystitis spectra (3 spectra out of 6) to another. Spectra are grouped into two clusters with much smaller distance between the clusters (labelled as Cluster I and Cluster II) compared to the dendrogram presented in Figure 4.3. This indicates that differences between spectra belonging to two different groups are quite small. Also, inaccuracy could be determined by small amount of cystitis cases.

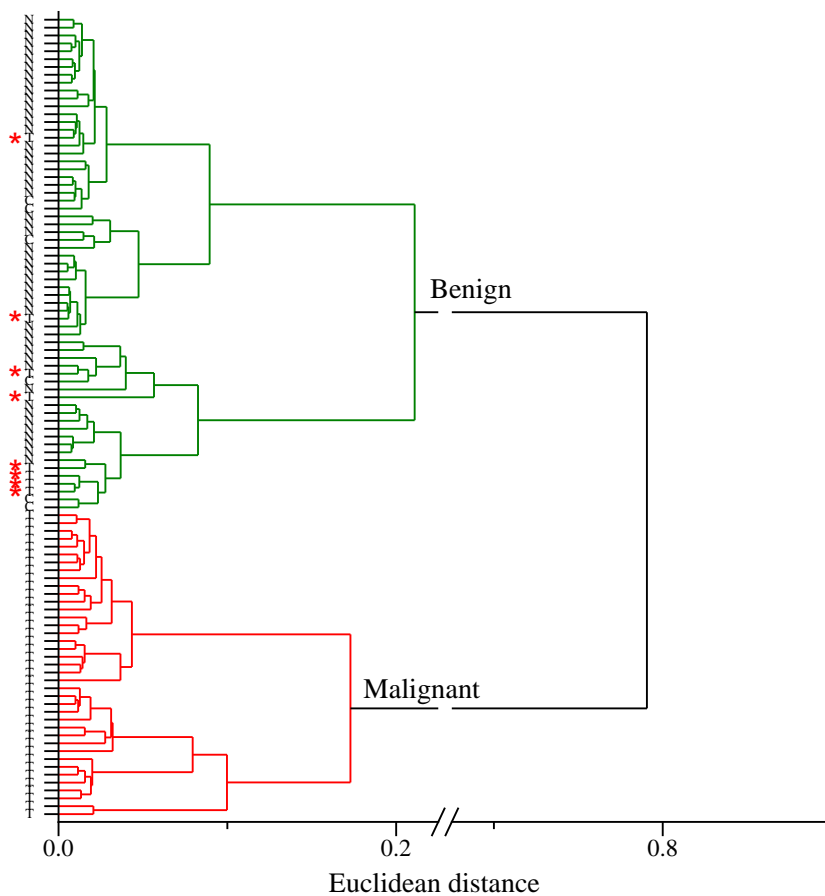


**Figure 4.3.** HCA dendrogram of benign and malignant tissues. Green cluster corresponds to the benign tissue class, red cluster corresponds to malignant tissue class.

Letters N, C and T represent spectra of each normal, cystitis and tumorous tissues respectively. \* symbol indicates tumorous tissue spectra which were assigned to benign tissue class. Analysis performed for the first derivative of spectra in spectral region from 950 to 1480  $\text{cm}^{-1}$ .

While applying HCA analysis (analysis performed for first derivative of spectra in spectral region between 950 and 1480  $\text{cm}^{-1}$ ) for normal and tumorous bladder tissues, spectra are classified into two well separated clusters; large distance between clusters reveals a good separation between both tissue classes. The dendrogram is shown in Figure 4.4.

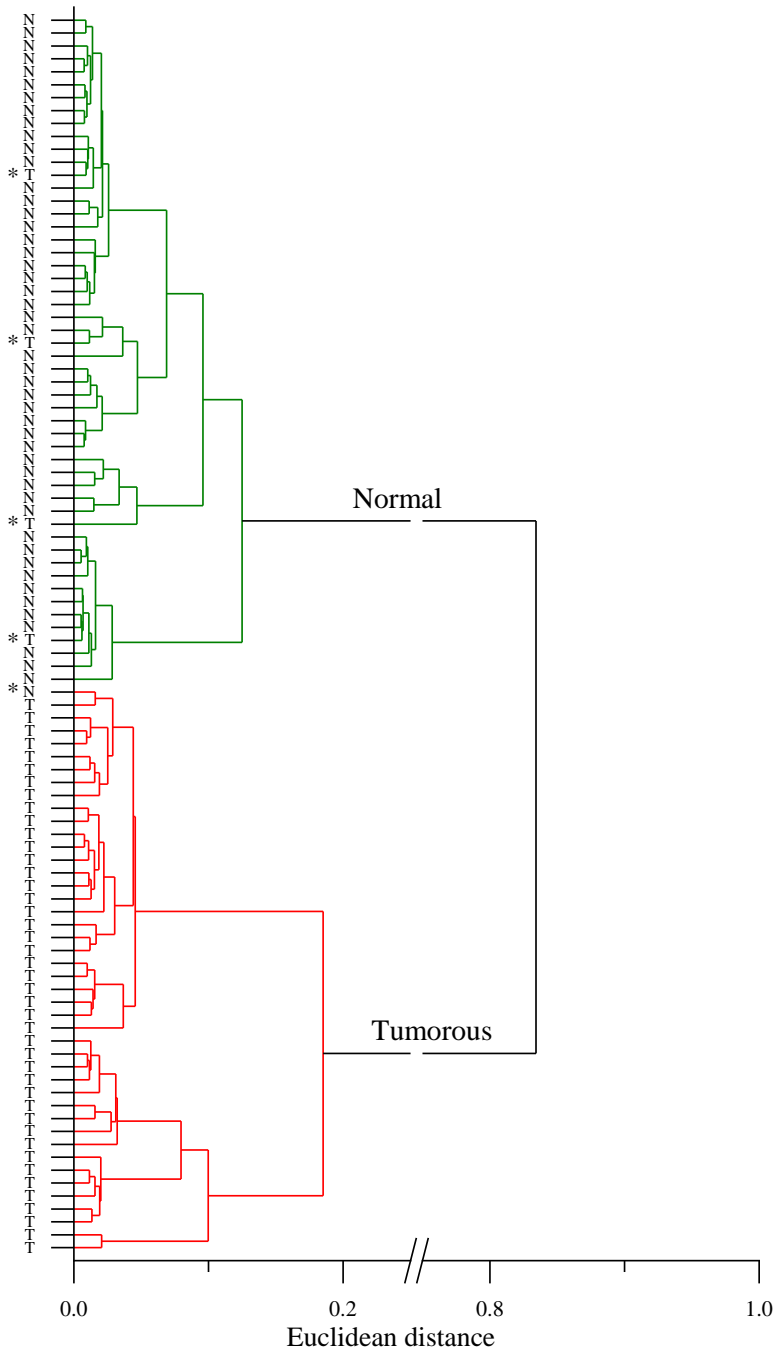


**Figure 4.4.** HCA dendrogram of normal and tumorous bladder tissues. Green cluster corresponds to the normal tissue class, red cluster corresponds to urothelial carcinoma tissue class. Letters N, and T represent spectra of each normal and tumorous tissues respectively. \* symbol indicates spectra which were assigned to the wrong tissue class.

Only 1 spectrum out of 49 normal tissue spectra and 4 spectra out of 47 tumorous tissue spectra were assigned to wrong classes (these spectra are indicated by \* symbol) that corresponds to 98 % accuracy for normal tissue and 91 % accuracy for urothelial carcinoma tissue identification respectively. Spectra which were assigned to wrong tissue classes are presented in the Appendix (Figures A-15 – A-16). Presented spectrum of normal tissue assigned to tumorous tissue class share more similarities with mean tumorous tissue spectrum than with mean normal tissue spectrum (Appendix, Figure A-15). One of the presented tumorous tissue spectra assigned to normal tissue class (Appendix, Figure A-16, (1)) possess characteristic features of lipid rich tissue. Another 3 spectra (2 – 4) share spectral properties characteristic to normal tissue (prominent spectral bands corresponding to collagen).

In order to evaluate the possibility to discriminate high-grade and low-grade tumors, HCA analysis was applied for first derivative of tumorous tissue spectra in spectral range between 950 and 1183  $\text{cm}^{-1}$  where spectral bands corresponding to spectral tumor marker glycogen are located. The dendrogram is presented in Appendix (Figure A-18). Most part of spectra of high-grade tumors (29 spectra out of 34) are grouped into one cluster with 7 spectra (out of 13) of low-grade tumors; while another cluster contains of 6 spectra of low-grade tumors and 5 spectra of high-grade tumors. Summarising these results, it could be stated that high-grade tumors can be identified with 85 % accuracy while low-grade tumors only with 46 % accuracy.

PCA analysis was applied for normal, tumorous and cystitis bladder tissue spectra in spectral range between 950 and 1480  $\text{cm}^{-1}$ . Results of PCA analysis are presented in Figure 4.5. Data is classified into two clusters, corresponding to normal (left side of the diagram) and tumorous (right side of the diagram) tissues. Green dots indicate spectra of each normal tissue, red and orange dots indicate spectra of each tumorous (high- and low-grade of malignancy respectively) tissue, blue dots indicate spectra of cystitis tissue samples. Normal and tumorous tissue classes are well separated, only 2 spectra out of 49 normal tissue spectra and 4 spectra out of 47 tumorous tissue spectra were assigned to wrong classes that correspond to identification accuracy of 96 % for normal tissue spectra and 91 % for tumorous tissue spectra. Distances between green dots corresponding to normal tissue samples are smaller than distances between red and orange dots corresponding to tumorous tissue samples thus indicating that the distribution of spectra is smaller in normal tissue class, normal tissue spectra are more similar to each other compared to tumorous tissue class. Misclassified spectra of normal and tumorous tissues are presented in the Appendix (Figures A-16 – A-17). Misclassified tumorous tissue spectra by applying PCA analysis match with misclassified spectra by applying HCA analysis. Misclassified normal tissue spectra (the Appendix, Figure A-17, (1 – 2)) by applying PCA analysis have atypical spectral profile

in 950 – 1185  $\text{cm}^{-1}$  range but characteristic spectral bands for normal tissue and assigned to collagen are prominent in these spectra. 4 out of 6 cystitis tissue spectra were assigned to normal tissue class while other 2 out of 6 cystitis tissue spectra were assigned to tumorous tissue class but the dots corresponding to these spectra are located not far away from the cluster corresponding to normal tissue.

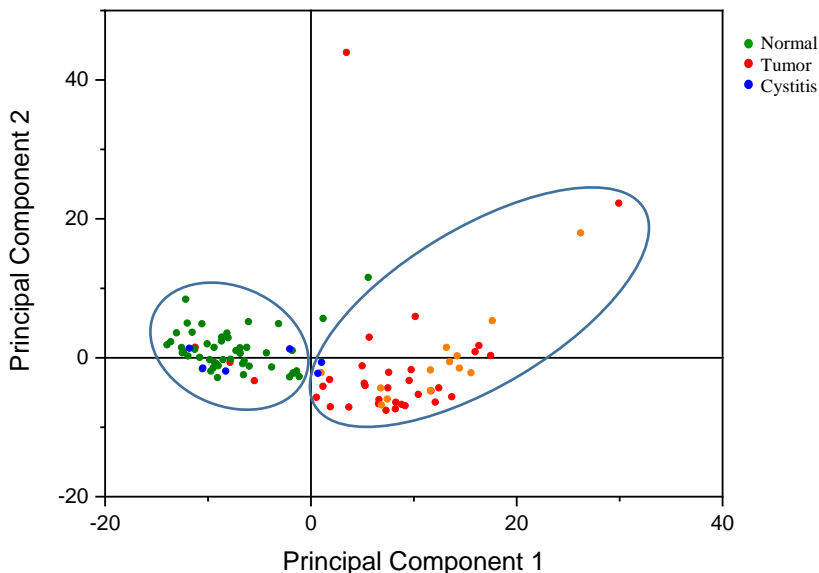


**Figure 4.5.** PCA diagram of urinary bladder tissue spectra.

Values of sensitivity, specificity, positive and negative prognostic values for tumorous urothelial carcinoma tissue identification were evaluated and are presented in Table 4.3.

**Table 4.3.** Summarized values of sensitivity, specificity, positive and negative prognostic values for application of HCA and PCA analysis for native tissue spectra.

	Method	
	HCA	PCA
Sensitivity	91 %	91 %
Specificity	98 %	96 %
PPV	98 %	96 %
NPV	92 %	92 %



Spectra of tissue smears were evaluated. Mean spectra of normal, tumorous (high- and low-grade urothelial carcinoma) tissue smears are shown in Figure 4.6.

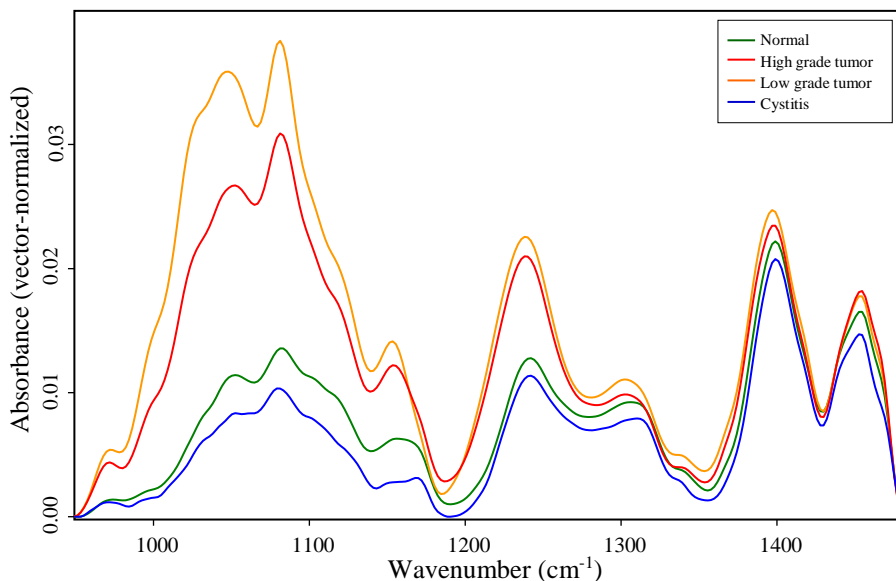


**Figure 4.6.** Mean ATR IR spectra of normal, urothelial carcinoma (high-grade tumor and low-grade tumor) and cystitis tissue smears. Spectra are baseline corrected and vector-normalized.

Differences between spectra of normal, tumorous and cystitis tissue smears are observed. While profiles of normal and cystitis tissue smear spectra are similar to each other, significant differences between normal and tumorous tissue smear spectra are observed. The main spectral band positions and their assignments are shown in Table 4.4. As in case of tissue spectra, higher levels of glycogen are observed in tumorous tissue smear spectra. This is indicated by shoulder at  $1027\text{ cm}^{-1}$  assigned to  $\nu(\text{C-O})$ ,  $\nu(\text{C-C})$ ,  $\delta(\text{C-O-H})$  vibrations and prominent spectral band at  $1154\text{ cm}^{-1}$  assigned to  $\nu(\text{C-O})$  vibrations of glycogen. Higher levels of glycogen are observed in low-grade tumors compared to high-grade urothelial carcinoma tumors, however, the amount of glycogen is still significantly higher than in normal tissue. Also, higher absorbance values in spectra of tumorous tissue smears are observed for the spectral band located at  $972\text{ cm}^{-1}$  which could be assigned to  $\nu(\text{PO}_4)$  vibrations of nucleic acids. Spectral bands located at similar positions can be assigned to  $\nu(\text{PO}_4)$  vibrations of proteins and vibrational modes of  $\text{OCH}_3$  groups of polysaccharides. Taking into account the increased absorbance values of spectral band located at  $1082\text{ cm}^{-1}$  assigned to  $\nu(\text{PO}_2)$  vibrations of nucleic

acids, this could be related to increased levels of nucleic acids in tumorous bladder tissue smears. Significantly higher absorbance values of the spectral band located at  $1242\text{ cm}^{-1}$  in tumorous tissue smear spectra could also be related to increased levels of nucleic acids since it could be assigned to  $\nu(\text{PO}_2^-)$  vibrations of nucleic acids. Spectral bands located at similar positions are assigned to Amide III groups of proteins but herewith increased absorbance values of spectral bands located at  $972\text{ cm}^{-1}$  and  $1082\text{ cm}^{-1}$ , these findings could be related to increased levels of nucleic acids in tumorous tissue smears. In contrast to native tissue spectra, spectral bands corresponding to collagen are not observable in tissue smear spectra.

**Table 4.4.** Spectral bands of tissue smear spectra and their assignments. Assignments set according to [158].

<b>Spectral band position, <math>\text{cm}^{-1}</math></b>			
<b>Normal tissue</b>	<b>Urothelial Carcinoma tissue</b>	<b>Non-specific cystitis</b>	<b>Assignment</b>
972	971	974	$\nu(\text{PO}_4)$ of nucleic acids and proteins OCH <sub>3</sub> of polysaccharides
996 (sh)	996(sh)	996	$\nu(\text{CO})$ , $\nu(\text{CC})$
1027 (sh)	1027 (sh)	1028 (sh)	$\nu(\text{C-O})$ , $\nu(\text{C-C})$ , $\delta(\text{C-O-H})$ of glycogen
1052	1052	1052	$\nu(\text{CO-O-C})$ $\nu(\text{C-O})$ , $\delta(\text{C-O})$ of the C-OH of carbohydrates
1082	1082	1082	$\nu(\text{PO}_2^-)$
1102 (sh)	Not present	1102 (sh)	Methyl-carbon stretching (polypeptides), $\nu(\text{PO}_2^-)$
1120 (sh)	1120 (sh)	Not present	$\nu(\text{C-O})$ , $\delta(\text{C-O})$ , $\delta(\text{C-O-H})$ , $\delta(\text{C-O-C})$ phosphodiester stretching
1154	1154	1154	$\nu(\text{C-O})$
1169 (sh)	Not present	1169 (sh)	$\nu(\text{C-O})$
1242	1239	1242	$\nu(\text{PO}_2^-)$ , Amide III

1306	1306	1310	Amide III
1340	1340	1340	CH <sub>2</sub> wagging
1398	1398	1398	δ(CH <sub>3</sub> )
1453	1453	1453	δ(CH <sub>3</sub> )

(sh) indicates a shoulder band

Although differences between mean spectra of tissue smears of different tissue types are well defined, as in case of native tissue spectra, variations of spectra inside these three tissue classes (normal, tumorous and cystitis tissue smears) are quite high (Figure 4.7).

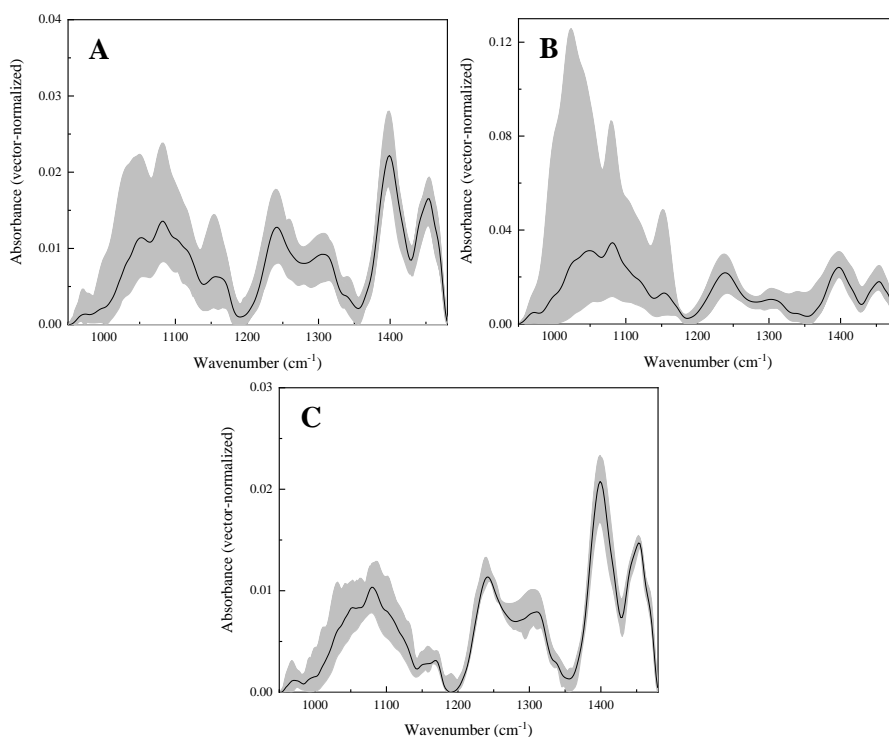


**Figure 4.7.** Mean spectra (black solid line) and variations of spectra of tissue taken from different patients (grey area) of normal (A), tumorous urothelial carcinoma (B) and cystitis (C) tissue. Spectra are baseline corrected and vector-normalized.

Black lines correspond to the mean spectra of all the samples taken from different patients, while grey areas indicate the variations of spectra in different tissue classes. Variations of spectra are quite high in tumorous tissue class (Figure 4.7 B), especially for the spectral bands corresponding to glycogen (located at 1028 and 1154  $\text{cm}^{-1}$ ) and could be considered as spectral tumor markers of urothelial carcinoma tissue smears. Variations in normal and cystitis tissue smear spectra classes are much smaller compared to tumorous tissue smears spectra.

Methods of multivariate statistical analysis were applied for the evaluation of the IR spectroscopy to delineate normal and pathological bladder tissue smears. Dendrogram representing results of HCA analysis for classification of benign and malignant tissues is shown in Figure 4.8. Analysis performed for tissue smears spectra in spectral region between 950 and 1480  $\text{cm}^{-1}$ .

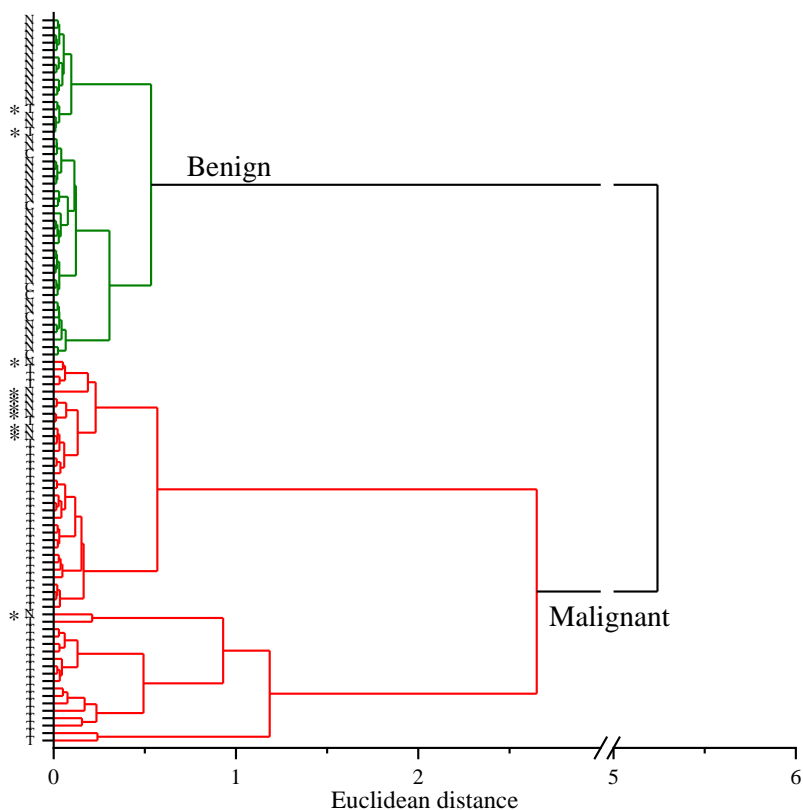


**Figure 4.8.** HCA dendrogram of benign and malignant tissue smears. Green cluster corresponds to the benign tissue smears class, red cluster corresponds to malignant tissue smears class. Letters N, C and T represent spectra of each normal, cystitis and tumorous tissue smears respectively. \* symbol indicates spectra which were assigned to the wrong tissue smear class. Analysis performed for spectra in spectral region from 950 to 1480  $\text{cm}^{-1}$ .

Spectra of all cystitis tissue smear samples are grouped into one cluster labelled as benign tissue class together with most part of normal tissue smear spectra. 8 spectra of normal tissue smears were assigned to malignant tissue class, thus allowing to discriminate benign tissue smears with 96 % accuracy. 2 spectra of tumorous tissue smears were assigned to benign tissue smear class corresponding to 96 % classification accuracy of malignant tissues. In order to discriminate normal and cystitis tissue smear samples, HCA analysis was performed in spectral region between 950 and 1480  $\text{cm}^{-1}$ . The dendrogram representing results of HCA analysis is presented in the Appendix (Figure A-19). Data is classified into two clusters, however, classification of normal and cystitis tissues is impossible. All 6 cystitis tissue smear spectra are classified into one cluster but 24 out of 46 normal tissue smear spectra are grouped together in the same cluster. Spectra are grouped into two clusters with much smaller distance between the clusters (labelled as Cluster I and Cluster II) compared to the dendrogram presented in Figure 4.8. This indicates that differences between spectra belonging to two different groups are quite small. Better accuracy could be reached by including more cases of cystitis into the study.

For the discrimination of normal and tumorous tissue smear spectra, HCA analysis was applied for the spectra in spectral range between 950 and 1480  $\text{cm}^{-1}$ . Dendrogram representing classification results is shown in Figure 4.9. Spectra are grouped into two well separated clusters with large distance between the clusters, thus revealing a good separation between both tissue smear classes. 8 spectra out of 46 normal tissue smear spectra and 2 spectra out of 46 tumorous tissue smear spectra were assigned to wrong tissue smear classes (misclassified spectra are indicated by \* symbol) that corresponds to 83 % accuracy for normal tissue smears and 96 % accuracy for tumorous tissue smears. Spectra which were assigned to wrong tissue smear classes are presented in the Appendix (Figures A-20 – A-21). Two of misclassified normal tissue smear spectra (Figure A-20, 1-2) have a typical profile of fatty tissue. Spectra 3 – 5 possess features characteristic to tumorous tissue smear spectra while profiles of spectra 6 – 8 are more similar to normal tissue smear spectra. Misclassified tumorous tissue smear spectra (Figure A-21) are more similar to normal tissue smear spectra. Interestingly, only one patient case of misclassified tumorous tissue smear matches with misclassified native tumorous tissue. Other misclassified patient cases corresponding to tumorous or normal tissues do not match.

For the discrimination of high-grade and low-grade urothelial carcinoma tissues, HCA analysis was applied for the tumorous tissue smear spectra in spectral range between 950 and 1185  $\text{cm}^{-1}$  where spectral bands of glycogen

are located. The dendrogram is presented in the Appendix (Figure A-22). Most part of spectra of high-grade tumorous tissue smears (26 spectra out of 33) are grouped into one cluster with 7 spectra (out of 13) of low-grade tumorous tissue smears. Meanwhile, another cluster contains of 6 spectra of low-grade and 7 spectra of high-grade tumorous tissue smears. The classification accuracy corresponds to 79 % for high-grade tumors and 46 % for low-grade tumors.

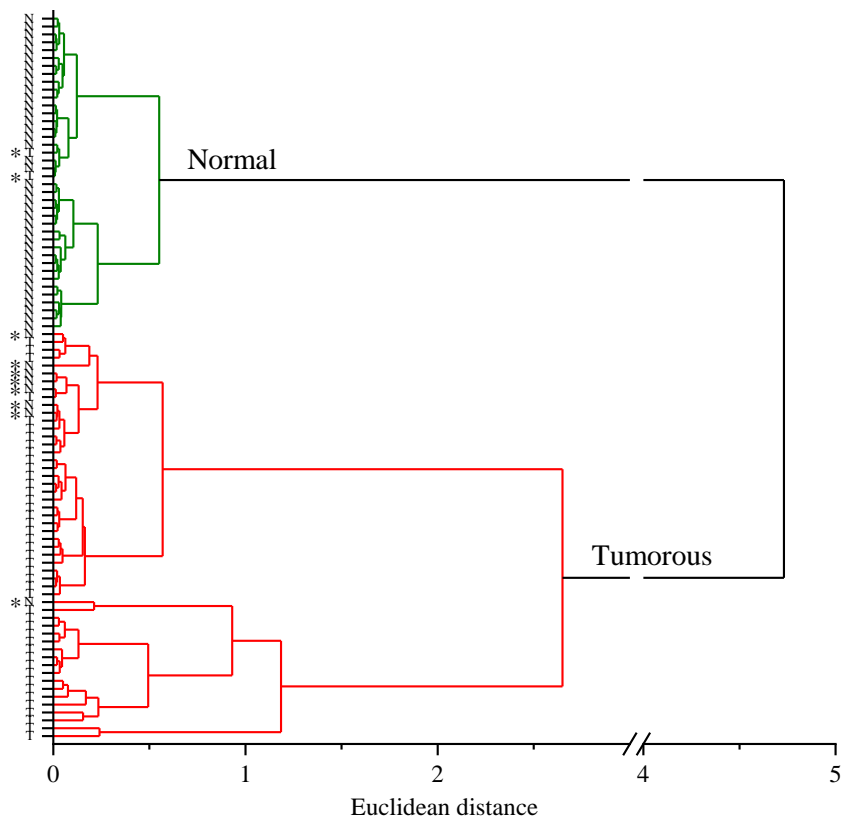


**Figure 4.9.** HCA dendrogram of normal and tumorous tissue smears. Green cluster corresponds to the normal tissue smears class; red cluster corresponds to tumorous tissue smears class. Letters N, C and T represent spectra of each normal, cystitis and tumorous tissue smear respectively. \* symbol indicates spectra which were assigned to the wrong tissue smear class. Analysis performed for spectra in spectral region from 950 to 1480  $\text{cm}^{-1}$ .

PCA analysis was applied for the first derivative of tissue smear spectra of normal, tumorous and cystitis tissues in spectral range between 1185 and 1354  $\text{cm}^{-1}$ . Results of PCA analysis are presented in Figure 4.10. Data are classified into two clusters, corresponding to normal (left side of the diagram) and tumorous (right side of the diagram) tissue smears. Green dots indicate spectra of each normal tissue, red and orange dots indicate spectra of each tumorous

(high- and low-grade of malignancy respectively) tissue, blue dots indicate spectra of cystitis tissue samples. Normal and tumorous tissue smear classes are well separated, only 3 spectra out of 46 normal tissue smear spectra and 5 spectra out of 46 tumorous tissue smear spectra were misclassified that correspond to identification accuracy of 93 % for normal tissue smear spectra and 89 % for tumorous tissue smear spectra. Distances between green dots corresponding to normal tissue smear samples are smaller compared to distances between red and orange dots corresponding to high-grade and low-grade tumorous tissue smear samples revealing smaller distribution of spectra in normal tissue smear class. Misclassified spectra of normal and tumorous tissue smears are shown in the Appendix (Figures A-23 – A-24). Misclassified normal tissue smear spectra (Appendix, Figure A-23) by applying PCA analysis matches with three misclassified spectra by applying HCA analysis. Spectra of 2 samples assigned to wrong class (spectra 1 – 2) has a typical profile of fatty tissue. One spectrum (spectrum 3) has a profile typical for tumorous tissue smears. By applying PCA analysis for the tissue spectra, this sample also was classified as tumorous tissue. One of misclassified tumorous tissue smear spectra (Appendix, Figure A-24, spectrum 1) has a profile of lipid rich tissue, another one spectrum (spectrum 2) has a typical profile of tumorous tissue smear in spectral range between 950 and 1185  $\text{cm}^{-1}$  but in spectral range between 1185 and 1354  $\text{cm}^{-1}$  has a typical profile of normal tissue smear spectra. Other 3 spectra (spectra 3 – 5) has a typical profile of normal tissue smear spectra in spectral range between 1185 and 1354  $\text{cm}^{-1}$ . All of cystitis tissue samples were assigned to normal tissue smear class.

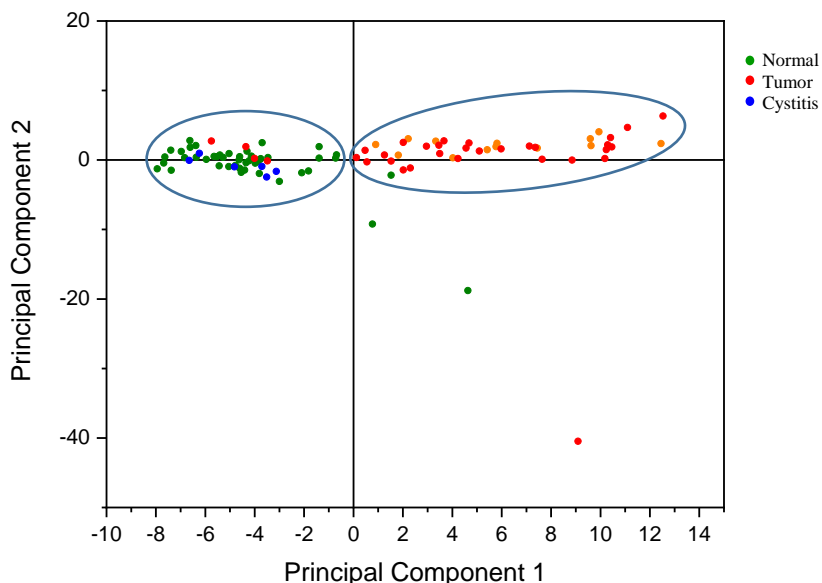


**Figure 4.10.** PCA diagram of urinary bladder tissue smears.

Summarized calculated values of sensitivity, specificity, positive and negative prognostic values of tissue smear spectra classification based on HCA and PCA analysis are presented in Table 4.5.

**Table 4.5.** Summarized values of sensitivity, specificity, positive and negative prognostic values for application of HCA and PCA analysis for tissue smear spectra.

	Method	
	HCA	PCA
Sensitivity	96 %	89 %
Specificity	83 %	93 %
PPV	85 %	93 %
NPV	95 %	90 %

Despite of relatively high classification results, application of the method for bladder tissue smear samples has some limitations compared to native tissue samples. Firstly, the sampling of tissue smears is possible not for all tissue samples. In some cases, it was impossible to obtain tissue smear of sufficient quality – signal to noise ratio of spectra was not high enough to observe characteristic spectral features. This can be related to individual tissue structure. In some cases, the tissue is quite firm and not enough amount of the residue material of the tissue is left on the ATR crystal. Secondly, the drying of the tissue smear takes more time compared to measurements of spectra of native tissue, thus native tissue samples are more suitable for intraoperative analysis.

The diagnostic accuracy of the method application for native tissue is high enough compared to currently applied approaches. Sensitivity values reach 91 % by applying both HCA and PCA methods, while specificity values reach 98 % and 96 % by applying HCA and PCA methods respectively. Currently, most widely used endoscopic approach for bladder cancer diagnostics is WLC with sensitivity and specificity values of 71 % and 72 % respectively [182]. PDD method based on fluorescence of the instilled agent reaches 92 % and 57 % sensitivity and specificity values respectively [182]. A novel approach Narrow band imaging (NBI) based on the illumination of the bladder with filtered white light is characterized by 96 % and 65 % sensitivity and specificity values respectively [181]. Compared to novel approaches (PDD and NBI) for bladder cancer diagnostics, fiber-based IR spectroscopy is characterized by similar values of sensitivity. In contrast to the mentioned methods, fiber-based IR spectroscopy shows considerably higher values of specificity describing better



true negative rates. Thus, allowing to decrease the cases then the follow-up of the patient is required.

## 5. CHAPTER 5. APPLICATION FOR PANCREAS CANCER

### 5.1. Pancreatic disorders

Pancreas is an organ of the gastrointestinal system carrying out important exocrine and endocrine functions in human body. The exocrine function is related to digestion – the pancreas secretes pancreatic juice and essential enzymes such as proteases, lipases, and amylases [184]. The exocrine portion of the pancreas consists of major cell types such as acinar, ductal, centroacinar and stellate cells. Acinar cells are responsible for synthesis, storage as well as secretion of enzymes and form into structures called acinus which connect to the ductal system [185]. The endocrine function covers the secretion of hormones such as insulin, glucagon, ghrelin, somatostatin, and pancreatic polypeptide which are responsible for the regulation of glucose levels in blood. Endocrine islets of Langerhans consisting of five cell types (alpha, beta, delta, epsilon and PP cells) are responsible for hormone secretion [186]. The failure of both exocrine and endocrine functions leads to digestion disorders and the development of diabetes mellitus.

Pancreatic disorders cover pathologies including malignant and non-malignant diseases. Pancreatitis is an inflammatory disease of the pancreas, and can be divided into two main categories: acute and chronic pancreatitis. Pancreatic tumors cover a variety of malignant and benign neoplasms which arise from different types of cells. Pancreatic ductal adenocarcinoma (PDAC) is the most common type of pancreatic cancer and accounts nearly 90 % of all cases of primary pancreatic tumors [187]. Only around 20 % of PDAC cases are resectable [188], [189]. Other types of malignant neoplasms are neuroendocrine tumors, colloidal carcinoma, solid-pseudopapillary tumors, acinar cell carcinoma, pancreatoblastoma tumors. The least common types of cancer include cases of adenosquamous, hepatoid, medullary signet ring cell and undifferentiated carcinomas [188]. Non-malignant or precancerous neoplasms include intraductal papillary mucinous neoplasm, mucinous cystic neoplasm, pancreatic intraepithelial neoplasia and serous cystadenoma [190].

Pancreatic cancer is one of the most lethal cancer types and is the seventh leading cause of cancer related deaths worldwide [1], the five-year survival rate for pancreatic adenocarcinoma reaches only 9 % [189]. Treatment of pancreatic cancer includes surgery which can be combined together with chemotherapy and chemoradiotherapy [190]. However, surgery is crucial [190], [191]. During the last years, neoadjuvant chemotherapy is being more and more widely applied in locally advanced PDAC cases in order to shrink the tumor before the consecutive resection; then applying chemotherapy after

the surgery. In all PDAC cases, final outcome of the patient highly depends on margin resection as well as lymph node statuses [192]. While performing a surgery, it is important to preserve as much healthy tissue as possible to maintain endocrine as well as exocrine functions of the organ and removing all of the cancerous tissue. Tumor margins are often surrounded by inflammatory tissue with infiltrating malignant cells. Macroscopically infiltrations are not always visible, thus, for the accurate complete removal of cancerous tissue frozen section examination is currently state of the art. However, evaluation of resection margins by applying this technique is limited by additional time required for tissue examination resulting in a prolongation of the surgery and by the visual evaluation of a small piece of tissue specimen by a pathologist often resulting in not clear diagnosis. In this regard, various approaches for intraoperative pancreas tissue delineation are being investigated. One of these methods is the approach of 5-aminolevulinic acid for fluorescence guided surgery; results of application for pancreatic cancer were reported recently [193]–[197]. This technique was applied for intraoperative detection of PDAC tumors but only for small entities. Therein, novel intraoperative approaches for intraoperative tissue assignment are required.

## 5.2. Experimental details

### 5.2.1. Tissue sample preparation

Human pancreatic tissue samples were obtained at the Department of Visceral, Thoracic and Vascular Surgery of the University Hospital Carl Gustav Carus, Technische Universität Dresden (Germany). The study was approved by the local ethics committee (EK 179052018). Samples were collected from pancreatic surgical resections, including resections due to pancreatitis and primary or secondary pancreatic tumors. Freshly resected tissue samples were macroscopically examined by a board-certified pathologist and assigned as ‘tumor’, ‘normal’ or ‘pancreatitis’. In most cases two tissue samples (normal and pathological tissue) for each patient were received. In some cases, only one type of tissue (normal or pathological) sample per patient was received due to status of the surgery. Resected tissue samples placed on ice were immediately transferred to the laboratory for the spectroscopy measurements.

For the intraoperative case analysis, measurements were performed next to the operating room in the operating room tract.

### 5.2.2. FT-IR spectroscopy measurements of tissue samples

Measurements were performed using fiber-based spectroscopy system described in the Chapter 2. Received tissue samples were sliced into several pieces and measurements were performed from the freshly cut surface. Number of slices and measured spectra depended on the size of the sample, usually varying between 1 and 12 cuts per sample. The fiber probe was pressed against the freshly cut surface area and spectra were measured afterwards.

Spectra were collected in 400 – 4000  $\text{cm}^{-1}$  spectral region with a 4  $\text{cm}^{-1}$  resolution. 50 interferograms were recorded, averaged and Fourier transformed into IR absorption spectrum. Blackmann-Harris 3-Term apodization function, zero filling factor of 2 and phase correction (Power Spectrum phase correction method) were used while applying the Fourier transformation. Software build in ATR correction was performed using spectral software OPUS.

### 5.2.3. Statistical analysis

Statistical analysis (HCA and PCA) was performed by using data analysis software OriginPro by applying standard procedures (Hierarchical Cluster Analysis and Principal Component Analysis) of the software package. Prior statistical analysis, spectra were pre-processed: atmospheric compensation, baseline correction, vector normalization and offset correction were applied by using spectroscopy software OPUS. While performing HCA, Ward cluster algorithm, Euclidean distance type were chosen. Different spectral regions were chosen for statistical analysis and different pre-processing of spectra (either first derivative of spectra was calculated by using spectroscopy software OPUS or not) was applied prior the analysis; however, only the best achieved results are presented in the following section.

## 5.3. Results and discussion

In total, cases of 60 patients were analysed. Samples of native unprocessed tissue were investigated. Summarised data is presented in Table 5.1. Final diagnosis is based on standard histology reports of the whole resected tissue specimen.

**Table. 5.1.** Tissue types collected during the study.

Tissue type	Number of tissue samples
Normal	44
Tumor	
<i>Primary</i>	
PDAC	25
Neuroendocrine carcinoma	3
Acinar cell carcinoma	1
Solid pseudopapillary neoplasm	1
IPMN <sup>B</sup>	2
Colloidal carcinoma	3
Ampullary adenocarcinoma	1
Undifferentiated carcinoma with osteoclast-like giant cells	1
Serous cystadenoma <sup>B</sup>	1
<i>Secondary</i>	
Stomach cancer	1
Renal cell carcinoma	1
Distal cholangiocellular carcinoma	4
Gallbladder carcinoma	1
Pancreatitis	13
<b>Total number of patients</b>	<b>60</b>

IPMN – intraductal papillary mucinous neoplasm.

B indicates benign tumors.

Both types of tissue (normal and pathological) were obtained not from every patient. In two cases, samples of two different tumors from the same patient were received; these samples were counted as different samples.

Spectra of each tissue specimen were collected at several different areas of the sample: tissue sample was sliced, and spectra were collected from each freshly cut surface. Biological samples tend to be inhomogeneous, hereby, as much as possible information about the sample constitution is collected. Some samples were constituted of fatty tissue areas resulting in spectral bands assigned to fatty acids dominating the tissue spectra. ATR IR spectrum of human adipose tissue and assignments of main spectral bands corresponding to fats are presented in the Appendix, Figure A-06. Spectra dominated by fats were not used for analysis; in total 1 sample of tumorous (out of 46 samples)

and 2 samples of normal (out of 46 samples) tissue were excluded from the study.

Mean spectra of pancreas normal, tumorous and pancreatitis tissues are presented in Figure 5.1.

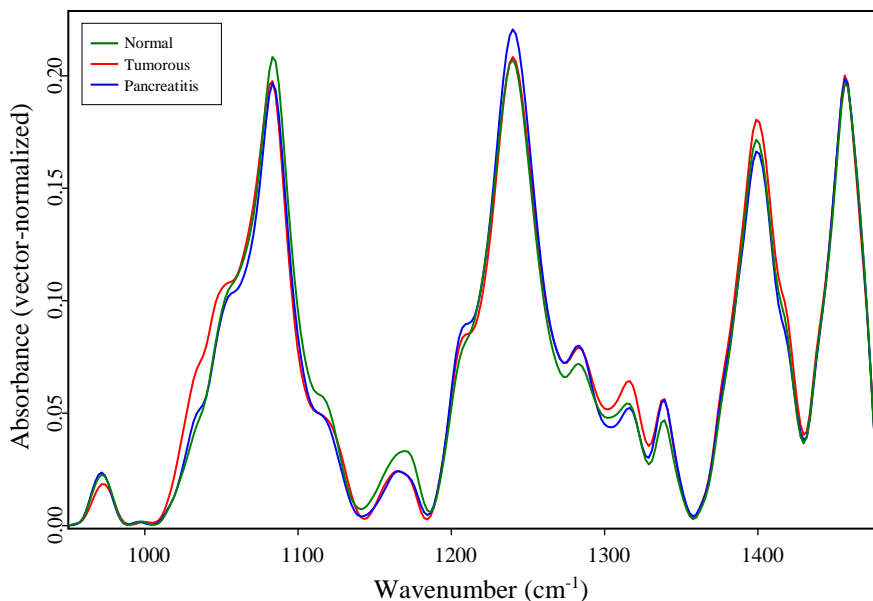


**Figure 5.1.** Mean ATR IR spectra of pancreas normal, tumorous and pancreatitis tissues. Spectra are baseline corrected and vector-normalized.

Spectra of different tissue types share similar properties, however, spectral differences allowing to discriminate different tissue types were established. Main spectral band positions and their assignments are shown in Table 5.2.

**Table 5.2.** Spectral bands and their assignments. Assignments set according to [158].

Spectral band position, cm <sup>-1</sup>	Assignment
972	$\nu(\text{PO}_4)$ of nucleic acids and proteins OCH <sub>3</sub> of polysaccharides
974	$\nu(\text{PO}_4)$ of nucleic acids and proteins OCH <sub>3</sub> of polysaccharides
1033	Collagen
	$\nu(\text{CO-O-C})$
1050	$\nu(\text{C-O}), \delta(\text{C-O})$ of the C-OH of carbohydrates
1055	$\nu(\text{PO}_2), \nu(\text{C-OH})$

1083	$\nu(\text{PO}_2^-)$ of nucleic acids
1117	$\nu(\text{C-O})$ of C-OH group
1164	$\nu(\text{C-O})$
1171	$\nu(\text{C-O})$
1207	Amide III
1240	$\nu(\text{PO}_2^-)$ , Amide III
1283	Amide III
1316	Amide III
1339	$\text{CH}_2$ wagging
1399	$\delta(\text{CH}_3)$
1417	$\nu(\text{C-N})$ , $\delta(\text{N-H})$ , $\delta(\text{C-H})$
1457	$\delta(\text{CH}_3)$

Spectra of pancreatic normal and pancreatitis tissue demonstrate higher absorbance values of the spectral band located at  $972\text{ cm}^{-1}$  which could be assigned to  $\nu(\text{PO}_4)$  vibrations of nucleic acids. This assignment of the band is not that straightforward. Spectral bands, located around  $970\text{ cm}^{-1}$  could be also assigned to  $\nu(\text{PO}_4)$  vibrations of proteins or vibrational modes of  $\text{OCH}_3$  groups of polysaccharides. Assignment of the band at  $972\text{ cm}^{-1}$  to  $\nu(\text{PO}_4)$  of nucleic acids could be confirmed by comparing the change of its absorbance values in normal and tumorous tissues with the absorbance values of the band located at  $1083\text{ cm}^{-1}$  and assigned to  $\nu(\text{PO}_2^-)$  vibrations of nucleic acids. Absorbance values of both of these bands are higher in normal tissue compared to tumorous one. These observations can be related to reduced amounts of nucleic acids in tumorous tissue. Spectral band located at  $1240\text{ cm}^{-1}$  could be assigned to  $\nu(\text{PO}_2^-)$  vibrations of nucleic acids, but it also can have contribution from vibrations of Amide III group of proteins. Thus, similar absorbance values of this spectral band in normal and tumorous tissue spectra can be explained by decrease of nucleic acids and increase of proteins in tumorous tissue. Reduced levels of nucleic acids in tumorous tissue can be explained by low tumor cellularity. It is known that PDAC tumors are one of the tumors with the lowest tumor cellularity compared to other cancer types [198], the fraction of neoplastic cells is often less than 20 % [199]. PDAC

tumors are characterized by growth of abundant tumor stroma which consists of ECM proteins, immune cells, cancer related fibroblasts, activated pancreatic stellate cells, blood vessels [199], [200]. This process is referred as desmoplastic reaction during which ECM matrix starts to grow due to synthesis of collagen by fibroblasts. Due to higher levels of extracellular components in tumorous tissue, less volume of cells is present in the tissue specimen, thus this results in decreased levels of nucleic acids in tumorous tissue. The presence of tumor stroma could also be observed in ATR IR spectra: more prominent spectral bands corresponding to collagen are observed in tumorous tissue spectrum compared to normal tissue spectrum. Spectral bands located at 1033, 1207, 1283 and 1339  $\text{cm}^{-1}$  could be related to altered collagen levels in tumorous pancreatic tissues. Although spectral band located at 1240  $\text{cm}^{-1}$  is one of the characteristic spectral bands of collagen, its absorbance values also depends on nucleic acid content, as discussed above. Spectral bands, corresponding to collagen, are prominent in pancreatitis tissue spectra as well. Increased levels of collagen in pancreatitis tissue are related to inflammatory processes. It is known that in case of chronic pancreatitis, fibrosis could occur resulting in collagen secretion and growth of ECM [201], [202].

Higher absorbance value of the spectral band located around 1170  $\text{cm}^{-1}$  in normal tissue spectrum is assigned to  $\nu(\text{C-O})$  vibrations and is related to fat content in tissue – more samples of normal tissues showed higher levels of fats compared to tumorous tissues. Differences of absorbance values of spectral bands located at 1399 and 1457  $\text{cm}^{-1}$  are assigned to  $\delta(\text{CH}_3)$  vibrations and are related to protein content. In general, differences between spectra of pancreas normal, tumorous and pancreatitis tissues are small. However, main differences are observed in spectra profiles between 1006 and 1140  $\text{cm}^{-1}$  and can be related to variations of protein, nucleic acid and polysaccharides content in tissues.

Variations of spectra within each tissue class (normal, tumorous and pancreatitis tissues) are observable (Figure 5.2).



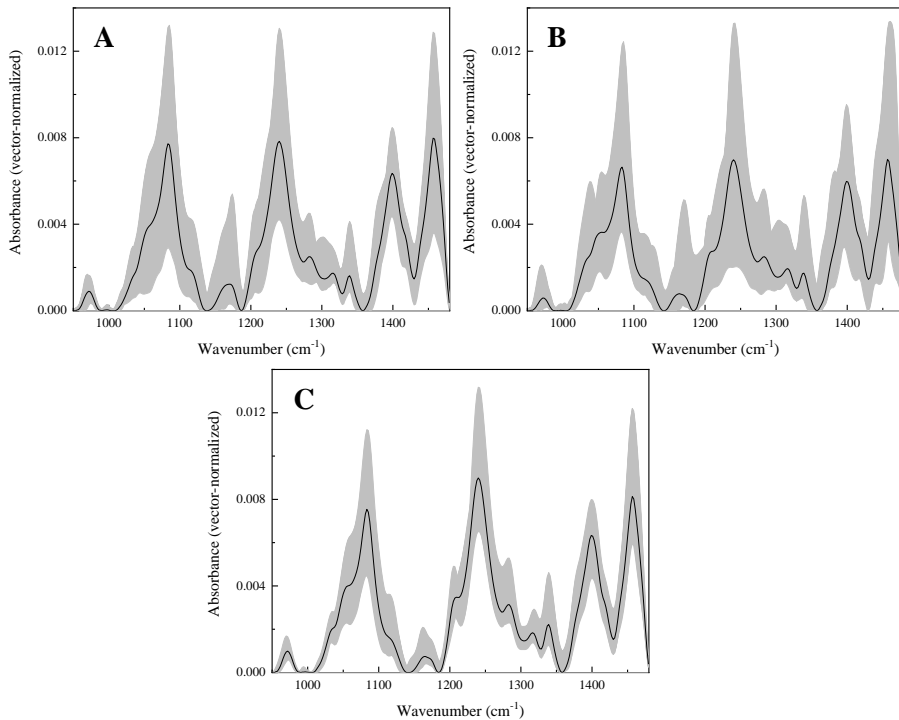


**Figure 5.2.** Mean spectra (black solid line) and variations of spectra of tissue taken from different patients (grey area) of normal pancreatic (A), pancreas tumorous (B) and pancreatitis (C) tissue. Spectra are baseline corrected and vector-normalized.

Black lines correspond to mean spectra of all the samples taken from different patients, while grey areas indicate the variations of spectra in different tissue classes. Variations of spectra in normal and tumorous classes are quite high. Variations of normal tissue spectra could be related to individual differences in tissue constitution. It could be determined by different proportions and activity of specific cells constituting pancreas and secreting enzymes and hormones among different individuals. Different levels of secreted enzymes and hormones could lead to biochemical alterations of the tissue. Variations within tumorous tissue class can be explained by mentioned reasons as well as variety of different tumor types analysed during the study (Table 5.1). Different tumors have their characteristic morphological and biochemical features resulting in differences observed in spectra. Smaller differences inside chronic pancreatitis tissue class can be explained by smaller number of tissue samples included in study compared to normal and tumorous tissue classes. Existing differences could be determined by different levels of fibrosis caused by inflammatory processes.

Methods of multivariate statistical analysis were applied for the evaluation of the IR spectroscopy to delineate normal and pathological pancreatic tissues. Dendrogram representing results of HCA analysis for classification of normal and tumorous tissues is presented in Figure 5.3. Analysis performed for the first derivative of spectra in spectral region from 950 to 1100  $\text{cm}^{-1}$ .

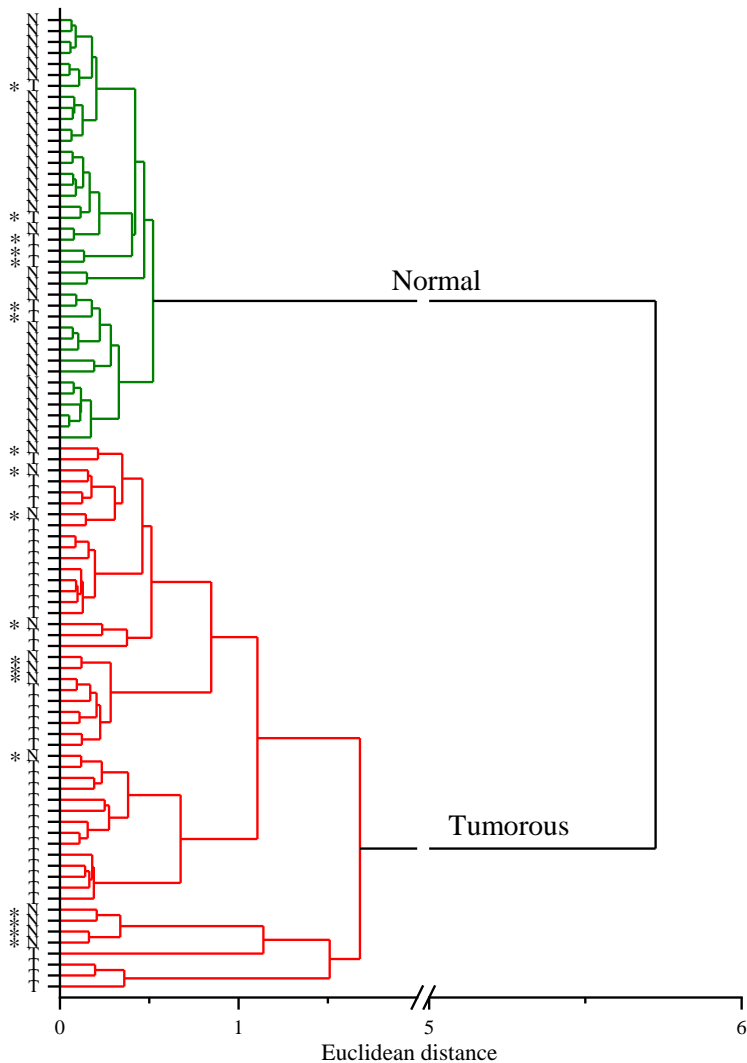


**Figure 5.3.** HCA dendrogram of normal and tumorous pancreatic tissues. Green cluster corresponds to the normal tissue class, red cluster corresponds to tumorous tissue class. Letters N and T represent spectra of each normal and tumorous tissues respectively. \* symbol indicates spectra which were assigned to the wrong tissue class.

Spectra are classified into two well separated clusters, however, 7 spectra out of 45 tumorous tissue spectra and 12 spectra out of 44 normal tissue spectra were assigned to wrong classes that corresponds to 84 % accuracy for tumorous tissue and 73 % accuracy for normal tissue identification. Spectra of normal tissues which were classified as tumorous tissues as well as spectra of tumorous tissues which were classified as normal tissues are presented in the Appendix (Figures A-25 –A-26). In order to evaluate the applicability for the delineation of pancreas normal and pancreatitis tissues as well as pancreas tumorous and pancreatitis tissues HCA analysis was applied for the spectra. Dendrogram representing results of HCA analysis for classification of normal and pancreatitis tissues is shown in the Appendix (Figure A-27). Spectra are classified into two clusters; however, spectra of normal and pancreatitis tissues are mixed in both clusters suggesting that normal and pancreatitis tissues cannot be classified by applying HCA analysis. Dendrogram representing results of HCA analysis for classification of tumorous and pancreatitis tissues is shown in the Appendix (Figure A-28). Data is classified into two clusters. 35 out of 45 spectra of tumorous tissue spectra are classified into one cluster (Cluster I) while 10 out of 13 spectra of pancreatitis tissue are classified into another cluster (Cluster II) corresponding to classification accuracy of 78 % and 77 %, respectively.

PCA analysis was applied for first derivative of spectra of pancreas normal, tumorous and pancreatitis tissue in spectral range between 950 and 1188  $\text{cm}^{-1}$ . Results of PCA analysis are presented in Figure 5.4. Data is classified into two clusters, corresponding to normal (upper side of the diagram) and tumorous (lower side of the diagram) tissues. Green, red and blue dots indicate spectra of each pancreatic normal, tumorous and pancreatitis tissue samples respectively. 6 spectra out of 45 tumorous tissue spectra and 7 spectra out of 44 normal tissue spectra were misclassified corresponding to 87 % accuracy for tumorous and 84 % accuracy for normal tissue identification. Wrongly assigned spectra are presented in the Appendix (Figures A-29 – A-30). Spectra of pancreatitis tissue are not classified into a separate cluster; most part of pancreatitis tissue spectra are classified to the same cluster as normal tissue spectra.

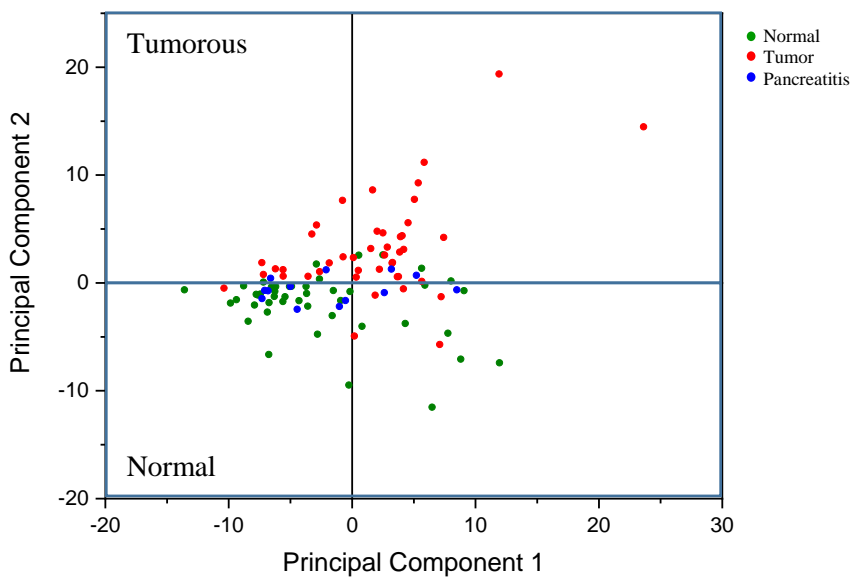


**Figure 5.4.** PCA diagram of pancreas tissue spectra.

Summarized calculated values of sensitivity, specificity, positive and negative prognostic values for tumorous pancreas tissue identification based on HCA and PCA analysis are presented in Table 5.3.

**Table 5.3.** Summarized values of sensitivity, specificity, positive and negative prognostic values for application of HCA and PCA analysis for pancreas tumorous tissue identification.

	Method	
	HCA	PCA
Sensitivity	84 %	87 %
Specificity	73 %	84 %
PPV	76 %	85 %
NPV	82 %	86 %

### 5.3.1. Intraoperative case analysis

In order to evaluate the applicability of the method for intraoperative resected tissue identification, case study for three patients was performed. For this reason, spectroscopy measurements were performed as a back table analysis in the operating room tract next to the operating room. Measurements were performed during the surgery immediately after tissue resection.

All three described patients were receiving a partial pancreatic resection. In the first case, a pancreatic head resection was performed on a 70-year-old male patient for an uncertain mass in the pancreas causing cholestasis and unintended weight loss. Intraoperative image of pancreatic head resection *in vivo* and resected tissue complex is presented in Figure 5.5.

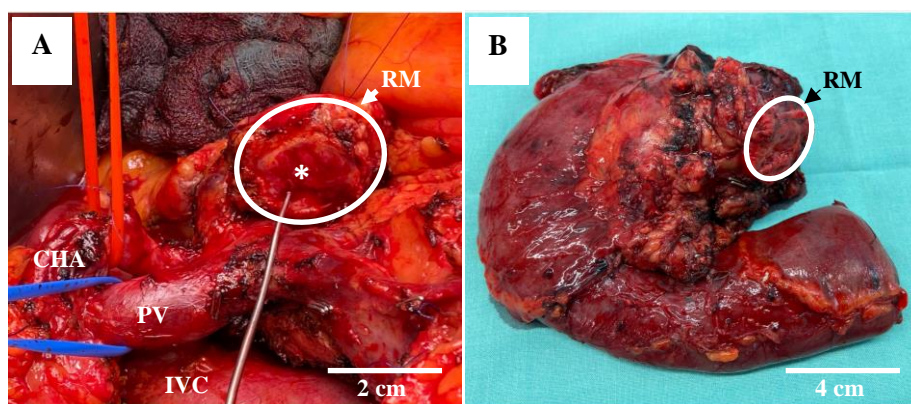


**Figure 5.5.** Intraoperative image of pancreatic head resection *in vivo* (A), resected tissue complex consisting of the pancreatic head and duodenum (B). RM – resection margin, CHA – common hepatic artery, PV – portal vein, IVC – inferior vena cava, \* - pancreatic duct.

Tissue specimen of the resection margin area was investigated. Tissue sample was split into two sections, one section was sent for the frozen section examination, another one was used for spectral analysis. Collected spectra (in total 10 spectra) were averaged and compared to mean spectra of pancreas normal, tumorous and pancreatitis tissue. Spectra are presented in Figure 5.6. After visual analysis of spectra, tissue type was assigned as pancreatitis. Simultaneously performed frozen section examination of the resected tissue margin assessed the tissue as well. After histological examination of the whole resected tissue complex, patient was diagnosed with autoimmune pancreatitis five days later that confirmed the results obtained by ATR IR spectroscopy.

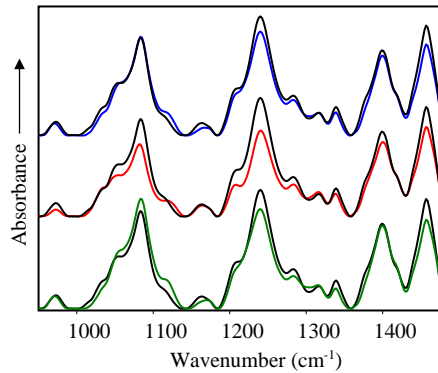


**Figure 5.6.** ATR IR spectrum of resected pancreatitis tissue (black line) compared to mean spectra of pancreatitis (blue line), normal pancreatic (green line) and tumorous (red line).

The second case was a 74-year-old female receiving a pancreatic head resection due to a lesion in the pancreatic head leading to recurrent vomiting episodes caused by a gastric outlet obstruction. Two samples were obtained which were assessed as normal and pancreatitis tissues after macroscopic evaluation by the pathologist. Collected spectra of tissue samples initially considered as normal (in total 4 spectra) and pancreatitis (in total 7 spectra) were averaged and mean spectra of both samples were compared to mean spectra of pancreas normal, tumorous and pancreatitis tissues. Spectra are presented in Figure 5.7. After visual analysis, tissue sample which was considered as normal tissue was assessed as pancreatitis. The tissue sample which was considered as pancreatitis tissue was assessed as tumorous tissue after spectra evaluation. Results of intraoperative tissue type identification by ATR IR spectroscopy were proven as correct by final pathology report.

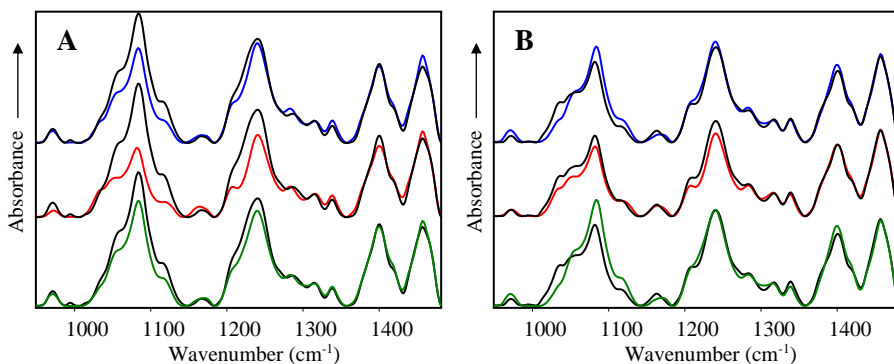


**Figure 5.7.** ATR IR spectra of resected pancreatitis tissue initially considered as normal tissue (black line, A) and resected tumorous tissue initially considered as pancreatitis (black line, B) compared to mean spectra of pancreatitis (blue line), normal pancreatic (green line) and tumorous (red line)

The third patient was a 73-year-old male receiving a pancreatic head resection due to a suspected distal cholangiocellular carcinoma infiltrating the pancreas according to computed tomography scans performed prior the surgery. Two samples of the resected tissue were received for the spectral analysis during the surgery. Both of them were initially assessed as normal tissues after macroscopic evaluation by the surgeon or pathologist respectively. Collected spectra of each sample (5 spectra for the first sample and 4 spectra for the second sample) were averaged and mean spectra of each sample were compared to mean spectra of pancreas normal, tumorous and pancreatitis tissues. Spectra are presented in Figure 5.8.

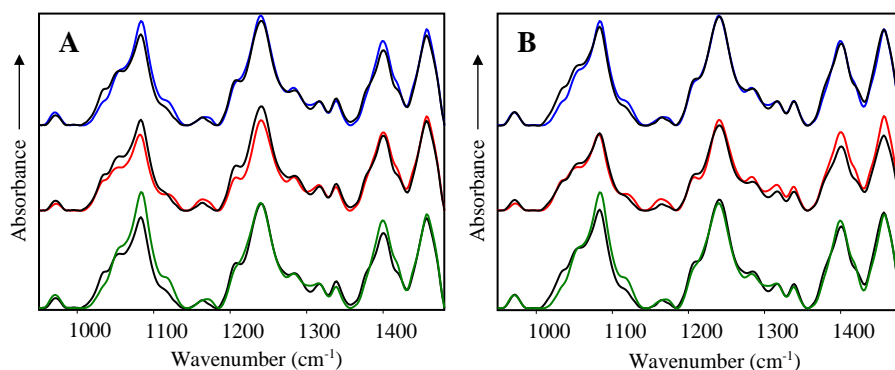


**Figure 5.8.** ATR IR spectra of resected tissue samples initially considered as normal tissue by the surgeon (black line, A) and pathologist (black line, B) compared to mean spectra of pancreatitis (blue line), pancreas tumor (red line) and normal pancreatic (green line) tissue.

After visual analysis of mean spectra, both tissue samples were identified as tumorous tissue. For the first tissue sample no common pathology report was available since this specimen was not regularly assigned for postoperative histological examinations. For this reason, a frozen section of this sample used for the spectroscopy measurements was stained by H&E and evaluated by a pathologist. It was confirmed that malignant cells were infiltrated into the examined tissue sample. The image of the H&E stained frozen section of the examined tissue is presented in Figure 5.9. The second tissue was identified as pancreatitis tissue with infiltrating distal cholangiocellular carcinoma by a pathologist. Therefore, the tissue classification by applying ATR IR spectroscopy was presumably correct.

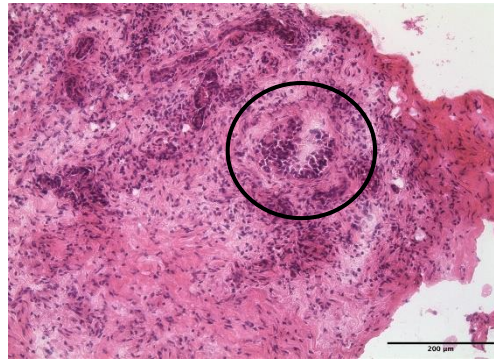


**Figure 5.9.** Image of a frozen section of the H&E stained resected tissue sample. The sample is the first sample analysed by ATR IR spectroscopy. The circled area marks a representative malignant lesion.

Described intraoperative case study suggests that application of fiber-based ATR IR spectroscopy may provide beneficial evaluation of the suspicious tissue area during the surgery. As it was shown, macroscopic evaluation of the tissue is not always correct since microscopic invasions of cancerous cells can be invisible; therefore, additional methods for tissue evaluation should be applied. Currently applied frozen section examination is a time consuming procedure while tissue examination by ATR IR spectroscopy can be proceeded in a few minutes providing objective results. Moreover, due to small dimensions of the described measuring set-up, the device can be placed on any table in the operating room not disturbing the flow of the surgery. This shows a potential of the method for intraoperative tissue evaluation.



## 6. CHAPTER 6. APPLICATION FOR LIVER CANCER

### 6.1. Liver tumors

The liver is one of the largest visceral organs in human body belonging to gastrointestinal system. The liver carries out a variety of functions including production and secretion of bile which is used in digestion; it supports metabolism, produces amino acids and proteins, decontaminates toxic substances, stores vitamins, iron, glycogen, participates in disposing of old and damaged erythrocytes, removes pathogens and exogenous antigens from blood circulation [159], [203], [204].

Various types of primary and secondary tumors can form in liver. Primary liver cancer is the sixth most frequently diagnosed malignancy worldwide with higher incidence and mortality rates in men [1]. The most common type of primary malignant liver tumors is hepatocellular carcinoma (HCC) [1], [205], [206] accounting for approximately 85 % of liver cancer cases [207]. This type of cancer arises from hepatocytes (liver parenchymal cells). Liver parenchyma is mainly constituted of hepatocytes of which liver lobules (functional liver units) are composed. Each lobule is a hexagonal structure with a central vein located in the center of the hexagon with a portal triad (portal vein, hepatic artery and bile duct) in each corner [203], [204]. The second most common primary liver tumor type is cholangiocellular carcinoma (CCC) [208] accounting for 10 % of diagnosed liver cancers [207]. This tumor type forms out of cholangiocytes (epithelial cells of the biliary tract). Other primary liver malignancies cover rare neoplasms such as hepatocholangiocarcinoma, fibromellar carcinoma, hepatic haemangioendothelioma, hepatic angiosarcoma and others [207]. Besides primary liver malignancies a variety of benign tumors can form in liver of which the most common types are hemangioma, focal nodular hyperplasia and hepatocellular adenoma [209], [210]. Liver metastases arise more often than primary liver tumors [211]. Liver is a common metastasis site partially due to a good blood supply and suitable conditions for tumors to grow. The most common cancers spreading to liver are colorectal cancer, pancreatic cancer, melanoma and lung cancer [212].

Treatment of liver malignancies include various methods such as surgical operation, chemotherapy and radiotherapy; however, surgical treatment is the only curative approach for most types of liver tumors [213]. Complete tumor removal ensuring negative tumor margins improves the outcome of a patient. Frozen section examination stays the main method for the intraoperative evaluation of tumor margins in liver [214]. Recently an increasing number of

reports describe usefulness of indocyanine green (ICG) fluorescence navigation in liver surgery; however, the application is still in an early phase since optimal parameters such as dose and timing of ICG injection should be established [215]. In this regard, fast, reliable and minimally invasive methods for intraoperative tumor margin assessment are needed for liver surgery.

## 6.2. Experimental details

### 6.2.1. Tissue sample preparation

Human liver tissue samples were obtained at the Department of Visceral, Thoracic and Vascular Surgery of the University Hospital Carl Gustav Carus, Technische Universität Dresden (Germany). The study was approved by the local ethics committee (BO-EK-26012020). Samples were collected from liver surgical resections due to primary or secondary liver tumors. Freshly resected tissue samples were macroscopically examined by a board-certified pathologist and assigned as ‘tumor’ or ‘normal’. In most cases two tissue samples (normal and tumorous tissue) for each patient were received. In some cases, only one type of tissue (normal or pathological) sample per patient was received due to status of the surgery. Resected tissue samples placed on ice were immediately transferred to the laboratory for the spectroscopy measurements.

### 6.2.2. FT-IR spectroscopy measurements of tissue samples

Measurements were performed using fiber-based spectroscopy system described in the Chapter 2. Received tissue samples were sliced into several pieces and measurements were performed from the freshly cut surface. Number of slices and measured spectra depended on the size of the sample, usually varied between 1 and 10 cuts per sample. The fiber probe was pressed against the freshly cut surface area and spectra were measured afterwards.

Spectra were collected in  $400 - 4000 \text{ cm}^{-1}$  spectral region with a  $4 \text{ cm}^{-1}$  resolution. 50 interferograms were recorded, averaged and Fourier transformed into IR absorption spectrum. Blackmann-Harris 3-Term apodization function, zero filling factor of 2 and phase correction (Power Spectrum phase correction method) were used while applying the Fourier transformation. Software build in ATR correction was performed using spectroscopy software OPUS.

### 6.2.3. Statistical analysis

HCA analysis was performed by using spectroscopy software OPUS by applying standard procedures of the OPUS software package. While performing HCA analysis, standard method (Euclidean distance) for second derivative of spectra were chosen. Analysis performed in 984 – 1141  $\text{cm}^{-1}$  spectral range.

PCA analysis was performed by using data analysis software OriginPro by applying standard procedures of the OriginPro software package. Analysis performed for the first derivative of spectra in 984 – 1141  $\text{cm}^{-1}$  spectral range.

Prior statistical analysis, spectra were pre-processed: atmospheric compensation, baseline correction, vector normalization and offset correction were applied by using spectroscopy software OPUS.

Different spectral regions were chosen for statistical analysis and different pre-processing of spectra (either first or second derivative of spectra was calculated by using spectroscopy software OPUS or not) was applied prior the analysis; however, the best results were obtained by using parameters and spectra pre-processing as mentioned above.

## 6.3. Results and discussion

In total, cases of 46 patients were analysed. Samples of native unprocessed tissue were investigated. Summarised data is presented in table 6.1. Final diagnosis is based on standard histology reports of the whole resected tissue specimen.

**Table 6.1.** Tissue types collected during the study.

Tissue type	Number of tissue samples
Normal	45
Tumor	
<i>Primary</i>	
HCC	14
CCC	8
<i>Secondary</i>	
Colorectal cancer	16
Gallbladder carcinoma	1
PDAC	1
Adenocarcinoma of esophagogastric junction	2
Adrenal gland carcinoma	1
Total number of patients	46

Spectra of each specimen were collected at several different areas of the sample: tissue sample was sliced, and spectra were collected from each freshly cut surface. In case of every sample, obtained spectra were averaged and resulting spectrum was used for further analysis.

Mean spectra of liver normal tissue and primary tumors (HCC and CCC) are presented in Figure 6.1. Main spectral band positions and their assignments are shown in Table 6.2.

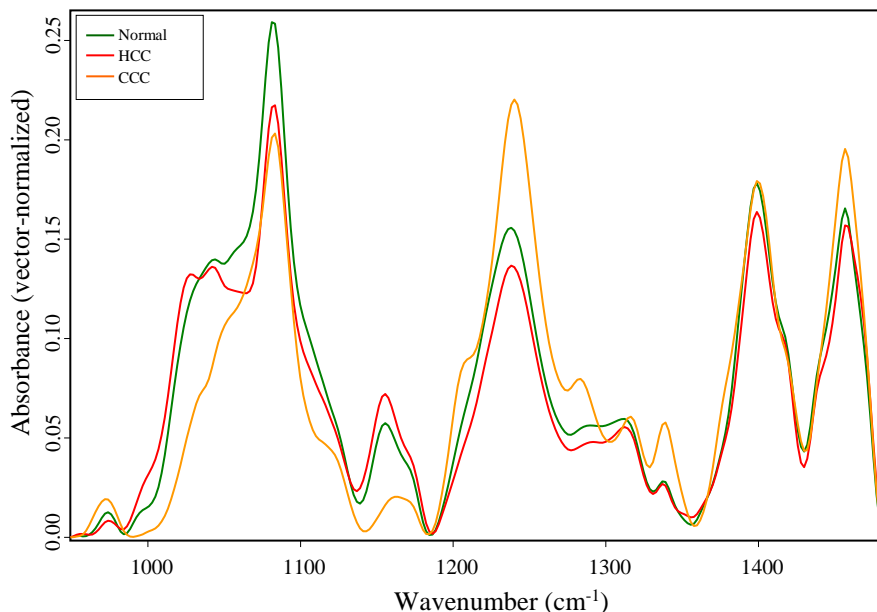


**Figure 6.1.** Mean ATR IR spectra of liver normal and primary liver tumor (hepatocellular carcinoma (HCC) and cholangiocarcinoma (CCC)) tissue. Spectra are baseline corrected and vector-normalized.

Mean spectra of normal and tumorous HCC tissue shows higher levels of glycogen compared to tumorous CCC tissue. This is illustrated by spectral bands located at 1027 assigned to  $\nu(\text{C-O})$ ,  $\nu(\text{C-C})$ ,  $\delta(\text{C-O-H})$  vibrations and  $1155 \text{ cm}^{-1}$  assigned to  $\nu(\text{C-O})$  vibrations. Presence of glycogen in liver tissue can be explained by liver function of glycogen storage which works as a reservoir of glucose required for other tissues in the body [216]. Hepatocytes accumulate glycogen and help to maintain proper blood glucose levels (store or produce glucose when required) by reacting to hormones [217]. Since liver parenchyma is constituted mainly of hepatocytes and HCC tumors arise from this cell type, glycogen is present in liver normal and tumorous HCC tissues.

Main differences between mean liver normal and tumorous HCC tissue spectra are observable in spectral range between 950 and 1185  $\text{cm}^{-1}$  where spectral bands mainly due to carbohydrates, phosphate groups are located. Absorbance values of spectral bands located at 1027 and 1055  $\text{cm}^{-1}$  corresponding to glycogen as described above are higher in mean spectrum of tumorous HCC tissue. At first glance it could be concluded that higher levels of glycogen in tumorous HCC tissue compared to liver normal tissue is a characteristic feature of HCC tumors; however, glycogen levels vary greatly from patient to patient inside normal and tumorous HCC tissue classes (Figure 6.2.).

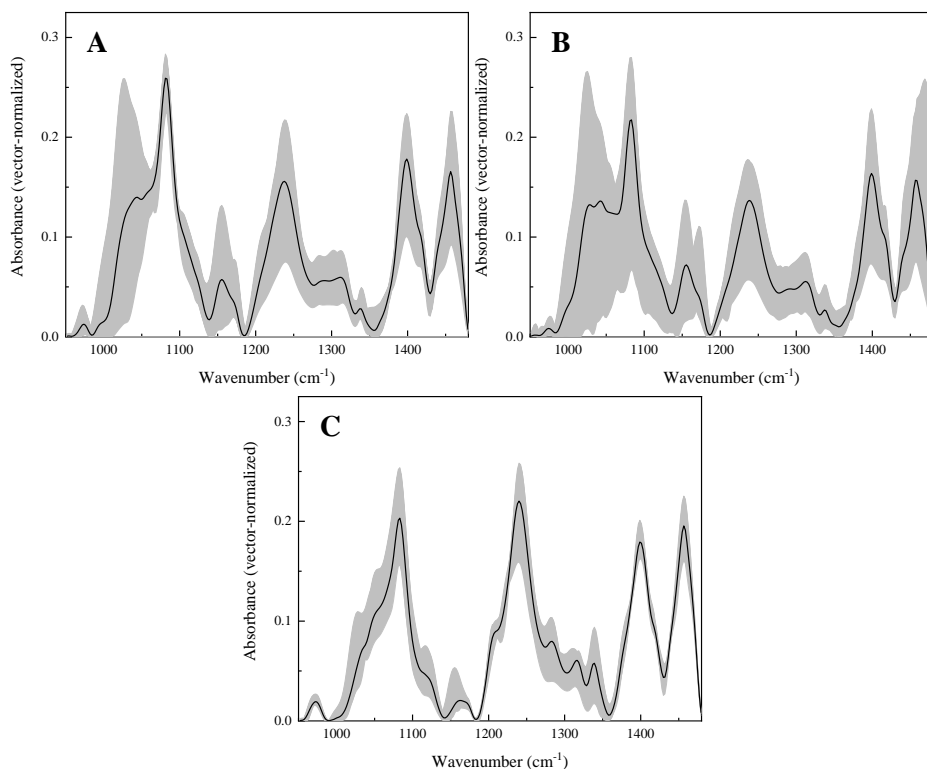


**Figure 6.2.** Mean spectra (black solid line) and variations of spectra of tissue taken from different patients (grey area) of liver normal (A), tumorous HCC (B) and CCC (C) tissue. Spectra are baseline corrected and vector-normalized.

Black lines correspond to the mean spectra of all the samples taken from different patients, while grey areas indicate the variations of spectra in different tissue classes. Variations in normal tissue class possibly could be caused by duration of fasting time before the surgery, lifestyle, habits and diet of individual patients, concomitant diseases such as diabetes mellitus, or

metabolism rates of the body. Mentioned reasons could determine glycogen levels in liver tissue. Moreover, variations in glycogen levels in tumorous HCC tissue could be related to the stage of the disease. It is reported that amount of glycogen in tumorous tissue is higher in early stages of HCC tumors and lower in later stages of HCC tumors compared to adjacent normal tissues [218]. Besides higher absorbance values of mentioned glycogen spectral bands, overall profiles of spectra in spectral range between 950 and 1185  $\text{cm}^{-1}$  are different for mean spectra of normal and HCC tissues. Differences in absorbance values for spectral bands located at 998, 1043 and 1057  $\text{cm}^{-1}$  are mostly related to carbohydrates used in cell metabolism (such as glycogen or glucose) or sugars of nucleic acids. Precise assignment of these spectral bands is difficult since these spectral bands appear as shoulders of more intense bands or are overlapping. Moreover, positions of the bands could depend on environment, for example positions of spectral bands for glycogen are different for solid glycogen and glycogen in water solution (the Appendix, Figure A-01)

Another difference between normal and tumorous HCC tissue is lower absorbance values of spectral bands located at 972, 1082 and 1237  $\text{cm}^{-1}$  for HCC tissue. Spectral band located at 972  $\text{cm}^{-1}$  can be assigned to  $\nu(\text{PO}_4)$  vibrations of nucleic acids and proteins, or  $\text{OCH}_3$  groups of polysaccharides. Spectral band located at 1082  $\text{cm}^{-1}$  could be assigned to  $\nu(\text{PO}_2)$  vibrations of nucleic acids. Spectral band located at 1237  $\text{cm}^{-1}$  is assigned to  $\nu(\text{PO}_2)$  vibrations and Amide III groups. Taking into account these observations, the decrease of absorbance values of these spectral bands could be related to reduced amounts of phosphate groups that could be related to changes in nucleic acids, proteins or changed metabolic pathways. To conclude, main differences between mean spectra of normal and tumorous HCC tissue could be related to carbohydrate content and amount of phosphate groups; however, for more precise conclusions more tissue samples should be included in the study due to high variations of spectra inside each tissue class.

While HCC tumors show presence of glycogen, reduced absorbance values of glycogen spectral bands of CCC tissue can be explained by nature of the tumor – CCC tumors forms out of cholangiocytes which do not accumulate glycogen. Besides the decreased absorbance values of the glycogen spectral bands, increased absorbance values of spectral bands corresponding to collagen located at 1034, 1207, 1240, 1283 and 1317  $\text{cm}^{-1}$  are observed. Increased collagen levels are related to growth of the desmoplastic stroma of the tumor which is rich in connective tissue containing collagen similar to PDAC tumors. This desmoplastic reaction is a common feature of CCC tumors [208], [219]–[221]. Variations in tumorous CCC tissue class are

smaller compared to normal and tumorous HCC tissue classes, this could be determined by smaller scope of CCC tumor samples (only 8 cases were included in the study).

**Table 6.2.** Spectral bands and their assignments. Assignments set according to [158].

<b>Spectral band position, cm<sup>-1</sup></b>			
<b>Normal tissue</b>	<b>Tumorous HCC tissue</b>	<b>Tumorous CCC tissue</b>	<b>Assignment</b>
Not present	956	Not present	$\nu(\text{PO}_4^{3-})$ , $\nu(\text{C-O})$ , $\nu(\text{C-C})$
972	971	974	$\nu(\text{PO}_4)$ of nucleic acids and proteins
997	998	998	$\text{OCH}_3$ of polysaccharides
1027 (sh)	1027	Not present	$\nu(\text{CO})$ , $\nu(\text{CC})$ ribose
Not present	Not present	1034	$\nu(\text{C-O})$ , $\nu(\text{C-C})$ , $\delta(\text{C-O-H})$ of glycogen
1043	1043	Not present	Collagen
Not present	Not present	1052	$\nu(\text{C-O})$ , $\delta(\text{C-O})$ of the C-OH of carbohydrates
1057	1057	Not present	$\nu(\text{CO-O-C})$
1082	1082	1082	$\nu(\text{C-O})$ , $\delta(\text{C-O})$ of the C-OH of carbohydrates
1123 (sh)	1123 (sh)	1123	$\nu(\text{PO}_2^-)$ , $\nu(\text{C-O})$ , $\nu(\text{C-C})$ , $\delta(\text{OCH})$
1155	1155	Not present	$\nu(\text{PO}_2^-)$
Not present	Not present	1162	$\nu(\text{C-O})$ , $\delta(\text{C-O})$ , $\delta(\text{C-O-H})$ , $\delta(\text{C-O-C})$
1172 (sh)	1172 (sh)	1172 (sh)	phosphodiester stretching
Not present	Not present	1207	$\nu(\text{C-O})$
1237	1237	1240	$\nu(\text{C-O})$
Not present	Not present	1283	$\nu(\text{C-O})$
1287	1287	Not present	Amide III
1312	1312	Not present	$\nu(\text{PO}_2^-)$ , Amide III
Not present	Not present	1317	Amide III
			$\delta(\text{N-H})$
			Amide III, $\nu(\text{P=O})$

1338	1338	1338	CH <sub>2</sub> wagging
1399	1399	1399	δ(CH <sub>3</sub> )
1417	1417	1417	ν(C-N), δ(N-H), δ(C-H)
1456	1456	1456	δ(CH <sub>3</sub> )

(sh) indicates a shoulder band

Mean spectra of hepatic metastases are presented in Figure 6.3. Main differences between mean liver normal and colorectal cancer metastasis tissue spectra are observable in spectral range between 950 and 1142 cm<sup>-1</sup> where spectral bands mainly due to carbohydrates, phosphate groups are located. A more significant difference is the reduced glycogen levels in colorectal metastasis spectrum. Spectra of other type of metastasis were measured only for 1 – 2 cases of each tissue type, thus for the more precise analysis more patients should be included.

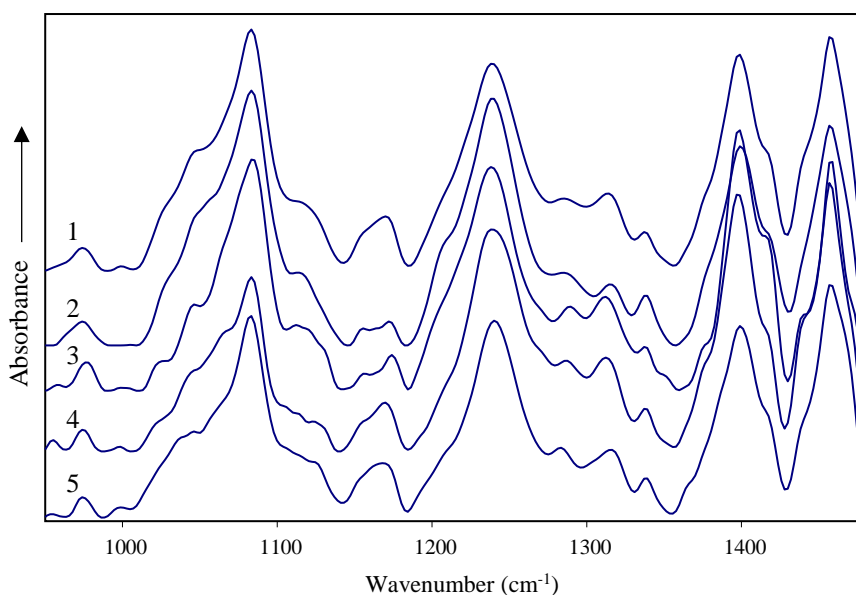


**Figure 6.3.** ATR IR spectra of liver metastasis: mean spectrum of CRC tissue (1), PDAC (2), adrenal gland (3), gallbladder carcinoma (4), and esophagogastric junction (5). Spectra are baseline corrected and vector-normalized.

Methods of multivariate statistical analysis were applied for the evaluation of the IR spectroscopy to delineate normal and tumorous liver tissues. Dendrogram representing results of HCA analysis is presented in Figure 6.4. Spectra are classified into two well separated clusters; large distance between clusters shows a good separation between two classes. 9 spectra out of 45



normal tissue spectra and 11 spectra out of 43 tumorous tissue spectra were assigned to wrong tissue classes (these spectra are indicated by \* symbol) that corresponds to 80 % identification accuracy for normal tissue and 74 % identification for tumorous tissue. Spectra which were assigned to wrong tissue classes are presented in the Appendix (Figures A-31 – A-32). All spectra of normal tissues classified as tumorous tissues show absence of glycogen spectral bands (Appendix, Figure A-31) while presence of glycogen is a common feature of liver tissue. Spectra of tumorous tissue which were assigned to normal tissue class show presence of glycogen (Appendix, Figure A-32). Most tumorous tissues wrongly assigned to normal tissue class are HCC tumors (7 out of 9 wrongly identified tissue spectra). As it was discussed above, presence of glycogen or even higher levels of glycogen compared to normal liver tissue is a common feature of a part of HCC tumors. These findings suggest that glycogen is an important criterion for tissue identification: presence of glycogen leads to correct tissue identification of normal liver tissue while higher levels of glycogen in tumorous tissue leads to misclassification.

Results of PCA analysis are presented in Figure 6.5. Data are classified into two clusters, corresponding to normal (bottom of the diagram) and tumorous (top of the diagram) tissues. Green and red dots indicate spectra of each normal and tumorous tissue sample respectively. 8 spectra out of 45 normal tissue spectra and 12 spectra out of 43 tumorous tissue spectra were assigned to wrong tissue classes that corresponds to 82 % identification accuracy for normal and 72 % accuracy for tumorous liver tissues.

Spectra which were assigned to wrong tissue classes are presented in the Appendix (Figures A-33 – A-34). All spectra of normal tissues classified as tumorous by applying PCA analysis, coincide with normal tissue spectra which were assigned to tumorous tissue class by applying HCA analysis. All these spectra show absence of glycogen spectral bands (Appendix, Figure A-33). Spectra of tumorous tissues assigned to normal tissue class show presence of glycogen and are mostly HCC tumors (7 out of 12 spectra assigned to normal tissue class) (Appendix, Figure A-34). Most tumors classified as normal tissues by applying PCA analysis (8 out of 12 cases) were also classified as normal tissues by applying HCA analysis.

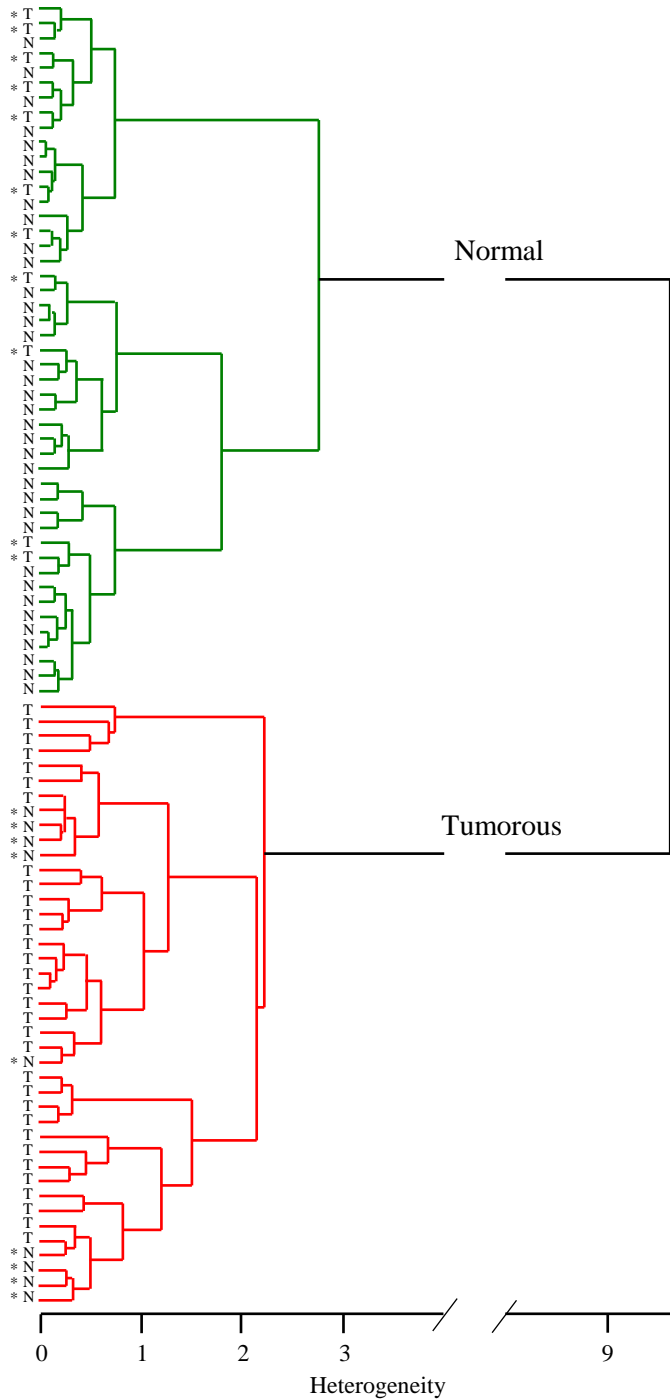


**Figure 6.4.** HCA dendrogram of normal and tumorous liver tissues. Green cluster corresponds to the normal tissue class, red cluster corresponds to tumorous tissue class. Letters N and T represent spectra of each normal tumorous tissues respectively. \* symbol indicates spectra which were assigned to the wrong tissue class.

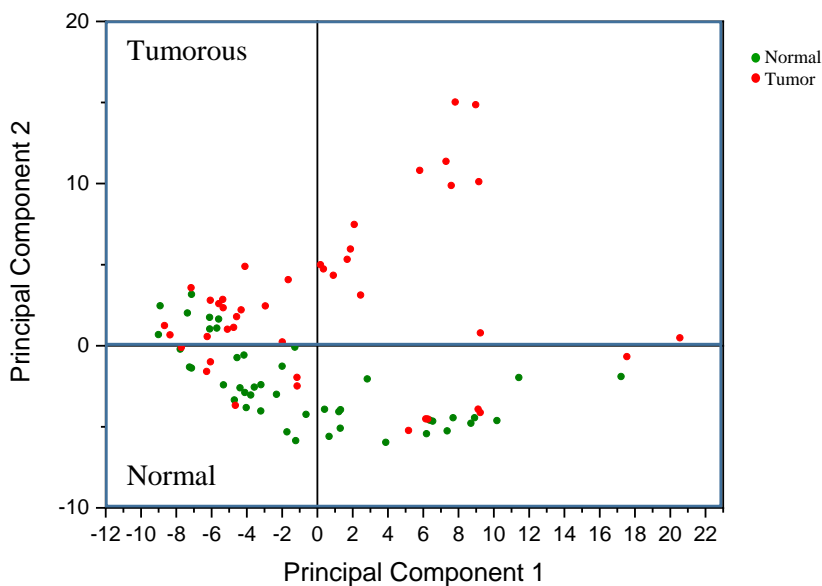


**Figure 6.5.** PCA diagram of liver tissue spectra.

Values of sensitivity, specificity, positive and negative prognostic values for tumorous liver tissue identification were evaluated and are presented in Table 6.3.

**Table 6.3.** Summarized values of sensitivity, specificity, positive and negative prognostic values for application of HCA and PCA analysis for tumorous liver tissue identification.

	Method	
	HCA	PCA
Sensitivity	74 %	72 %
Specificity	80 %	82 %
PPV	78 %	79 %
NPV	77 %	76 %

Both methods of statistical analysis give similar results for identification of tumorous liver tissues: while HCA analysis shows slightly higher sensitivity, specificity is slightly better for PCA analysis. As it was mentioned above, most part of normal tissue spectra which are classified as tumorous tissues and tumorous tissue spectra which were classified as normal tissues, coincide for both statistical analysis methods, thus, revealing similar feasibility of HCA and PCA analysis methods. In general, presence of

glycogen in liver tissue is the most important criterion for tissue type identification: since it is a common feature of normal and HCC tumor tissues, variations in levels of glycogen in tissues lead to assignment to wrong tissue classes. If spectra are assigned to so called wrong classes, it could not be assured that tissue spectra are in fact misclassified: tissue types before the spectroscopy measurements were evaluated only macroscopically. Macroscopic evaluation is not accurate in all cases, therefore, tissue sample can be correctly assigned by spectroscopic investigation even if the macroscopic examination of the tissue shows opposite results. In this regard, misclassification partly can rely on the histological tissue evaluation. Evaluation of the same tissue sample by applying IR spectroscopy and performing routine histological microscopic analysis of stained tissue would give more accurate conclusions. Moreover, much higher database of tissue spectra would give more accurate conclusions concerning spectral markers and accuracy of statistical analysis.

## OVERVIEW AND FUTURE PROSPECTS

The potential of fiber-based ATR IR spectroscopy application for normal and tumorous tissue delineation of various organs (kidney, urinary bladder, pancreas and liver) was shown here. The method can be successfully applied for the tissue analysis performed under intraoperative conditions.

However, the application of the method is not that straightforward. It was shown that there is not one universal spectral marker for identification of different types of cancer while different methods of statistical analysis are required for the discrimination of normal and pathological tissues of different organs. The specific set of spectral markers is required for each organ tissue. Every organ is different, has its own functions, thus biochemical composition varies among different organs. Moreover, a variety of cancer types can arise in human body – every type of cancer has its own metabolic and morphologic features resulting in different biochemical composition. It was shown that depending on tissue type different spectral markers allowing delineation of normal and tumorous tissues are observed. For instance, increased levels of glycogen in tumorous kidney and urinary bladder tissues are related to increased energy demand in tumorous tissue due to higher cell proliferation. Decreased collagen levels in tumorous bladder tissues are related to increased secretion of collagenase, which destroys the normal host tissue. Increased levels of collagen in tumorous pancreas and liver cholangiocellular carcinoma tissue are related to desmoplastic reaction which is related to growth of ECM. During the study, a relatively small number of patients (between 30 - 150 for each type of organ) was included in the study. Number of patients is statistically relevant for establishment of spectral tumor markers of most frequently diagnosed tumors and to show the potential of the method to be applied for the intraoperative tissue assessment. For the more accurate tissue identification more data is required – during the study only a few samples of rarer tumor types were investigated, thus larger database of such tumor types is crucial for tumor marker identification and for tissue type classification. Larger database would be beneficial for supervised statistical analysis or even for artificial intelligence based classification.

Another limitation – the current IR fiber probe technology does not allow to use the probe for endoscopic surgeries since fibers are fragile while the shaft of the probe is relatively wide and unsuitable for surgeries such as transurethral resections. Although mentioned aspects make some intraoperative applications more difficult, in fact they do not prohibit intraoperative applications in general. The method is suitable for open

surgeries. At the current stage of technology development, the method could be readily applied to open surgeries after completion of clinical trials.

## CONCLUSIONS

1. The applied fiber-based spectroscopy system is suitable for the measurements of spectra of different types of tissue samples: freshly resected unprocessed tissue samples and tissue smears. S/N in the fingerprint spectral region is above 40 which is suitable for the collection of informative spectra. The research showed that the penetration depth of IR radiation into the sample reaches 0.5 – 1.9  $\mu\text{m}$  that is enough to obtain spectra containing biochemical composition of both tissue components – cells and non-cellular components such as extracellular matrix (ECM).
2. The main spectral markers for identification of tumorous kidney tissues are increased absorbance values of spectral bands located at 1027 and 1155  $\text{cm}^{-1}$  corresponding to glycogen and decreased absorbance values of spectral bands located at 972 and 1240  $\text{cm}^{-1}$  related to reduced levels of fructose 1,6-bisphosphatase in cancerous kidney tissues. Applied statistical methods allow to identify tumorous kidney tissues with up to 91 % sensitivity and 100 % specificity.
3. The main spectral markers for identification of tumorous urinary bladder tissues are increased absorbance values of spectral bands located at 1028 and 1154  $\text{cm}^{-1}$  assigned to glycogen and decreased absorbance values of spectral bands located at 1033, 1206, 1240, 1282, 1317 and 1339  $\text{cm}^{-1}$  assigned to collagen. Applied statistical methods allow to identify tumorous urinary bladder tissues with up to 91 % sensitivity and 98 % specificity.
4. Tumorous pancreas tissue can be identified from the profile of spectrum in spectral region between 1000 and 1083  $\text{cm}^{-1}$  where spectral bands corresponding mainly to carbohydrates, proteins and nucleic acids are located. Decreased absorbance values of spectral bands located at 972 and 1083  $\text{cm}^{-1}$  related to reduced amounts of nucleic acids and increased values of spectral bands located at 1033, 1207, 1283 and 1339  $\text{cm}^{-1}$  corresponding to collagen in tumorous pancreas tissues. Applied statistical methods allow to identify tumorous pancreas tissues with up to 87 % sensitivity and 84 % specificity.
5. Tumorous liver tissues can be identified from changed amounts of glycogen indicated by spectral bands located at 1027 and 1155  $\text{cm}^{-1}$  and collagen indicated by spectral bands located at 1034, 1207, 1240, 1283 and 1317  $\text{cm}^{-1}$  depending on tumor type. Applied statistical methods allow to identify tumorous liver tissues with up to 74 % sensitivity and 80 % specificity.

6. The fiber-based spectroscopy system at the current level of technology development could be used for tumorous tissue identification in open surgeries after completion of clinical trials.



## BIBLIOGRAPHY

- [1] H. Sung et al. Global Cancer Statistics 2020: GLOBOCAN Estimates of Incidence and Mortality Worldwide for 36 Cancers in 185 Countries, *CA. Cancer J. Clin.*, **71**, p. 209-249, 2021.jn
- [2] H. Yao et al. The Use of FTIR-ATR Spectrometry for Evaluation of Surgical Resection Margin in Colorectal Cancer: A Pilot Study of 56 Samples, *J. Spectrosc.*, **2014**, 13890, 2014.
- [3] S. Liu et al. Precise diagnosis of intraoperative frozen section is an effective method to guide resection strategy for peripheral small-sized lung adenocarcinoma, *J. Clin. Oncol.*, **34**, 4, p. 307–313, 2016.
- [4] E. M. Layfield et al. Frozen Section Evaluation of Margin Status in Primary Squamous Cell Carcinomas of the Head and Neck: A Correlation Study of Frozen Section and Final Diagnoses, *Head Neck Pathol.*, **12**, 2, 2018.
- [5] F. Zaiem et al. Accuracy and Reproducibility of Frozen Section Diagnosis in Ovarian Tumors A 10-Year Experience at a Tertiary Cancer Center, *Arch Pathol Lab Med*, **146**, p. 626–631, 2022.
- [6] J. A. Chavez et al. Pancreatic Frozen Section Guides Operative Management With Few Deferrals and Errors Five-Year Experience at a Large Academic Institution, *Arch. Pathol. Lab. Med.*, **146**, 1, p. 84–91, 2022.
- [7] S. B. Sams and J. A. Wisell, Discordance between Intraoperative Consultation by Frozen Section and Final Diagnosis: A Classification Model to Guide Quality Improvement, *Int. J. Surg. Pathol.*, **25**, 1, p. 41–50, 2017.
- [8] T. Nagaya et al. Fluorescence-Guided Surgery, *Front. Oncol.*, **7**, 314, 2017.
- [9] A. K. Shah, Postoperative pathologic assessment of surgical margins in oral cancer: A contemporary review, *J. Oral Maxillofac. Pathol.*, **22**, 1, p. 78, 2018.
- [10] H. L. Stewart and D. J. S. Birch, Fluorescence Guided Surgery, *Methods Appl. Fluoresc.*, **9**, 4, 042002, 2021.
- [11] S. Hernot et al. Latest developments in molecular tracers for fluorescence image-guided cancer surgery, *Lancet Oncol.*, **20**, 7, p. e354–e367, 2019.
- [12] J. S. D. Mieog et al. Fundamentals and developments in fluorescence-guided cancer surgery, *Nat. Rev. Clin. Oncol.*, **19**, 1, p. 9–22, 2022.

- [13] S. Cui et al. Raman Spectroscopy and Imaging for Cancer Diagnosis, *J. Healthc. Eng.*, **2018**, 8619342, 2018.
- [14] H. Lui et al. Real-time raman spectroscopy for in vivo skin cancer diagnosis, *Cancer Res.*, **72**, 10, p. 2491–2500, 2012.
- [15] L. Lim et al. Clinical study of noninvasive in vivo melanoma and nonmelanoma skin cancers using multimodal spectral diagnosis, *J. Biomed. Opt.*, **19**, 11, 117003, 2014.
- [16] J. Schleusener et al. In vivo study for the discrimination of cancerous and normal skin using fibre probe-based Raman spectroscopy, *Exp. Dermatol.*, **24**, 10, p. 767–772, 2015.
- [17] J. Desroches et al. Characterization of a Raman spectroscopy probe system for intraoperative brain tissue classification, *Biomed. Opt. Express*, **6**, 7, 2380, 2015.
- [18] D. Malonek et al. Rapid intraoperative diagnosis of gynecological cancer by ATR-FTIR spectroscopy of fresh tissue biopsy, *J. Biophotonics*, **13**, 9, e202000114, 2020.
- [19] D. Lazaro-Pacheco et al. Deciphering the structural and chemical composition of breast cancer using FTIR spectroscopy, *Appl. Spectrosc. Rev.*, **57**, 3, p. 234–248, 2022.
- [20] G. Steiner et al. A new approach for clinical translation of infrared spectroscopy: exploitation of the signature of glioblastoma for general brain tumor recognition, *J. Neurooncol.*, **161**, 1, p 57–66, 2023.
- [21] M. Kujdowicz et al. In Vitro Spectroscopy-Based Profiling of Urothelial Carcinoma: A Fourier Transform Infrared and Raman Imaging Study, *Cancers (Basel)*, **13**, 1, p. 123, 2021.
- [22] D. Sheng et al. A study of structural differences between liver cancer cells and normal liver cells using FTIR spectroscopy, *J. Mol. Struct.*, **1099**, p. 18–23, 2015.
- [23] L. Li et al. Characterization of ovarian cancer cells and tissues by Fourier transform infrared spectroscopy, *J. Ovarian Res.*, **11**, 1, p. 64, 2018.
- [24] J. Ollesch et al. It's in your blood: spectral biomarker candidates for urinary bladder cancer from automated FTIR spectroscopy, *J. Biophotonics*, **7**, 3–4, p. 210–221, 2014.

- [25] J. Ollesch et al. FTIR spectroscopy of biofluids revisited: an automated approach to spectral biomarker identification, *Analyst*, **138**, 14, p. 4092–4102, 2013.
- [26] A. Sala et al. Liquid Biopsy for Pancreatic Cancer Detection Using Infrared Spectroscopy, *Cancers*, **14**, 3048, 2022.
- [27] K. Thumanu et al. Diagnosis of liver cancer from blood sera using FTIR microspectroscopy: a preliminary study, *J. Biophotonics*, **7**, 3–4, p. 222–231, 2014.
- [28] X. Yang et al. Diagnosis of liver cancer by FTIR spectra of serum, *Spectrochim. Acta Part A Mol. Biomol. Spectrosc.*, **263**, 120181, 2021.
- [29] P. D. Lewis et al. Evaluation of FTIR Spectroscopy as a diagnostic tool for lung cancer using sputum, *BMC Cancer*, **10**, 1, 640, 2010.
- [30] M. Kujdowicz et al. Towards the Point of Care and noninvasive classification of bladder cancer from urine sediment infrared spectroscopy. Spectral differentiation of normal, abnormal and cancer patients, *Microchem. J.*, **168**, 106460, 2021.
- [31] S. Gok et al. Bladder cancer diagnosis from bladder wash by Fourier transform infrared spectroscopy as a novel test for tumor recurrence, *J. Biophotonics*, **9**, 9, p. 967–975, 2016.
- [32] V. Untereiner et al. Bile analysis using high-throughput FTIR spectroscopy for the diagnosis of malignant biliary strictures: a pilot study in 57 patients, *J. Biophotonics*, **7**, 3–4, p. 241–253, 2014.
- [33] R. Di Santo et al., Machine Learning-Assisted FTIR Analysis of Circulating Extracellular Vesicles for Cancer Liquid Biopsy, *J. Pers. Med.*, **12**, 6, 949, 2022.
- [34] A. Zlotogorski-Hurvitz, et al. FTIR-based spectrum of salivary exosomes coupled with computational-aided discriminating analysis in the diagnosis of oral cancer, *J. Cancer Res. Clin. Oncol.*, **145**, 3, p. 685–694, 2019.
- [35] X.-L. Yap et al. Detection of Prostate Cancer via IR Spectroscopic Analysis of Urinary Extracellular Vesicles: A Pilot Study, *Membranes (Basel)*, **11**, 8, p. 591, 2021.
- [36] C. Krafft et al. A specific spectral signature of serum and plasma-derived extracellular vesicles for cancer screening, *Nanomedicine Nanotechnology, Biol. Med.*, **13**, 3, p. 835–841, 2017.

- [37] J. Didžiapetrienė, *Vėžio biologija*. Vilnius, 2013.
- [38] N. M. Anderson and M. C. Simon, The tumor microenvironment, *Curr. Biol.*, **30**, 16, p. R921–R925, 2020.
- [39] A. Fouladzadeh et al. The development of tumour vascular networks, *Commun. Biol.*, **4**, 1, 1111, 2021.
- [40] D. R. Schmidt et al. Metabolomics in cancer research and emerging applications in clinical oncology, *CA. Cancer J. Clin.*, **71**, 4, p. 333–358, 2021.
- [41] R. A. Gatenby and R. J. Gillies, Why do cancers have high aerobic glycolysis?, *Nat. Rev. Cancer*, **4**, 11, p. 891–899, 2004.
- [42] C. E. Zois et al. Glycogen metabolism in cancer, *Biochem. Pharmacol.*, **92**, 1, p. 3–11, 2014.
- [43] P. Lu et al. The extracellular matrix: A dynamic niche in cancer progression, *J. Cell Biol.*, **196**, 4, p. 395–406, 2012.
- [44] A. Baba, C. Cătoi. Chapter 3: Tumor Cell Morphology. In *Comparative Oncology*; The Publishing House of the Romanian Academy: Bucharest, Romania, 2007. Available online: <https://www.ncbi.nlm.nih.gov/books/NBK9557/> (accessed on 14 September 2022)
- [45] D. L. Woernley, Infrared absorption curves for normal and neoplastic tissues and related biological substances., *Cancer Res.*, **12**, 7, p. 516–23, 1952.
- [46] G. Steiner et al. Detection and grading of human gliomas by FTIR spectroscopy and a genetic classification algorithm, *Proc. SPIE 4614, Biomedical Vibrational Spectroscopy II*, p. 127-133, 2002.
- [47] F. Chen et al. Human serum mid-infrared spectroscopy combined with machine learning algorithms for rapid detection of gliomas, *Photodiagnosis Photodyn. Ther.*, **35**, 102308, 2021.
- [48] A. G. Theakstone et al. Rapid Spectroscopic Liquid Biopsy for the Universal Detection of Brain Tumours, *Cancers (Basel)*, **13**, 15, 3851, 2021.
- [49] J. M. Cameron et al. Clinical Spectroscopy: Lost in Translation?, *Appl. Spectrosc.*, **76**, 4, p. 393–415, 2022.

- [50] Q. Wu et al. Deciphering the Biochemical Similarities and Differences Among Human Neuroglial Cells and Glioma Cells Using Fourier Transform Infrared Spectroscopy, *World Neurosurg.*, **168**, p. e562–e569, 2022.
- [51] W. Peng et al. Grade classification of human glioma using a convolutional neural network based on mid-infrared spectroscopy mapping, *J. Biophotonics*, **15**, 4, 2022.
- [52] K. Łach et al. Infrared Spectroscopy as a Potential Diagnostic Tool for Medulloblastoma, *Molecules*, **28**, 5, 2390, 2023.
- [53] A. G. Theakstone, et al. Investigating centrifugal filtration of serum-based FTIR spectroscopy for the stratification of brain tumours, *PLoS One*, **18**, 2, e0279669, 2023.
- [54] G. Steiner et al. Distinguishing and grading human gliomas by IR spectroscopy, *Biopolymers*, **72**, 6, p. 464–471, 2003.
- [55] C. Krafft, et al. Analysis of human brain tissue, brain tumors and tumor cells by infrared spectroscopic mapping, *Analyst*, **129**, 10, 921, 2004.
- [56] O. Uckermann et al., Optical Analysis of Glioma: Fourier-Transform Infrared Spectroscopy Reveals the IDH1 Mutation Status, *Clin. Cancer Res.*, **24**, 11, p. 2530–2538, 2018.
- [57] J. M. Cameron et al. Interrogation of IDH1 Status in Gliomas by Fourier Transform Infrared Spectroscopy, *Cancers (Basel)*, **12**, 12, 3682, 2020.
- [58] D. Kong et al. Morphological and Biochemical Properties of Human Astrocytes, Microglia, Glioma, and Glioblastoma Cells Using Fourier Transform Infrared Spectroscopy, *Med. Sci. Monit.*, **9**, 26, e925754, 2020.
- [59] K. Gajjar et al. Diagnostic segregation of human brain tumours using Fourier-transform infrared and/or Raman spectroscopy coupled with discriminant analysis, *Anal. Methods*, **5**, 1, p. 89–102, 2013.
- [60] J. M. Cameron et al., Stratifying Brain Tumour Histological Sub-Types: The Application of ATR-FTIR Serum Spectroscopy in Secondary Care, *Cancers (Basel)*, **12**, 7, 1710, 2020.
- [61] W. Peng et al. Grade diagnosis of human glioma using Fourier transform infrared microscopy and artificial neural network, *Spectrochim. Acta Part A Mol. Biomol. Spectrosc.*, **260**, 119946, 2021.

- [62] M. Smolina and E. Goormaghtigh. Gene expression data and FTIR spectra provide a similar phenotypic description of breast cancer cell lines in 2D and 3D cultures, *Analyst*, **143**, 11, p. 2520–2530, 2018.
- [63] A. Markouizou, J. Anastassopoulou, P. Kolovou, T. Theophanides, and P. Tsekeris, Fourier Transform Infrared Spectroscopy in the Study of Discrimination of Lobular Breast Cancers, *Cancer Diagnosis Progn.*, **2**, 6, p. 750–757, 2022.
- [64] M. Kołodziej et al. Characterisation of breast cancer molecular signature and treatment assessment with vibrational spectroscopy and chemometric approach, *PLoS One*, **17**, 3, e0264347, 2022.
- [65] S. Rehman et al. Fourier Transform Infrared Spectroscopic Analysis of Breast Cancer Tissues; Identifying Differences between Normal Breast, Invasive Ductal Carcinoma, and Ductal Carcinoma In Situ of the Breast, *Appl. Spectrosc. Rev.*, **45**, 5, p. 355–368, 2010.
- [66] A. Tiwari and S. Gong. Electrochemical detection of a breast cancer susceptible gene using cDNA immobilized chitosan-co-polyaniline electrode, *Talanta*, **77**, 3, p. 1217–1222, 2009.
- [67] N. Simsek Ozek, et al. Characterization of microRNA-125b expression in MCF7 breast cancer cells by ATR-FTIR spectroscopy, *Analyst*, **135**, 12, 3094, 2010.
- [68] M. Verdonck et al. Characterization of human breast cancer tissues by infrared imaging, *Analyst*, **141**, 2, p. 606–619, 2016.
- [69] R. Eckel et al. Characteristic infrared spectroscopic patterns in the protein bands of human breast cancer tissue, *Vib. Spectrosc.*, **27**, 2, pp. 165–173, 2001.
- [70] J. Backhaus et al. Diagnosis of breast cancer with infrared spectroscopy from serum samples, *Vib. Spectrosc.*, **52**, 2, p. 173–177, 2010.
- [71] D. L. D. Freitas et al. Spectrochemical analysis of liquid biopsy harnessed to multivariate analysis towards breast cancer screening, *Sci. Rep.*, **10**, 1, 12818, 2020.
- [72] H. Ghimire et al. Protein Conformational Changes in Breast Cancer Sera Using Infrared Spectroscopic Analysis, *Cancers (Basel)*, **12**, 7, 1708, 2020.

- [73] U. Zelig et al. Early detection of breast cancer using total biochemical analysis of peripheral blood components: a preliminary study, *BMC Cancer*, **15**, 1, 408, 2015.
- [74] I. C. C. Ferreira et al. Attenuated Total Reflection-Fourier Transform Infrared (ATR-FTIR) Spectroscopy Analysis of Saliva for Breast Cancer Diagnosis, *J. Oncol.*, **2020**, 4343590, p. 1-11, 2020.
- [75] K. V. Kepesidis et al. Breast-cancer detection using blood-based infrared molecular fingerprints, *BMC Cancer*, **21**, 1, 1287, 2021.
- [76] R. C. Tomas et al. Detection of breast cancer by ATR-FTIR spectroscopy using artificial neural networks, *PLoS One*, **17**, 1, e0262489, 2022.
- [77] J. Depciuch et al. The Spectroscopic Similarity between Breast Cancer Tissues and Lymph Nodes Obtained from Patients with and without Recurrence: A Preliminary Study, *Molecules*, **25**, 14, 3295, 2020.
- [78] L. B. Mostaçõ-Guidolin, et al. Molecular and chemical characterization by Fourier transform infrared spectroscopy of human breast cancer cells with estrogen receptor expressed and not expressed, *Spectroscopy*, **24**, 5, p. 501–510, 2010.
- [79] Y. Gao et al., Fourier transform infrared microspectroscopy monitoring of 5-fluorouracil-induced apoptosis in SW620 colon cancer cells, *Mol. Med. Rep.*, **11**, 4, p. 2585–2591, 2015.
- [80] E. Barlev et al. A novel method for screening colorectal cancer by infrared spectroscopy of peripheral blood mononuclear cells and plasma, *J. Gastroenterol.*, **51**, 3, p. 214–221, 2016.
- [81] M. Madhavi, et al. Preparation and in vitro/in vivo characterization of curcumin microspheres intended to treat colon cancer, *J. Pharm. Bioallied Sci.*, **4**, 2, 164, 2012.
- [82] M. J. Walsh et al. High-resolution mid-infrared imaging for disease diagnosis, in *Proc. SPIE 8219, Biomedical Vibrational Spectroscopy V: Advances in Research and Industry*, 82190R, 2012.
- [83] B. Rigas and P. T. Wong. Human colon adenocarcinoma cell lines display infrared spectroscopic features of malignant colon tissues, *Cancer Res.*, **52**, 1, p. 84–8, 1992.

- [84] L. Dong et al., Evaluation of FTIR spectroscopy as diagnostic tool for colorectal cancer using spectral analysis, *Spectrochim. Acta Part A Mol. Biomol. Spectrosc.*, **122**, p. 288–294, 2014.
- [85] J. Ollesch et al. Clinical application of infrared fibre-optic probes for the discrimination of colorectal cancer tissues and cancer grades, *Vib. Spectrosc.*, **91**, pp. 99–110, 2017.
- [86] Q.-B. Li et al. In vivo and in situ detection of colorectal cancer using Fourier transform infrared spectroscopy, *World J. Gastroenterol.*, **11**, 3, p. 327–30, 2005.
- [87] L. R. Drăgan et al. Fourier Transform Infrared (FT-IR) Spectroscopy and Proton Nuclear Magnetic Resonance ( $^1\text{H}$  NMR) Relaxometry and Diffusometry for the Identification of Colorectal Cancer in Blood Plasma, *Anal. Lett.*, **56**, 2, p. 286–302, 2023.
- [88] J. J. Villamanca et al., Predicting the Likelihood of Colorectal Cancer with Artificial Intelligence Tools Using Fourier Transform Infrared Signals Obtained from Tumor Samples, *Appl. Spectrosc.*, **76**, 12, p. 1412–1428, 2022.
- [89] J. Nallala et al. Characterization of colorectal mucus using infrared spectroscopy: a potential target for bowel cancer screening and diagnosis, *Lab. Investig.*, **100**, 8, p. 1102–1110, 2020.
- [90] S. Tiwari et al. Colon Cancer Grading Using Infrared Spectroscopic Imaging-Based Deep Learning, *Appl. Spectrosc.*, **76**, 4, p. 475–484, 2022.
- [91] D. Cameron et al. Detecting colorectal cancer using infrared spectroscopy, *Br. J. Surg.*, **109**, 4, p. e61–e62, 2022.
- [92] M. Khanmohammadi and A. B. Garmarudi, Infrared spectroscopy provides a green analytical chemistry tool for direct diagnosis of cancer, *TrAC Trends Anal. Chem.*, **30**, 6, p. 864–874, 2011.
- [93] X. Li et al. Identification of Colitis and Cancer in Colon Biopsies by Fourier Transform Infrared Spectroscopy and Chemometrics, *Sci. World J.*, **2012**, 936149, p. 1–4, 2012.
- [94] C. Hughes et al., SR-FTIR spectroscopy of renal epithelial carcinoma side population cells displaying stem cell-like characteristics, *Analyst*, **135**, 12, 3133, 2010.
- [95] V. Šablinskis et al. Infrared spectroscopic imaging of renal tumor tissue, *J. Biomed. Opt.*, **16**, 9, 096006, 2011.



- [96] V. Urboniene, et al. Identification of kidney tumor tissue by infrared spectroscopy of extracellular matrix, *J. Biomed. Opt.*, **19**, 8, 087005, 2014.
- [97] M. Pucetaite et al., Rapid intra-operative diagnosis of kidney cancer by attenuated total reflection infrared spectroscopy of tissue smears, *J. Biophotonics*, **11**, 5, e201700260, 2018.
- [98] R. Bandzeviciute et al. Fiber based infrared spectroscopy of cancer tissues, *J. Mol. Struct.*, **1220**, 128724, 2020.
- [99] V. Sablinskas et al. Fiber attenuated total reflection infrared spectroscopy of kidney tissue during live surgery, *J. Biophotonics*, **13**, 7, 2020.
- [100] C. Chen et al. A novel diagnostic method: FT-IR, Raman and derivative spectroscopy fusion technology for the rapid diagnosis of renal cell carcinoma serum, *Spectrochim. Acta Part A Mol. Biomol. Spectrosc.*, **269**, 120684, 2022.
- [101] W. Peng et al. Diagnosis of intraoperative hepatocellular carcinoma based on FTIR vibration spectroscopy using supervised machine learning, in *AOPC 2020: Optical Spectroscopy and Imaging; and Biomedical Optics*, 1156604, 2020.
- [102] Y. Yang et al. Study of tumor cell invasion by Fourier transform infrared microspectroscopy, *Biopolymers*, **78**, 6, p. 311–317, 2005.
- [103] K. Yano et al. Direct Measurement of Human Lung Cancerous and Noncancerous Tissues by Fourier Transform Infrared Microscopy: Can an Infrared Microscope Be Used as a Clinical Tool?, *Anal. Biochem.*, **287**, 2, p. 218–225, 2000.
- [104] H. P. Wang et al. Microscopic FTIR studies of lung cancer cells in pleural fluid, *Sci. Total Environ.*, **204**, 3, p. 283–287, 1997.
- [105] C. M. Krishna et al. FTIR and Raman microspectroscopy of normal, benign, and malignant formalin-fixed ovarian tissues, *Anal. Bioanal. Chem.*, **387**, 5, p. 1649–1656, 2007.
- [106] R. Mehrotra et al. Analysis of ovarian tumor pathology by Fourier Transform Infrared Spectroscopy, *J. Ovarian Res.*, **3**, 1, 27, 2010.
- [107] K. Al-Jorani et al. ATR-FTIR spectroscopy shows changes in ovarian cancer cells after incubation with novel organoamidoplatinum(ii) complexes, *Analyst*, **143**, 24, p. 6087–6094, 2018.

- [108] P. Giamougiannis et al. Detection of ovarian cancer ( $\pm$  neo-adjuvant chemotherapy effects) via ATR-FTIR spectroscopy: comparative analysis of blood and urine biofluids in a large patient cohort, *Anal. Bioanal. Chem.*, **413**, 20, p. 5095–5107, 2021.
- [109] J.-I. Chang et al. Characterization of human cervical precancerous tissue through the fourier transform infrared microscopy with mapping method, *Gynecol. Oncol.*, **91**, 3, p. 577–583, 2003.
- [110] S. Mark et al. Fourier transform infrared microspectroscopy as a quantitative diagnostic tool for assignment of premalignancy grading in cervical neoplasia, *J. Biomed. Opt.*, **9**, 3, 558, 2004.
- [111] A. Podshyvalov et al. Distinction of cervical cancer biopsies by use of infrared microspectroscopy and probabilistic neural networks, *Appl. Opt.*, **44**, 18, 3725, 2005.
- [112] E. Bogomolny et al. Monitoring of viral cancer progression using FTIR microscopy: A comparative study of intact cells and tissues, *Biochim. Biophys. Acta - Gen. Subj.*, **1780**, 9, p. 1038–1046, 2008.
- [113] S. G. El-Tawil et al. Comparative study between Pap smear cytology and FTIR spectroscopy: a new tool for screening for cervical cancer, *Pathology*, **40**, 6, p. 600–603, 2008.
- [114] M. S. Petrov et al. Usefulness of infrared spectroscopy in diagnosis of acute pancreatitis, *ANZ J. Surg.*, **77**, 5, p. 347–351, 2007.
- [115] V. Notarstefano et al. Investigation of human pancreatic cancer tissues by Fourier Transform Infrared Hyperspectral Imaging, *J. Biophotonics*, **13**, 4, 2020.
- [116] K. Szymoński et al. Spectroscopic screening of pancreatic cancer, *Clin. Spectrosc.*, **3**, 100016, 2021.
- [117] C. Teske et al., Label-free differentiation of human pancreatic cancer, pancreatitis, and normal pancreatic tissue by molecular spectroscopy, *J. Biomed. Opt.*, **27**, 7, 2022.
- [118] R. Bandzeviciute et al. Fiber-based ATR-IR spectroscopy for an intraoperative diagnosis of normal pancreatic tissue, pancreatitis, and malignant pancreatic lesions, in *Proc. SPIE 12368, Advanced Biomedical and Clinical Diagnostic and Surgical Guidance Systems XXI*, 2023.

- [119] M. J. German et al. Infrared Spectroscopy with Multivariate Analysis Potentially Facilitates the Segregation of Different Types of Prostate Cell, *Biophys. J.*, **90**, 10, p. 3783–3795, 2006.
- [120] M. J. Baker et al. FTIR-based spectroscopic analysis in the identification of clinically aggressive prostate cancer, *Br. J. Cancer*, **99**, 11, p. 1859–1866, 2008.
- [121] E. Gazi et al. A Correlation of FTIR Spectra Derived from Prostate Cancer Biopsies with Gleason Grade and Tumour Stage, *Eur. Urol.*, **50**, 4, p. 750–761, 2006.
- [122] D. K. R. Medipally et al. Vibrational spectroscopy of liquid biopsies for prostate cancer diagnosis, *Ther. Adv. Med. Oncol.*, **12**, 175883592091849, 2020.
- [123] M. A. Mackanos and C. H. Contag, FTIR microspectroscopy for improved prostate cancer diagnosis, *Trends Biotechnol.*, **27**, 12, p. 661–663, 2009.
- [124] G. Güler, et al. Characterization of CD133+/CD44+ human prostate cancer stem cells with ATR-FTIR spectroscopy, *Analyst*, **144**, 6, p. 2138–2149, 2019.
- [125] P. T. Wong et al. Distinct infrared spectroscopic patterns of human basal cell carcinoma of the skin., *Cancer Res.*, **53**, 4, p. 762–5, 1993.
- [126] D. R. Bortoletto et al. Vibrational spectra calculation of squamous cell carcinoma in the amide band region, *Vib. Spectrosc.*, **97**, p. 135–139, 2018.
- [127] Z. Hammody et al. Characterization of Malignant Melanoma Using Vibrational Spectroscopy, *Sci. World J.*, **5**, p. 173–182, 2005.
- [128] F. Peñaranda et al. Discrimination of skin cancer cells using Fourier transform infrared spectroscopy, *Comput. Biol. Med.*, **100**, p. 50–61, 2018.
- [129] Z. Hammody, et al. Distinction of malignant melanoma and epidermis using IR micro-spectroscopy and statistical methods, *Analyst*, **133**, 3, 372, 2008.
- [130] A. Tfayli et al. Discriminating nevus and melanoma on paraffin-embedded skin biopsies using FTIR microspectroscopy, *Biochim. Biophys. Acta - Gen. Subj.*, **1724**, 3, p. 262–269, 2005.

- [131] A. Zwielly et al. Discrimination between drug-resistant and non-resistant human melanoma cell lines by FTIR spectroscopy, *Analyt.*, **134**, 2, p. 294–300, 2009.
- [132] R. Minnes et al. Using Attenuated Total Reflection–Fourier Transform Infra-Red (ATR-FTIR) spectroscopy to distinguish between melanoma cells with a different metastatic potential, *Sci. Rep.*, **7**, 1, 4381, 2017.
- [133] H. Ghimire et al. ATR-FTIR spectral discrimination between normal and tumorous mouse models of lymphoma and melanoma from serum samples, *Sci. Rep.*, **7**, 1, 16993, 2017.
- [134] B. R. Shakya et al. Discrimination of melanoma cell lines with Fourier Transform Infrared (FTIR) spectroscopy, *Spectrochim. Acta Part A Mol. Biomol. Spectrosc.*, **254**, 119665, 2021
- [135] M. Kyriakidou et al. FT-IR Spectroscopy Study in Early Diagnosis of Skin Cancer, *In Vivo (Brooklyn)*., **31**, 6, p. 1131-1137, 2017
- [136] N. Wald et al. Infrared spectra of primary melanomas can predict response to chemotherapy: The example of dacarbazine, *Biochim. Biophys. Acta - Mol. Basis Dis.*, **1862**, 2, p. 174–181, 2016.
- [137] A. Zwielly et al. Grading of intrinsic and acquired cisplatin-resistant human melanoma cell lines: an infrared ATR study, *Eur. Biophys. J.*, **40**, 6, p. 795–804, 2011.
- [138] H. Ukkonen et al. Changes in the microenvironment of invading melanoma and carcinoma cells identified by FTIR imaging, *Vib. Spectrosc.*, **79**, p. 24–30, 2015.
- [139] N. Wald et al. Identification of melanoma cells and lymphocyte subpopulations in lymph node metastases by FTIR imaging histopathology, *Biochim. Biophys. Acta - Mol. Basis Dis.*, **1862**, 2, p. 202–212, 2016.
- [140] N. Wald and E. Goormaghtigh, Infrared imaging of primary melanomas reveals hints of regional and distant metastases, *Analyt.*, **140**, 7, p. 2144–2155, 2015.
- [141] E. Ly et al. Histopathological characterization of primary cutaneous melanoma using infrared microimaging: a proof-of-concept study, *Br. J. Dermatol.*, **162**, 6, p. 1316–1323, 2010.
- [142] E. Giorgini et al. FTIR microspectroscopic characterization of Spitz nevi, *Spectrochim. Acta Part A Mol. Biomol. Spectrosc.*, **141**, p. 99–103, 2015.

- [143] G. Tosi et al. FTIR microspectroscopy of melanocytic skin lesions: a preliminary study, *Analyst*, **135**, 12, 3213, 2010.
- [144] C. Pezzeri et al. Fourier transform infrared imaging analysis in discrimination studies of bladder cancer, *Analyst*, **138**, 19, 5719, 2013.
- [145] M. Stefanakis et al. The Impact of Tissue Preparation on Salivary Gland Tumors Investigated by Fourier-Transform Infrared Microspectroscopy, *J. Clin. Med.*, **12**, 2, 569, 2023.
- [146] V. Zohdi et al. Importance of Tissue Preparation Methods in FTIR Micro-Spectroscopical Analysis of Biological Tissues: ‘Traps for New Users,’ *PLoS One*, **10**, 2, e0116491, 2015.
- [147] E. Ly et al. Combination of FTIR spectral imaging and chemometrics for tumour detection from paraffin-embedded biopsies, *Analyst*, **133**, 2, p. 197–205, 2008.
- [148] B. Bird et al. Detection of breast micro-metastases in axillary lymph nodes by infrared micro-spectral imaging, *Analyst*, **134**, 6, p. 1067, 2009.
- [149] M. J. Pilling et al. Infrared spectral histopathology using haematoxylin and eosin (H&E) stained glass slides: a major step forward towards clinical translation, *Analyst*, **142**, 8, p. 1258–1268, 2017.
- [150] G. Tao et al. Infrared fibers, *Adv. Opt. Photonics*, **7**, 2, 379, 2015.
- [151] N. S. Kapany and R. J. Simms, Recent developments in infrared fiber optics, *Infrared Phys.*, **5**, 2, p. 69–80, 1965.
- [152] J. A. Harrington, *Infrared Fibers and Their Applications*. SPIE, 2004.
- [153] M. M. Rad, H. Eren, and M. Maier, Optical Loss: Principles and Applications, in *The Measurement Instrumentation and Sensors Handbook*, 2nd ed., J. G. Webster and H. Eren, Eds. 2014, p. 53.
- [154] H. M. Heise, S. Delbeck, and L. Kupper, Recent Advances in Sensor Developments Based on Silver Halide Fibers for Mid-Infrared Spectrometric Analysis, in *Molecular and Laser Spectroscopy*, V. P. Gupta, Ed. Elsevier Inc., 2018, pp. 39–63.
- [155] R. Gautam et al. Review of multidimensional data processing approaches for Raman and infrared spectroscopy, *EPJ Tech. Instrum.*, **2**, 1, 8, 2015.

- [156] R. Trevethan, Sensitivity, Specificity, and Predictive Values: Foundations, Pliabilities, and Pitfalls in Research and Practice, *Front. Public Heal.*, **5**, 307, 2017.
- [157] A. G. Lalkhen, A. McCluskey. Clinical tests: sensitivity and specificity, *Continuing Education in Anaesthesia Critical Care & Pain*, **8**, 6, p. 221–223, 2008.
- [158] A. C. S. Talari et al. Advances in Fourier transform infrared (FTIR) spectroscopy of biological tissues, *Appl. Spectrosc. Rev.*, **52**, 5, p. 456–506, 2017.
- [159] T. Vestonas, Anatomijos atlasas. Vilnius: Gamta, 1997.
- [160] Z. Tian and M. Liang. Renal metabolism and hypertension, *Nat. Commun.*, **12**, 1, 963, 2021.
- [161] H. M. Wadei and S. C. Textor, The role of the kidney in regulating arterial blood pressure, *Nat. Rev. Nephrol.*, **8**, 10, p. 602–609, 2012.
- [162] “Kidney cancer statistics.” <https://www.wcrf.org/cancer-trends/kidney-cancer-statistics/> (accessed Feb. 20, 2023)
- [163] H. Moch et al. The 2016 WHO Classification of Tumours of the Urinary System and Male Genital Organs—Part A: Renal, Penile, and Testicular Tumours, *Eur. Urol.*, **70**, 1, p. 93–105, 2016.
- [164] J. J. Hsieh et al. Renal cell carcinoma, *Nat. Rev. Dis. Prim.*, **3**, 1, 17009, 2017.
- [165] V. F. Muglia and A. Prando. Renal cell carcinoma: histological classification and correlation with imaging findings., *Radiol. Bras.*, **48**, 3, p. 166–74, 2015.
- [166] I. J. Frew and H. Moch, A Clearer View of the Molecular Complexity of Clear Cell Renal Cell Carcinoma, *Annu. Rev. Pathol. Mech. Dis.*, **10**, 1, p. 263–289, 2015.
- [167] Y.-L. Chen et al. No safe renal warm ischemia time—The molecular network characteristics and pathological features of mild to severe ischemia reperfusion kidney injury, *Front. Mol. Biosci.*, **9**, 1006917, 2022.
- [168] R. H. Thompson et al. Every Minute Counts When the Renal Hilum Is Clamped During Partial Nephrectomy, *Eur. Urol.*, **58**, 3, p. 340–345, 2010.

- [169] T. J. Guzzo et al. Intraoperative Molecular Diagnostic Imaging Can Identify Renal Cell Carcinoma, *J. Urol.*, **195**, 3, p. 748–755, 2016.
- [170] S. Tobis et al. Near Infrared Fluorescence Imaging After Intravenous Indocyanine Green: Initial Clinical Experience With Open Partial Nephrectomy for Renal Cortical Tumors, *Urology*, **79**, 4, p. 958–964, 2012.
- [171] L. S. Krane et al. Is Near Infrared Fluorescence Imaging Using Indocyanine Green Dye Useful in Robotic Partial Nephrectomy: A Prospective Comparative Study of 94 Patients, *Urology*, **80**, 1, p. 110–118, 2012.
- [172] Y.-K. Yang et al. Clinical Benefits of Indocyanine Green Fluorescence in Robot-Assisted Partial Nephrectomy, *Cancers (Basel)*, **14**, 12, 3032, 2022.
- [173] P. Bannasch, Sequential cellular changes during chemical carcinogenesis, *J. Cancer Res. Clin. Oncol.*, **108**, 1, p. 11–22, 1984.
- [174] H. Xie et al. Glycogen metabolism is dispensable for tumour progression in clear cell renal cell carcinoma, *Nat. Metab.*, **3**, 3, p. 327–336, 2021.
- [175] A. Soltysova et al. Deregulation of energetic metabolism in the clear cell renal cell carcinoma: A multiple pathway analysis based on microarray profiling, *Int. J. Oncol.*, **47**, 1, p. 287–295, 2015.
- [176] Y. Xiao and D. Meierhofer, Glutathione Metabolism in Renal Cell Carcinoma Progression and Implications for Therapies, *Int. J. Mol. Sci.*, **20**, 15, 3672, 2019.
- [177] K. Saginala et al. Epidemiology of Bladder Cancer, *Med. Sci.*, **8**, 1, 15, 2020.
- [178] K. C. DeGeorge, H. R. Holt, and S. C. Hodges, “Bladder Cancer: Diagnosis and Treatment,” 96, 8, 2017. Accessed: Sep. 21, 2022. [Online]. Available: [www.aafp.org/afp](http://www.aafp.org/afp).
- [179] M. Miyake et al. Exploration of risk factors predicting outcomes for primary T1 high-grade bladder cancer and validation of the Spanish Urological Club for Oncological Treatment scoring model: Long-term follow-up experience at a single institute, *Int. J. Urol.*, **22**, 6, p. 541–547, 2015.
- [180] R. J. Sylvester et al. Predicting Recurrence and Progression in Individual Patients with Stage Ta T1 Bladder Cancer Using EORTC Risk Tables: A

Combined Analysis of 2596 Patients from Seven EORTC Trials, *Eur. Urol.*, **49**, 3, p. 466–477, 2006.

[181] G. I. Russo et al., Performance of Narrow Band Imaging (NBI) and Photodynamic Diagnosis (PDD) Fluorescence Imaging Compared to White Light Cystoscopy (WLC) in Detecting Non-Muscle Invasive Bladder Cancer: A Systematic Review and Lesion-Level Diagnostic Meta-Analysis, *Cancers (Basel)*, **13**, 17, 4378, 2021.

[182] G. Mowatt et al. Photodynamic diagnosis of bladder cancer compared with white light cystoscopy: Systematic review and meta-analysis, *Int. J. Technol. Assess. Health Care*, **27**, 1, p. 3–10, 2011.

[183] K. Stevenson et al. Functional changes in bladder tissue from type III collagen-deficient mice, *Mol. Cell. Biochem.*, **283**, 1–2, p. 107–114, 2006.

[184] D. C. Whitcomb and M. E. Lowe, Human Pancreatic Digestive Enzymes, *Dig. Dis. Sci.*, **52**, 1, p. 1–17, 2007.

[185] S. J. Pandol, Normal Pancreatic Function, *Pancreapedia: Exocrine Pancreas Knowledge Base*, 2015.

[186] T. L. Mastracci and L. Sussel, The endocrine pancreas: insights into development, differentiation, and diabetes, *Wiley Interdiscip. Rev. Dev. Biol.*, **1**, 5, p. 609–628, 2012.

[187] S. Wang et al. The molecular biology of pancreatic adenocarcinoma: translational challenges and clinical perspectives, *Signal Transduct. Target. Ther.*, **6**, 1, 249, 2021.

[188] J. Kleeff et al. Pancreatic cancer, *Nat. Rev. Dis. Prim.*, **2**, 1, 16022, 2016.

[189] P. Rawla et al. Epidemiology of Pancreatic Cancer: Global Trends, Etiology and Risk Factors, *World J. Oncol.*, **10**, 1, 10, 2019.

[190] C. L. Wolfgang et al. Recent Progress in Pancreatic Cancer, *CA. Cancer J. Clin.*, **63**, 5, 318, 2013.

[191] A. M. Schlitter and I. Esposito. Definition of Microscopic Tumor Clearance (R0) in Pancreatic Cancer Resections, *Cancers*, **2**, 4, p. 2001–2010, 2010.

[192] C. Teske et al. Impact of resection margin status on survival in advanced N stage pancreatic cancer – a multi-institutional analysis, *Langenbecks Arch Surg.*, **406**, 5, p. 1481–1489, 2021.



- [193] P. L. Labib et al. 5-Aminolevulinic acid for fluorescence-guided surgery in pancreatic cancer: Cellular transport and fluorescence quantification studies, *Transl. Oncol.*, **14**, 1, 2021.
- [194] K. Orth, et al. Fluorescence detection of small gastrointestinal tumours: principles, technique, first clinical experience, *Langenbeck's Arch. Surg.*, **385**, 7, p. 488–494, 2000.
- [195] T. Zöpf et al. Improved preoperative tumor staging by 5-aminolevulinic acid induced fluorescence laparoscopy, *Gastrointest. Endosc.*, **62**, 5, p. 763–767, 2005.
- [196] Y. Yonemura. Selection of Patients by Membrane Transporter Expressions for Aminolevulinic Acid (ALA)-Guided Photodynamic Detection of Peritoneal Metastases, *Int. J. Sci.*, **1**, 9, p. 66–77, 2015.
- [197] K. Harada et al. Photodynamic diagnosis of peritoneal metastasis in human pancreatic cancer using 5-aminolevulinic acid during staging laparoscopy, *Oncol. Lett.*, **16**, 1, p. 821-828, 2018.
- [198] S. Hyun and D. Park. Challenges in genomic analysis of model systems and primary tumors of pancreatic ductal adenocarcinoma, *Comput. Struct. Biotechnol. J.*, **20**, p. 4806–4815, 2022.
- [199] Y. Masugi, The Desmoplastic Stroma of Pancreatic Cancer: Multilayered Levels of Heterogeneity, Clinical Significance, and Therapeutic Opportunities, *Cancers*, **14**, 13, 3293, 2022.
- [200] D. Öhlund, et al. Type IV collagen stimulates pancreatic cancer cell proliferation, migration, and inhibits apoptosis through an autocrine loop, *BMC Cancer*, **13**, 1, 154, 2013.
- [201] G. Klöppel et al. Fibrosis of the pancreas: The initial tissue damage and the resulting pattern, *Virchows Arch.*, **445**, 1, 1–8, 2004.
- [202] T. A. Wynn. Cellular and molecular mechanisms of fibrosis, *J. Pathol.*, **214**, 2, p. 199–210, 2008.
- [203] A. Kalra, E. Yetiskul, C. J. Wehrle, and F. Tuma, Physiology, Liver. StatPearls Publishing LLC, 2022. Accessed: Jan. 16, 2023. [Online]. Available: <https://www.ncbi.nlm.nih.gov/books/NBK535438/>.
- [204] D. P. Bogdanos, B. Gao, and M. E. Gershwin, “Liver Immunology,” in *Comprehensive Physiology*, Wiley, 2013, p. 567–598.

- [205] J. M. Llovet et al. Hepatocellular carcinoma, *Nat. Rev. Dis. Prim.*, **7**, 6, 2021.
- [206] A. J. Craig et al. Tumour evolution in hepatocellular carcinoma, *Nat. Rev. Gastroenterol. Hepatol.*, **17**, 3, p. 139–152, 2020.
- [207] E. Gigante et al. New insights into the pathophysiology and clinical care of rare primary liver cancers, *JHEP Reports*, **3**, 1, 100174, 2021.
- [208] B. Blechacz. Cholangiocarcinoma: Current Knowledge and New Developments, *Gut Liver*, **11**, 1, p. 13–26, 2017.
- [209] S. J. Patacsil et al. A Review of Benign Hepatic Tumors and Their Imaging Characteristics, *Cureus*, **12**, 1, e6813, 2020.
- [210] K. J. Oldhafer, et al. Benign Liver Tumors, *Visc. Med.*, **36**, 4, p. 292–303, 2020.
- [211] J. Watson et al. Primary and secondary liver tumours, *InnovAiT Educ. Inspir. Gen. Pract.*, **9**, 8, p. 477–482, 2016.
- [212] D. I. Tsilimigras et al. Liver metastases, *Nat. Rev. Dis. Prim.*, **7**, 1, 27, 2021.
- [213] H. Petrowsky et al. Modern therapeutic approaches for the treatment of malignant liver tumours, *Nat. Rev. Gastroenterol. Hepatol.*, **17**, 12, p. 755–772, 2020.
- [214] M. E. Pittman and R. K. Yantiss. Frozen Sections of the Liver, *Surg. Pathol. Clin.*, **11**, 2, p. 453–466, 2018.
- [215] T. Wakabayashi et al. Indocyanine Green Fluorescence Navigation in Liver Surgery, *Ann. Surg.*, **275**, 6, p. 1025–1034, 2022.
- [216] M. Bollen et al. Specific features of glycogen metabolism in the liver, *Biochem. J.*, **336**, **1**, p. 19–31, 1998.
- [217] P. J. Klover and R. A. Mooney, Hepatocytes: critical for glucose homeostasis, *Int. J. Biochem. Cell Biol.*, **36**, 5, p. 753–758, 2004.
- [218] Q. Liu et al. Glycogen accumulation and phase separation drives liver tumor initiation, *Cell*, **184**, 22, p. 5559–5576.e19, 2021.
- [219] A. Gentilini, et al. The Role of Stroma in Cholangiocarcinoma: The Intriguing Interplay between Fibroblastic Component, Immune Cell Subsets and Tumor Epithelium, *Int. J. Mol. Sci.*, **19**, 10, 2885, 2018.

- [220] N. Guedj et al. Prognostic value of desmoplastic stroma in intrahepatic cholangiocarcinoma, *Mod. Pathol.*, **34**, 2, p. 408–416, 2021.
- [221] A. E. Sirica and G. J. Gores. Desmoplastic stroma and cholangiocarcinoma: Clinical implications and therapeutic targeting, *Hepatology*, **59**, 6, p. 2397–2402, 2014.
- [222] A. A. Christy and P. K. Egeberg. Quantitative determination of saturated and unsaturated fatty acids in edible oils by infrared spectroscopy and chemometrics, *Chemom. Intell. Lab. Syst.*, **82**, 1-2, p. 130–136, 2006.
- [223] Matwiczuk et al. Use of FTIR Spectroscopy and Chemometrics with Respect to Storage Conditions of Moldavian Dragonhead Oil, *Sustainability*, **11**, 22, 6414, 2019.

# APPENDIX

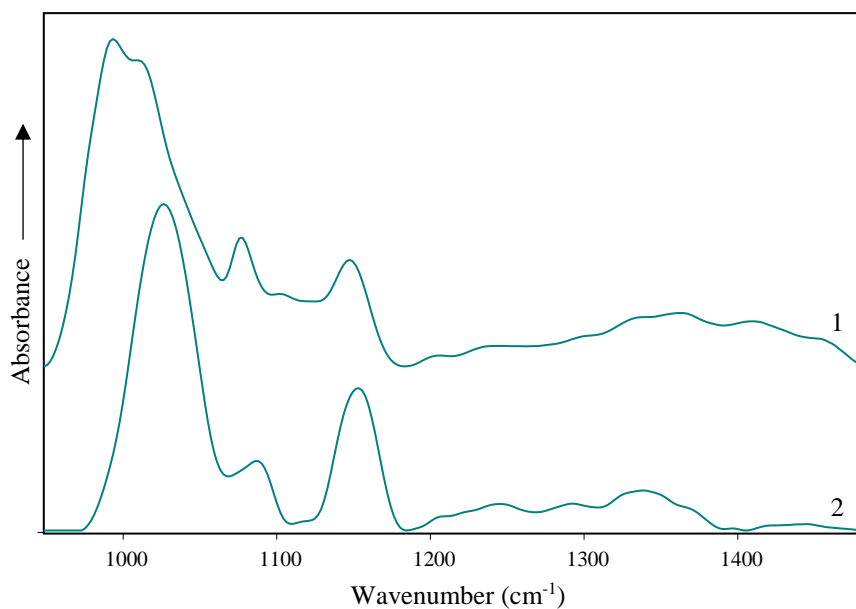


**Figure A-01.** ATR IR spectra of 0.01 M glycogen solution: dried (1), in water (2). Positions of main spectral bands are different for dried substance and water solution. Differences could be caused by solvation, intermolecular bonding for solution and crystallisation for dried substance.

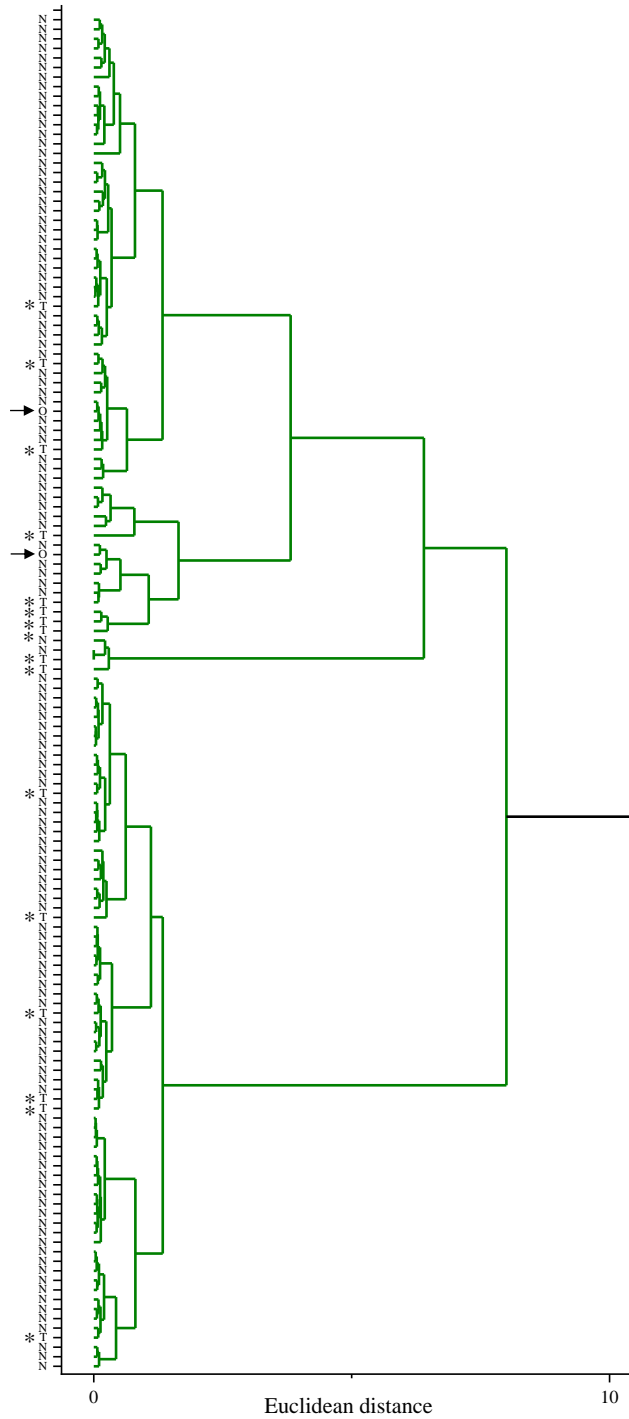


**Figure A-02.** Enlarged cluster of non-tumorous kidney tissue smears of HCA dendrogram. Letters N, T and O represent spectra of each non-tumorous, tumorous and other types of kidney tissues respectively. \* symbol indicates tumorous tissue smear spectra which were assigned to normal tissue class; arrows indicate other types (Table 3.1) of pathological kidney tissue.

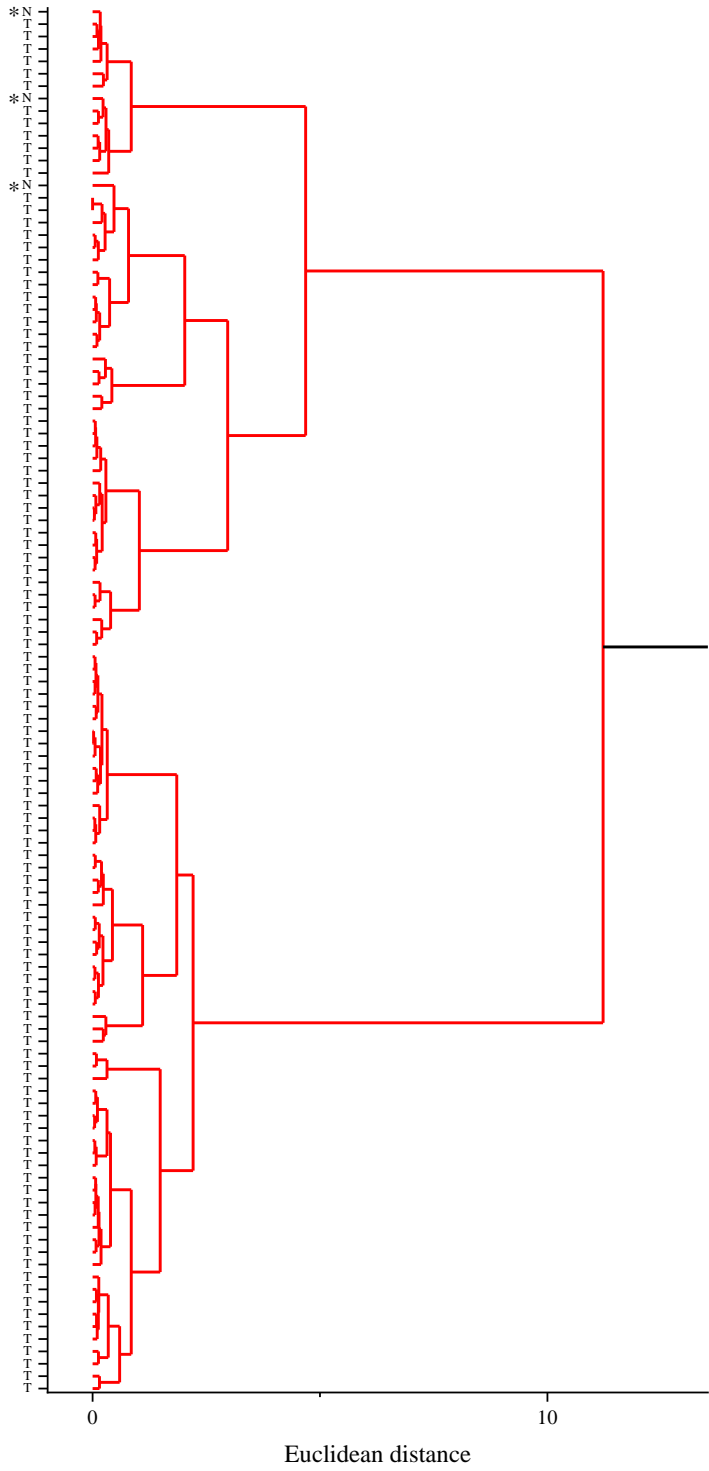


**Figure A-03.** Enlarged cluster of tumorous kidney tissue smears of HCA dendrogram. Letters N and T represent spectra of each non-tumorous and tumorous kidney tissues respectively. \* symbol indicates tumorous tissue smear spectra which were assigned to normal tissue class.

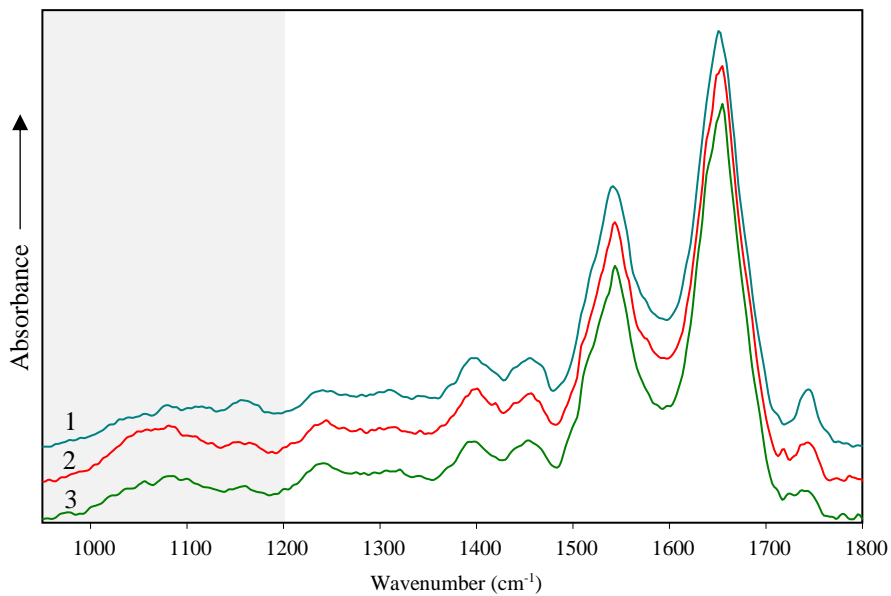


**Figure A-04.** ATR IR spectra of normal kidney tissue smears which were assigned to tumorous tissue cluster after application of HCA analysis. Grey area corresponds to the spectral region for which HCA analysis was performed.



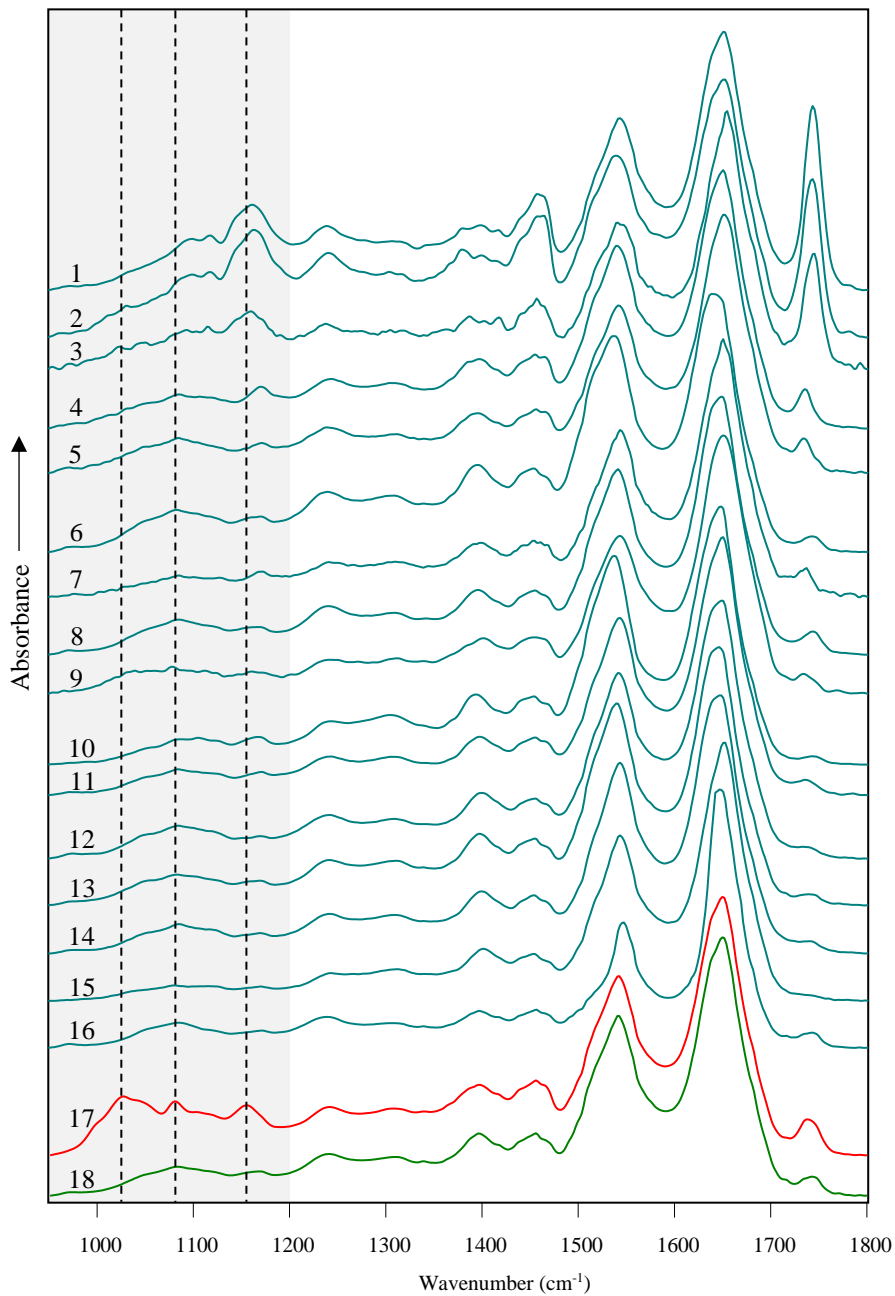


**Figure A-05.** ATR IR spectra of tumorous kidney tissue smears (1-16) assigned to normal tissue cluster after application of HCA analysis, mean spectrum of tumorous kidney tissue smear (17) and mean spectrum of normal kidney tissue smear (18). Grey area corresponds to the spectral region for which HCA analysis was performed.

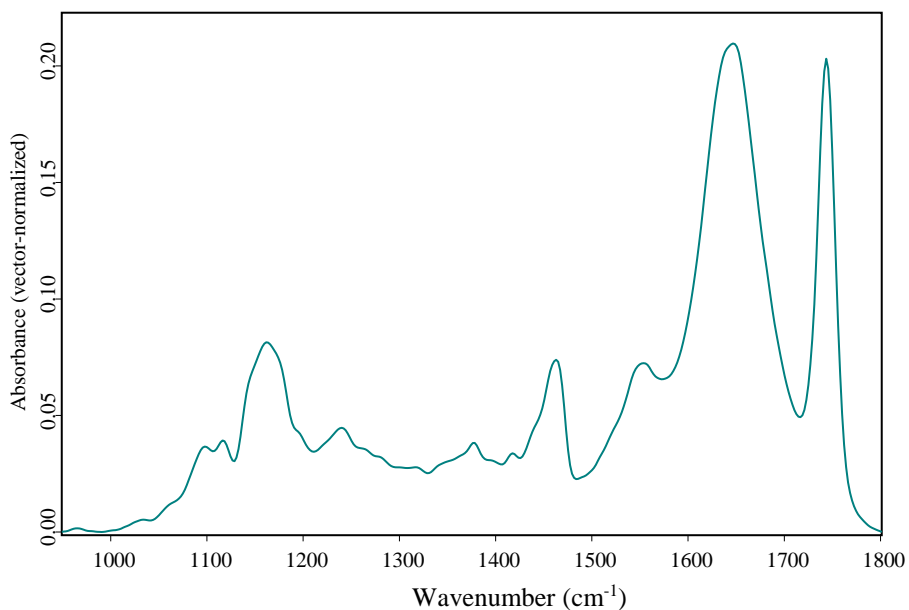


**Figure A-06.** ATR IR spectrum of adipose tissue. Spectrum is baseline corrected and vector-normalized.

**Table A-1.** Main positions and assignments of spectral bands assigned to fats of adipose tissue. Assignments set according to [222], [223]

Spectral band position, cm <sup>-1</sup>	Assignment
1097	$\nu(-C-O)$
1116	$\nu(-C-O)$
1162	$\nu(-C-O)$
1239	$\nu(-C-O), \delta(-CH_2)$
1377	$\nu(-CH), \delta(-CH_3)$
1463	$\delta(-CH)$
1743	$\nu(-C=O)$

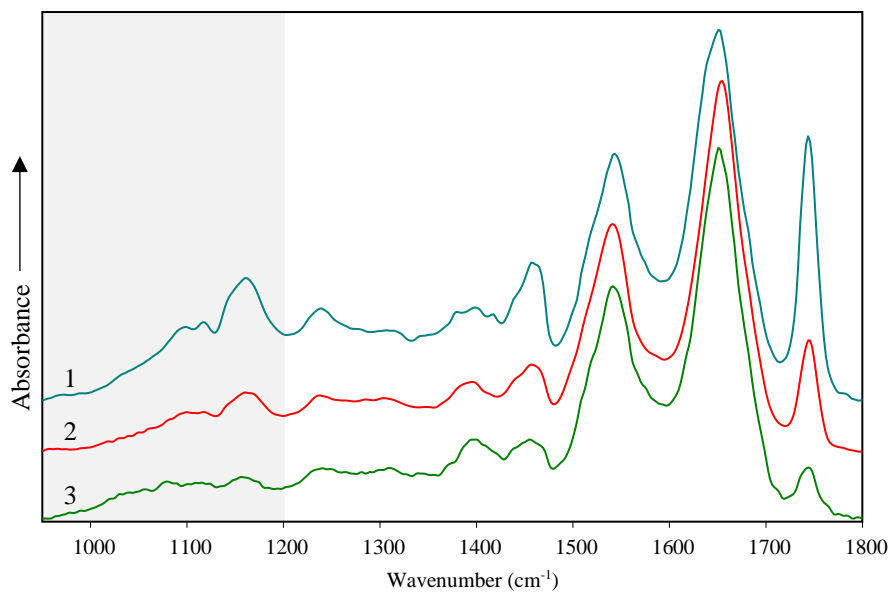


**Figure A-07.** ATR IR spectra of normal kidney tissue smears which were assigned to tumorous tissue cluster after application of PCA analysis. Grey area corresponds to the spectral region for which PCA analysis was performed.

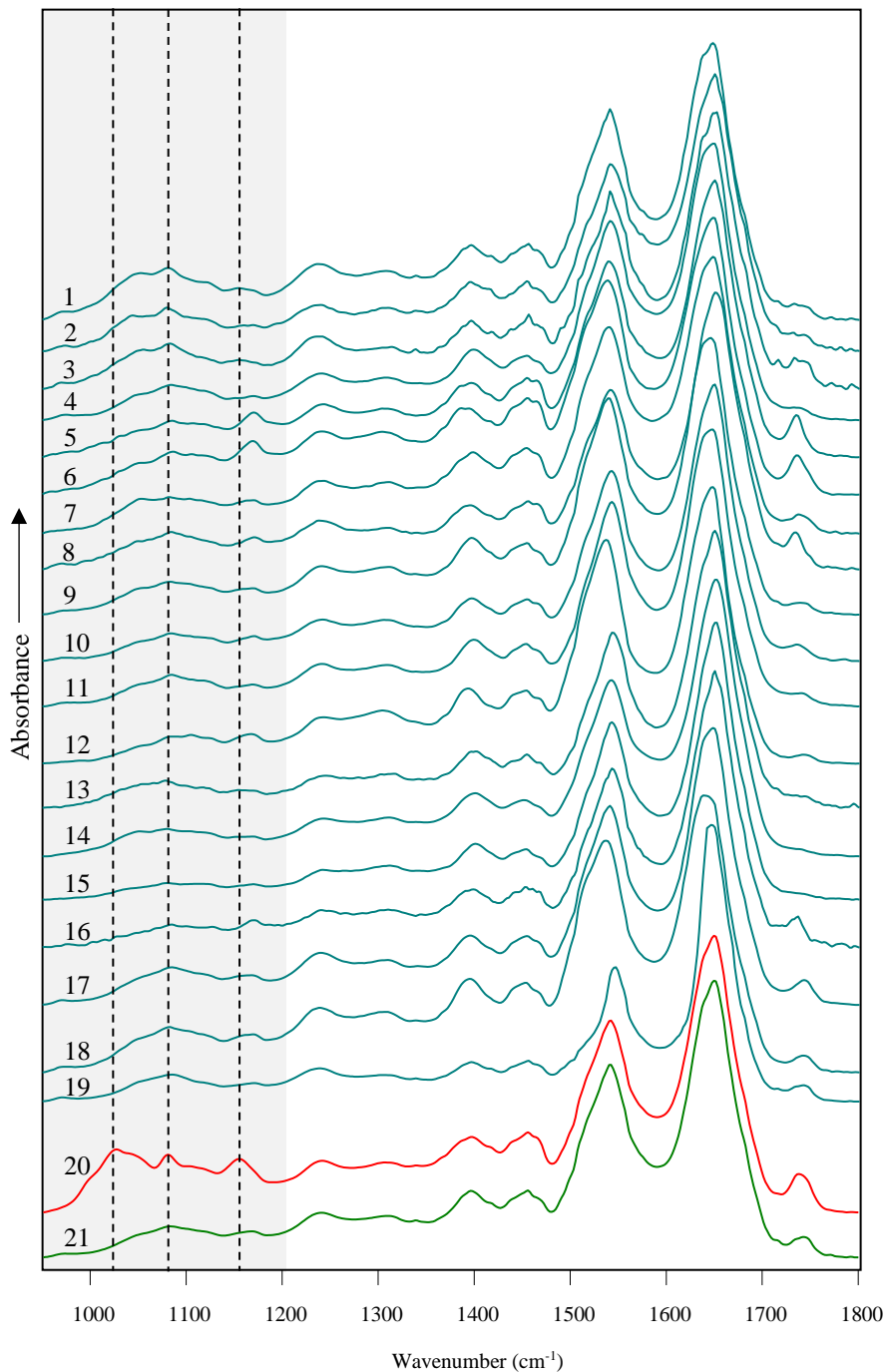


**Figure A-08.** ATR IR spectra of tumorous kidney tissue smears (1-19) assigned to normal tissue cluster after application of PCA analysis, mean spectrum of tumorous kidney tissue smear (20) and mean spectrum of normal kidney tissue smear (21). Grey area corresponds to the spectral region for which PCA analysis was performed. Dashed lines indicate spectral bands assigned to glycogen.

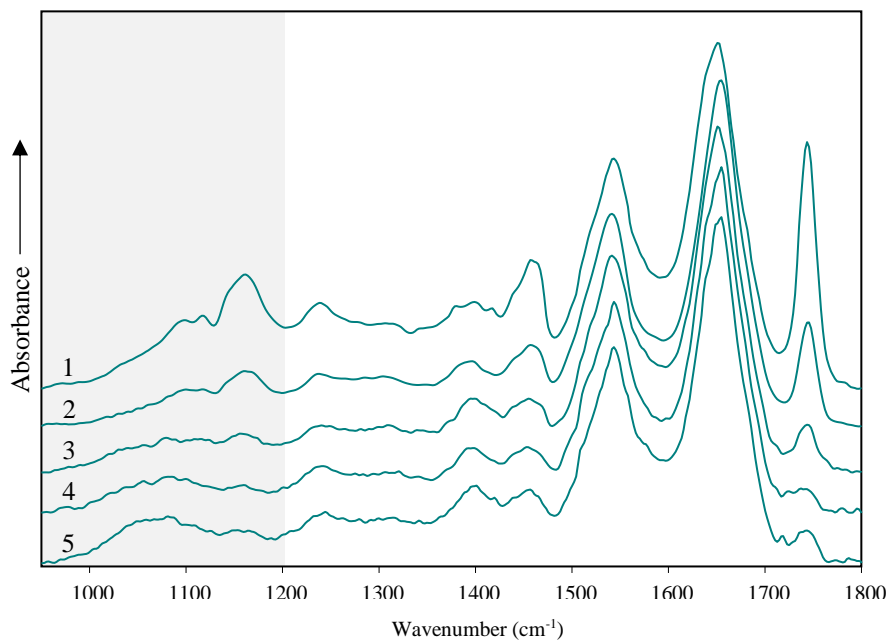


**Figure A-09.** ATR IR spectra of normal kidney tissue smears assigned as tumorous tissue after application of developed model for automated tissue identification. Grey area corresponds to the spectral region for which analysis was performed.

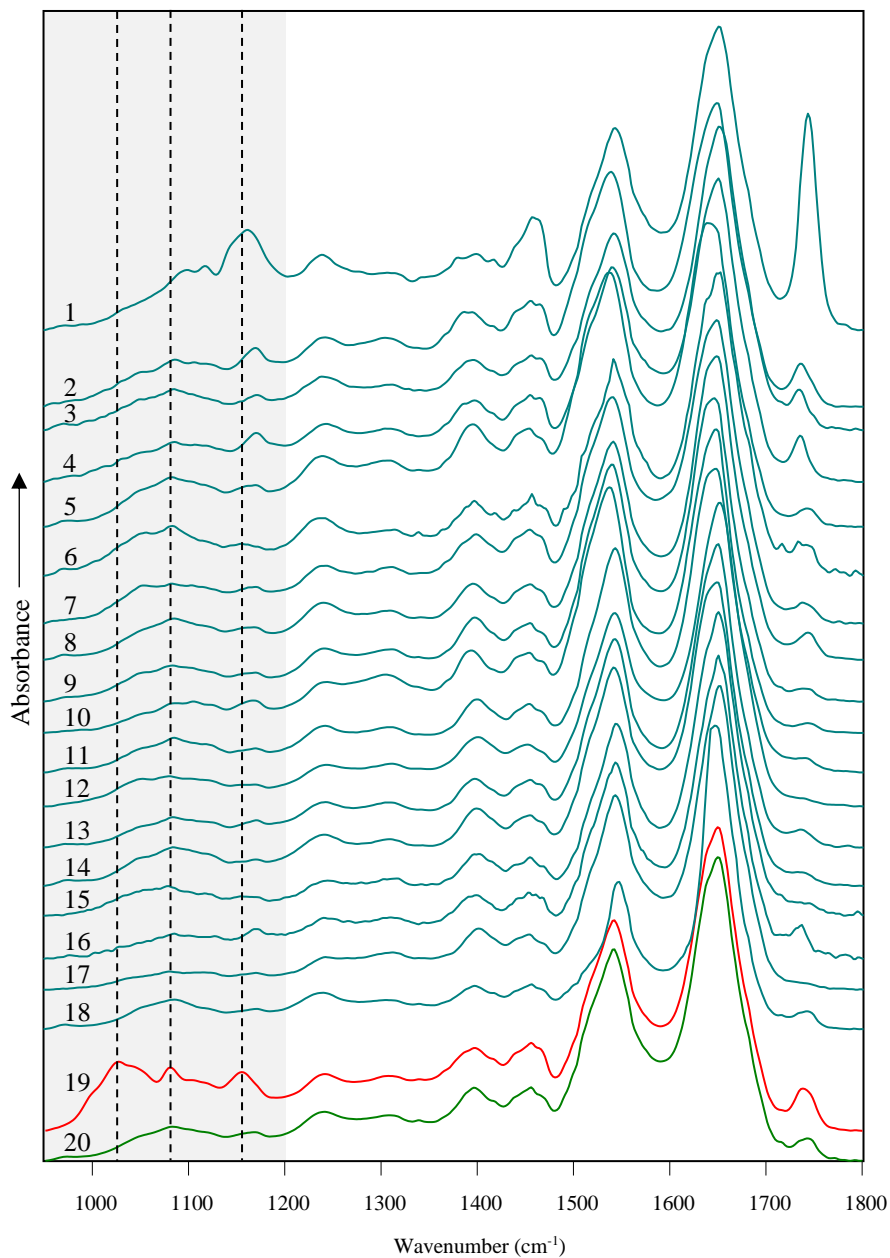


**Figure A-10.** ATR IR spectra of tumorous kidney tissue smears (1-18) assigned as normal tissue after application of developed model for automated tissue identification, mean spectra of tumorous (19) and normal (20) tissue smears. Grey area corresponds to the spectral region for which analysis was performed. Dashed lines indicate spectral bands assigned to glycogen.

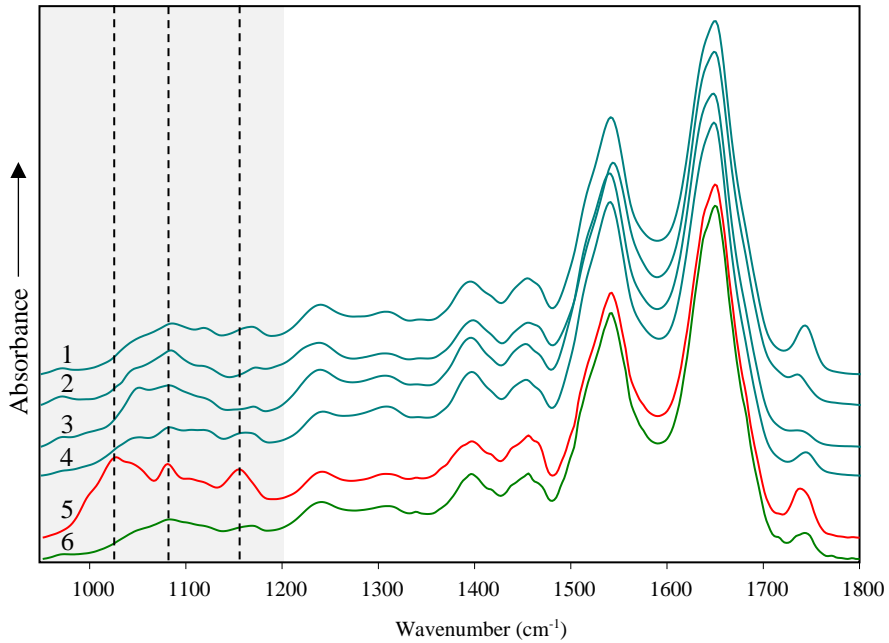


**Figure A-11.** ATR IR spectra of tumorous kidney tissue smears (1-4) assigned as normal tissue after application of HCA analysis, mean spectra of tumorous (5) and normal (6) tissue smears. Grey area corresponds to the spectral region for which HCA analysis was performed. Dashed lines indicate spectral bands assigned to glycogen.

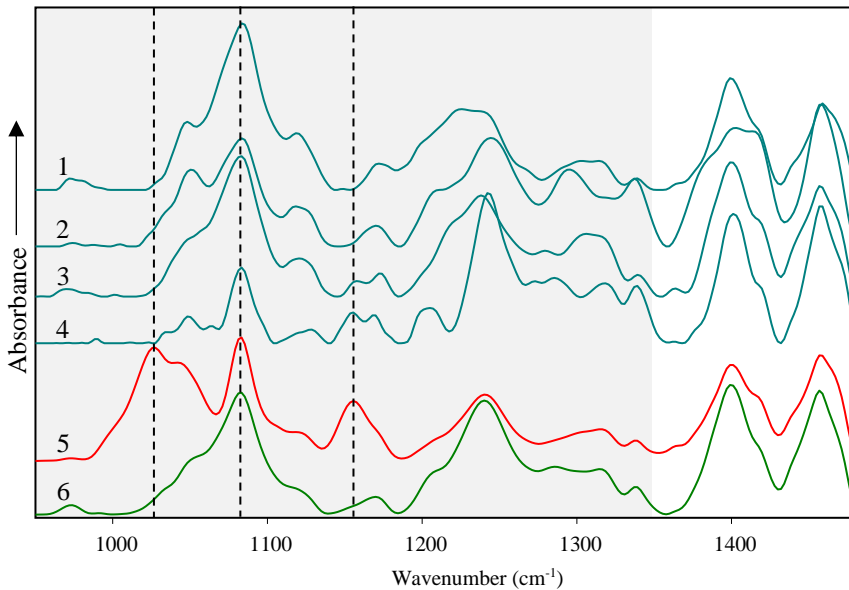


**Figure A-12.** ATR IR spectra of tumorous kidney tissue (1-4) assigned as normal tissue after application of HCA analysis, mean spectra of tumorous (5) and normal (6) tissues. Grey area corresponds to the spectral region for which HCA analysis was performed. Dashed lines indicate spectral bands assigned to glycogen.

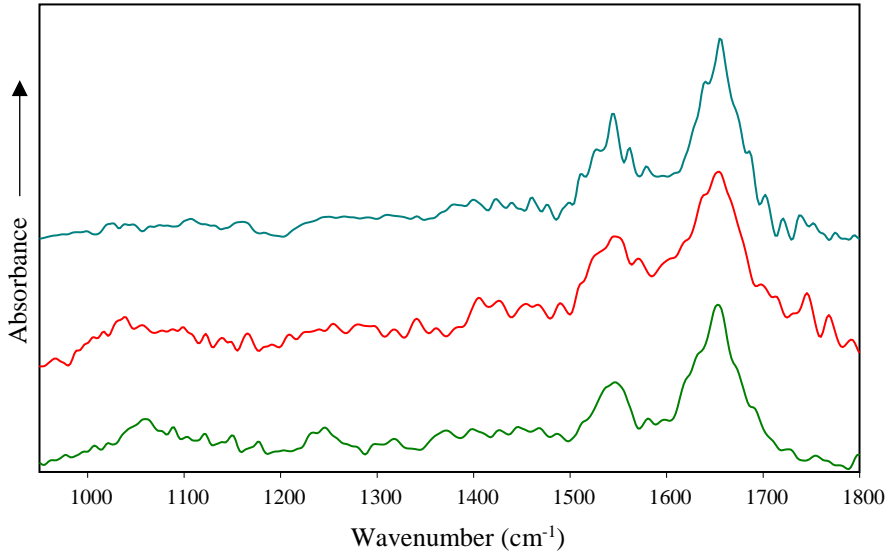


**Figure A-13.** ATR IR spectra of bladder tissue smears of insufficient quality for spectral analysis.

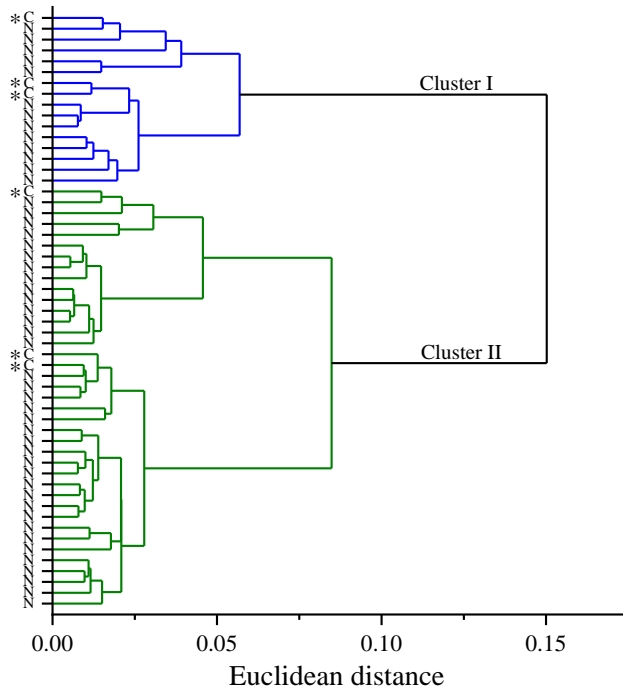


**Figure A-14.** HCA dendrogram of normal bladder and cystitis tissues. Letters N and C represent spectra of each normal and cystitis tissues respectively. \* symbol indicates spectra of cystitis for better visualization.



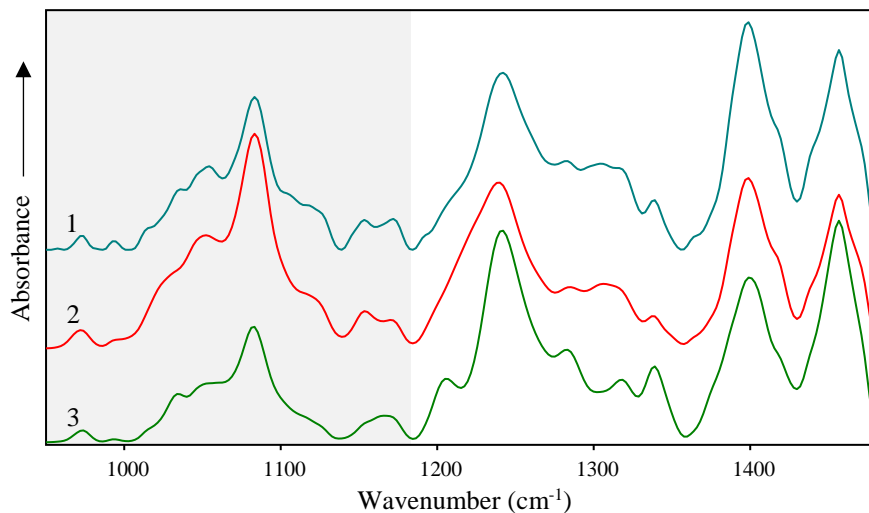


**Figure A-15.** ATR IR spectrum of normal bladder tissue (1) assigned to tumorous tissue cluster after application of HCA analysis, mean spectrum of tumorous urothelial carcinoma tissue (2) and mean spectrum of normal bladder tissue (3). Grey area corresponds to the spectral region for which HCA analysis was performed.

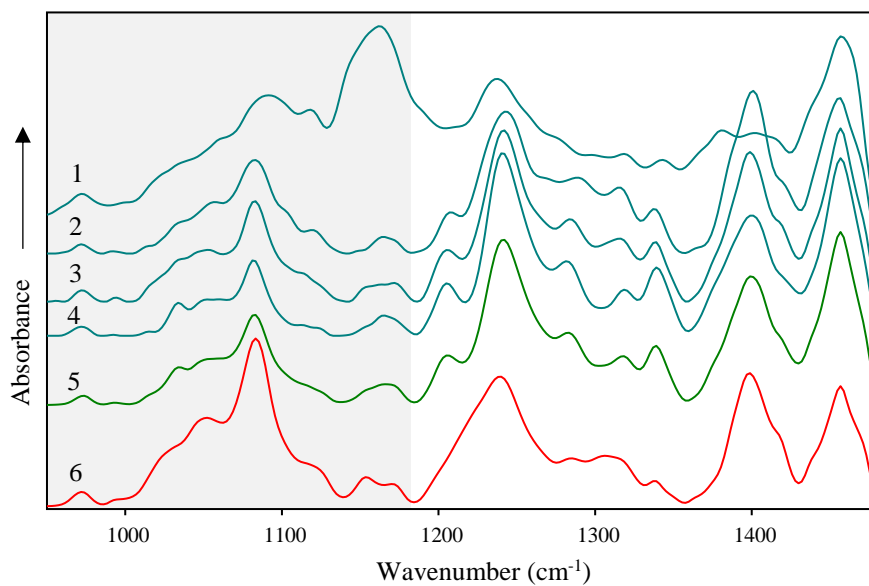


**Figure A-16.** ATR IR spectra of tumorous bladder tissue (1-4) assigned to normal tissue cluster after application of HCA and PCA analysis, mean spectrum of normal bladder tissue (5) and mean spectrum of urothelial carcinoma tissue (6). Grey area corresponds to the spectral region for which HCA analysis was performed. PCA analysis was performed in the whole shown spectral region (950 - 1480  $\text{cm}^{-1}$ ).

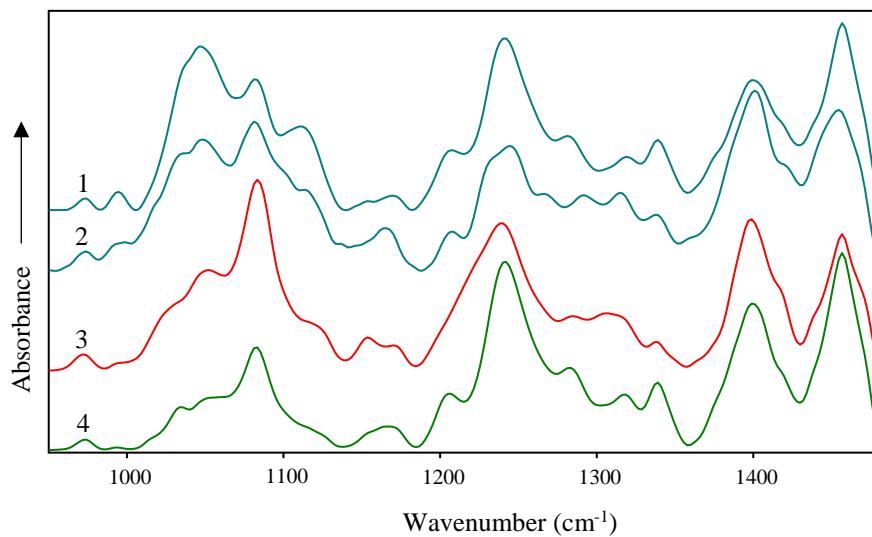


**Figure A-17.** ATR IR spectra of normal bladder tissue (1-2) assigned to tumorous tissue cluster after application of PCA analysis, mean spectrum of urothelial carcinoma tissue (3) and mean spectrum of normal bladder tissue (4).

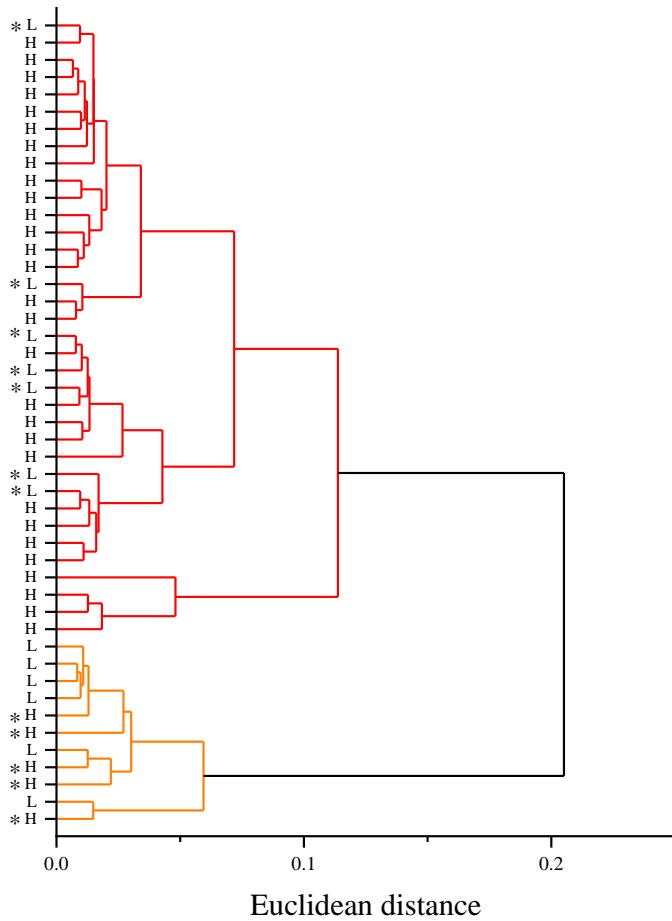


**Figure A-18.** HCA dendrogram of high-grade and low-grade urothelial carcinoma tissues. Letters H and L represent spectra of each high-grade and low-grade tumorous tissues respectively. \* symbol indicates spectra assigned to the wrong class.

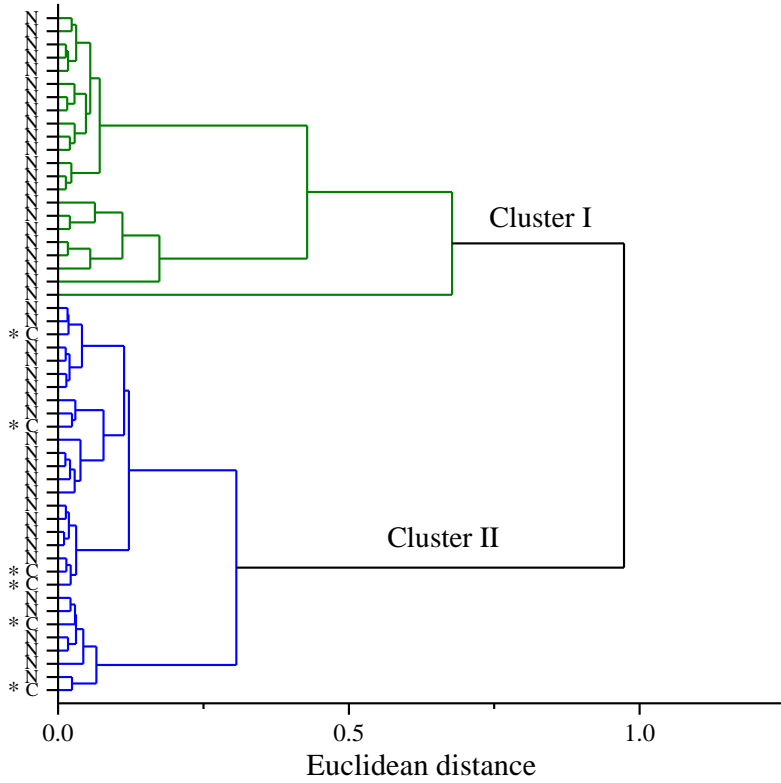


**Figure A-19.** HCA dendrogram of normal bladder and cystitis tissue smears. Letters N and C represent spectra of each normal and cystitis tissue smears respectively. \* symbol indicates spectra of cystitis for better visualization.

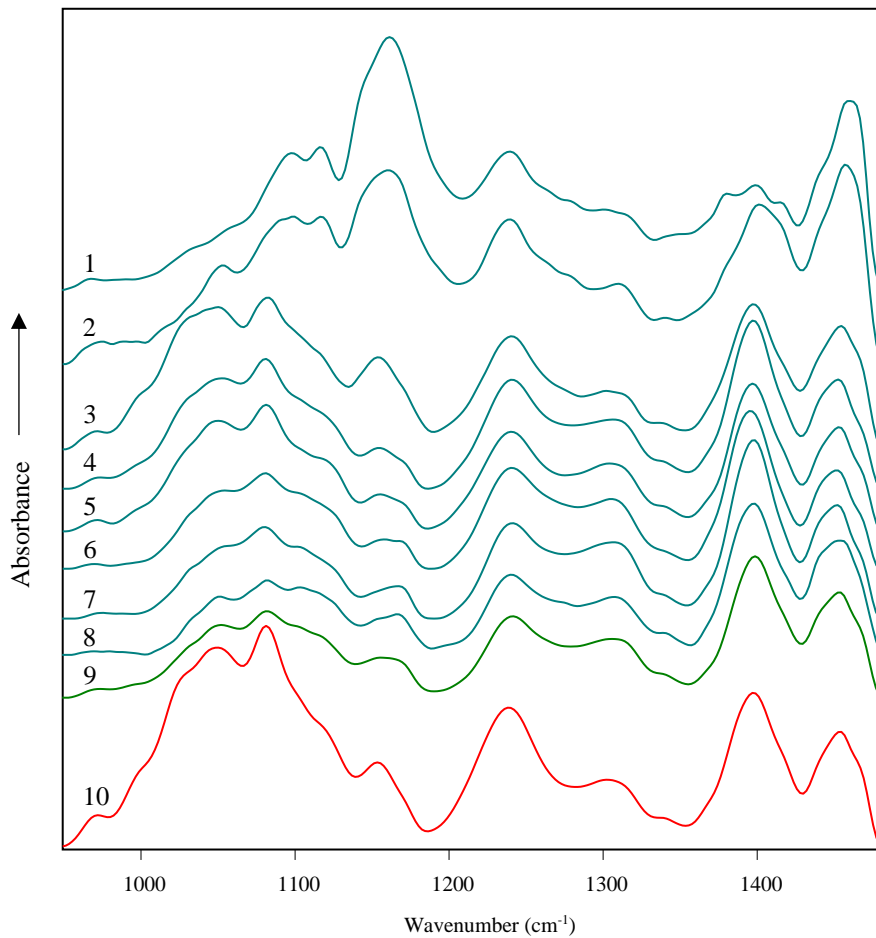


**Figure A-20.** ATR IR spectra of normal bladder tissue smears (1-8) assigned to tumorous tissue smears cluster after application of HCA analysis, mean spectrum of normal bladder tissue smears (9) and mean spectrum of urothelial carcinoma tissue smears (10).

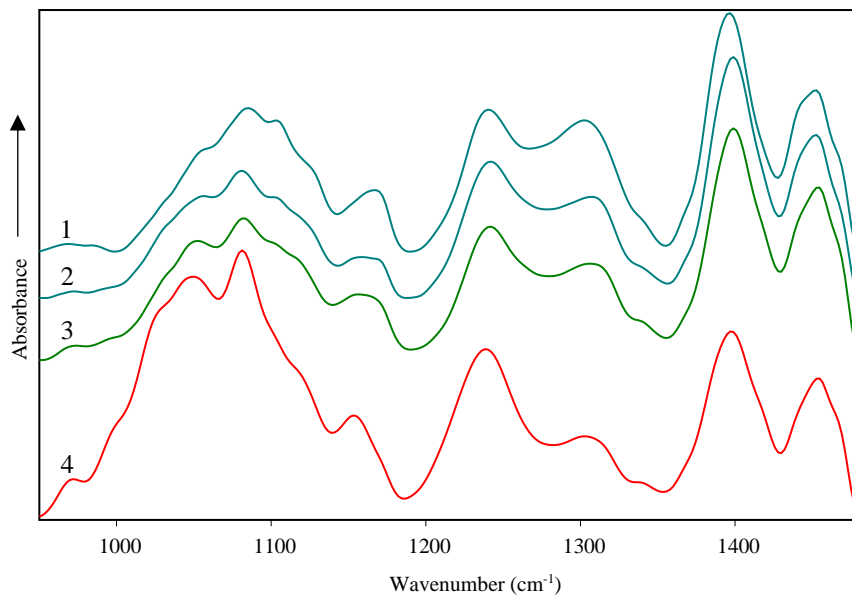


**Figure A-21.** ATR IR spectra of tumorous bladder tissue smears (1-2) assigned to normal tissue smears cluster after application of HCA analysis, mean spectrum of normal bladder tissue smears (3) and mean spectrum of urothelial carcinoma tissue smears (4).

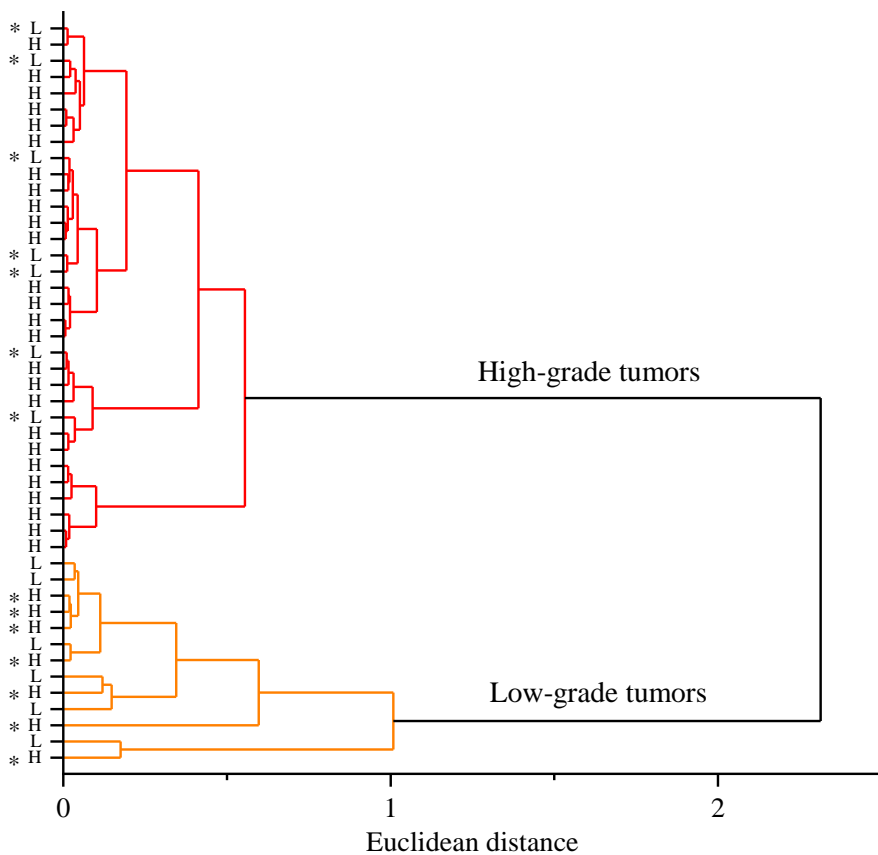


**Figure A-22.** HCA dendrogram of high-grade and low-grade urothelial carcinoma tissue smears. Letters H and L represent spectra of each high-grade and low-grade tumorous tissue smears respectively. \* symbol indicates spectra assigned to the wrong class.

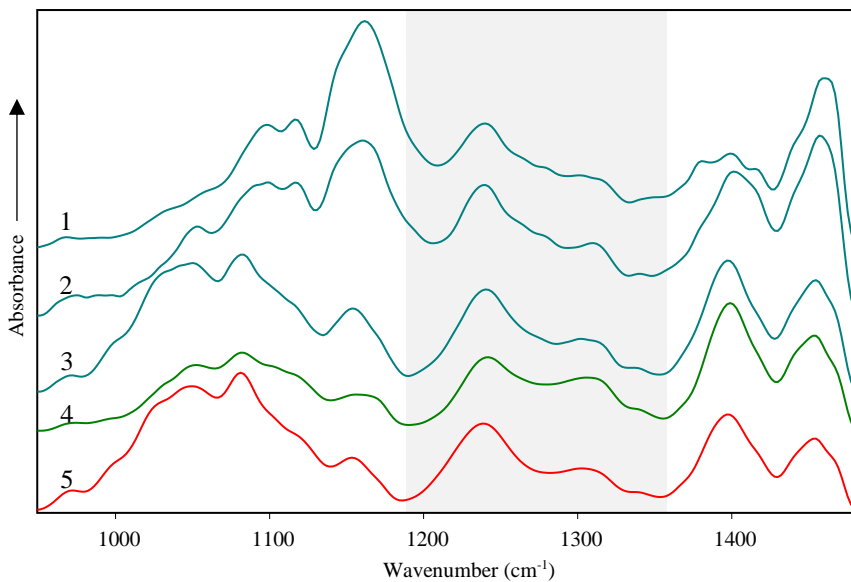


**Figure A-23.** ATR IR spectra of normal bladder tissue smears (1-3) assigned to tumorous tissue smears cluster after application of PCA analysis, mean spectrum of normal bladder tissue smears (4) and mean spectrum of urothelial carcinoma tissue smears (5). Grey area corresponds to the spectral region for which PCA analysis was performed.

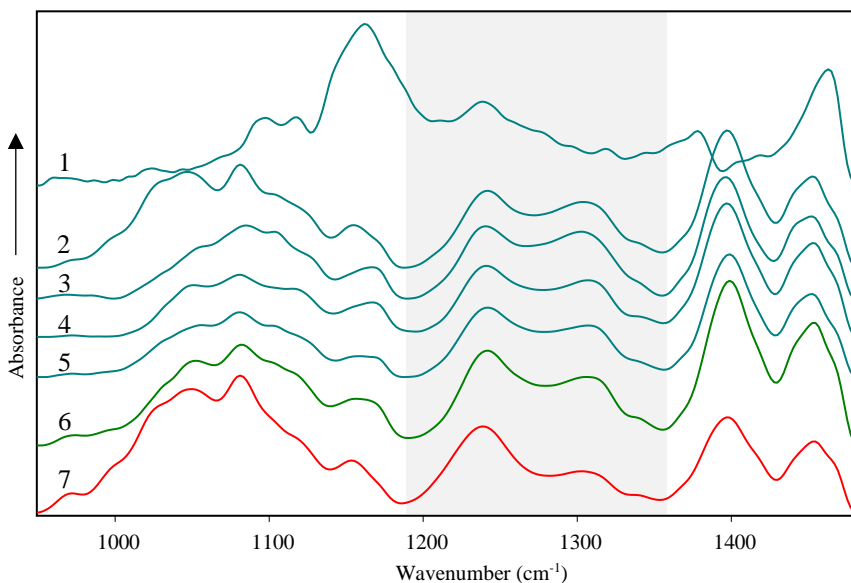


**Figure A-24.** ATR IR spectra of tumorous bladder tissue smears (1-5) assigned to normal tissue smears cluster after application of PCA analysis, mean spectrum of normal bladder tissue smears (6) and mean spectrum of urothelial carcinoma tissue smears (7). Grey area corresponds to the spectral region for which PCA analysis was performed.



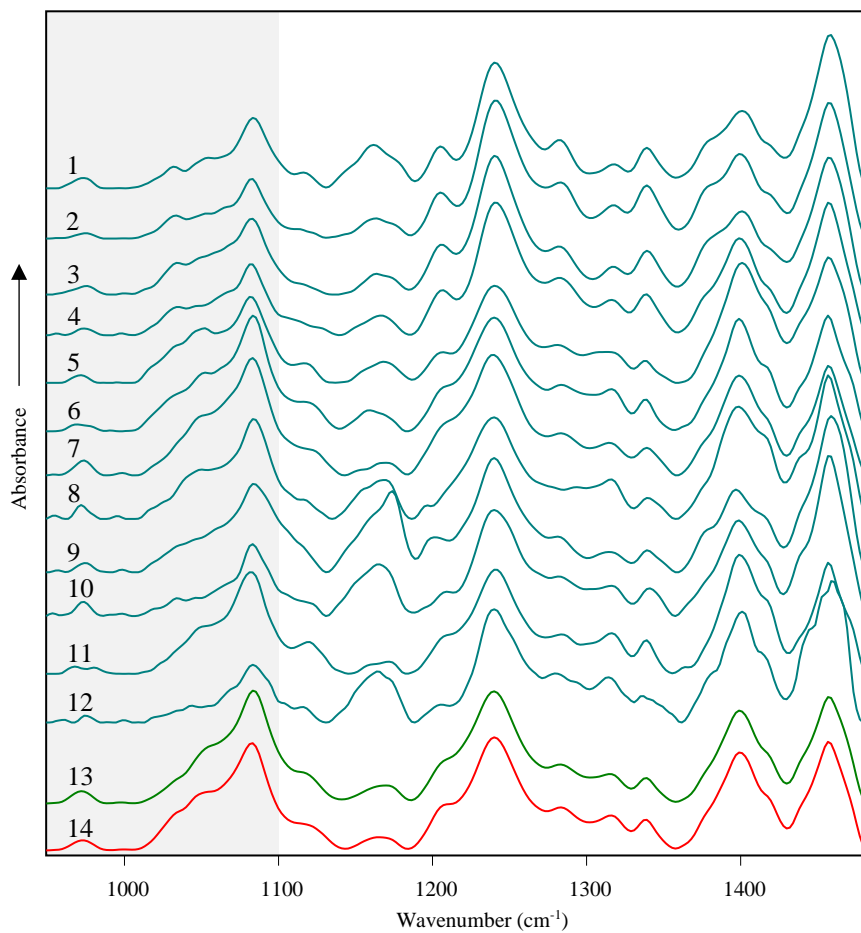


**Figure A-25.** ATR IR spectra of normal pancreas tissues (1-12) assigned to tumorous tissue cluster after application of HCA analysis, mean spectrum of normal pancreas tissue (13) and mean spectrum of pancreas tumorous tissue (14). Grey area corresponds to the spectral region for which HCA analysis was performed.

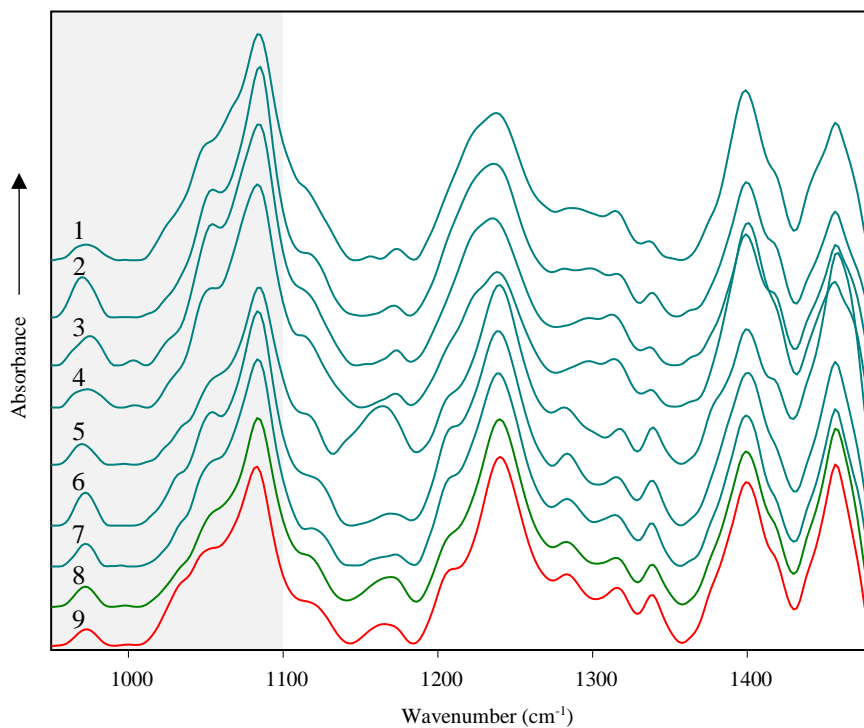


**Figure A-26.** ATR IR spectra of tumorous pancreas tissues (1-7) assigned to normal tissue cluster after application of HCA analysis, mean spectrum of normal pancreas tissue (8) and mean spectrum of pancreas tumorous tissue (9). Grey area corresponds to the spectral region for which HCA analysis was performed.

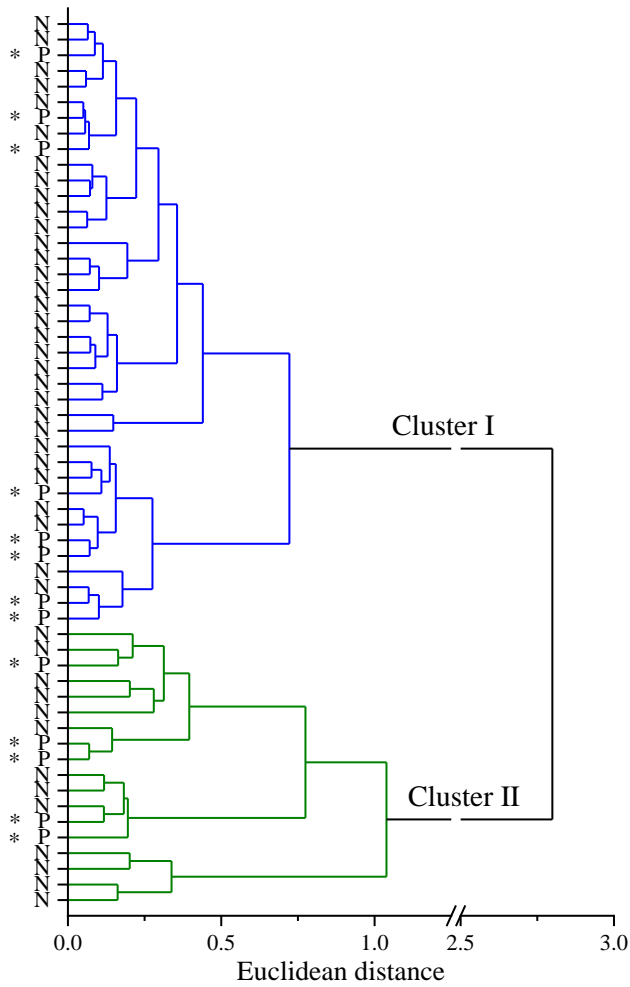


**Figure A-27.** HCA dendrogram of pancreatic normal and pancreatitis tissues. Letters N and P represent spectra of each normal and pancreatitis tissues respectively. \* symbol indicates spectra of pancreatitis for better visualization.

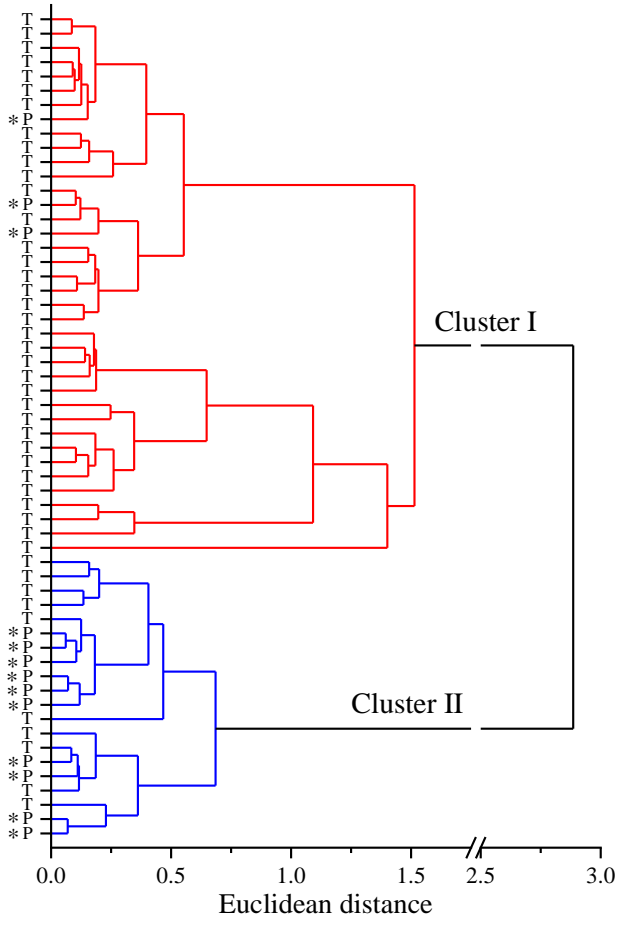


**Figure A-28.** HCA dendrogram of tumorous pancreas and pancreatitis tissues. Letters T and P represent spectra of each tumorous and pancreatitis tissues respectively. \* symbol indicates spectra of pancreatitis for better visualization.

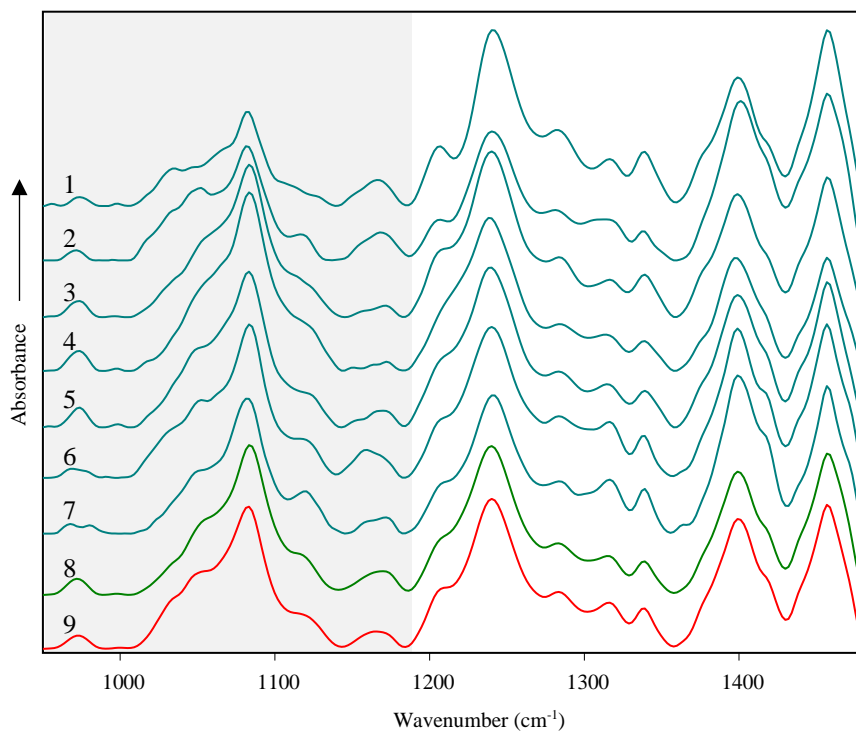


**Figure A-29.** ATR IR spectra of normal pancreas tissues (1-7) assigned to tumorous tissue cluster after application of PCA analysis, mean spectrum of normal pancreas tissue (8) and mean spectrum of pancreas tumorous tissue (9). Grey area corresponds to the spectral region for which PCA analysis was performed.

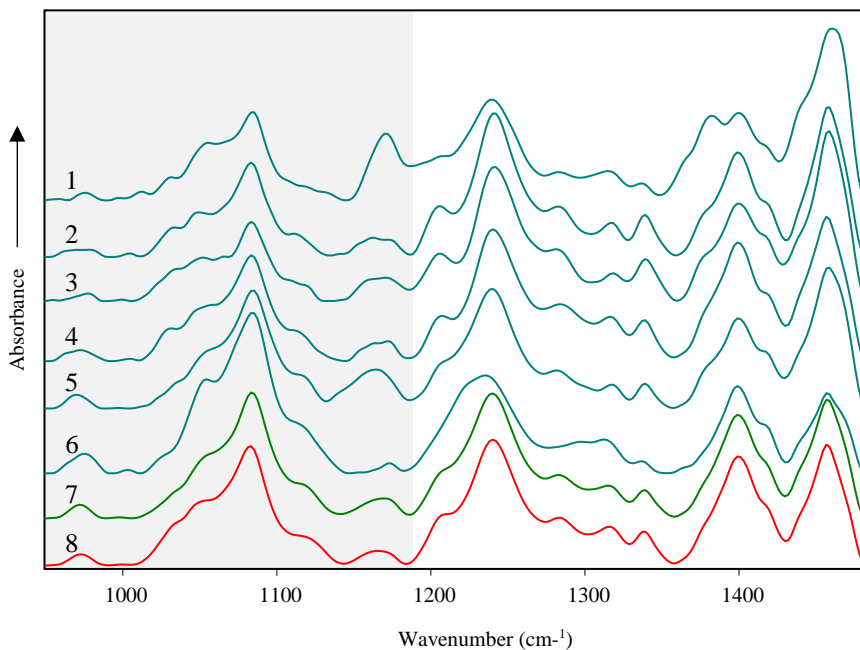


**Figure A-30.** ATR IR spectra of tumorous pancreas tissues (1-6) assigned to normal tissue cluster after application of PCA analysis, mean spectrum of normal pancreas tissue (7) and mean spectrum of pancreas tumorous tissue (8). Grey area corresponds to the spectral region for which PCA analysis was performed.

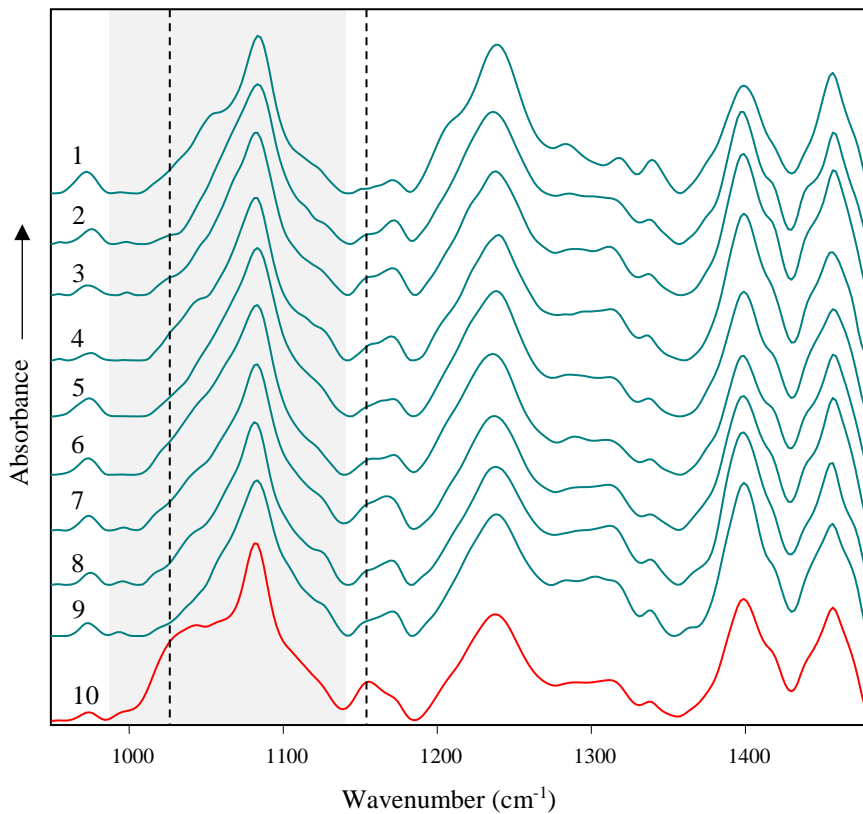


**Figure A-31.** ATR IR spectra of normal liver tissue (1-9) assigned to tumorous tissue cluster after application of HCA analysis, mean spectrum of normal liver tissue (10). Grey area indicates spectral region for which spectral analysis was performed, dashed lines correspond to glycogen spectral bands.

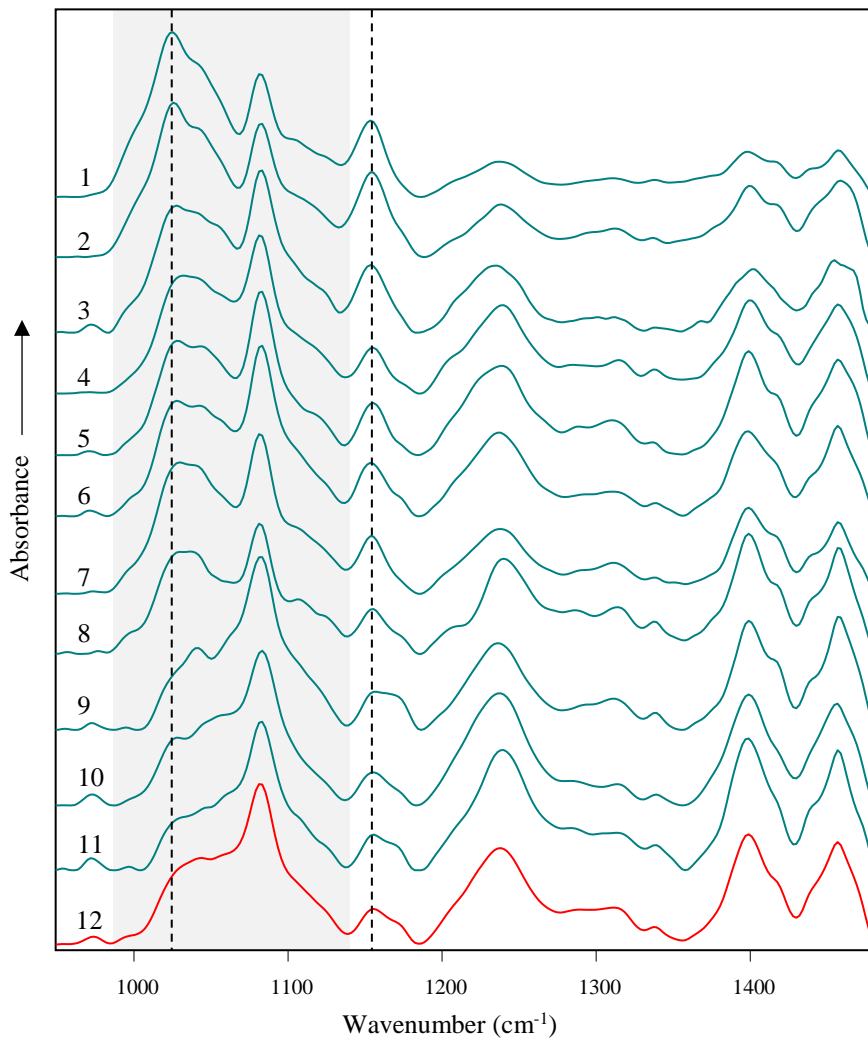


**Figure A-32.** ATR IR spectra of tumorous liver tissues (1 - 11) assigned to normal tissue class after application of HCA analysis: HCC (1 – 9), CCC (10), CRC (11) tumors, mean spectrum of normal liver tissue (12). Grey area indicates spectral region for which spectral analysis was performed, dashed lines correspond to glycogen spectral bands.



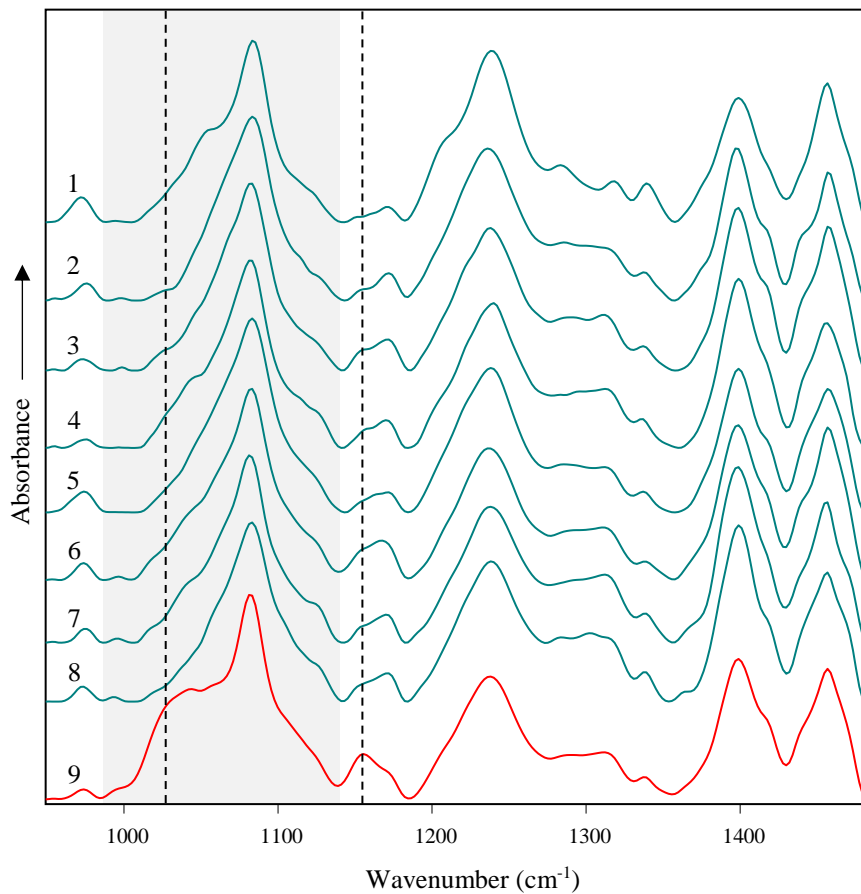


**Figure A-33.** ATR IR spectra of normal liver tissue (1-8) assigned to tumorous tissue cluster after application of PCA analysis, mean spectrum of normal liver tissue (9). Grey area indicates spectral region for which spectral analysis was performed, dashed lines correspond to glycogen spectral bands.

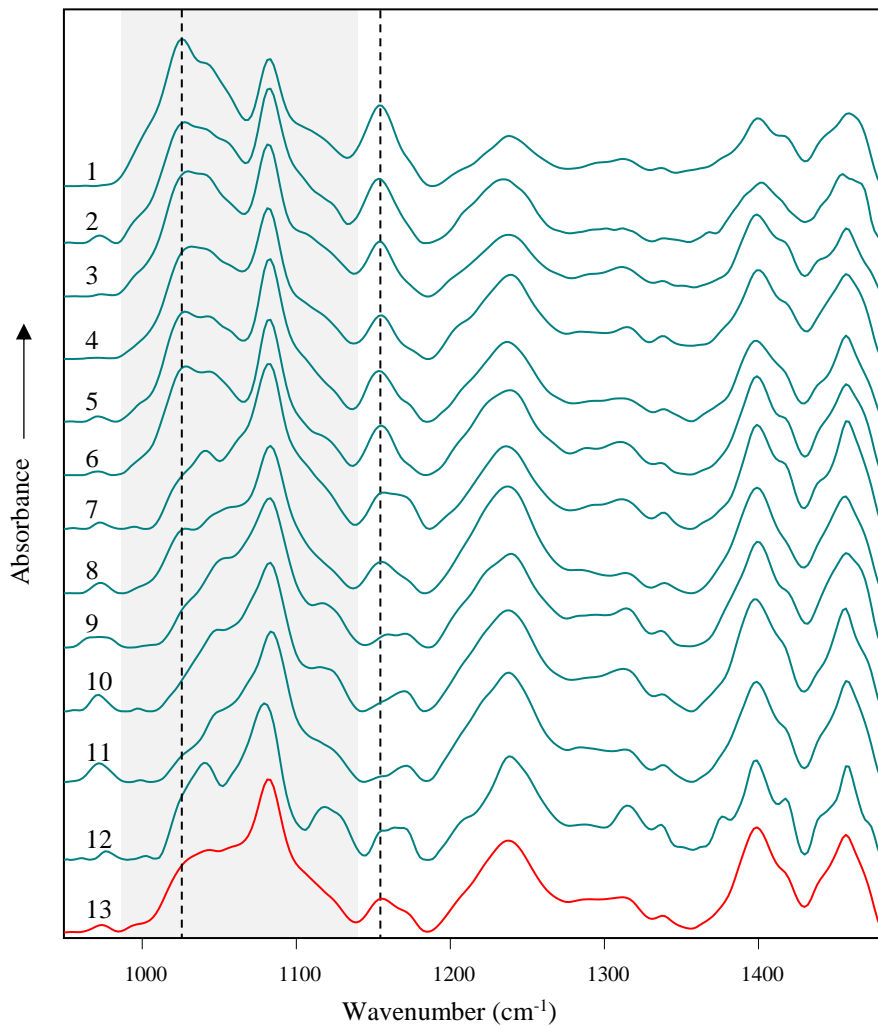


**Figure A-34.** ATR IR spectra of tumorous liver tissues (1 - 12) assigned to normal tissue class after application of PCA analysis: HCC (1 - 7), CCC (8 - 9), CRC (10 - 12) tumors, mean spectrum of normal liver tissue (13). Grey area indicates spectral region for which spectral analysis was performed, dashed lines correspond to glycogen spectral bands.

# SANTRAUKA LIETUVIŲ KALBA

## ĮVADAS

Vėžys yra viena dažniausių mirties priežasčių: apskaičiuotas naujų susirgimų skaičius 2020-aisiais metais siekė 19,3 milijonus, o vėžio sukeltų mirčių skaičius – 10 milijonų atvejų pasaulyje [1]. Dažniausiai taikomi vėžio gydymo būdai yra chirurginė operacija, chemoterapija, spindulinis gydymas ir kiti gydymo būdai, kurie bendru atveju gali būti taikomi kartu. Dažniausiai taikomas ir kai kuriais atvejais vienintelis gydymo būdas – chirurginė operacija. Paciento ligos baigtis, gyvenimo kokybė po operacijos ir išgyvenamumas priklauso nuo piktybinio naviko rezekcijos kraštų.

Siekiant išvengti naviko atsinaujinimo, jis turi būti visiškai pašalintas, kai, tuo tarpu, kiek tik įmanoma daugiau sveikų funkcionuojančių audinių turi būti išsaugota siekiant sumažinti komplikacijų riziką ir išsaugoti gyvybines organo funkcijas. Mikroskopinės navikinių ląstelių infiltracijos rezekcijos vietoje gali būti makroskopiškai nepastebimos, todėl yra atliekamas intraoperatyvus histologinis tyrimas siekiant padėti chirurgui įvertinti rezekcijos kraštus ir užtikrinti mikroskopinių naviko infiltracijų nebuvimą pjūvio vietoje. Histologinis šaldytų pjūvių ištyrimas dažnai yra taikomas siekiant padėti chirurgui nuspręsti, kurioje vietoje turi būti atliktas pjūvis, tačiau turi keletą trūkumų. Rezekuoto audinio ištyrimas užima papildomai laiko, dėl to pailgėja operacijos ir anestezijos trukmė. Analizuojamas audinio bandinys turi būti užšaldomas naudojant skystą azotą, pjaustomas ir dažomas hematoksilinu ir eosinu (H&E) prieš tiriant mikroskopu. Tyrimas atliekamas specializuotoje laboratorijoje, todėl operacijos metu pašalintas audinys turi būti perkeliamas iš operacinės į patologijos laboratoriją. Audinio transportavimas, paruošimas ir analizė gali užtrukti apie 40 minučių [2] ir, jei audinio bandinys yra netinkamos kokybės, tyrimas turi būti kartojamas. Nors šaldytų pjūvių ištyrimas yra laikomas patikimu metodu ir kaip standartas yra rutiniškai taikomas audinių įvertinimui [3]–[6], kai kuriuose moksliniuose darbuose yra aprašomi neatitikimai tarp šaldytų pjūvių ištyrimo ir galutinės diagnozės [7]; neatitikimai stebimi 5 -15 % atvejų [8]. Tikslumas ir neatitikimų rodikliai varijuoja priklausomai nuo audinio tipo ir institucijos, kurioje tyrimas atliekamas [4], [7]. Netikslumai dažniausiai yra nulemti interpretavimo ar bandinio paruošimo klaidų [4]. Diagnozės tikslumas yra nulemtas bandinio kokybės, riboto analizės laiko operacijos metu bei gydytojo patologo patirties. Bandinio paruošimo klaidos gali atsirasti dėl techninių priežasčių: dėl šaldymo gali būti stebimos audinių struktūros pažaidos, taip pat, apsunkintas audinio pjovimas ir dažymas gali nulemti interpretavimo sunkumus. Taip pat,

tik kelios dominančios audinio sritys gali būti tiriamos dėl riboto laiko [9]. Dėl išvardytų priežasčių, yra reikalingi greiti ir patikimi metodai, kurie galėtų būti taikomi intraoperatyviam audinių tyrimui.

Optinės spektroskopijos metodai, įskaitant fluorescenciją, Ramano sklaidos ir infraraudonąją (IR) spektroskopiją, tampa vis plačiau taikomi biologinių audinių tyrimams chirurginės onkologijos srityje. Fluorescencijos metodai yra jau taikomi chirurgijoje. Fluorescencinis vaizdinimas yra taikomas keliems onkologinių operacijų tipams [8], [10]. Operacijos metu metodas leidžia vizualizuoti skirtingus audinių tipus, tokius kaip normalūs ir vėžiniai audiniai, kurie nebūtų matomi plika akimi. Tačiau šiuo atveju yra keletas metodo ribojimų. Siekiant vizualizuoti skirtingus audinių tipus, fluorescencijos kontrastinė medžiaga turi būti įvesta į organizmą prieš atliekant analizę ir leidžiant jai susikaupti tikslinėje navikinio darinio srityje. Skirtingiems audiniams turi būti parenkamos tinkamos specifinės medžiagos, kadangi skirtingi navikai turi skirtingus žymenis. Šiuo metu dažniausiai naudojami fluoroforai yra indocianino žaliasis (angl. indocyanine green – ICG), metileno mėlis (angl. methylene blue), 5-aminolevulino rūgštis (angl. 5-aminolevulinic acid - 5-ALA) ir fluoresceino natrio druska (angl. fluorescein sodium), tačiau, tinkamos kontrastinės medžiagos dar nėra atrastos skirtingiems navikų tipams [8]. Siekiant surasti tinkamą kontrastinę medžiagą, turi būti atsižvelgiama į farmakokinetinį medžiagos profilį, tiriamojo audinio biologinių žymenų savybes [11], [12].

Dėl minėtų priežasčių, virpesinės spektroskopijos (Ramano sklaidos ir IR sugerties) metodai turi pranašumą, kadangi taikant šiuos metodus yra nereikalingos specifinės cheminės medžiagos galinčios prisijungti prie vėžinių biologinių žymenų molekulių, nereikalingas audinio dažymas ar cheminis apdorojimas prieš tyrimą.

Spontaninės ir koherentinės Ramano sklaidos spektroskopijos metodai buvo pritaikyti žmogaus ir gyvūnų navikinių audinių identifikavimui ir parodė daug žadančius rezultatus [13]. Ypatingai, panaudota šviesolaidinė metodika, skirta įvairių audinių tipų tyrimui, parodė galimybes metodą pritaikyti tyrimams *in vivo* sąlygomis [14]–[17]. Tačiau Ramano sklaidos spektroskopija turi keletą trūkumų. Ramano sklaida yra sąlyginai silpnas procesas, todėl jautrūs detektoriai turi būti naudojami siekiant registruoti tinkamą Ramano sklaidos signalą. Priklausomai nuo lazerio, naudojamo sužadinti Ramano sklaidai, spinduliuotės bangos ilgio ir galios gali būti stebimas nepageidaujamas fluorescencijos fonas Ramano sklaidos spektruose. Taip pat, turi būti atkreipiamas dėmesys į aplinkinius šviesos šaltinius: kitų šviesos šaltinių, naudojamų operacijoje, spinduliuotės bangos ilgiai gali sutapti su detektoriaus registruojamos spinduliuotės bangos ilgiais, tokiu būdu

darant įtaką registruojamiems spektrams. Lazerinės spinduliuotės, naudojamos Ramano sklaidos sužadimui, naudojimas gali būti sudėtingas: lazerio spinduliuotės galia ir integravimo trukmė turi būti kruopščiai parenkami taip, kad būtų išvengta audinio pažeidų ir tuo pat metu užtikrinant pakankamą Ramano sklaidos signalo stiprumą bei duomenis gaunant per racionalią laiko trukmę, siekiant išlaikyti kuo trumpesnę tyrimo trukmę neprailginant operacijos ir anestezijos trukmės.

Tuo tarpu IR spektriniuose tyrimuose naudojama mažos galios spinduliuotė nepažeidžia biologinių audinių, o spektras gali būti užregistruojamas ganėtinai greitai. IR spektroskopija taikoma vėžio tyrimams, metodą taikant skirtingiems bandinių tipams: audiniams, ląstelėms, seilėms, šlapimui, šlapimo pūslės nuoplovoms, tulžiai ir net tarpląsteliniais nešikliams (angl. extracellular vesicles) [33]–[36]. Taikomi metodai apima IR spinduliuotės pralaidumo, mikrospektroskopijos ir pažeistojo visiškojo vidaus atspindžio (angl. attenuated total reflection – ATR) metodus. Daugeliu atvejų, atliekant eksperimentą taikant standartinius metodus, reikalingas specialus bandinio paruošimas, bandinio perkėlimas į specialų bandinių skyrių spektrometro viduje. Taip pat, standartiniai spektrometrai paprastai yra dideli ir nemanėringi, kas yra kliūtis siekiant pritaikyti metodą operacinėje. Šviesolaidinės optikos taikymas IR spektroskopijai leistų priartinti metodą prie klinikinės diagnostikos. Tai suteiktų galimybę atlikti tyrimus *in situ* sąlygomis be reikalavimo perkelti audinį į prietaiso vidų. Šviesolaidinė optika gali būti taikoma kartu su mažų matmenų prietaisais, kas leidžia įrangą perkelti praktiškai į bet kurią operacinės vietą netrukdant operacijos eigai.

## TIKSLAS IR UŽDAVINIAI

Atsižvelgiant į iššūkius, susijusius su navikinių audinių diagnostika, paminėtus anksčiau, yra reikalinga portabili, veikianti realiu laiku ir patikima spektrinė sistema, tinkama taikyti audinių tyrimams *in situ* ar net *in vivo* sąlygomis. Šios disertacijos tikslas – pritaikyti šviesolaidinę ATR IR spektrinę sistemą biologinių audinių tyrimams, galimiems vykdyti intraoperatyviomis sąlygomis. Siekiant įvykdyti tikslą, iškeliami šie uždaviniai:

1. Nustatyti šviesolaidinės ATR IR spektrinės sistemos tinkamą konfigūraciją bei parametrus biologinių audinių tyrimui.
2. Pritaikyti šviesolaidinę ATR IR spektrinę sistemą rezekuotų žmogaus įvairių organų (inkstų, šlapimo pūslės, kasos ir kepenų) audinių spektrų registravimui.
3. Nustatyti spektrinius žymenis, tinkamus inkstų, šlapimo pūslės, kasos ir kepenų navikinių audinių identifikavimui.

4. Pritaikyti statistinės analizės metodus skirtingų audinių grupių spektrų klasifikavimui.
5. Įvertinti šviesolaidinės ATR IR spektroskopijos galimybes ir trūkumus intraoperatyviai vėžinių audinių diagnostikai.

## GINAMIEJI TEIGINIAI

1. Spektrinė sistema, sudaryta iš šviesolaidinio ATR IR zondo, sujungto su standartiniu mobiliu FT-IR spektrometru ir išoriniu MCT tipo detektoriumi, yra pakankamai jautri rezekuotų audinių informatyvių spektrų registravimui.
2. Spektrai, užregistruoti naudojant šviesolaidinę spektrinę sistemą, leidžia nustatyti specifines savybes, būdingas skirtingiems audinių tipams. Spektriniai žymenys, tokie kaip glikogenas, kolagenas ir fruktozės-1,6-bisfosfatazė gali būti naudojami normalių ir navikinių audinių identifikavimui.
3. Nėra vieno universalaus spektrinio navikų žymens, tinkamo visų žmogaus organų vėžio aptikimui. Kiekvienam organui turi būti nustatytas specifinių navikinių spektrinių žymenų rinkinys.
4. Šviesolaidinė ATR IR spektroskopija kartu su statistinės analizės metodais, taikomais įvairių žmogaus organų (inkstų, šlapimo pūslės, kasos ir kepenų) audinių ATR IR spektrams leidžia sėkmingai identifikuoti normalius ir navikinius audinius iki 100 % tikslumu.

## PUBLIKACIJŲ DOKTORANTŪROS TEMA SĄRAŠAS

### *Publikacijos recenzuojamuose žurnaluose*

1. M. Pučetaitė, M. Velička, V. Urbonienė, J. Čeponkus, R. Bandzevičiūtė, F. Jankevičius, A. Želvys, V. Šablinskas, G. Steiner, Rapid intra-operative diagnosis of kidney cancer by ATR-IR spectroscopy of tissue smears, *Journal of biophotonics*, 2018, **11**, 1. DOI: 10.1002/jbio.201700260.
2. V. Šablinskas, R. Bandzevičiūtė, M. Velička, J. Čeponkus, V. Urbonienė, F. Jankevičius, A. Laurinavičius, D. Dasevičius, G. Steiner, Fiber attenuated total reflection infrared spectroscopy of kidney tissue during live surgery, *Journal of biophotonics*, 2020, **13**, 1. DOI: 10.1002/jbio.202000018.
3. R. Bandzevičiūtė, J. Čeponkus, M. Velička, V. Urbonienė, F. Jankevičius, A. Želvys, G. Steiner, V. Šablinskas, Fiber based

- infrared spectroscopy of cancer tissues, *Journal of molecular structure*, 2020, **1220**, 1. DOI: 10.1016/j.molstruc.2020.128724.
4. R. Bandzevičiūtė, G. Platkevičius, J. Čeponkus, A. Želvys, A. Čekauskas, V. Šablinskas, Differentiation of Urothelial Carcinoma and Normal Bladder Tissues by Means of Fiber-based ATR IR Spectroscopy, *Cancers*, 2023, **15**, 499. DOI: 10.3390/cancers15020499
  5. R. Bandzeviciute, G. Steiner, K. Liedel, J. Golde, E. Koch, T. Welsch, C. Kahlert, D. Stange, M. Distler, J. Weitz, J. Ceponkus, V. Sablinskas, and C. Teske, Fast and label-free intraoperative discrimination of malignant pancreatic tissue by attenuated total reflection infrared spectroscopy, *Journal of Biomedical Optics*, 2023, 2023, **28**, 045004. DOI: 10.1117/1.JBO.28.4.045004

### **Konferencijų darbai**

1. V. Šablinskas, M. Velička, M. Pučetaitė, V. Urbonienė, J. Čeponkus, R. Bandzevičiūtė, F. Jankevičius, T. Sakharova, O. Bibikova, G. Steiner, Proc. SPIE 10497, Imaging, Manipulation, and Analysis of Biomolecules, Cells, and Tissues XVI, 1049713. 2018 DOI: 10.1117/12.2289393
2. R. Bandzeviciute, G. Steiner, K. Liedel, J. Golde, E. Koch, T. Welsch, C. Kahlert, D. Stange, M. Distler, J. Weitz, J. Ceponkus, V. Sablinskas, and C. Teske, Fiber-based ATR-IR spectroscopy for an intraoperative diagnosis of normal pancreatic tissue, pancreatitis, and malignant pancreatic lesions, Proc. SPIE 12368, Advanced Biomedical and Clinical Diagnostic and Surgical Guidance Systems XXI, 123680H. 2023 DOI: 10.1117/12.2647405.

### **PUBLIKACIJŲ NE DOKTORANTŪROS TEMA SĄRAŠAS**

1. V. Vicka, A. Vickienė, J. Tutkus, J. Stanaitis, R. Bandzevičiūtė, D. Ringaitienė, S. Vosylius, J. Šipylaitė, Immediate aspiration of the drug infused via central venous catheter through the distally positioned central venous dialysis catheter: An experimental study, *JVA: The journal of vascular access*, 2021, **22**, 94. DOI: 10.1177/1129729820924555.
2. R. Bikmurzin, R. Bandzevičiūtė, A. Maršalka, A. Maneikis, L. Kalėdienė, FT-IR Method Limitations for  $\beta$ -Glucan Analysis, *Molecules*, 2022, **27**, 4616. DOI: 10.3390/molecules27144616.

3. M. Snicorius, M. Drevinskaite, M. Miglinas, A. Cekauskas, M. Stadulyte, R. Bandzeviciute, J. Ceponkus, V. Sablinskas, A. Zelvys, A Novel Infrared Spectroscopy Method for Analysis of Stone Dust for Establishing Final Composition of Urolithiasis, 2023, **47**, 36-42. DOI: 10.1016/j.euros.2022.11.007.

## PRANEŠIMAI KONFERENCIJOSE

1. R. Bandzevičiūtė, V. Urbonienė, F. Jankevičius, V. Šablinskas, Computer Assisted Identification of Cancerous Kidney Tissue by Means of FTIR Spectroscopy, Open Readings 61, Vilnius, Lithuania, 2018.
2. V. Sablinskas, M. Velicka, M. Pucetaite, V. Urboniene, J. Ceponkus, R. Bandzeviciute, F. Jankevicius, G. Steiner, In situ detection of cancerous kidney tissue by means of fiber ATR-FTIR spectroscopy, SPIE Photonics West, San Francisco, USA, 2018.
3. M. Velicka, M. Pucetaite, V. Urboniene, R. Bandzeviciute, J. Ceponkus, F. Jankevicius, V. Sablinskas, G. Steiner, ATR-FTIR spectroscopy: towards in vivo detection of cancerous tissue areas, 34th European Congress on Molecular Spectroscopy, Coimbra, Portugal, 2018.
4. R. Bandzevičiūtė, R. Platakytė, S. Adomavičiūtė, M. Velička, J. Čeponkus, V. Urbonienė, F. Jankevičius, V. Šablinskas, Optical fiber based spectroscopic device for in vivo detection of pathological tissue areas, Life Science Baltics, Vilnius, Lithuania, 2018.
5. G. Mickūnaitė, R. Bandzevičiūtė, Vibrational Spectroscopy of Human Gallstones, Open Readings 62, Vilnius, Lithuania, 2019.
6. R. Bandzeviciute, M. Velicka, J. Ceponkus, V. Urboniene, F. Jankevicius, V. Sablinskas, G. Steiner, Fiber Based Infrared Spectroscopy of Various Cancer Tissues, 15th International Conference on Molecular Spectroscopy, Wroclaw-Wojanow, Poland, 2019.
7. G. Mickūnaitė, R. Bandzevičiūtė, J. Čeponkus, G. J. Rudzikaitė, E. Olekaitė, A. Kirkliauskienė, V. Hendrixson, V. Šablinskas, Tulžies pūslės akmenų susiformavimo tyrimas Ramano sklaidos spektroskopiniu metodu, 43-ioji Lietuvos Nacionalinė fizikos konferencija, Kaunas, Lithuania, 2019.
8. R. Bandzevičiūtė, J. Čeponkus, M. Velička, V. Urbonienė, G. Mickūnaitė, F. Jankevičius, V. Šablinskas, G. Steiner, Šviesolaidinė



- ATR infraraudonoji spektroskopija vėžinių audinių diagnostikai, 43-joji Lietuvos Nacionalinė fizikos konferencija, Kaunas, Lithuania, 2019.
9. G. Mickūnaitė, A. Kamarauskienė, J. Čeponkus, E. Lastauskienė, R. Bandzevičiūtė, Study of Pathogenic Bacteria And Fungi by Means of FT-IR ATR Spectroscopy, Open Readings 64, Vilnius, Lithuania, 2021.
  10. R. Bandzevičiūtė, G. Platkevičius, J. Čeponkus, G. Mickūnaitė, A. Čekauskas, A. Želvys, V. Šablinskas, Detection of Malignant Human Bladder Tissue by Means of Fiber Based ATR IR Spectroscopy, Open Readings 64, Vilnius, Lithuania, 2021.
  11. G. Anužienė, R. Bandzevičiūtė, E. Lastauskienė, J. Čeponkus, Patogeninių mikroorganizmų identifikavimas ATR IR spektriniu metodu, 44-oji Lietuvos Nacionalinė fizikos konferencija, Vilnius, Lithuania, 2021.
  12. R. Bandzevičiūtė, J. Čeponkus, V. Šablinskas, C. Teske, G. Steiner, Šviesolaidinės ATR IR spektroskopijos taikymas kasos vėžinių audinių tyrimui, 44-oji Lietuvos Nacionalinė fizikos konferencija, Vilnius, Lithuania, 2021.
  13. M. Stadulytė, R. Bandzevičiūtė, J. Čeponkus, M. Snicorius, A. Želvys, V. Šablinskas, Infrared Spectroscopy of Urinary Deposits. Open Readings 65, Vilnius, Lithuania, 2022.
  14. G. Anužienė, R. Bandzevičiūtė, E. Lastauskienė, J. Čeponkus, ATR IR Spectroscopy Application for the Identification of Pathogenic Bacteria And Fungi, Open Readings 65, Vilnius, Lithuania, 2022.
  15. R. Bandzevičiūtė, K. Liedel, C. Teske, C. Riediger-Schweipert, J. Čeponkus, V. Šablinskas, G. Steiner, Application of Fiber ATR IR Spectroscopy for Tumorous Liver Tissue Identification, Open Readings 65, Vilnius, Lithuania, 2022.
  16. M. Snicorius, A. Želvys, M. Miglinas, M. Stadulytė, R. Bandzevičiūtė, J. Čeponkus, V. Šablinskas, FTIR ATR spectroscopy of urinary sediments and computed tomography as prediction tools for final stone composition, 7th Baltic Meeting in conjunction with the EAU (Baltic22), Vilnius, Lithuania, 2022.
  17. G. Platkevičius, R. Bandzevičiūtė, J. Čeponkus, A. Čekauskas, A. Želvys, V. Šablinskas, Ex vivo analysis of bladder urothelium and bladder cancer tissues by means of fiber based attenuated total reflection infrared spectroscopy, 7th Baltic Meeting in conjunction with the EAU (Baltic22), Vilnius, Lithuania, 2022.

18. R. Bandzevičiūtė, J. Čeponkus, C. Teske, K. Liedel, G. Platkevičius, A. Želvys, V. Šablinskas, G. Steiner, Application of Fiber-based FT-IR ATR Spectroscopy for Tissue Diagnostics During Oncological Surgery, 3rd Baltic Biophysics Conference , Vilnius, Lithuania, 2022.
19. G. Anužienė, A. Čiužas, R. Bandzevičiūtė, E. Lastauskienė, J. Čeponkus, Identification of Pathogenic Bacteria and Fungi by Means of ATR-IR Spectroscopy, 3rd Baltic Biophysics Conference , Vilnius, Lithuania, 2022.
20. R. Bandzevičiūtė, G. Steiner, K. Liedel, J. Golde, E. Koch, T. Welsch, C. Kahlert, D. Stange, M. Distler, J. Weitz, J. Čeponkus, V. Šablinskas, C. Teske, Fiber-based ATR-IR spectroscopy for an intraoperative diagnosis of normal pancreatic tissue, pancreatitis, and malignant pancreatic lesions, SPIE Photonics West, San Francisco, USA, 2023.

## DARBO NAUJUMAS IR AKTUALUMAS

Šiame darbe aprašomas tyrimas, kurio metu IR spektroskopijos metodika taikoma žmogaus normalių ir navikinių audinių tyrimui ir yra tinkama taikyti intraoperatyviomis sąlygomis. Virpesinės spektroskopijos metodai audinių charakterizavimui ir audinio tipo identifikavimui yra taikomi jau dešimtmečius. Tačiau IR spektroskopija vis dar nėra taikoma klinikiniuose tyrimuose dėl keleto priežasčių. Įranga, naudojama IR spektrų registravimui taikant tradicinius metodus, yra didelių gabaritų ir netinkama naudoti operacinėje, kai, tuo tarpu, audinio mėginiai, paimti iš paciento, turi būti perkeltami į specialų bandinių skyrių prietaiso viduje. Taip pat, bandiniai turi būti specialiai paruošiami prieš tyrimą. Dėl minėtų priežasčių IR spektroskopija buvo labiau tinkamas metodas taikyti audinių charakterizavimui laboratorijos sąlygomis nei klinikinėje diagnostikoje.

Šiame darbe šviesolaidinė spektrinė sistema buvo taikoma IR spektrų registravimui. Naudojant šviesolaidinį zondą, tyrimus galima atlikti *in situ* ar net *in vivo* sąlygomis, kas yra svarbu siekiant taikyti metodą operacijos metu. Yra paskelbta keletas publikacijų, kurios parodė šviesolaidinės ATR IR spektroskopijos taikymo potencialą navikinių audinių tyrimuose. Tačiau dėl tyrimų stokos, metodas vis dar nėra taikomas klinikiniuose tyrimuose. Šiame darbe šviesolaidinė ATR IR spektroskopija buvo taikoma įvairių žmogaus organų normalių ir navikinių audinių atskyrimui. Šioje disertacijoje pristatomi rezultatai parodo metodo galimybes ateityje metodą taikyti padedant chirurgams įvertinti rezekcijos kraštą operacijos metu.

## DISERTACIJOS SANDARA

Disertaciją sudaro įvadas, šeši skyriai, literatūros sąrašas, priedai bei santrauka lietuvių kalba.

Pirmajame skyriuje apžvelgiamos IR spektroskopijos taikymo vėžinių audinių diagnostikai galimybės, pasaulyje atliekami tyrimai, šviesolaidžių panaudojimo IR spektroskopijoje galimybės, pagrindiniai statistiniai metodai taikomi spektrinei analizei, aprašomas medicininių diagnostinių tyrimų tikslumo įvertinimas.

Antrajame skyriuje aprašoma tyrimams naudota šviesolaidinė spektrinė sistema, jos optimizavimas ir pritaikymas vėžinių audinių tyrimui, parametrai bei tyrimo galimybės.

Trečiajame, ketvirtajame, penktajame ir šeštajame skyriuose aprašomi tyrimo rezultatai, metodą pritaikius žmogaus inkstų, šlapimo pūslės, kasos ir kepenų audinių tyrimams. Šiuose skyriuose glaustai pristatomos pagrindinės minėtų organų funkcijos, dažniausi onkologiniai susirgimai, pagrindiniai metodai, taikomi vėžinių audinių identifikavimui chirurginės operacijos metu. Pateikiami nustatyti pagrindiniai spektriniai vėžinių audinių žymenys, leidžiantys identifikuoti kiekvieno iš minėtų organų vėžinius audinius, įvertinamas taikomo metodo jautrumas, specifiškumas, teigiama bei neigiama prognostinės vertės.

## TYRIMŲ METODIKA

### *Tiriamieji audiniai*

Disertacijoje aprašomi tyrimai taikant šviesolaidinę spektrinę sistemą žmogaus inkstų, šlapimo pūslės, kasos ir kepenų vėžiniams bei normaliems audiniams. Žmogaus inkstų ir šlapimo pūslės audiniai gauti iš Vilniaus universiteto ligoninės Santaros klinikų Urologijos centro (Lietuva). Tyrimai patvirtinti Vilniaus regiono bioetikos komiteto (dokumento numeris inkstų audinių spektriniais tyrimams: 158200-15-803-312, dokumento numeris šlapimo pūslės audinių spektriniais tyrimams: 2019/12-1178-665). Žmogaus kasos ir kepenų bandiniai gauti iš Drezdeno technikos universiteto ligoninės Carl Gustav Carus klinikų Visceralinės, krūtinės ląstos ir kraujagyslių chirurgijos skyriaus (Vokietija). Tyrimai patvirtinti vietos etikos komiteto (dokumento numeris kasos audinių spektriniais tyrimams: EK 179052018, dokumento numeris kepenų spektriniais tyrimams: BO-EK-26012020). Bandiniai tyrimams paimti chirurginių operacijų, atliekamų dėl įtariamų navikų ar lėtinių ligų (pavyzdžiui, pankreatito), metu. Daugeliu atvejų vienos

operacijos metu iš paciento paimami dviejų tipų (normalaus ir patologinio) audinių bandiniai spektriniams tyrimams. Kai kurių pacientų atveju dėl specifinės operacijos eigos paimti tik vieno tipo (normalaus ar patologinio) audinių bandiniai. Spektriniai tyrimai atliekami iškart po chirurginės operacijos specializuotoje laboratorijoje arba patalpoje, esančioje prie operacinės. Kiekvienu atveju patologijos (naviko) tipas nustatomas rutiniškai atliekamų histologinių tyrimų metu.

### ***Įranga***

Dalis tyrimų atlikta naudojant komercinį FT-IR spektrometrą Alpha (Bruker Optik GmbH, Ettlingen, Vokietija) toliau įvardijamą kaip spektrometras Alpha, prie jo prijungus ATR priedėlį „Platinum ATR“ su įmontuotu deimantiniu vieno atspindžio ATR elementu. Kita dalis tyrimų atlikta naudojant šviesolaidinę spektrinę sistemą, sudarytą iš spektrometro Alpha, sujungto su šviesolaidiniu zondų (Art Photonics GmbH, Berlin, Vokietija) su tvirtinamu antgaliu su įmontuotu germanio ATR elementu ir išoriniu skystu azotu šaldomu MCT (angl. Mercury Cadmium Telluride) tipo detektoriumi (Infrared Associates, Inc. Model IRA-20-00131).

### ***Bandinių paruošimas ir spektrų registravimas***

Šiame darbe aprašomi rezultatai tiriant dviejų tipų bandinius: rezekuotus neapdorotus audinius bei audinių tepinėlius. Kiekvieno audinio bandinio atveju, padaromas šviežias pjūvis ir pjūvio puse audinys priglaudžiamas prie ATR elemento. Audinių spektrai registruojami prie tiriamojo audinio bandinio švelniai prispaudžiant šviesolaidinį zondą ir laikant jį prispaustą tol, kol bus užregistruotas bandinio spektras. Audinių tepinėlių spektrai registruojami prie vidaus atspindžio elemento (šviesolaidinio zondo germanio ATR elemento arba spektrometro Alpha deimantinio ATR elemento) priglaudžiant ir atitraukiant tiriamąjį audinį. Tokiu būdu ant ATR elemento padaromas audinio tepinėlis, kuris paliekamas kelioms minutėms išdžiūti ore; jo spektras užregistruojamas. Audinio bandinyje padaromi keli pjūviai (pjūvių kiekis priklauso nuo tiriamojo bandinio dydžio) ir kiekvienu atveju užregistruojamas naujas spektras.

Naudojant tiek komercinį spektrometrą Alpha, tiek šviesolaidinę spektrinę sistemą, spektrai registruojami 4000 - 400  $\text{cm}^{-1}$  spektriniame intervale su 4  $\text{cm}^{-1}$  spektrine skyra. Kiekvieno registruojamo spektro atveju, registruojamos 64 ar 50 interferogramų, apskaičiuojamas jų vidurkis ir atliekant Furje transformaciją apskaičiuojamas IR sugerties spektras. Furje transformacija

atliekama taikant „Blackmann-Haris 3-Term” apodizacijos funkciją, papildymą 2 nuliais ir atliekant fazės korekciją naudojant „Power Spectrum“ korekcijos metodą. Tam, kad būtų galima palyginti skirtingais spektrometrais užregistruotus spektrus, naudojant programinį paketą OPUS (Bruker Optik GmbH, Ettlingen, Vokietija) atliekama ATR korekcija.

### ***Statistinė spektrų analizė***

Siekiant įvertinti taikomo metodo tinkamumą normalių ir vėžinių audinių atskirymui, atlikta statistinė spektrų analizė. Taikyti metodai apima hierarchinę klasterių analizę (angl. Hierarchical cluster analysis – HCA), principinių komponentų analizę (angl. Principal component analysis – PCA) bei parašytą audinių automatinio atpažinimo programą, kurios veikimo principas remiasi analizuojamojo spektro palyginimu su spektrų bibliotekos spektrais.

HCA analizė atlikta naudojant programinį paketą OriginPro (OriginLab corporation) arba programinį paketą OPUS. PCA analizė atlikta naudojant programinį paketą OriginPro. Spektrų bibliotekos sukūrimas bei palyginimas, audinių automatinio atpažinimo programos rašymas atliktas naudojant programinį paketą OPUS. Skirtingų organų audinių spektrų analizei metodai taikomi skirtingose spektrinėse srityse, atsižvelgiant į pagrindinius spektrinius požymius, leidžiančius identifikuoti skirtingus audinių tipus. Metodai taikomi ir skirtingai apdorojus spektrus – neskaičiuojant išvestinės, skaičiuojant pirmos arba antros eilės išvestines. Kiekvienu atveju statistinės analizės metodai taikomi įvairiose spektrinėse srityse bei skirtingai apdorojant spektrus, tačiau disertacijoje pateikiami tik geriausi statistinės analizės rezultatai.

## **SVARBIAUSI REZULTATAI**

### ***Šviesolaidinės spektrinės sistemos kūrimas bei parametru ištyrimas***

Šviesolaidinė spektrinė sistema sukurta Vilniaus universiteto Fizikos fakulteto Cheminės fizikos institute bendradarbiaujant kartu su Vokietijos įmone „Art photonics“ (Art Photonics GmbH, Berlin, Vokietija). Sistema sudaryta iš šviesolaidinio zondo (Art Photonics GmbH, Berlin, Vokietija) sujungto su spektrometru Alpha. Spektrometro Alpha priedėlis, skirtas IR spinduliuotės pralaidumo eksperimentams atlikti, buvo modifikuotas taip, kad būtų tinkamas naudoti prijungus šviesolaidžius. Spinduliuotė priedėlyje iš šaltinio į šviesolaidį bei iš šviesolaidžio į detektorių yra nukreipiama

įmontuotais dviem plokščiaisiais ir dviem paraboliniais veidrodžiais. Šviesolaidžiai prie spektrometro ir detektoriaus prijungiami SMA (angl. SubMiniature version A) tipo jungtimis. Šviesolaidinis zondas sudarytas iš dviejų sidabro halido šviesolaidžių, sujungtų su laikikliu, kurio gale tvirtinamas keičiamas ATR antgalis – kūgio formos germanio vidaus atspindžio elementas, eksperimento metu turintis sąlytį su žmogaus audiniais. Galimybė keisti antgalius užtikrina eksperimento sterilumą, kas yra svarbu tiriant žmogaus audinius *in situ* ar *in vivo* sąlygomis. Sistema sujungta su išoriniu skystu azotu šaldomu jautriu MCT (angl. Mercury Cadmium Telluride) tipo detektoriumi (Infrared Associates, Inc. Model IRA-20-00131). Šviesolaidis su detektoriumi sujungiamas naudojant specialiai šiai sistemai pritaikytą adapterį.

Yra žinoma, kad biologinių darinių spektrai, registruojami spektrometru Alpha yra pakankamai aukštos kokybės tam, kad galėtų būti identifikuojami spektriniai skirtumai, leidžiantys atskirti normalius ir navikinius audinius. Siekiant įvertinti sukurtos šviesolaidinės spektrinės sistemos tinkamumą ir galimybes audinių spektriniais tyrimams, apskaičiuotas ir palygintas signalo-triukšmo santykis (angl. signal-to-noise ratio – S/N) spektrams, registruotiems spektrometru Alpha ir šviesolaidine spektrine sistema. Atliekant šviesolaidinės spektrinės sistemos parametrų optimizavimą, sistema sudaroma esant kelioms įrangos konfigūracijoms: naudojamas arba vidinis spektrometro Alpha DTGS (angl. deuterated triglycine sulphate) tipo detektorius, arba išorinis skystu azotu šaldomas MCT tipo detektorius. S/N santykio vertės apskaičiuotos mažos koncentracijos vandeninio etanolio tirpalo (etanolio koncentracija tirpale 1:100) spektrams, etanolio spektrinei juostai, esančiai ties  $1045\text{ cm}^{-1}$ . Palyginus S/N vertes skirtinguose spektriniuose intervaluose, nustatyta, jog šviesolaidinės spektrinės sistemos konfigūracija, kuomet yra naudojamas vidinis DTGS detektorius, yra netinkama spektrų registravimui – S/N vertės yra mažos. Spektrų, registruotų šviesolaidine spektrine sistema, kuomet yra prijungtas MCT detektorius, S/N vertės yra palyginamo dydžio su šio rodiklio vertėmis registruojant spektrus spektrometru Alpha. Spektrinėje srityje nuo  $4000$  iki  $2800\text{ cm}^{-1}$ , S/N vertės yra žemos dėl šviesolaidžio sukeltos spinduliuotės sklaidos ir sugerties šioje spektrinėje srityje. Nors S/N vertės yra žemos minėtoje spektrinėje srityje, šio rodiklio vertės spektrinėje srityje nuo  $1800$  iki  $950\text{ cm}^{-1}$  yra palyginamo dydžio su S/N vertėmis, spektrus registruojant spektrometru Alpha. Šioje spektrinėje srityje yra stebimos svarbiausios biologiniams dariniams būdingos spektrinės juostos, tad galima teigti, jog spektrinė sistema su prijungtu išoriniu MCT detektoriumi yra tinkama biologinių darinių spektrų registravimui. Siekiant įsitikinti, kad sistema tinkama audinių spektrų registravimui,

užregistruoti to paties paciento normalaus ir navikinio žmogaus inkstų audinių tepinėlių spektrai spektrometru Alpha ir šviesolaidine spektrine sistema su prijungtu MCT detektoriumi. Spektrai, užregistruoti naudojant abiejų tipų įrangą yra tapatūs, spektrų kokybė abiem atvejais yra aukšta, stebimi tie patys spektriniai požymiai, leidžiantys identifikuoti normalius ir navikinius audinius. Tai patvirtina, jog šviesolaidinė spektrinė sistema su prijungtu MCT detektoriumi yra tinkama aukštos kokybės biologinių darinių spektrų registravimui.

Biologiniai audiniai yra sudaryti iš kelių skirtingų komponentų, pavyzdžiui, ląstelių, tarpląstelinio užpildo (angl. extracellular matrix – ECM). Tiriant audinius, yra svarbu žinoti, kuriuos komponentus stebime audinyje. Tuo tikslu buvo apskaičiuotas IR spinduliuotės išsiskverbimo į bandinį gylis. Pirmiausia, taikant optinę koherentinę tomografiją (angl. optical coherence tomography – OCT), nustatyti ATR elemento, įmontuoto šviesolaidinio zondo antgalyje, matmenys. Tuomet, remiantis nustatytais ATR elemento matmenimis, nustatyta spinduliuotės pluošto eiga elemente bei apskaičiuotas išsiskverbimo į bandinį gylis taikant Hariko (Harrick) formulę. Spinduliuotės išsiskverbimo gylio vertės varijuoja tarp 0,5 ir 1,9  $\mu\text{m}$  priklausomai nuo spinduliuotės kritimo kampo ir bangos ilgio. Šio išsiskverbimo gylio pakanka norint stebėti ląstelinius ir tarpląstelinius audinio komponentus.

### ***Inkstų vėžinių audinių tyrimas***

Inkstų vėžiniai audiniai buvo tiriami spektrų registravimui naudojant spektrometrą Alpha ir šviesolaidinę spektrinę sistemą. Naudojant standartinį spektrometrą Alpha buvo registruojami inkstų audinių tepinėlių spektrai, į tyrimą įtraukiant 127 pacientus. Svarbiausi spektriniai požymiai, leidžiantys atskirti normalius ir navikinius inkstų audinius, yra stebimi spektrinėje srityje nuo 950 iki 1200  $\text{cm}^{-1}$ . Šioje spektrinėje srityje yra stebimos angliavandenius, glikoproteinus bei fosfatines grupes atitinkančios spektrinės juostos. Navikinių audinių tepinėlių spektruose stebimos didesnio optinio tankio spektrinės juostos, esančios ties 1027  $\text{cm}^{-1}$  ir atitinkančios glikogeno  $\nu(\text{C-O})$ ,  $\nu(\text{C-C})$ ,  $\delta(\text{C-O-H})$  bei ties 1155  $\text{cm}^{-1}$  atitinkančios glikogeno  $\nu(\text{C-O})$  virpesius. Navikinių audinių spektruose stebima didesnio optinio tankio spektrinė juosta, esanti ties 1081  $\text{cm}^{-1}$ , kuri, remiantis eksperimentiniais duomenimis, taip pat yra priskiriama glikogenui. Stebimas padidėjęs glikogeno kiekis navikiniuose audiniuose yra būdingas kai kuriems navikams – navikuose kaupiamas glikogenas yra naudojamas kaip energijos šaltinis, reikalingas vėžinių ląstelių proliferacijai [42], [173]. Yra žinoma, kad glikogeno kaupimas ląstelių

citozolyje yra būdingas šviesiųjų inksto ląstelių karcinomai (ccRCC) [166], [174], [175].

Siekiant įvertinti metodo galimybes identifikuoti normalius ir navikinius audinius, atlikta statistinė spektrų analizė taikant standartinius metodus (HCA ir PCA) bei parašyta automatinio audinių atpažinimo programa, kurios veikimas remiasi analizuojamojo ir bibliotekos spektrų palyginimu. Įvertintas inkstų navikinių audinių atpažinimo tikslumas taikant skirtingus analizės metodus, apskaičiuotos jautrumo, specifiškumo, teigiamos prognostinės (PPV) bei neigiamos prognostinės (NPV) vertės, kurios pateikiamos S-01 lentelėje.

**S-01 lentelė.** Apibendrintos jautrumo, specifiškumo, PPV ir NPV vertės navikinių inkstų audinių identifikavimui taikant HCA, PCA analizės metodus bei parašytą programą. Spektrai registruojami spektrometru Alpha.

	<b>Metodas</b>		
	<b>HCA</b>	<b>PCA</b>	<b>Automatinio audinių atpažinimo programa</b>
Jautrumas	87 %	85 %	81 %
Specifiškumas	98 %	98 %	95 %
PPV	97 %	97 %	94 %
NPV	89 %	87 %	84 %

Naudojant šviesolaidinę spektrinę sistemą buvo registruojami neapdorotų inkstų audinių bei audinių tepinėlių spektrai, į tyrimą įtraukiant 34 pacientus. Audinių tepinėlių spektrai, registruoti naudojant šviesolaidinę spektrinę sistemą, yra ekvivalentūs audinių tepinėlių spektrams, registruotiems naudojant standartinį spektrometrą Alpha: navikinių audinių spektruose stebimos didesnio optinio tankio glikogeną atitinkančios spektrinės juostos ties 1027, 1081 ir 1155  $\text{cm}^{-1}$ . Atlikus statistinę spektrų analizę, įvertintas taikomo metodo tikslumas navikinių audinių atpažinimui (S-02 lentelė).

**S-02 lentelė.** Apibendrintos jautrumo, specifiškumo, PPV ir NPV vertės navikinių inkstų audinių identifikavimui taikant HCA, PCA analizės metodus bei parašytą programą. Spektrai registruojami šviesolaidine spektrine sistema.

	<b>Metodas</b>		
	<b>HCA</b>	<b>PCA</b>	<b>Automatinio audinių atpažinimo programa</b>
Jautrumas	88 %	88 %	88 %
Specifiškumas	100 %	100 %	100 %
PPV	100 %	100 %	100 %
NPV	89 %	89 %	89 %



Palyginus normalaus ir navikinio audinio spektrus, galima pastebėti, jog navikinio audinio spektruose stebimos didesnio optinio tankio glikogenui priskiriamos spektrinės juostos, esančios ties 1027, 1081 ir 1155  $\text{cm}^{-1}$ , ir mažesnio optinio tankio spektrinė juosta, esanti ties 1240  $\text{cm}^{-1}$ , kuri gali būti siejama su fruktozės-1,6-bisfosfazės kiekio sumažėjimu navikiniame audinyje. Yra žinoma, kad ccRCC navikuose fruktozės-1,6-bisfosfazės kiekis sumažėja ir yra siejamas su Warburgo mechanizmo nulemtais metabolizmo pokyčiais audinyje [166], [175], [176]. Navikinių audinių identifikavimo tikslumas įvertintas atlikus statistinę spektrų analizę (taikant HCA ir PCA metodus). Apibendrintos jautrumo, specifiškumo, PPV ir NPV vertės pateikiamos S-03 lentelėje.

**S-03 lentelė.** Apibendrintos jautrumo, specifiškumo, PPV ir NPV vertės navikinių inkstų audinių identifikavimui taikant HCA ir PCA analizės metodus. Spektrai registruojami šviesolaidine spektrine sistema.

	Metodas	
	HCA	PCA
Jautrumas	88 %	91 %
Specifiškumas	100 %	100 %
PPV	100 %	100 %
NPV	89 %	92 %

Palyginus rezultatus, gautus tiriant audinių tepinėlių ir neapdorotų audinių spektrus, galima pastebėti, jog abiejų bandinių tipų atvejais gaunamas panašus navikinių audinių atpažinimo tikslumas. Tai leidžia daryti išvadą, jog abiejų tipų bandiniai (audinių tepinėliai ir neapdoroti audiniai) yra tinkami navikinių audinių identifikavimui, tačiau audiniai yra geresnis pasirinkimas siekiant taikyti metodą audinių identifikavimui chirurginės operacijos metu dėl trumpesnės spektrų registravimo trukmės.

### *Šlapimo pūslės vėžinių audinių tyrimas*

Šlapimo pūslės audiniai buvo tiriami spektrų registravimui naudojant šviesolaidinę spektrinę sistemą analizuojant du bandinių tipus – neapdorotus audinius ir audinių tepinėlius. Į tyrimą įtraukti 54 pacientai.

Svarbiausi spektriniai požymiai, leidžiantys identifikuoti normalius ir navikinius urotelio karcinomos audinius, - kolagenui priskiriamos mažesnio intensyvumo spektrinės juostos esančios ties 1033, 1206, 1240, 1282, 1317 ir 1339  $\text{cm}^{-1}$ , glikogenui priskiriamos didesnio intensyvumo spektrinės juostos ties 1028 ir 1154  $\text{cm}^{-1}$  bei nukleorūgštims priskiriamos didesnio intensyvumo

spektrinės juostos esančios ties 972 ir 1082  $\text{cm}^{-1}$  navikinio audinio spektre. Sumažėjęs kolageno kiekis gali būti siejamas su fermento kolagenazės sekrecija navikiniame audinyje [44]. Padidėjęs glikogeno kiekis yra būdingas kai kuriems navikų tipams ir yra naudojamas kaip energijos šaltinis ląstelių proliferacijai [42], [173]. Padidėjęs nukleorūgščių kiekis siejamas su padidėjusia naviko ląstelių proliferacija. Taikant statistinės analizės metodus (HCA ir PCA) įvertintas metodo tikslumas urotelio karcinomos audinių identifikavimui (S-04 lentelė).

**S-04 lentelė.** Apibendrintos jautrumo, specifiškumo, PPV ir NPV vertės navikinių šlapimo pūslės audinių identifikavimui taikant HCA ir PCA analizės metodus.

	Metodas	
	HCA	PCA
Jautrumas	91 %	91 %
Specifiškumas	98 %	96 %
PPV	98 %	96 %
NPV	92 %	92 %

Svarbiausi požymiai, leidžiantys identifikuoti navikinius urotelio karcinomos audinius tiriant tepinėlius – padidėjęs glikogeno bei nukleorūgščių kiekis audinyje. Padidėjusį glikogeno kiekį navikiniame audinyje iliustruoja didesnio intensyvumo spektrinės juostos, esančios ties 1027 ir 1154  $\text{cm}^{-1}$ , tuo tarpu nukleorūgščių kiekį – spektrinės juostos ties 972, 1082 ir 1242  $\text{cm}^{-1}$ . Taikant HCA ir PCA metodus, įvertintas metodo tikslumas navikinio audinio identifikavimui (S-05 lentelė).

**S-05 lentelė.** Apibendrintos jautrumo, specifiškumo, PPV ir NPV vertės navikinių šlapimo pūslės audinių tepinėlių identifikavimui taikant HCA ir PCA analizės metodus.

	Metodas	
	HCA	PCA
Jautrumas	96 %	89 %
Specifiškumas	83 %	93 %
PPV	85 %	93 %
NPV	95 %	90 %

Palyginus rezultatus, gautus analizuojant neapdorotų audinių ir audinių tepinėlių spektrus, galima pastebėti, jog pasiektas audinių identifikavimo tikslumas yra panašus. Tačiau audinių tepinėlių tyrimas turi keletą trūkumų: ne visais atvejais pavyksta paruošti tinkamos kokybės audinio tepinėlių,

spektrų registravimas trunka ilgiau nei registruojant neapdoroto audinio spektrus. Dėl šių priežasčių, intraoperatyviam audinių tyrimui yra tinkamesni neapdoroti audinių bandiniai.

### ***Kasos vėžinių audinių tyrimas***

Kasos audiniai tiriami spektrų registravimui naudojant šviesolaidinę spektrinę sistemą analizuojant neapdorotus audinius. Į tyrimą įtraukta 60 pacientų.

Kasos navikinių audinių spektruose stebimos mažesnio intensyvumo spektrinės juostos ties 972 ir 1083  $\text{cm}^{-1}$ , priskiriamos nukleorūgštims ir didesnio intensyvumo spektrinės juostos ties 1033, 1207, 1283 ir 1339  $\text{cm}^{-1}$ , priskiriamos kolagenui. Sumažėjęs nukleorūgščių kiekis navikiniame audinyje gali būti siejamas su mažesne kasos adenokarcinomos (PDAC) ląstelių koncentracija navikiniame audinyje [198], o navikuose padidėjęs kolageno kiekis siejamas su naviko desmoplazija [199], [200]. Atlikus statistinę analizę (HCA ir PCA), įvertintas metodo tikslumas navikinių audinių klasifikavimui (S-06 lentelė).

**S-06 lentelė.** Apibendrintos jautrumo, specifiškumo, PPV ir NPV vertės navikinių kasos audinių identifikavimui taikant HCA ir PCA analizės metodus.

	<b>Metodas</b>	
	<b>HCA</b>	<b>PCA</b>
Jautrumas	84 %	87 %
Specifiškumas	73 %	84 %
PPV	76 %	85 %
NPV	82 %	86 %

Siekiant įvertinti metodo tinkamumą intraoperatyviai audinių diagnostikai, spektriniais tyrimais atlikti įrangą perkėlus į patalpą, esančią prie operacinės. Atlikta trijų pacientų atvejo analizė. Visais tirtais atvejais išvados (nustatytas audinio tipas – normalus, navikinis ar pankreatito audinys) atlikus spektrinę analizę ir histologinius tyrimus sutapo, tačiau 66 % nesutapo su pirminės makroskopinės analizės, atliktos operuojančio chirurgo ar gydytojo patologo, išvadomis. Remiantis šiais rezultatais galima teigti, jog taikomo metodo tikslumas yra didesnis už makroskopinės analizės tikslumą.

## *Kepenų vėžinių audinių tyrimas*

Kepenų audiniai tiriami spektrų registravimui naudojant šviesolaidinę spektrinę sistemą analizuojant neapdorotus audinius. Į tyrimą įtraukti 46 pacientai.

Kepenų navikinių audinių spektruose stebimos pakitusios glikogenui ir kolagenui priskiriamų spektrinių juostų optinio tankio vertės priklausomai nuo naviko tipo. Cholangioceliulinės karcinomos audinių spektruose stebimos padidėjusios kolagenui priskiriamų spektrinių juostų, esančių ties 1034, 1207, 1240, 1283 ir 1317  $\text{cm}^{-1}$ , optinio tankio vertės, atitinkančios kolageno kiekio padidėjimą navikiniame audinyje, nulemtą naviko desmoplazijos [208], [219]–[221] bei sumažėjusios spektrinių juostų, esančių ties 1027 ir 1155  $\text{cm}^{-1}$ , optinio tankio vertės parodančios glikogeno kiekio sumažėjimą nulemtą skirtingų ląstelių, sudarančių normalius kepenų ir cholangioceliulinės karcinomos audinius, prigimties. Hepatoceliulinės karcinomos atveju stebimi glikogeno kiekio audinyje pakitimai, kurie nėra sistemingi. Atlikus statistinę analizę (HCA ir PCA), įvertintas metodo tikslumas navikinių audinių klasifikavimui (S-07 lentelė).

**S-07 lentelė.** Apibendrintos jautrumo, specifiškumo, PPV ir NPV vertės navikinių kepenų audinių identifikavimui taikant HCA ir PCA analizės metodus.

	Metodas	
	HCA	PCA
Jautrumas	74 %	72 %
Specifiškumas	80 %	82 %
PPV	78 %	79 %
NPV	77 %	76 %

## IŠVADOS

1. Taikoma šviesolaidinė spektrinė sistema yra tinkama įvairių tipų audinių bandinių - šviežiai rezekuotų neapdorotų audinių ir audinių tepinėlių - spektrų registravimui. S/N vadinamojoje pirštų antspaudų spektrinėje srityje yra didesnis nei 40, kas yra tinkama informatyvių spektrų registravimui. Tyrimo metu nustatyta, jog IR spinduliuotės įsiskverbimo į bandinį gylis siekia 0,5 – 1,9  $\mu\text{m}$ ; tai yra pakankamas gylis siekiant užregistruoti spektrus, kuriuose būtų stebima informacija

- apie abiejų audinių komponentų (ląstelių ir neląstelinių struktūrų, tokių kaip tarpląstelinis užpildas (ECM)) biocheminę sudėtį.
2. Svarbiausi spektriniai žymenys, leidžiantys identifikuoti navikinius inkstų audinius, yra padidėjusios spektrinių juostų, esančių ties 1027 ir 1155  $\text{cm}^{-1}$ , priskiriamų glikogenui, optinio tankio vertės bei sumažėjusios spektrinių juostų, esančių ties 972 ir 1240  $\text{cm}^{-1}$ , optinio tankio vertės, susijusios su fruktozės-1,6-bisfosfatazės sumažėjimu vėžiniuose inkstų audiniuose. Taikant statistinės analizės metodus gautos jautrumo ir specifiškumo vertės navikinių inkstų audinių identifikavimui siekia iki 91 % ir 100 % atitinkamai.
  3. Svarbiausi spektriniai žymenys, leidžiantys identifikuoti navikinius šlapimo pūslės audinius, yra padidėjusios spektrinių juostų, esančių ties 1028 ir 1154  $\text{cm}^{-1}$ , priskiriamų glikogenui, optinio tankio vertės bei sumažėjusios spektrinių juostų, esančių ties 1033, 1206, 1240, 1282, 1317 ir 1339  $\text{cm}^{-1}$ , priskiriamų kolagenui, optinio tankio vertės. Taikant statistinės analizės metodus gautos jautrumo ir specifiškumo vertės navikinių šlapimo pūslės audinių identifikavimui siekia iki 91 % ir 98 % atitinkamai.
  4. Navikiniai kasos audiniai gali būti identifikuojami pagal spektro kontūrą spektrinėje srityje nuo 1000 iki 1083  $\text{cm}^{-1}$ , kur stebimos spektrinės juostos, priskiriamos angliavandeniams, baltymams ir nukleorūgštims. Sumažėjusios spektrinių juostų, esančių ties 972 ir 1083  $\text{cm}^{-1}$ , optinio tankio vertės siejamos su sumažėjusiu nukleorūgščių kiekiu, tuo tarpu padidėjusios spektrinių juostų, esančių ties 1033, 1207, 1283 ir 1339  $\text{cm}^{-1}$ , optinio tankio vertės siejamos su padidėjusiu kolageno kiekiu kasos navikiniuose audiniuose. Taikant statistinės analizės metodus gautos jautrumo ir specifiškumo vertės navikinių kasos audinių identifikavimui siekia iki 87 % ir 84 % atitinkamai.
  5. Navikiniai kepenų audiniai gali būti identifikuojami pagal pasikeitusį glikogeno, kuriam priskiriamos spektrinės juostos stebimos ties 1027 ir 1155  $\text{cm}^{-1}$ , ir kolageno, kuriam priskiriamos spektrinės juostos stebimos ties 1034, 1207, 1240, 1283 ir 1317  $\text{cm}^{-1}$ , kieki audiniuose priklausomai nuo naviko tipo. Taikant statistinės analizės metodus gautos jautrumo ir specifiškumo vertės navikinių kepenų audinių identifikavimui siekia iki 74 % ir 80 % atitinkamai.
  6. Esamo technologinio išvystymo lygio šviesolaidinė spektrinė sistema gali būti naudojama navikinių audinių identifikavimui atvirų operacijų metu atlikus klinikinius tyrimus.

## ACKNOWLEDGEMENTS

PhD studies was an interesting few-year journey full of challenges and lessons. This journey would not be successful without collaboration and support of other people. Thus, I would like to express my sincere gratitude for all the people who were by my side during this journey and thanks to whom it was possible.

First of all, I would like to thank my supervisor prof. Justinas Čėponkus for his guidance and help in the research, for his support and advice, shared knowledge and encouragement. I would like to thank other colleagues from the Institute of Chemical Physics of Vilnius University as well – prof. Valdas Šablinskas, dr. Vidita Urbonienė, dr. Kęstutis Aidas. Many thanks go to the *Molekulė* team – Martynas, Dovilė, Rasa, Sonata, Gerda and Jogilė for a friendly atmosphere, moral support, warm conversations and fruitful discussions. You always brightened up the days in the office. I would like to thank the colleagues from Vilnius University Hospital Santaros Clinics, especially Gediminas for the help collecting tissue samples.

I would like to express my gratitude to colleagues from Dresden University of Technology, especially to prof. Gerald Steiner and dr. Christian Teske for guiding the research, shared knowledge and experience, warm acceptance and concern during my stay in Dresden. I would like to thank Katja, Daniel and Dylan for the help collecting tissue samples and help while working in the lab. I would like to thank the KSM group for the friendliness.

I would like to express my sincere gratitude to my family: parents Rita and Juozas, sister Gabrielė, grandmothers Janinas for their unconditional support, help, believing in me and all the valuable advice given in difficult situations. I would like to thank my close friends Viktorija A., Viktorija L. and Barbora for being by my side.

Finally, I would like to thank all the patients who gave their consent to participate in the study presented in this thesis and surgeons for the collaboration and the important work saving people's lives.

## CURRICULUM VITAE

**Name:** Rimantė  
**Surname:** Bandzevičiūtė  
**E-mail:** rimante.bandzeviciute@gmail.com

### Education:

2018-2022 Vilnius University, Faculty of Physics  
*Ph.D studies*  
2016-2018 Vilnius University, Faculty of Physics  
*Master degree, Magna Cum Laude*  
2012-2016 Vilnius University, Faculty of Physics  
*Bachelor degree, Cum Laude*

### Work experience:

2018-present Vilnius University, Institute of Chemical Physics,  
*Lecturer*  
2018 Vilnius University, Institute of Chemical Physics,  
*Technician*  
2016-2018 Vilnius University, Institute of Chemical Physics,  
*Engineer*

### Traineeships:

2021 October – Technische Universität Dresden, University Hospital  
2021 December, Carl Gustav Carus, Department of Visceral, Thoracic  
2022 March – and Vascular Surgery,  
2022 June *Research Assistant*  
  
2019 October – Technische Universität Dresden, Faculty of Medicine,  
2019 December Department of Anaesthesiology and Critical Care  
Medicine, Clinical Sensing and Monitoring,  
*Trainee*  
  
2018 July – 2018 Technische Universität Dresden, Faculty of Medicine,  
August Department of Anaesthesiology and Critical Care  
Medicine, Clinical Sensing and Monitoring,  
*Student Asssistant*

**Other:**

2019-2022	Member of organizing comitee of International Conference for Students of Physics and Natural Sciences ‘Open Readings’
2021-2022	Member of SPIE student chapter of Vilnius University
2021	Member of OSA student chapter of Vilnius University



## NOTES

## NOTES

## NOTES

Vilniaus universiteto leidykla  
Saulėtekio al. 9, III rūmai, LT-10222 Vilnius  
El. p. [info@leidykla.vu.lt](mailto:info@leidykla.vu.lt), [www.leidykla.vu.lt](http://www.leidykla.vu.lt)  
[bookshop.vu.lt](http://bookshop.vu.lt), [journals.vu.lt](http://journals.vu.lt)  
Tiražas 30 egz.